



MECHANICAL TESTING OF ULTRA-HIGH TEMPERATURE CERAMICS

AT 1500°C IN AIR –

DEVELOPMENT OF AN EXPERIMENTAL FACILITY AND TEST METHOD

DISSERTATION

Sheena L. Winder, Major, USAF

AFIT-ENY-DS-15-M-259

DEPARTMENT OF THE AIR FORCE
AIR UNIVERSITY

Air Force Institute of Technology

Wright-Patterson Air Force Base, Ohio

DISTRIBUTION STATEMENT A.
APPROVED FOR PUBLIC RELEASE; DISTRIBUTION UNLIMITED

The views expressed in this dissertation are those of the author and do not reflect the official policy or position of the United States Air Force, Department of Defense, or the United States Government.

This material is declared a work of the U.S. Government and is not subject to copyright protection in the United States.

AFIT-ENY-DS-15-M-259

MECHANICAL TESTING OF ULTRA-HIGH TEMPERATURE CERAMICS AT
1500°C IN AIR –
DEVELOPMENT OF AN EXPERIMENTAL FACILITY AND TEST METHOD

DISSERTATION

Presented to the Faculty

Graduate School of Engineering and Management

Air Force Institute of Technology

Air University

Air Education and Training Command

In Partial Fulfillment of the Requirements for the

Degree of Doctor of Philosophy

Sheena L. Winder, BS, MS

Major, USAF

March 2015

AFIT-ENY-DS-15-M-259

MECHANICAL TESTING OF ULTRA-HIGH TEMPERATURE CERAMICS
AT 1500°C IN AIR –
DEVELOPMENT OF AN EXPERIMENTAL FACILITY AND TEST METHOD

Sheena L. Winder, BS, MS
Major, USAF

Committee Membership

Dr. Marina B. Ruggles-Wrenn Chairman
Chair

Dr. Robert L. Hengehold
Member

Dr. Larry W. Burggraf
Member

ADEDEGI B. BADIRU, PhD
Dean, Graduate School of Engineering
And Management

Abstract

With a melting point in excess of 3000°C and a high density, ultra-high temperature ceramics (UHTCs) are a candidate material for hypersonic flight vehicles, atmospheric re-entry vehicles, and rocket propulsion systems. When ceramics are under consideration as a structural material, creep is an important design criterion and frequently a life-limiting condition. However, the characterization of mechanical behavior at temperatures in excess of 1300°C has many challenges to overcome. Of utmost importance is the selection of materials for test fixtures within the test environment. Materials selected must maintain their structural integrity at required temperatures in extreme environments over long durations. In addition, thermo-chemical interaction between the test material and the test fixtures are to be expected at these temperatures. Materials selected must not cause degradation of the test material or interfere with the acquisition of data.

An Experimental Facility and Test Method were developed for the mechanical testing of hafnium diboride (HfB_2)-UHTCs at 1500°C in air. The thermal compatibility of HfB_2 with SX YAG, Pt foil, and alumina was investigated. Exploratory creep tests of hafnium diboride (HfB_2)-UHTCs validated single-crystal (SX) yttrium aluminum garnet (YAG) pushrods as acceptable for the application of a constant load over long durations. Platinum foil proved unstable in the presence of HfB_2 at 1500°C, rendering it unsuitable as an interlayer between HfB_2 and SX YAG. Exploratory testing also validated high purity alumina spacers for utilization in the prevention of the thermo-chemical interaction

between HfB₂ and SX YAG. The results of this research represent a significant contribution towards the use of UHTCs in extreme environments associated with hypersonic flight and atmospheric re-entry.

With God All Things Are Possible

Thank you for my mom and dad.

Thank you for the love and support of my husband and two little boys in achieving this milestone. It was crazy, but it would have been miserable without seeing their faces and hearing their laughter.

Acknowledgements

I express my sincere appreciation to my research advisor, Dr. Marina Ruggles-Wrenn, for her guidance, mentorship, and tremendous support throughout the course of the ups and downs of my research. I extend a thank you to Dr. Larry Burggraf and Dr. Robert Hengehold for agreeing to serve as members of my committee, as well as their insight. I would like to thank my supervisor, Diana Carlin, for her patience and support. I would, also, like to thank my sponsor, Dr. Ali Sayir, Program Director, from the Air Force Office of Scientific Research for his continued support of this research endeavor.

Thank you to all the men and women of AFIT, AFRL, UES, and Wright State University who provided immeasurable assistance through this endeavor. I thank my mom for her assistance with time and polishing.

I want everybody to know my appreciation for my husband who was there every step of the way. He got to polish specimens, setup experiments, pull all-nighters, listen to presentation, and endlessly edit. He was a key to my success.

Thank you.

Table of Contents

Abstract.....	iv
Dedication.....	vi
Acknowledgements.....	vii
Table of Contents.....	viii
List of Figures.....	xii
List of Tables.....	xxiv
I. Introduction.....	1
1.1 Organization of Dissertation.....	1
1.2 Materials for Hypersonic Flight.....	2
1.3 Ultra-High Temperature Ceramics (UHTCs)	5
1.4 Problem Statement	8
1.5 Material Description	9
1.6 Methodology	11
II. Background....	12
2.1 Ultra-High Temperature Ceramics (UHTCs)	12
2.2 Synthesis of Diboride-Based UHTCs	13
2.3 Densification of Diboride-Based UHTCs	14
2.4 Oxidation of Diboride-Based UHTCs	17
2.5 Model Framework and Formulation	21
2.6 Mechanical Behavior of Diboride-Based UHTCs	22
2.7 Thermo-chemical Compatibility and Mechanical Behavior of Diboride-Based UHTCs	25
2.8 Implications for Current Research	28

III. Research Plan and Implementation.....	29
3.1 Research Materials.....	30
3.1.1 HfB ₂ -containing UHTCs	31
3.1.2 Load Train Materials	34
3.2 Characterization of HfB ₂ Specimens with Varying SiC Content	34
3.2.1 Density.....	35
3.2.2 Microstructure	36
3.2.3 Grain Size	38
3.2.4 Physical Dimensions	39
3.3 Experimental Facility.....	39
3.4 Test Methodology	48
3.4.1 Testing Facility Temperature Calibration	49
3.4.2 Obtaining High Temperature Strain Measurements.....	52
3.5 Interactions within the Test Environment between Test Fixtures and HfB ₂	53
IV. High Temperature Compatibility of HfB ₂ with Pt Foil, SX YAG, and Alumina.....	58
4.1 Thermal Compatibility of HfB ₂ and Pt Foil at 1500°C and 1600°C in Air	58
4.1.1 Thermal Compatibility of HfB ₂ and Pt at 1500°C and 1600°C in Air – Experimental Setup.....	59
4.1.2 Thermal Compatibility of HfB ₂ and Pt Foil during Compression Creep – Test 1 Analysis.....	60
4.1.3 Thermal Compatibility of HfB ₂ and Pt Foil in the Presence of SX YAG under Zero Load – Test 2 Analysis.....	65
4.1.4 Thermal Compatibility of HfB ₂ and Pt Foil under Zero Load – Test 3 Analysis.....	69
4.1.5 Thermal Compatibility of HfB ₂ , Pt Foil, and SX YAG at 1600°C in Air under Zero Load – Test 4 Analysis.....	72

4.1.6 Thermal Compatibility of HfB ₂ and Pt at 1500°C and 1600°C in Air – Discussion	74
4.2 Thermo-chemical Compatibility of HfB ₂ with SX YAG at 1500°C in Air	77
4.2.1 Thermo-chemical Compatibility of HfB ₂ with SX YAG at 1500°C in Air – Experimental Setup.....	77
4.2.2 Thermo-chemical Compatibility of HfB ₂ with SX YAG at 1500°C in Air – HfB ₂ in Contact with SX YAG (Case A).....	78
4.2.3 Thermo-chemical Compatibility of HfB ₂ with SX YAG at 1500°C in Air – HfB ₂ Separated from SX YAG by Alumina (Case B and Case C).....	85
4.2.4 Thermo-chemical Compatibility of HfB ₂ with SX YAG at 1500°C in Air – HfB ₂ in Close Proximity but Not in Contact with SX YAG (Case D)	90
4.2.5 Thermo-chemical Compatibility of HfB ₂ with SX YAG at 1500°C in Air – HfB ₂ in Contact with SX YAG and another HfB ₂ specimen Approximately 3 mm apart from SX YAG (Case E).....	92
4.2.6 Thermo-chemical Compatibility of HfB ₂ with SX YAG at 1500°C in Air – Discussion.....	97
4.3 High Temperature Compatibility of HfB ₂ with Pt Foil, SX YAG, and Alumina.....	103
V. Validation of Experimental Test Facility and Test Method.....	106
5.1 Creep Specimen Interaction with Alumina.....	108
5.2 CTE and Thermal Strain Comparisons at 1500°C in Air	111
5.2.1 HfB ₂ - CTE and Thermal Strain	111
5.2.2 HfB ₂ - 20 vol% SiC - CTE and Thermal Strain	113
5.3 Pilot Compression Creep Tests at 1500°C in Air	115
5.3.1 Pilot Compression Creep Tests – HfB ₂	116
5.3.2 Pilot Compression Creep Tests – HfB ₂ – 10, 20 vol% SiC.....	120
VI. Oxidation and Recession of HfB ₂ -containing UHTCs at 1500°C in Air	124
6.1 Oxidation of HfB ₂ under Compressive Load at 1500°C in Air	127
6.2 Oxidation of HfB ₂ -20 vol% SiC under Compressive Load at 1500°C in Air ..	142

VII. Concluding Remarks	150
Appendix A: Oxidation Model Framework and Formulation	155
Appendix B: Creep in Ceramics	167
Appendix C: Specimen Appearance after Compression Creep Testing at 1500°C in Air.....	173
Appendix D: Compression Creep Tests at 1500°C	181
Appendix E: Characterization Equipment Used	186
Appendix F: Sample Preparation	188
Appendix G: Archimedes Method	196
Appendix H: Isolating SX YAG	198
Appendix I: Catalysis.....	201
Appendix J: Gibbs Free Energy	204
Appendix K: Electron Charging	207
Appendix L: Specimen Damage	210
Appendix M: Load Train	214
Appendix N: Heat Treatment at 1500°C in an Argon Environment.....	216
References	218

List of Figures

	Page
Fig. 1. A comparison of the melting temperatures and specific gravities of selected materials. Several borides, nitrides and carbides have melting temperatures exceeding 3000°C and are considered UHTCs. (After Ushakov <i>et al.</i> [12] and Fahrenholtz [13]). ...	5
Fig. 2. Schematic of the oxidation products formed during oxidation of HfB ₂ at temperatures in the 1000-1800°C range. (Parthasarathy <i>et al.</i> [104], Used with permission).....	19
Fig. 3. HfB ₂ -SiC. SEM micrograph courtesy of C. Carney (AFRL/RXLN).	33
Fig. 4. HfB ₂ -SiC. TEM micrograph courtesy of R. S. Hay (AFRL/RXCC).	33
Fig. 5. Schematic of HfB ₂ -based UHTC test specimen.	34
Fig. 6. Schematic of Archimedes density apparatus.	36
Fig. 7. SEM micrographs showing microstructure of (a) HfB ₂ -a, (b) HfB ₂ -c, (c) HfB ₂ -20SiC-a, and (d) HfB ₂ -20SiC-c.	37
Fig. 8. EBSD micrographs for various HfB ₂ -containing campaigns. (a) HfB ₂ -a, (b) HfB ₂ -c, (c) HfB ₂ -10SiC, (d) HfB ₂ -20SiC-a, and (e) HfB ₂ -20SiC-c.	39
Fig. 9. (a) Single zone resistance heated furnace and (b) "pie slice" door for furnace.	41
Fig. 10. (a) Schematic of extensometer rod placement on test specimen, and (b) photograph of extensometer and rods in place during high temperature testing.	42
Fig. 11. (a) A MoSi ₂ heating element, and (b) in place MoSi ₂ heating elements.	44
Fig. 12. Alumina blocks supporting the MoSi ₂ elements on the exterior of the furnace.	44
Fig. 13. Fans provide additional cooling to the end rods of the MoSi ₂ elements outside the furnace.	44
Fig. 14. Foil-backed alumina wrapped around Experimental Facility for testing of UHTC specimens at 1300-1600°C.	45
Fig. 15. Cooling coils wrapped around the MTS hydraulic wedge grips.	46
Fig. 16. Alumina extensometer rods that were deformed after 14.9 hrs at 1500°C under a 25 MPa load for 14.1 hrs.	46

Fig. 17. Furnace support structure and rail system. (a) Back view of furnace support, (b) side view of furnace support, and (c) side view of furnace support with furnace in place. The top of the rail is highlighted in red for orientation.....	48
Fig. 18. Experimental set-up for compression testing of HfB ₂ -SiC specimens.....	50
Fig. 19. Temperature calibration of experimental facility for testing of UHTC specimens at 1300-1600°C.	51
Fig. 20. Schematics of (a) originally-planned extensometer location and (b) final Test Method extensometer location.	53
Fig. 21. (a) Schematic of initial validation test of HfB ₂ . and (b) Photograph of HfB ₂ -1a specimen after ~15 hrs at 1500°C in laboratory air under a 25 MPa compressive stress..	54
Fig. 22. EDS line analysis of (a) Hf, (b) O, (c) Al, and (d) Y returns of HfB ₂ -1a specimen after 14.9 hrs at 1500 °C under a compressive load of 25 MPa for 14.1 hrs in the presence of SX YAG and Pt foil. Al- and Y-containing deposits are limited to the deposit region.	55
Fig. 23. SEM micrographs showing deposits seen on surface of Pt foil.	55
Fig. 24. (a) Photograph of HfB ₂ -3a after aborted test run to 1500°C for 1 hr, followed by 1 hr temperature fluxuation from 900 - 1500 °C and (b) Photograph of HfB ₂ -3a after test run at 1500°C for 7.3 hrs at 1500°C under a compressive load (25, 50 MPa) for 6.2 hrs.	56
Fig. 25. Micrograph of x-ray count returns of cross-section, indicating Al- and Y-containing deposit is limited to the surface of the oxide layer.	57
Fig. 26. SEM micrograph showing as-processed HfB ₂ sample annotating several of the empty grain boundaries.....	59
Fig. 27. Schematic drawing of the heat treatment experimental setup for HfB ₂ and Pt interaction evaluation. (a) (b) HfB ₂ and SX YAG separated by Pt foil under no load, (b) HfB ₂ in contact with Pt foil only, and (c) Pt-wrapped HfB ₂	60
Fig. 28. (a) SEM micrograph and (b) EDS Pt map analysis of area of contact between HfB ₂ specimen and Pt foil/SX YAG pushrod after 7.3 hrs at 1500°C under a compressive load (25, 50 MPa) for 6.2 hrs. There is not any discernible Pt present at this interface. Note that the HfB ₂ oxidized, forming a HfO ₂ layer. There was also a layer containing Al, Hf, O, and Y.....	62
Fig. 29. (a) SEM micrograph of unoxidized bulk of HfB ₂ specimen after 7.3 hrs at 1500°C under a compressive load (25, 50 MPa) for 6.2 hrs in the presence of SX YAG and Pt foil. Several areas of Pt-containing species in the HfB ₂ grain boundaries have been annotated. (b) EDS spectra of Pt-containing area.	63

Fig. 30. SEM micrograph showing deposits on Pt foil of HfB ₂ specimen after 7.3 hrs at 1500°C, 6.2 hrs under a compressive load (25, 50 MPa) in the presence of SX YAG. Post-test, intact Pt foil has been annotated.....	63
Fig. 31. TEM micrograph of Pt in triple point in unoxidized bulk of HfB ₂ specimen after 7.3 hrs at 1500°C, 6.2 hrs under a compressive load (25, 50 MPa) in the presence of SX YAG.....	64
Fig. 32. TEM micrograph of Pt in grain boundary in unoxidized bulk of HfB ₂ specimen after 7.3 hrs at 1500°C, 6.2 hrs under a compressive load (25, 50 MPa) in the presence of SX YAG.....	64
Fig. 33. TEM micrograph of chunk of Pt in grain boundary in unoxidized bulk of HfB ₂ specimen after 7.3 hrs at 1500°C, 6.2 hrs under a compressive load (25, 50 MPa) in the presence of SX YAG.	65
Fig. 34. Photographs of HfB ₂ specimen after 24 hrs at 1500°C under zero load in the presence of SX YAG and Pt foil. A crustaceous white deposit has formed over the entire surface of the HfB ₂ specimen. (a) Top and side view. (b) Annotated image of original vicinity of Pt foil on the bottom of the HfB ₂ specimen.	66
Fig. 35. EDS wide-area analysis of original area of Pt foil on deposit on HfB ₂ specimen after 24 hrs at 1500°C under no load in the presence of SX YAG. It is covered in the white deposit comprised of Al, C, Hf, O, and Y. Note the lack of a distinct Pt peak.....	67
Fig. 36. Reflected light optical micrograph of cross-section of HfB ₂ specimen after 24 hrs at 1500°C under no load in the presence of SX YAG and Pt foil. Note that no Pt foil is evident in the original area of contact of the Pt foil with the HfB ₂ specimen and that the deposit in this area is thinner than the surfaces of the HfB ₂ specimen exposed to the tube furnace environment.	68
Fig. 37. SEM micrograph showing cross-sections of the (a) surface exposed to the tube furnace environment and (b) HfB ₂ and Pt foil/SX YAG contact area of HfB ₂ specimen exposed to tube furnace environment after 24 hrs at 1500°C under no load in the presence of Pt foil and SX YAG.....	68
Fig. 38. EDS map analysis of Al and Y locations in the cross-section of the HfB ₂ and Pt foil/SX YAG contact area of HfB ₂ specimen exposed to tube furnace environment after 24 hrs at 1500°C under zero load in the presence of Pt foil and SX YAG	69
Fig. 39. SEM micrograph showing unoxidized bulk of HfB ₂ specimen after 24 hrs at 1500°C under zero load in the presence of Pt foil and SX YAG. Pt-containing species are found in many of the HfB ₂ grain boundaries.	69
Fig. 40. Optical micrograph of HfB ₂ specimen after 24 hrs at 1500°C under zero load and without the presence of SX YAG.....	70

Fig. 41. Cross-sectional SEM micrograph of the surface of the HfB ₂ specimen exposed to the tube furnace environment after heat treatment with Pt for 24 hrs at 1500°C in air.	71
Fig. 42. Annotated SEM micrograph showing HfB ₂ oxidized while in contact with Pt under no load at 1500°C for 24 hrs without the presence of SX YAG. Platinum containing species (arrows) are seen in the grain boundaries throughout the unoxidized HfB ₂ .	71
Fig. 43. SEM micrograph showing cross-section of Pt-wrapped HfB ₂ topped with SX YAG after 24 hrs at 1600°C in tube furnace in air.	73
Fig. 44. EDS map of (a) Hf and (b) Pt in Test 4.	73
Fig. 45. Schematic diagram of solid-solid and solid-liquid interface energies. (After Clark [145], Used with permission).	77
Fig. 46. Schematic drawing of the heat treatment experimental setup: (Case A) HfB ₂ in contact with SX YAG, (Case B) HfB ₂ and SX YAG separated by alumina spacer, (Case C) HfB ₂ specimen separated from SX YAG by a very large 3-mm-thick 99.8% pure alumina spacer, (Case D) HfB ₂ specimen in close proximity (~3 mm) but not in contact with SX YAG, and (Case E) one piece of HfB ₂ was placed in direct contact with SX YAG and another approximately 3 mm apart from SX YAG.	78
Fig. 47. Photographs of HfB ₂ after heat treatment in contact with SX YAG for 12 hrs at 1500°C in air. (a) HfB ₂ surface exposed to furnace environment and (b) HfB ₂ surface that was in contact with SX YAG.	80
Fig. 48. Photographs of HfB ₂ after heat treatment in contact with SX YAG for 18 hrs at 1500°C in air. (a) HfB ₂ surface exposed to furnace environment and (b) HfB ₂ surface that was in contact with SX YAG.	80
Fig. 49. XRD of HfB ₂ surface exposed to the furnace environment. HfB ₂ heat treated in contact with SX YAG for 18 hrs at 1500°C in air. c-YSH and PX YAG phases are readily identified.	81
Fig. 50. Photograph of surface of SX YAG in direct contact with HfB ₂ for 18 hrs at 1500°C in the tube furnace when HfB ₂ and SX YAG were in contact.	82
Fig. 51. SEM micrographs showing HfB ₂ cross-section after heat treatment in contact with SX YAG for 12 hrs at 1500°C in air. (a) Cross-sectional view. (b) HfB ₂ surface exposed to furnace environment. Note the three regions: unoxidized HfB ₂ , HfO ₂ scale, and a crustaceous deposit.	83
Fig. 52. SEM micrographs showing HfB ₂ cross-section after heat treatment in contact with SX YAG for 18 hrs at 1500°C in air. (a) Cross-sectional view. (b) HfB ₂ surface exposed to furnace environment. Note the three regions: unoxidized HfB ₂ , HfO ₂ scale, and a crustaceous deposit.	84

Fig. 53. EDS line analysis of specimen after heat treatment in contact with SX YAG for 12 hrs at 1500°C in air. The EDS line analysis showing level of presence of Al, Y, and Hf in the unoxidized HfB ₂ , in the HfO ₂ scale and in the crustaceous layer. Note that the Al- and Y-containing deposit resides on the surface of the oxide scale.	85
Fig. 54. HfB ₂ after heat treatment in contact with SX YAG for 18 hrs at 1500°C in air. The EDS map analysis showing areas of Al, Y, and Hf. Note that the Al- and Y-containing deposit resides on the surface of the oxide scale.	85
Fig. 55. Photographs of HfB ₂ heat treated for 18 hrs at 1500°C in air with Al ₂ O ₃ separating the HfB ₂ from SX YAG. (a) HfB ₂ surface exposed to furnace environment, (b) HfB ₂ surface that was in contact with Al ₂ O ₃ . (Case B)	87
Fig. 56. Photographs of HfB ₂ heat treated for 18 hrs at 1500°C in air with large alumina spacer separating the HfB ₂ from SX YAG. (a) HfB ₂ surface exposed to furnace environment, (b) HfB ₂ surface that was in contact with Al ₂ O ₃ . (Case C)	87
Fig. 57. HfB ₂ heat treated for 18 hrs at 1500°C in air with alumina separating the HfB ₂ from SX YAG. XRD return of the HfB ₂ surface exposed to the furnace environment shows m-HfO ₂ , YBO ₃ and Al ₂ O ₃ phases.....	88
Fig. 58. SEM micrographs of HfB ₂ heat treated for 18 hrs at 1500°C in air with alumina separating the HfB ₂ from SX YAG. (a) Cross-sectional view. (b) HfB ₂ surface exposed to furnace environment. (c) HfB ₂ surface that was in contact with alumina.	89
Fig. 59. SEM micrographs of HfB ₂ heat treated for 18 hrs at 1500°C in air with very large alumina spacer separating the HfB ₂ from SX YAG. (a) Cross-sectional view. (b) HfB ₂ surface exposed to furnace environment. (c) HfB ₂ surface that was in contact with alumina.....	90
Fig. 60. Photograph of HfB ₂ heat treated for 18 hrs at 1500°C in air in close proximity (~3 mm) but not in contact with SX YAG.....	91
Fig. 61. SEM micrographs of HfB ₂ specimen heat treated for 18 hrs at 1500°C in air in close proximity (~3 mm) but not in contact with SX YAG. SEM micrographs of the HfB ₂ surface, (a) red-hued and (b) cream-colored areas of Fig. 60.....	91
Fig. 62. SEM micrographs of HfB ₂ heat treated for 18 hrs at 1500°C in air in close proximity (~3 mm) but not in contact with SX YAG. (a) Cross-sectional view. (b) HfB ₂ surface facing SX YAG. (c) HfB ₂ surface facing away from SX YAG.	92
Fig. 63. Photographs of one piece of HfB ₂ in contact with SX YAG and another, approximately 3 mm apart from SX YAG after heat treatment for 18 hrs at 1500°C in air. (a) In-contact HfB ₂ surface exposed to furnace environment, (b) In-contact HfB ₂ surface that was in contact with SX YAG, (c) In-proximity HfB ₂ surface exposed to furnace environment, and (d) In-proximity HfB ₂ surface that was in proximity.....	93

Fig. 64. XRD return of surfaces exposed to the tube furnace environment of a) HfB ₂ in contact with SX YAG in the presence of another HfB ₂ and (b) HfB ₂ in the presence of HfB ₂ in contact with SX YAG.....	95
Fig. 65. SEM micrographs of (a) pink-hued and (b) yellow-hued area and (c) XRD returns of atomic percentage of Al of surface of HfB ₂ separated from HfB ₂ in contact with SX YAG by air and exposed to tube furnace air environment for 18 hrs at 1500°C.	96
Fig. 66. SEM micrograph of cross-section of one piece of HfB ₂ in contact with SX YAG with another (not pictured), approximately 3 mm apart from SX YAG after heat treatment for 18 hrs at 1500°C in air.	96
Fig. 67. Schematic showing surface deposits produced during heat treatment for 18 hrs at 1500°C in air: (a) HfB ₂ in contact with SX YAG, (b) HfB ₂ and SX YAG separated by alumina spacer, (c) HfB ₂ in close proximity (~3 mm) but not in contact with SX YAG..	97
Fig. 68. SEM micrograph of gaseous products that condensed on surfaces of Pt foil	98
Fig. 69. Schematic of surface layer of HfO ₂ with hydroxyl groups.	103
Fig. 70 Schematic drawings of (a) original test method load train utilizing Pt foil and (b). revised test method load train utilizing alumina.	105
Fig. 71. Photographs and optical micrographs of representative examples of crust found on compression samples. (a) HfB ₂ -a, (b) HfB ₂ -c, (c) HfB ₂ -10 vol% SiC, and (d) HfB ₂ -20 vol% SiC.	108
Fig. 72. Photographs of (Left) As-provided alumina spacer, (center) alumina spacer in contact with HfB ₂ and exposed to an air environment for 18 hrs at 1500°C, and (right) alumina spacer in an argon environment for 18 hrs at 1500°C.....	109
Fig. 73. Volatility diagram for B-B ₂ O ₃ at 227°C as calculated in Opeka <i>et al.</i> [22]. (Reprinted with permission.)	110
Fig. 74. Volatility diagram for Al-Al ₂ O ₃ at 227°C as calculated in Opeka <i>et al.</i> [22]. (Reprinted with permission.)	110
Fig. 75. Thermal strains of HfB ₂ from room temperature to 1500°C to include approximately 1 hr of thermal soak.	112
Fig. 76. Thermal strains of HfB ₂ -20 vol% SiC from room temperature to 1500°C to include approximately 1 hr of thermal soak.	114
Fig. 77. Example plot to determine creep equation stress exponent.....	116
Fig. 78. Minimum creep rate as a function of applied stress for HfB ₂ specimens at 1500°C in air.	117

Fig. 79. Minimum creep rate as a function of applied stress (sans 75 MPa compressive tests) for HfB ₂ specimens at 1500°C in air.	118
Fig. 80. Normalized minimum creep rates as a function of applied stress for HfB ₂ specimens at 1500°C in air.	119
Fig. 81. Normalized steady-state creep rate as a function of applied stress (sans 75 MPa compressive tests) for HfB ₂ specimens at 1500°C in air.	119
Fig. 82. Minimum creep rate as a function of applied stress for HfB ₂ -20 vol% SiC specimens at 1500°C in air.	122
Fig. 83. Normalized minimum creep rate as a function of applied stress for HfB ₂ -20 vol% SiC specimens at 1500°C in air.	123
Fig. 84. SEM micrographs of columnar oxide scale on HfB ₂ heat treated at 1500°C (a) alone under zero load, (b) in contact with Pt under zero load, (c) separated from SX YAG by alumina under zero load, and (d) separated from SX YAG by alumina under 25 MPa compression	125
Fig. 85. SEM micrographs of equiaxed oxide scale on HfB ₂ heat treated (a) in direct contact with SX YAG and (b) separated from SX YAG by alumina under higher compressive loads.	126
Fig. 86. Oxidation thicknesses of HfB ₂ specimens under various compressive loads at 1500°C in air. MP represents the model prediction curve.	127
Fig. 87. Oxidation curves of various HfB ₂ microstructures under various compressive loads at 1500°C in air. Points without labels are the tube furnace heat treatment results. MP represents the model prediction curve.....	129
Fig. 88. Recession curves of various HfB ₂ microstructures under various compressive loads at 1500°C in air. MP represents the model prediction curve.....	129
Fig. 89. SEM micrograph of as-provided HfB ₂ -a campaign with several (a) HfO ₂ subgrains and within grain boundaries and (b) Si within open triple points and grain boundaries annotated.	130
Fig. 90. SEM micrograph image showing unoxidized bulk of HfB ₂ -3a specimen after 7.3 hrs at 1500 °C under a compressive load (25, 50 MPa) for 6.2 hrs.	131
Fig. 91. SEM micrograph showing as-processed HfB ₂ -c campaign microstructure.	131
Fig. 92. Volatility diagram of ZrB ₂ -SiC at 1500°C. (Fahrenholtz [196], Reprinted with permission.).....	132

Fig. 93. SEM micrograph of cross sectional view of the HfB_2 specimen heat treated for 18 hrs at 1500°C in air in contact with alumina.	134
Fig. 94. Schematic of heat treatment tests evaluated for the possible effect of alumina on oxidation scale thickness.....	134
Fig. 95. Schematic of "alumina-free" cutting plane.....	135
Fig. 96. Schematic of mechanisms involved in oxidation of ZrB_2 in air at temperatures in the $1400\text{--}1800^\circ\text{C}$ range. The distance L represents the diffusion distance in a pore over which gaseous oxygen must diffuse to reach the boria. (Parthasarathy <i>et al.</i> [104], Reprinted with permission.).....	139
Fig. 97. Vapor pressure diagram of various B-O species as a function of oxygen partial pressure at 1500°C as calculated in Fahrenholtz and Hilmas [128]. (Reprinted with permission).....	140
Fig. 98. (a) Schematic of HfB_2 in proximity to SX YAG. Photographs of the (b) Back side of SX YAG (FEGH), (c) side of SX YAG (EACG), and (d) front side of SX YAG that was exposed to HfB_2 (ABDC) for 18 hrs at 1500°C in an air.	141
Fig. 99. Photo micrographs of representative $\text{HfB}_2\text{--}20\text{SiC}$ -a specimen after compression creep testing at 1500°C	142
Fig. 100. Photograph and SEM micrographs of representative $\text{HfB}_2\text{--}20\text{SiC}$ -c specimen after compression creep testing at 1500°C	143
Fig. 101. SEM micrographs of representative areas of HfO_2 or HfSiO_4 from different $\text{HfB}_2\text{--}20$ vol% SiC on and within borosilicate glass.	144
Fig. 102. SEM micrograph of undulating variations in glass and oxide layer thicknesses of $\text{HfB}_2\text{--}20$ vol% SiC specimens after compression creep testing at 1500°C in air.	145
Fig. 103. SEM micrograph of little to no borosilicate glass protection and oxide layer of $\text{HfB}_2\text{--}20$ vol% SiC specimens after compression creep testing at 1500°C in air.	145
Fig. 104. SEM micrograph of bubble on surface of $\text{HfB}_2\text{--}20$ vol% SiC after compression creep testing at 1500°C in air.	146
Fig. 105. SEM micrograph with annotated gap between specimen and CaldoFix.	147
Fig. 106. SEM micrograph with crack in CaldoFix annotated.	147
Fig. 107. Comparison of model predictions to experimental results of borosilicate glass layer of $\text{HfB}_2\text{--}20$ vol% SiC after compression creep testing at 1500°C in air.	148

Fig. 108. Comparison of model predictions to experimental results of oxide scale of HfB ₂ -20 vol% SiC after compression creep testing at 1500°C in air.	149
Fig. 109. Schematic of mechanisms involved in oxidation of HfB ₂ in air at temperatures in the 1000-1800°C range. (Parthasarathy <i>et al.</i> [104], Used with permission)	156
Fig. 110. (a) SEM image of the microstructure of oxidation scale formed in a HfB ₂ -SiC sample and (b) a schematic of the oxidation products and morphology assumed in the model . (Parthasarathy <i>et al.</i> [110], Reprinted with permission.)	161
Fig. 111. Typical creep strain vs. time curve.....	168
Fig. 112. HfB ₂ -1a: Temp ramp for 0.95 hrs, then at 1500°C for 14.9 hours (0.86 hrs thermal soak, 14.1 hrs under 25 MPa load). (a) Front (b) Back (c) Left (d) Right.....	173
Fig. 113. HfB ₂ -3a Temp ramp for 1.2 hrs, then at 1500°C for 7.3 hours (1.0 hrs thermal soak, 5.1 hrs under 25 MPa load, followed by 1.1 hrs under 50 MPa load). (a) Front (b) Back (c) Left (d) Right.....	174
Fig. 114. HfB ₂ -4a First Run: Temp ramp for 0.89 hrs, then at 1500°C for 7.12 hours (0.95 hrs thermal soak, 3.50 hrs under 50 MPa load, followed by 2.31 hrs under 75 MPa load) (a) Front (b) Back (c) Left (d) Right. Second Run: Specimen shattered.	174
Fig. 115. HfB ₂ -5a. First Run. Temp ramp for 0.98 hrs, then at 1500°C for 4.1 hours (1.0 hrs thermal soak, 3.0 hrs under 100 MPa load. Front	174
Fig. 116. HfB ₂ -5a: Second Run: Temp ramp for 0.99 hrs, then at 1500°C for 2.41 hours (1.0 hrs thermal soak, 1.3 hrs under 125 MPa load). (a) Front (b) Back (c) Left (d) Right.....	175
Fig. 117. HfB ₂ -1c: Temp ramp for 1.04 hrs, then at 1500°C for 17.0 hours (0.99 hrs thermal soak, 16 hrs under 25 MPa load). (a) Front (b) Back (c) Left (d) Right.....	175
Fig. 118. HfB ₂ -2c: Temp ramp for 1.02 hrs, then at 1500°C for 7.86 hours (0.98 hrs thermal soak, 6.86 hrs under 50 MPa load). (a) Front (b) Back (c) Left (d) Right.....	176
Fig. 119. HfB ₂ -3c: Temp ramp for 0.96 hrs, then at 1500°C for 9.20 hours (0.96 hrs thermal soak, 8.24 hrs under 75 MPa load). (a) Front (b) Back (c) Left (d) Right.....	176
Fig. 120. HfB ₂ -4c: First Run: Temp ramp for .74 hrs, then at 1500°C for 1.31 hours (0.74 hrs thermal soak, 0.57 hrs under 75 MPa load). Second Run: Temp ramp for 1.27 hrs, then at 1500°C for 3.43 hours (0.6 hrs thermal soak, 2.83 hrs under 75 MPa load). (a) Front (b) Back (c) Left (d) Right.....	177
Fig. 121. HfB ₂ -10SiC-1: Temp ramp for 1.18 hrs, then at 1500°C for 7.26 hours (1.04 hrs thermal soak, 5.10 hrs under 25 MPa load, 1.11 hrs under 50 MPa load, followed by 2.11 hrs under 75 MPa load. (a) Front (b) Back (c) Left (d) Right	177

Fig. 122. HfB ₂ -20SiC-1a: Temp ramp for 0.98 hrs, then at 1500°C for 12.2 hours (1.00 hrs thermal soak, 5.05 hrs under 25 MPa load, 4.15 hrs under 50 MPa load, followed by 1.00 hrs under 75 MPa load). (a) Front (b) Back (c) Left (d) Right	178
Fig. 123. HfB ₂ -20SiC-2a: Temp ramp for 1.00 hrs, then at 1500°C for 16.0 hours (1.00 hrs thermal soak, 15.0 hrs under 25 MPa load): (a) Front (b) Back (c) Left (d) Right	178
Fig. 124. HfB ₂ -20SiC-3a. Temp ramp for 1.04 hrs, then at 1500°C for 16.0 hours (1.00 hrs thermal soak, 15.0 hrs under 25 MPa load). (a) Front (b) Back (c) Left (d) Right	179
Fig. 125. HfB ₂ -20SiC-5a: Temp ramp for 0.85 hrs, then at 1500°C for 4.26 hours (1.05 hrs thermal soak, 3.16 hrs under 100 MPa load). (a) Front (b) Back (c) Left (d) Right	179
Fig. 126. HfB ₂ -20SiC-6a: Temp ramp for 0.97 hrs, then at 1500°C for 18.2 hours (1.00 hrs thermal soak, 17.2 hrs under 50 MPa load). (a) Front (b) Back (c) Left (d) Right	180
Fig. 127. HfB ₂ -20SiC-1c: Temp ramp for 1.28 hrs, then at 1500°C for 16.0 hours (0.89 hrs thermal soak, 15.1 hrs under 25 MPa load). (a) Front (b) Back (c) Left (d) Right	180
Fig. 128. HfB ₂ -20SiC-2c: Temp ramp for 1.28 hrs, then at 1500°C for 9.55 hours (0.75 hrs thermal soak, 8.80 hrs under 50 MPa load). (a) Front (b) Back (c) Left (d) Right	180
Fig. 129. Strain curves of step-wise creep tests of various HfB ₂ specimens.	182
Fig. 130. Strain curves of single load creep tests of various HfB ₂ specimens.....	182
Fig. 131. 75 MPa compressive creep curves of various HfB ₂ specimens.....	183
Fig. 132. Strain curves of step-wise creep tests of various HfB ₂ -SiC specimens.....	184
Fig. 133. Creep curve for HfB ₂ -20 vol% SiC parallelepiped specimens at 1500°C in air at various compressive loads.	185
Fig. 134. ACUPEAK 1330 pycnometer to determine volume via pressure differentials.	186
Fig. 135. Zeiss optical microscope.	186
Fig. 136. Rigaku Ultima IV X-Ray Diffractometer	186
Fig. 137. Hitachi TM 3000 Tabletop Microscope SEM and Hitachi Bruker Quantax EDS	186
Fig. 138. FEI/Philips XL30 SEM	187
Fig. 139. FEI/Philips CM-200T TEM.....	187
Fig. 140. Struers Hot Mounting Cito-Press 20.	189
Fig. 141. Buehler Vibromet I (400-VPS-274).	189

Fig. 142. Twelve-in polishing wheel with TexMet P polishing paper, lapping tool, and lapping holder for the test specimen.	191
Fig. 143. Allied High Tech MultiPrep Polisher	192
Fig. 144. Struers CitoVac vacuum chamber.	193
Fig. 145. Fisher Scientific Forced Air Isotemp Oven	194
Fig. 146. South Bay Technology Inc saw Model 600.....	194
Fig. 147. Schematic drawing of cutting planes of mounted specimen.	195
Fig. 148. AFRL Archimedes apparatus setup.....	197
Fig. 149. Photograph of Pt Sputtercoated SX YAG	199
Fig. 150. SEM micrograph of Pt sputter deposition	199
Fig. 151. SEM micrograph of cross-sectional view of Pt sputter deposition	199
Fig. 152. Schematic of tube furnace test to evaluate Pt deposition.	200
Fig. 153. Photograph of SX YAG with sputtercoated Pt "blown off" after heat treatment.	200
Fig. 154. Activation energy (E_a) needed for reactions with and without a catalyst.	201
Fig. 155. Molecular structures for (a) AlBO_2 and (b) YBO_3 [214].....	203
Fig. 156. Gibbs free energies of possible reactions in the system of direct contact between HfB_2 and SX YAG.	206
Fig. 157. Gibbs free energies of possible reactions in the system of an alumina spacer between HfB_2 and SX YAG.	206
Fig. 158. SEM micrograph of representative image of a charged oxide layer.	207
Fig. 159. SEM micrograph of representative image of drifting.....	208
Fig. 160. Edwards Auto 306 Turbo Evaporator.....	209
Fig. 161. Gatan Precision Etching Coating System Model 682	209
Fig. 162. Optical image of post-test pre-polish cross-section revealing crack in HfB_2 -3a after 7.3 hrs at 1500 °C under a compressive load (25, 50 MPa) for 6.2 hours.....	210
Fig. 163. SEM micrograph of post-test pre-polish crack in HfB_2 -3a (Fig. 158) after 7.3 hrs at 1500 °C under a compressive load (25, 50) for 6.2 hours.	211

Fig. 164. SEM micrograph of post-test pre-polish outer oxide scale and upper edge of crack intersection of HfB ₂ -3a after 7.3 hrs at 1500 °C under a compressive load (25, 50 MPa) for 6.2 hours.	211
Fig. 165. SEM micrograph of longitudinal view of crack that appeared on cross-section of HfB ₂ -3a after 7.3 hrs at 1500 °C under a compressive load (25, 50 MPa) for 6.2 hours	212
Fig. 166. (a) Optical image of pre-test top face of HfB ₂ -4a specimen and (b) Crack-annotated post-test optical image of bottom face of HfB ₂ -4a specimen after 7.1 hrs at 1500 °C under a compressive load (50, 75 MPa) for 5.8 hours.....	213
Fig. 167. (a) Optical image of pre-test bottom face of HfB ₂ -4a specimen and (b) Crack-annotated post-test optical image of bottom face of HfB ₂ -4a specimen after 7.1 hrs at 1500 °C under a compressive load (50, 75 MPa) for 5.8 hours.....	213
Fig. 168. Representative photographs of alumina spacer failure sequence. (a) Crack initiation on outer edge of spacer. (b) Crack all the way through alumina spacer. (c) Alumina spacer failure.	215
Fig. 169. Photographs of the (a) side surface and (b) top surface of HfB ₂ exposed to tube furnace argon environment for 18 hours at 1500°C when HfB ₂ and SX YAG were in direct contact.	217

List of Tables

	Page
Table 1. Theoretical and average densities for the various HfB ₂ -SiC compositions.....	36
Table 2. Average grain sizes for the various HfB ₂ -SiC compositions.....	38
Table 3. Maximum atomic% of select elements in various constituents of HfB ₂ specimen subjected to Test 4.	73
Table 4. Calculated CTE and equilibrium thermal strains for various HfB ₂ specimens under various compressive loads at 1500°C in air.....	113
Table 5. Calculated CTE and thermal strains for various HfB ₂ -20 vol% SiC specimens under various compressive loads.	115
Table 6. Summary of creep results for HfB ₂ specimens at 1500°C in air.	116
Table 7. Summary of normalized creep results for HfB ₂ specimens at 1500°C in air. ..	119
Table 8. Summary of creep results for HfB ₂ -20 vol% SiC specimens at 1500°C in air.	121
Table 9. Summary of normalized creep results for HfB ₂ -20vol% SiC specimens at 1500°C in air.....	122
Table 10. Average oxide scale thicknesses (mm) of oxide scales of different cases of HfB ₂ heat treated in contact with alumina for 18 hrs at 1500°C in air.	136
Table 11. Oxide scale thicknesses (mm) of various areas of 3 different cross-sections of HfB ₂ after heat treatment for 18 hrs at 1500°C in air.	137
Table 12. Creep Mechanism Exponents [17,179,181].....	171
Table 13. Summary of comparisons between AlBO ₂ and YBO ₃	203

MECHANICAL TESTING OF ULTRA-HIGH TEMPERATURE CERAMICS
AT 1500°C IN AIR –
DEVELOPMENT OF AN EXPERIMENTAL FACILITY AND TEST METHOD

I. Introduction

1.1 Organization of Dissertation

The first chapter of the dissertation begins with an overview of the motivation for the proposed research followed by an overview of the engineering field of ultra-high temperature ceramic (UHTC) materials. The motivation for the proposed research is presented together with the research problem statement. Research materials are described and research methodologies are discussed.

The second chapter is an overview of recent research in the area of engineered UHTCs.

The third chapter is a description of the research materials and their characteristics, the developed Experimental Facility, and Test Methods.

Chapter four is the investigation into the high temperature compatibility of HfB_2 with SX YAG, Pt foil, and alumina. This investigation was to determine which materials would not degrade HfB_2 in an oxidizing environment at 1500°C.

Validation of the research materials, experimental facility, and test methods is discussed in the fifth chapter. Thermal and creep strains were evaluated to validate the method of calibrating temperature set-points and measuring strains.

The sixth chapter is a narrative of the oxidation response of the HfB_2 -containing specimens exposed to SX YAG and alumina. A comparison is made of the oxidation of the validation test specimens discussed in Chapter 5 to those HfB_2 -containing specimens that were heat treated under zero load.

Concluding remarks, including efforts for future research, are offered in the seventh chapter.

1.2 Materials for Hypersonic Flight

The 1903 Wright Flyer was the first powered, heavier-than-air machine to achieve controlled, sustained flight with a pilot aboard [1]. The Wright Flyer flew for 59 sec in a straight path of 852 feet. In 1927, the “Spirit of St Louis” (Ryan NYP) reached a maximum speed of 129 miles per hour [2]. In 1947, “Glamorous Glennis” (Bell X-1) was the first aircraft to travel at a speed exceeding the speed of sound. The Bell X-1 aircraft reached a speed of 700 miles per hour [3]. The current manned airspeed record is held by the 1960s North American X-15 [4]. The X-15 reached speeds of Mach 6.7 making it the first aircraft to achieve hypersonic flight [5]. Note that speed above Mach 5 (five times the speed of sound) is termed hypersonic. Unfortunately, the X-15 could not maintain those speeds without detrimentally affecting its flight capabilities. The leading edges of the X-15 aircraft suffered severe melting damage during flight, negatively impacting the flight dynamics. Furthermore, the use of an ablator-insulator material to

handle the aerodynamic heating, resulted in a measureable increase in drag after charring had started [6]. This performance rendered the X-15 aircraft unacceptable for a sustained hypersonic flight or for repeated use. Thus, the X-15 remained a research aircraft. At present, the fastest operational manned aircraft is the Lockheed SR-71. Due to material limitations, the SR-71 was designed to achieve Mach 3+ flight, reaching a maximum speed of Mach 3.3 [3]. Today, sustainable, repeatable hypersonic speed is still the current prize in the game of aerodynamics.

Advanced aero- and space applications, such as hypersonic flight vehicles and spacecraft reentry thermal protection systems, require structural materials that have superior long-term mechanical properties. These materials must be able to perform under high temperature, high pressure, and varying environmental factors, such as moisture. In addition to mechanical properties, weight is a key consideration in selecting materials for flight-related applications (Fig. 1). The lower densities of ceramic materials combined with their higher use temperatures promise improved high-temperature performance when compared to conventional nickel-based superalloys. Material limitations are a key factor in development of hypersonic vehicles. Their design and actual service temperatures are limited by the properties of available materials (strength, oxidation resistance, thermal conductivity, specific gravity, etc).

Requirements for materials used in hypersonic flight and spacecraft reentry vehicles depend on their location on the vehicle and desired vehicle aerodynamics. Carbon-carbon composite materials with silicon carbide (SiC) coatings proved to be adequate for reusable blunt leading edges as on the Shuttle Orbiter, which must sustain 1500°C on reentry [7]. On the other hand, the design of modern hypersonic vehicles

employs sharp leading edges in order to achieve drag reduction. While sharp leading edges improve the maneuverability of the flight vehicle at hypersonic speeds, they also give rise to thin boundary layers [8], resulting in extreme surface heating of the wing leading edge by gas streams. At hypersonic speeds, the wing leading edges could reach temperatures above 2000°C [9-11]. Furthermore, the wing leading edges and the skin of the vehicle must operate in an environment that combines extreme temperatures with corrosive gases (both oxidizing and reducing) and dynamic pressures on the order of 71.82 kPa.

At present, structural materials for use in high temperature oxidizing environments are limited to SiC, Si₃N₄, oxide ceramics, and composites of these materials. Due to active oxidation, the maximum use temperature for Si-based ceramics is limited to 1600°C in air and to lower temperatures in water vapor environments. Oxides resist oxidation but exhibit high creep rates at higher temperatures. The development of structural materials for use in rapid heating and oxidizing environments at temperatures above 1600°C is a task of great engineering importance. The development of new materials for sustained use in the extreme environments experienced by a maneuverable hypersonic vehicle is currently an emphasis research area for the US Air Force.

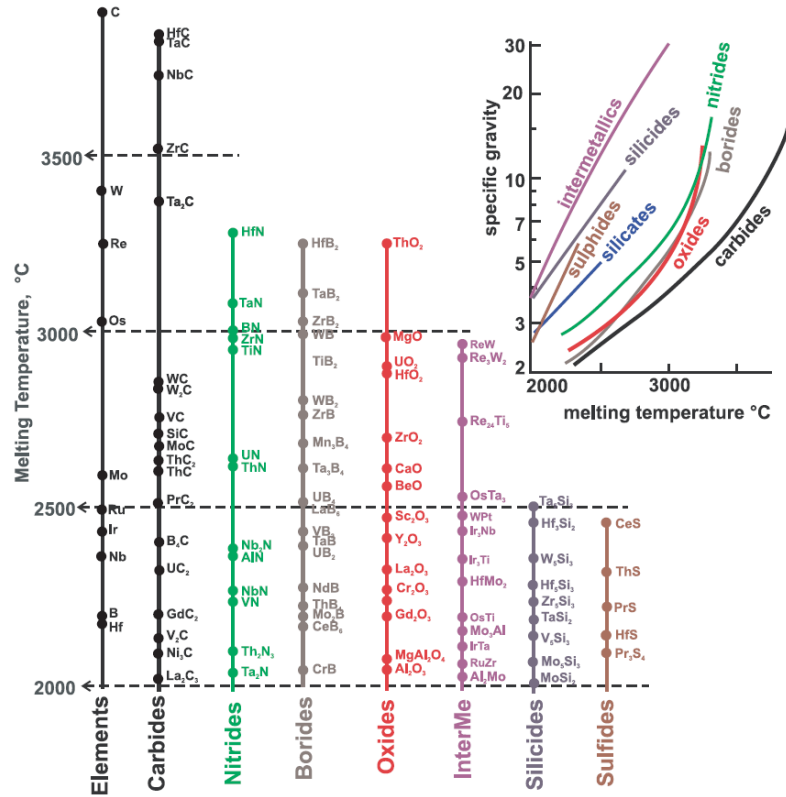


Fig. 1. A comparison of the melting temperatures and specific gravities of selected materials. Several borides, nitrides and carbides have melting temperatures exceeding 3000°C and are considered UHTCs. (After Ushakov *et al.* [12] and Fahrenholtz [13]).

1.3 Ultra-High Temperature Ceramics (UHTCs)

UHTCs are capable of withstanding temperatures in the 1900-2500°C range, which makes them candidate materials for airframe leading edges on sharp-bodied re-entry vehicles and hypersonic flight vehicles [13-19]. UHTCs are a class of materials, often based on transition-metal (Hf, Zr, or Ta) carbides, nitrides and borides. The transition metals are highly refractory. As a result, the UHTCs exhibit melting temperatures in excess of 3000°C, hardness, chemical stability, high electrical and thermal conductivity [13-18,20-27] and oxidation resistance. Unlike many structural ceramics, UHTCs have relatively high densities that help maintain structural integrity [8].

This combination of properties makes the UHTCs potential candidates for a variety of aerospace applications, such as sharp leading edges and thermal protection systems for reusable atmospheric re-entry vehicles and hypersonic flight vehicles [8,15-19,26,28,29].

UHTCs were studied extensively in the 1960s and 1970s [30]. This research performed by the United States Air Force and NASA focused on the thermochemistry, phase equilibria, and oxidation behavior of transition-metal borides, carbides, and nitrides [31-35]. While the transition-metal carbides were found to exhibit good thermal and electrical conductivity, they showed low oxidation resistance. Additionally, it proved difficult to process and manufacture the carbide-based UHTCs to sufficient density [14]. The transition-metal nitrides also displayed poor oxidation resistance. In an oxidizing environment both transition-metal carbides and transition-metal nitrides form single-phase, porous metal dioxide scales [18]. These scales provide ingress routes for the oxidizing environment to invade and degrade the bulk material. The transition-metal nitrides can also form N_2 or NO_x gas bubbles behind the oxide layers, which subsequently burst through and destroy the oxide scales [19].

Transition-metal borides offer oxidation resistance superior to that of carbides and nitrides. In oxidizing environments, the transition-metal borides form B_2O_3 (boria) oxidation products [13]. At temperatures up to 1200°C , liquid boria provides oxidation resistance by filling porosity in the fine-grained oxides. At temperatures above 1200°C , oxidation resistance is improved due to formation of a protective metal dioxide scale [13,24].

One of the major outcomes of the early work performed by the U. S. Air force and NASA was the identification of hafnium diboride (HfB_2) and zirconium diboride (ZrB_2) as good high-temperature oxidation-resistant materials. During the last 30 years, research into the discovery of new classes of materials and development of processing methods for UHTCs has been sporadic. As a result, fundamental research data available on the mechanical performance and manufacturability of UHTCs is scarce. Little has been reported on the high-temperature mechanical behavior and the high-temperature mechanical properties of the UHTCs.

UHTCs are prime candidates for advanced aerospace applications such as sharp leading edges and thermal protection systems for reusable atmospheric re-entry vehicles and hypersonic flight vehicles. Before UHTCs can be used in such applications, their structural integrity and long-term environmental durability must be addressed. Characterization of the mechanical behavior of the candidate UHTCs at relevant service temperatures and environments is required for design of structural components. Methods for characterizing mechanical behavior of UHTCs in harsh environments must be developed and experimentally verified.

However, high temperature mechanical testing is not a trivial task. Numerous studies have concentrated on oxidation behavior of the UHTCs [13,20,26,27,36-39]. This is a relatively easy task in that no instrumentation is required to survive temperatures in excess of 1300°C . Most studies reported in the literature evaluated the oxidation behavior of the SiC-doped UHTCs by exposing samples to elevated temperatures in closed air furnaces [32,33,40,41]. These studies do not have the same concerns with long-term high temperature material interaction or structural stability of the test fixtures.

1.4 Problem Statement

UHTCs offer a good combination of properties which make them suitable for extreme chemical and thermal environments associated with hypersonic flight, atmospheric re-entry, and rocket propulsion [22,42-44]. Due to their high melting temperatures, transition metal diborides, such as ZrB_2 and HfB_2 , are being considered as candidates for leading edges of sharp-bodied re-entry vehicles and hypersonic vehicles [13,33,45].

However, the high temperature characterization of mechanical behavior in excess of 1300 °C has many obstacles that must be overcome. Of utmost importance is material selection for test fixtures within the test environment. Materials selected must be able to maintain their structural integrity over long durations. If this does not occur, a controllable, consistent load is impossible to achieve. Also, the data that is obtained will not be trustworthy if strain measurement fixtures warp and flex during testing. In addition, thermo-chemical interaction between the test material and the test fixtures is to be expected at these temperatures. The investigation of high temperature materials to find solutions to overcome these obstacles was the main goal of this work.

A high temperature compression test facility was constructed, test methods were developed, and both were validated by a pilot creep study of HfB_2 - 0-20 vol% SiC under static loading at temperatures ranging from 1300 to 1600°C in air. The oxidation behavior of HfB_2 - 0-20 vol% SiC was evaluated to ensure that material thermo-compatibility was valid for both monolithic HfB_2 and HfB_2 with additions of SiC.

The objectives of this research can be summarized in the following problem statement:

Design and build an experimental facility for mechanical testing of UHTC samples at 1300-1600°C in air. Identify appropriate high temperature test fixture material. Develop a test method for mechanical testing of UHTCs in compression in air environment at temperatures ranging from 1300 to 1600°C. Validate the Experimental Facility and Test Method for mechanical testing of UHTCs in compression in an air environment at temperatures ranging from 1300 to 1600°C.

1.5 Material Description

Recently ZrB₂-based UHTCs have received the most attention due to their lower density and cost. However, HfB₂-based ceramics have demonstrated themselves to be more oxidation resistant and appropriate for high temperature structural use [46-48]. This research will focus on HfB₂-based UHTCs. Monolithic HfB₂-HfC (~4 mol% for densification) will be evaluated to establish a baseline for high-temperature material interaction between HfB₂, Pt foil, SX YAG, and alumina and validate the developed Experimental Facility and Test Method.

Silicon carbide (SiC) is a widely used additive which reduces the oxidation rate of diboride UHTCs by forming a protective scale of borosilicate glass [18,32,41,47,49-52]. Also, the addition of SiC promotes the refinement of the UHTC microstructure, allowing for increased densification of the material and thus, improving the toughness and strength

of the material [25,33,53-64]. This study will also utilize HfB_2 specimens with 10 and 20 vol% additions of SiC to validate the developed Experimental Facility and Test Methods for HfB_2 with additions of 10 and 20 vol% SiC.

Due to the small nature of the test specimens, the experimental test facility was designed for compression creep testing. Single crystal (SX) yttrium aluminum garnet (YAG, $\text{Y}_3\text{Al}_5\text{O}_{12}$) was chosen as the pushrod material to provide the compressive load as it is known to be one of the most creep resistant oxides [16-23]. Previous work by Armani [65] reported on the excellent creep properties of SX YAG at 1300 °C. SX YAG is also under investigation as a potential matrix and/or fiber material for ceramic matrix composites [16-23]. Silicon carbide (SiC) rods would provide more creep resistance at 1500°C and higher, but are more likely to contaminate the test specimen strain and oxidation measurements. The oxidation of SiC results in the formation of silicon dioxide (g) (SiO_2), and HfB_2 releases boria (g) during oxidation. The SiO_2 reacts with B_2O_3 forming a borosilicate glass which slows the diffusion of oxygen through the oxide scale, retarding the HfB_2 oxidation process [18,32,41,47,49-52]. As borosilicate glass has been proven to flow [66], the possibility exists that it could flow and coat the test specimen with a protective layer.

Alumina is another high temperature material known for its structural stability at elevated temperatures. It is used extensively in oxide matrix composites for high temperature applications. For these reasons, it was chosen as an interlayer between the HfB_2 -containing specimens and the SX YAG pushrods during validation pilot compressive creep tests.

1.6 Methodology

The key objectives outlined in the problem statement were accomplished by the following tasks:

1. Designed and built experimental facility for mechanical testing of UHTC specimens at temperatures from 1300-1600°C in laboratory air.
2. Evaluated thermo-chemical compatibility of test fixture candidate materials with HfB_2 with and without additions of SiC at 1500°C in laboratory air
3. Determined appropriate materials necessary for high temperature mechanical testing of HfB_2 with and without additions of SiC at 1500°C in laboratory air.
4. Developed a method for accurately measuring the strain of UHTC specimens in compression at temperatures from 1300-1600°C range in laboratory air.
5. Validated material selection, Experimental Facility, material selection, and Test Method with pilot creep tests of HfB_2 specimens with 0, 10, and 20 vol% of SiC at 1500°C in laboratory air.

II. Background

Advanced aerospace applications require structural materials that can operate at temperatures up to 2400°C. The long-life applications include components such as rocket nozzles, nosetips, and leading edges for hypersonic missiles and hypersonic flight vehicles. As such, the materials must be chemically and physically stable at elevated temperatures. In addition, they must also retain strength, toughness, and creep resistance at operational temperatures. The refractory metal diborides, known as ultra-high temperature ceramics (UHTCs), exhibit the high melting temperatures, as well as the ability to form refractory oxide scales. The UHTCs capable of withstanding temperatures in the 1700-2500°C range are a leading candidate for aerospace structural applications operating in extreme environments.

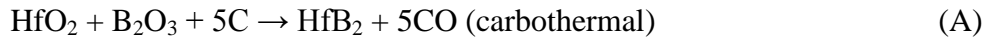
2.1 Ultra-High Temperature Ceramics (UHTCs)

Transition metal diborides, such as ZrB_2 and HfB_2 , belong to the family of materials known as UHTCs. The boride-based UHTCs have melting temperatures in excess of 3000°C, as well as a unique combination of chemical stability, excellent thermal and electrical conductivities, and corrosion resistance [13,17,20,22-27,53,59,67-70]. Unlike many structural ceramics, UHTCs have relatively high densities, assisting in maintaining structural integrity [8]. These properties make the boride-based UHTCs suitable for the extreme chemical and thermal environments associated with hypersonic flight, atmospheric re-entry, and rocket propulsion.

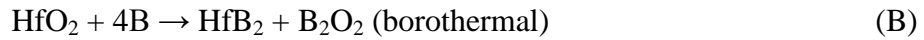
2.2 Synthesis of Diboride-Based UHTCs

The diboride-based UHTCs can be synthesized by several methods. The most widely used synthesis routes are reduction processes, chemical processes, and reactive processes.

The reduction process frequently employs carbon and boron as reducing agents. Carbothermal and borothermal reductions can be used to produce ZrB₂ or HfB₂ [71-74]. Carbothermal and borothermal reduction reactions are given by:

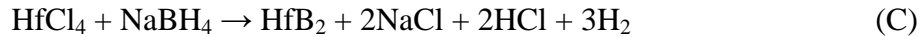


and



The reduction processes are highly endothermic. For example, carbothermal reduction is thermodynamically favorable only at temperatures at ~ 1500°C. Hence, temperatures of ~ 2000°C are generally required to synthesize diborides via the reduction route. The final diboride powder also contains carbon, B₂O₃, and oxide impurities.

The chemical routes include reactions with boron-containing polymers and pre-ceramic polymers. For example, nanocrystalline ZrB₂ and HfB₂ can be synthesized by a reaction between anhydrous chlorides and sodium borohydride (NaBH₄):



This reaction proceeds at temperatures above 500°C and under pressure [75,76]. The resulting diboride powders can have crystalline sizes as small as 10-20 nm.

The reactive route to synthesize the diborides can be simply a reaction of elemental precursor powders:





Both zirconium and hafnium exhibit high affinity for oxygen. Therefore, the above mentioned reactions must be performed in inert or reducing atmospheres to prevent the formation of oxide impurities. Furthermore, Rxns. D and E are highly exothermic and favorable at all temperatures. If the reaction is allowed to proceed in an uncontrolled manner, the heat can ignite a self-propagating reaction and produce temperatures high enough to promote local melting of the zirconium or hafnium [77-80]. Hence, these reactions can be employed to synthesize ZrB_2 and HfB_2 by self-propagating high-temperature synthesis (SHS), also called combustion synthesis [78-80]. The SHS-derived diboride powders typically show improved sinterability. But SHS gives rise to high heating and cooling rates which produce high concentrations of defects in the resulting diborides.

2.3 Densification of Diboride-Based UHTCs

Development and characterization of non-oxide ceramics has lagged behind that of oxides due to densification difficulties. Monolithic metal diborides have a hexagonal crystal structure that leads to anisotropic grain growth and entrapped porosity. In other words, coarsening is more likely to occur than densification. Increasing the density is critical to improving the strength and fracture toughness of ceramics. Recently considerable effort was devoted to improving densification and microstructure of the UHTCs. Main methods for densification of diborides are hot pressing, pressureless sintering, reactive routes, and spark plasma sintering.

Because diborides exhibit strong covalent bonding and low self-diffusion, high temperatures (+2000°C) and high external pressures (800-1500 MPa) are required to densify these materials via hot pressing (HP). It was demonstrated that the use of metal (Zr, Hf, Cr, Y, and/or Al) and ceramic (SiC, MoSi₂, and/or TaB₂) additives promoted superior densification of ZrB₂ and HfB₂. Key studies by Fenter [33] identified ZrB₂ - and HfB₂ - 20 vol% SiC and 18 vol% SiC + 10 vol% C as the most promising compositions. Good densification can be achieved at lower HP temperatures and pressures when finer starting powders are used together with the additives that minimize grain growth, produce a liquid phase, or result in solid solution formation. Recent studies showed that both ZrB₂ and HfB₂ can be hot pressed to near full density by adding Ni [53,81], Si₃N₄ [54,81], MoSi₂ [20,61,82], or SiC [67,83-85]. Many of these additives reduced the densification temperature requirements for ZrB₂. However, even with these additives, pressures of 20–50 MPa were still required.

Pressureless sintering (PS) of diborides is an attractive densification method as it could enable near-net shape fabrication of components using standard powder processing methods. When employing PS, the approaches commonly used to enhance densification are reduction of starting particle size and the use of sintering aids. Possible sintering aids include liquid phase formers, solid solution formers, and reactive agents. The densification of pure diborides proceeds due to grain boundary and volume diffusion, which require temperatures near 1800°C [13,86]. PS processing temperatures near 1750°C were recently reported [69]. The presence of oxide or metallic impurities in the powders is likely behind the lower processing temperature. For example, the presence of B₂O₃ impurity was shown to lower the processing temperatures below 1800°C.

However, the presence of B_2O_3 impurity was also shown to enhance the grain growth and promote coarsening; thereby, inhibiting densification and limiting the maximum achievable density to $\leq 95\%$ [87,88]. It has been demonstrated that the addition of silicides (such as $MoSi_2$) had a beneficial effect on densification of borides [36,60-62,64,89]. Recent research has also shown that ZrB_2 can be densified using reactive additives [22,90]. In these studies, ZrB_2 was PS to $> 98\%$ density with small amounts of WC ($\sim 2 \text{ vol}\%$).

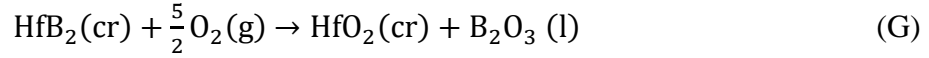
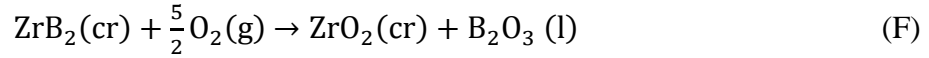
Reactive routes to densification are based on combining synthesis and densification into a single-step. Reduction reactions like (A) and (B) or elemental reactions (D) and (E) can be used to process diborides by reactive HP (RHP). A very fine nanocrystalline powder can be produced by reacting zirconium and boron. However, a HP temperature of 2100°C was required to achieve 99% density for ZrB_2 [91]. A combined synthesis and densification process was developed for ZrB_2 -SiC and HfB_2 -SiC [92,93] that proceeds by reactions of elemental precursors (Zr, B, and SiC). The use of the SiC precursor dramatically improves the resulting microstructure by reducing diboride grain size, while also lowering the densification temperature. When Zr, B, and SiC were used as precursors, a near 95% density was achieved by RHP at 1650°C . Not only was the densification temperature significantly reduced, but the resulting grain size was also smaller. An average grain size for ZrB_2 -SiC processed by RHP was $\sim 0.5 \mu\text{m}$ compared with the average grain size of $\sim 12 \mu\text{m}$ obtained for dense ZrB_2 processed by RHP.

The spark plasma sintering (SPS) process consists of simultaneously applying a uniaxial load and an electric current to a powder compact. The SPS process resembles the HP process in that the powder compact is heated. However, while the HP process employs indirect heating, the SPS process applies an electrical field to heat the powder compact. Of course, the powder must be electrically conductive. Heating rates in hundreds of °C/min facilitate rapid densification and minimizes grain growth. Monteverde *et al.* [94] used SPS to achieve full density for HfB₂ - 30 vol% SiC with a uniform microstructure and a mean grain size of ~2 µm. The SPS process was accomplished by heating to 2100 °C at 100°C/min and holding for 2 minutes at 2100°C and at 30 MPa. SPS has been shown to produce better results than hot pressing when comparing doped UHTCs. Medri *et al.* [95] evaluated ZrB₂ - 30 vol% ZrC - 10 vol% SiC - 3.7 vol% Si₃N₄ synthesized via HP and by SPS. The HP specimen reached only ~ 90% density. Contrastingly, the SPS specimen exhibited a near constant densification rate of $2 \times 10^{-4} \text{ s}^{-1}$ over 1750-2100°C and reached full density. Sciti *et al.* [61], Bellosi *et al.* [82], and Monteverde *et al.* [96] reported similar results in HP vs. SPS comparison studies of HfB₂ - 15 vol% MoSi₂, ZrB₂ - 15 vol% MoSi₂, and HfB₂ - 30 vol% SiC - 2 vol% TaSi₂, respectively.

2.4 Oxidation of Diboride-Based UHTCs

Many potential applications of the UHTCs involve elevated temperatures and oxidizing environments, making oxidation resistance a vital issue. Numerous studies have focused on improving the oxidation resistance of the UHTCs [13,20,26,27,36-39]. In general, the oxidation of the diborides exposed to air at elevated temperatures can be

considered stoichiometric [13,32]. In the case of ZrB₂ and HfB₂ the oxidation reactions are given by:



Both reactions are thermodynamically favorable at all temperatures. Oxidation of the metal diboride results in an evaporation-resistant refractory metal oxide that forms a porous skeleton on the surface of the specimen. At temperatures below 700°C, the weight change will remain negligible for both ZrB₂ and HfB₂. At temperatures below 1100°C, ZrO₂, as well as HfO₂, react with B₂O₃ to form a continuous scale that provides passive protection from oxidation [97-102]. At temperatures between 1100°C and 1400°C, the weight change occurs, which is a combination of mass loss due to evaporation of B₂O₃ and mass gain due to formation of condensed oxides [100,103]. Samples continue to gain weight because the mass of ZrO₂ (or HfO₂) is greater than the mass of ZrB₂ (or HfB₂) reacted plus the mass of B₂O₃ lost. Oxidation of the metal diboride results in an evaporation-resistant refractory metal oxide that forms a porous skeleton on the surface of the specimen. This oxide scale consists of two layers. The oxidation of boron results in production of glassy liquid boria (B₂O₃) that fills the base of the refractory metal oxide skeleton forming the inner. At the same time, the liquid boria at the surface evaporates, leaving a refractory metal oxide outer porous layer which does not offer protection from further oxidation [68,104-107]. Figure 2 is a schematic of the products of the HfB₂ oxidation process.

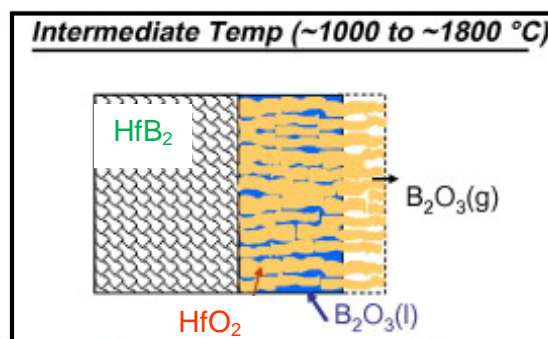


Fig. 2. Schematic of the oxidation products formed during oxidation of HfB_2 at temperatures in the 1000-1800°C range. (Parthasarathy *et al.* [104], Used with permission)

A common approach to improving the oxidation resistance of ZrB_2 - and HfB_2 -based ceramics above 1200°C is the use of additives that modify the composition of the oxide scale. The most widely used additive is SiC, which reduces the oxidation rate of ZrB_2 and HfB_2 by forming a protective silica-rich layer [32,41,47,49-52]. At temperatures below 1100°C, the oxidation rate of SiC is several orders of magnitude slower than that of diborides. Hence, the addition of SiC does not modify the oxidation resistance of the diborides in this temperatures regime [47,100]. At temperatures below 1100°C, the oxide scale formed on ZrB_2 -SiC has the same composition ($\text{ZrO}_2 + \text{B}_2\text{O}_3$) as that formed on pure ZrB_2 . As the temperature exceeds 1100°C, the oxidation rate of SiC increases and the evaporation rate of B_2O_3 become considerable. As a result, a silica-rich layer of borosilicate glass forms on ZrB_2 -SiC, which provides protection from oxidation [10,15,18,108]. Compared to liquid B_2O_3 , borosilicate glass has a higher melting temperature, higher viscosity, and lower oxygen diffusivity. Thus, the layer of borosilicate glass limits oxygen diffusion through only the uppermost layers of the

UHTC. However, at temperatures above 1400 °C, the protective layer of borosilicate glass burns off, and rapid active oxidation of SiC occurs. This ultimately leads to increased oxidation and material loss of the diboride [10,16].

Clougherty *et al.* [32] did some of the original work that determined that SiC improved the oxidation resistance of UHTCs. Additions of 10, 20, and 30 vol% SiC were examined for both ZrB₂ and HfB₂ over a temperature range of 1027-2152 °C. A combination of a gas analysis method and post-oxidation metallography was employed to determine the extent of oxidation. The studies revealed that the materials containing 20 vol% SiC (i.e. HfB₂ - 20 vol% SiC and ZrB₂ - 20 vol% SiC) exhibited the best oxidation resistance.

Carney *et al.* [109] explored improving the oxidation resistance of HfB₂ – 15 vol% SiC by adding tungsten boride (WB) or tungsten carbide (WC). Both the WC and WB additives were seen to promote sintering while reducing the grain size of HfB₂; thus, increasing density. The WC- and WB- containing HfB₂-SiC samples oxidized at 1600 °C and at 1800 °C producing oxide scales similar to that exhibited by the pure HfB₂-SiC sample. However, when oxidized at 2000 °C, the WC- and WB- containing samples exhibited a near 30% reduction in the scale thickness. A glass phase of higher viscosity was found in the outermost regions of the scale, while the inner regions of the scale were dominated with a denser HfO₂ that inhibited oxygen penetration to the sample. Apparently, additions of WC and WB promoted densification of the HfO₂ scale; thereby, restricting oxygen ingress into the sample during oxidation.

Nguyen *et al.* [47] studied the oxidation of HfB_2 - 20 vol% SiC, ZrB_2 - 20 vol% SiC, and, ZrB_2 - 30 vol% C - 4 vol% SiC in 90% water vapor and 10% oxygen environment at 1200, 1300, and 1400°C at 101.33 kPa. The total exposure time at each temperature was 10 hrs. Specimen weight change was evaluated. In addition, X-ray diffraction, surface, cross-sectional scanning electron microscopy, and energy dispersive spectroscopy were utilized to assess the oxidation behavior. Results revealed that low-velocity water vapor did not have a significant effect on oxidation rates compared to stagnant air.

Monteverde and Scatteia [45] explored the resistance to thermal shock and oxidation of ZrB_2 - 15 vol% SiC and $(\text{ZrB}_2 + \text{HfB}_2)$ - 15 vol% SiC materials. Both compositions were oxidized at 1450°C for 20 hrs. The presence of SiC resulted in a formation of silica-based protective glass scale, which served to improve oxidation resistance of the diborides. Resistance to thermal shock was studied by measuring retained flexural strength after water quenching at 20°C. The ZrB_2 - 15 vol% SiC and $(\text{ZrB}_2 + \text{HfB}_2)$ - 15 vol% SiC materials retained over 70% of their initial mean flexural strength provided the thermal shock did not exceed 385°C and 475°C, respectively. The addition of HfB_2 to the ZrB_2 - SiC improved thermal shock resistance of the material. This improvement was attributed to better heat transfer properties, which serve to reduce thermal gradients across the specimen.

2.5 Model Framework and Formulation

Parthasarathy *et al.* [104] developed a mechanistic model that interprets the oxidation behavior of the diborides of Zr, Hf, and Ti (referred to as Me as a group) in the

temperature range of ~1000-1800 °C. The model predicts metal recession, oxide scale thickness, and weight change as functions of time at temperature and oxygen partial pressure.

SiC is a common additive used to improve oxidation resistance of refractory metal diborides. The model framework developed for interpreting oxidation kinetics of refractory diborides [104] was expanded to account for oxidation kinetics of SiC-containing refractory diborides [110] in the 1200-2000 °C temperature range. The augmented model retains the framework of the initial model, but also takes into account the presence of SiC and its oxidation products, SiO₂ and CO.

An in-depth review of both models can be found in Appendix A.

2.6 Mechanical Behavior of Diboride-Based UHTCs

Characterizing the mechanical behavior of UHTCs at temperature above 1300 °C in an oxidizing environment introduces at least two challenges that are not present at room temperature and/or in an inert environment. At high temperatures, thermo-chemical interactions between test material and test fixtures are dramatically increased. An oxidizing environment also introduces degradation of materials within the test chamber. Both of these factors can decrease testing durations, in some cases to the point of obtaining enough measurements impossible. For these reasons, there are fewer studies reported in literature concerning the mechanical behavior of diboride-based UHTCs.

During high temperature flexural tests, the HfB_2 ceramics exhibited nearly linear elastic behavior to failure at 1090°C [23]. In contrast, at 1230°C , the stress-deflection curve revealed significant plastic deformation, suggesting that some creep deformation occurred before fracture. Similar results were reported for ZrB_2 ceramics subjected to four-point flexural tests at temperatures in the $23\text{-}1925^\circ\text{C}$ range [17].

Creep is an important design criterion and frequently a life limiting condition for high temperature application ceramic materials. (A review of creep of ceramics can be found in Appendix B.) A candidate material must be able to maintain structural integrity and dimensions while under application. Nonetheless, only a limited number of studies of the creep behavior of UHTCs have been reported in literature to-date. Most studies that reported high-temperature mechanical properties for the diborides focused on flexural strength measurements or fracture toughness [13,15,22,24,62,63,111].

Earlier investigations into flexural creep of two-phase $\text{ZrB}_2\text{-ZrN}$ ceramics [112] and into compression creep of two-phase ZrC-ZrB_2 ceramics [113] reported the experimental results, but did not determine creep stress exponents or identify the creep mechanisms. The reported results were a evaluation of variable (e.g. temperature and stress levels) changes.

Bird *et al.* [114] conducted flexural creep studies of $\text{ZrB}_2\text{-}20\text{ vol\% SiC}$ at temperatures of $1400\text{-}1820^\circ\text{C}$ in an argon environment. They investigated creep loads of $16\text{ - }97\text{ MPa}$ through the aforementioned temperature range. They reported that their findings indicated two creep mechanism regimes. Below 1500°C creep behavior is

dominated by ZrB_2 or ZrB_2 -SiC interphase boundary sliding accommodated and dominated by ZrB_2 lattice diffusion. Above 1500 °C, ZrB_2 and/or ZrB_2 -SiC interphase boundary sliding becomes the dominate creep mechanism.

Melendez-Martinez *et al.* [57] evaluated compressive creep behavior of pure ZrB_2 and ZrB_2 - 4 wt% Ni in uniaxial tests conducted with a dead-weight load at 1400, 1500, and 1600 °C in argon. Creep stresses ranged from 47 MPa to 472 MPa for pure ZrB_2 and from 10 MPa to 63.5 MPa for Ni-doped ZrB_2 . The pure ZrB_2 exhibited ductile behavior and showed high creep resistance. In contrast, at 1400 and 1500 °C the Ni-doped ZrB_2 had poor creep performance. The ZrB_2 - 4 wt% Ni exhibited ductile behavior only at low stresses and failed catastrophically at 63.5 MPa at 1400 °C and at 39.8 MPa at 1500 °C.

Talmy *et al.* [17] studied flexural creep of ZrB_2 - 0–50 vol% SiC ceramics at temperatures in the 1200–1500 °C range in oxidizing atmosphere. Creep behavior was characterized as a function of temperature, stress (varying between 30 and 180 MPa), and SiC particle size (varying between 2 and 10 μm). Creep behavior was strongly influenced by SiC content and particle size. Creep rate increased with increasing SiC content and decreasing SiC particle size, especially at temperatures above 1300 °C. Cracking and grain shifting were observed on the tensile side of the ZrB_2 - 0–50 vol% SiC samples. Cracks propagated through the SiC phase, further confirming the conclusion that grain boundary sliding of the SiC grains was the controlling creep mechanism for this composition. Furthermore, it was found that oxidation of both compositions was accelerated under stress.

2.7 Thermo-chemical Compatibility and Mechanical Behavior of Diboride-Based UHTCs

One of the major outcomes of early work performed by the U. S. Air Force and NASA on UHTCs, was the identification of hafnium diboride (HfB_2) and zirconium diboride (ZrB_2) as good high-temperature oxidation-resistant materials [115]. But fundamental research data available on the compatibility of UHTCs with other high temperatures materials is scarce. Thermal studies of UHTCs with other materials has been related to the use of additives to increase densification and reduce grain size to improve mechanical properties or to improve oxidation resistance [8,9,15,16,18,25,32,33,36,37,41,46,53,53-55,58,59,61-64,109,115-120].

The extensive oxidation studies have gained significant insight into the mechanisms and behavior of the UHTCs as a function of temperature, gas chemistry, and pressure. Clearly, UHTC materials must be chemically and physically stable at elevated temperatures. However, they must also retain strength, toughness, and creep resistance at the use temperatures. Yet, little has been reported on the thermo-chemical compatibility or mechanical behavior of UHTCs at elevated temperatures.

Thermal studies of UHTCs with other materials has been related to how UHTCs react with various sintering properties to increase densification and reduce grain size to improve mechanical properties [25,33,41,53-64]. Densification of ZrB_2 and HfB_2 is difficult due to strong covalent bonds, requiring sintering temperatures of almost 2200°C at pressures of 20-30 MPa or temperatures of $1790\text{-}1840^\circ\text{C}$ at pressures of 800-1500 MPa [13,121]. SiC is a common additive that has been shown to improve the sintering of UHTCs to increase densification to almost 100% at lower temperatures and/or pressures

[15,32,36,38,70,84,85,92-94,96,116,121]. SiC limits the UHTC diboride (MeB_2) grain growth during the sintering process [17,121]. During the sintering process, traces of oxide can form on the surface of the HfB_2 particles [45]. This contamination promotes vapor phase transport (which promotes grain growth) at temperatures lower than that which is needed for mass transport, which allows for effective densification to occur. SiC can remove this oxide coating, allowing mass transport, and thus densification, to take place at lower temperatures.

UHTCs and their oxides are being considered as high temperature toughening mechanism and coatings for thermal barriers and composite matrix materials [33]. As an *in situ* toughening phase, Sciti *et al.* [122] and Silvestroni *et al.* [123] found that SiC whiskers and chopped fibers, as an *in situ* toughening phase, can improve the thermal shock and low fracture toughness of UHTCs [122,123]. Chemical compatibility and interface mechanics, including CTE mismatches, have created the most difficulties in their coupled usage [22]. Streckert *et al.* [124] were able to overcome bridging, tracking, and cracking issues in coating SCS-6 (Si-C), NicalonTM (Si-C-O), or Saphikon (SX Al_2O_3) fibers with ZrO_2 and HfO_2 through dip coating, solvent exclusion, and in-situ curing of stable alkoxide solutions processes. Corral and Loehman's [125] investigation of UHTC coating processes to protect C-C composites from high temperature oxidation required precursors to form an adherent thermal protection layer.

Many studies reported in the literature regarding the thermo-chemical behavior of HfB_2 with other materials concerns the oxidation behavior of the doped UHTCs when exposing samples to elevated temperatures [8,9,15,33,36,37,40,41,46,109,115-120,126]. HfB_2 and ZrB_2 were to have the greatest oxidation resistance due to the presence of liquid

B_2O_3 , which fills the pores of the oxide scale [8,16,18,32]. The addition of SiC increases the oxidation resistance of HfB_2 and ZrB_2 via two mechanisms. The first is the continuous evolution of CO. This keeps the HfO_2 porous and permits the non-destructive escape of the B_2O_3 gas [127]. The second mechanism is the creation of SiO_2 , into which B_2O_3 dissolves to create a protective surface layer of borosilicate glass, which prevents the inward diffusion of oxygen [45,66,109,127,128]. 20 vol% SiC was found to provide the optimal increase in oxidation resistance for high temperature cyclic applications [22]. Monteverde [121] used mass gain to compare oxidation resistance. He found that the mass gain changed from 10.5 mg/cm² to 3.38 mg/cm² with the addition of 15 vol% SiC at 1450 °C in dry air for 20 hrs. The mass of the metal oxide formed is greater than the mass of diboride lost plus the mass of B_2O_3 evaporated [100]. Fahrenholtz and Hilmas [13] found that 20 vol% SiC caused a mass gain of ~0.02 mg/mm² while the monolithic gained 0.12 mg/mm². Clougherty [32] realized a fourfold reduction of the depth of HfB_2 .

Densification and oxidation studies have been extensive and successful, gaining significant insight into the mechanisms and behavior of the UHTCs as a function of temperature, gas chemistry, and pressure. Conversely, the subject of thermo-chemical stability of UHTCs with other high-temperature materials has received only limited attention, with most of that attention focused on the interactions with additives used to improve densification and oxidation resistance. However, additional selection criteria for use of HfB_2 -UHTCs in advanced aerospace applications include chemical compatibility with other materials as well as thermal and environmental stability. Mah and Parthasarathy [129,130] reported an interaction between HfB_2 and single-crystal $Y_3Al_5O_{12}$ (SX YAG). The use of HfB_2 jig for the flexure tests resulted in an increase in

toughness of SX YAG at 1600°C in air. The study focused on reduction of SX YAG into YAlO_3 (yttrium aluminum perovskite, YAP), $\text{Y}_4\text{Al}_2\text{O}_9$ (yttrium aluminum monoclinic, YAM) and Y_2O_3 , but did not consider the effects of the interaction on the HfB_2 .

Hafnium diboride containing UHTCs are very attractive for high temperature structural use. Hence their thermo-chemical compatibility with other high temperature structural materials is of high interest.

2.8 Implications for Current Research

Prior investigations demonstrate that HfB_2 is a promising candidate material for use in high-temperature applications such as hypersonic vehicle sharp leading edges, and rocket nosedcaps [18,45,109]. However, the review of published literature reveals only few studies of the mechanical and creep performance of HfB_2 -based ceramics over the range of temperatures encountered in potential applications. Results of prior studies also demonstrate that the HfB_2 -based ceramics exhibited significant plastic deformation at temperatures above 1100°C. Plastic deformation was observed in flexure tests as well as in compression tests. The presence of plastic deformation indicates that creep deformation occurs before failure.

Creep deformation represents one of the critical criteria for structural application of UHTCs at elevated temperatures in operational environments. A thorough understanding of creep performance of the HfB_2 -based UHTCs at elevated temperature in oxidizing environment is critical to assuring structural integrity and environmental durability of these materials in aerospace applications.

High temperature testing of HfB₂-containing UHTCs at 1300-1700 °C in an oxidizing environment is no trivial matter. The questions remain: *Which test fixture materials can maintain their structural integrity at these high temperatures. Will these materials interact with one another and/or HfB₂-containing UHTCs at these high temperatures? Can a test facility be designed to accurately measure strain at temperatures from 1300-1700°C.* These questions must be answered before systematic creep testing of HfB₂-containing UHTCs to characterize mechanical behavior can be conducted.

III. Research Plan and Implementation

The experimental facility designed and built and the experimental methods developed specifically met the following objectives:

- Design and build an experimental facility for mechanical testing of UHTC samples at 1300-1600°C in air,
- Identify appropriate high temperature test fixture material,
- Develop a test method for mechanical testing of UHTCs in compression in an air environment at temperatures ranging from 1300 to 1600°C,
- Validate the experimental facility and test method for mechanical testing of UHTCs in compression in air environment at temperatures ranging from 1300 to 1600°C.

The first objective was met by building the experimental facility described in Section 3.3. The second objective was accomplished through heat treatment tests of monolithic HfB₂ specimens in various configurations with SX YAG and high purity alumina at 1500°C in laboratory air. A detailed description is given in Section 3.5.2. The third objective was achieved by testing of SX YAG specimens in compression creep at 1500°C in laboratory air as described in Sections 3.4.2. The fourth objective was determined with a series of pilot creep tests of HfB₂ specimens with 0, 10, and 20 vol% of SiC at 1500°C in laboratory air as described in Section 4.3.

3.1 Research Materials

3.1.1 HfB₂-containing UHTCs

The HfB₂ used in this work was fabricated using commercially available HfB₂ powder (Cerac, Milwaukee Wisconsin), which had a purity of 99.5% and a mean particle size of 4.6- μ m. A 100 g of HfB₂ powder was loaded into a 40-mm graphite die coated with BN and lined with graphite foil. The powder was sintered using spark plasma sintering with a heating and cooling rate of 50°C/min and a maximum temperature of 2100°C. The hold time at 2100°C was 30 min. A pressure of 40 MPa was applied during heating to 1600°C and held throughout the remainder of the sintering cycle. The pressure was released to 4 MPa during cool-down to 450°C. Near full density was achieved.

The HfB₂-SiC specimens were supplied by the Air Force Research Laboratory, Materials and Manufacturing Directorate. The HfB₂-SiC billets were fabricated using mixtures of commercially available HfB₂ and SiC powders. The HfB₂ powder (Cerac, Milwaukee Wisconsin) has a purity of 99.5% and a mean particle size of 4.6- μ m. The β -SiC powder has a purity of 97.5% and a particle size of 45–55 nm. The β -SiC powder was used in as received condition. Conversely, the HfB₂ powder was pre-milled for 60 hrs in isopropanol using SiC grinding media in order to reduce the grain size. Particles in the pre-milled HfB₂ were measured using a laser diffraction particle size analyzer (LS230, Beckman Coulter, Brea, CA). The pre-milled HfB₂ powder had an average particle size of 1.3 μ m.

Mixtures of the pre-milled HfB_2 powder and the as-received SiC powder were milled for 18 hrs in isopropanol using SiC grinding media. Then the powders were stirred and dried at room temperature followed by 18 hrs of dry milling with SiC grinding media. Next, the powder mixture was sieved through an 80-mesh screen before sintering. The sifted and dried powder mixture was loaded into a graphite die with a 40-mm diameter, which is coated with BN and lined with graphite foil. The sample was sintered using spark plasma sintering (SPS: FCT System GmbH Model HPD 25-1, Ramstein, Germany) with a heating and cooling rate of $50^\circ\text{C}/\text{min}$ and a maximum temperature of 2100°C (achieved using 6 V and 3.4 kA). The SPS hold time is 20 min. The process temperature is measured by an optical pyrometer focused on the bottom of a bore hole in the punch approximately five millimeters from the powder. A vacuum of 150 Pa is maintained during the entire heating cycle. A DC current with a single pulse and a pulse sequence of 10 μs on and 5 μs off is used for heating. A uniaxial load of 32 MPa is applied during the heat up to 1600°C and held during the remainder of the heating cycle. Fig. 3 and Fig. 4 are SEM micrographs of HfB_2 -20 wt% SiC samples processed using the aforementioned methodology. The SEM micrograph of HfB_2 -20 wt% SiC samples in Fig. 3 reveal regular microstructure with negligible residual porosity. The sample shown in Fig. 3 has a density $> 99\%$. The annotated SiC grains in Fig. 4 have a diameter of 2-3- μm . The SEM micrographs show that the grains are homogeneously dispersed within the HfB_2 matrix.

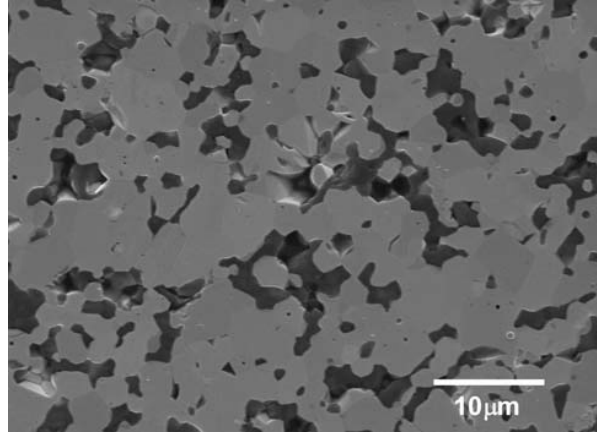


Fig. 3. HfB_2 -SiC. SEM micrograph courtesy of C. Carney (AFRL/RXLN).

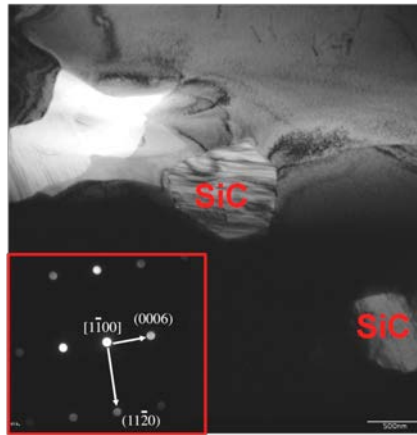


Fig. 4. HfB_2 -SiC. TEM micrograph courtesy of R. S. Hay (AFRL/RXCC).

The fabricated billets of HfB_2 -based UHTCs are sectioned into approximately 6.5-mm x 6.5-mm x 19-mm test specimens using electric discharge machining (EDM). The specimen drawing is shown in Fig. 5. After machining, the specimen surfaces are polished to 45 μm to remove oxidation caused by EDM, remove surface flaws, and to provide a consistent surface finish. Two horizontal grooves spaced 12.7 mm apart are machined near the top and bottom of the test specimen to provide for better contact with the extensometer extension rods. These grooves are spaced to match the zero position of the extensometer.

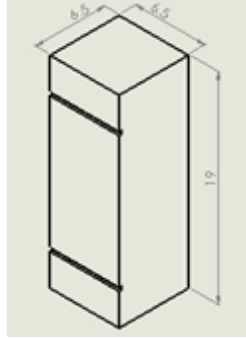


Fig. 5. Schematic of HfB₂-based UHTC test specimen.

3.1.2 Load Train Materials

The high purity, undoped SX YAG rods of 10-mm diameter were supplied by VLOC (New Port Richey, FL) [131]. The YAG single crystals were produced using the Czochralski growing process. In this process, the YAG material and negligible amounts of sintering dopant are melted in an iridium crucible that is heated by induction. The four to eight week single crystal growing process (depends on length) is monitored and controlled by computers. After removal from the furnace, the defect-free regions of low stress are mapped using a Fizeau interferometer. The 10-mm diameter rods were cut from the defect-free portions of the YAG crystals.

The 99.8% purity Al₂O₃ (AD-998) was manufactured by Coorstek (Golden, CO).

3.2 Characterization of HfB₂ Specimens with Varying SiC Content

Physical characteristics, such as initial density and grain size, of specimens must be characterized to ensure that the specimens are appropriate for mechanical testing. The second campaigns of monolithic HfB₂ and HfB₂-20 vol% SiC both were unfit due to inadequate microstructures. The HfB₂-b specimen was only 77% dense, and the HfB₂-20SiC-b had too little grain growth. All specimens were polished and prepared according

to the method in Appendix F and Appendix K. X-rays were used to non-destructively inspect the pre-test specimens for internal damage. However, the monolithic HfB_2 pucks were too dense even for the X-rays at 300 kV, 10 mA to penetrate. It is indeterminable if the cracks that developed in two of the specimens during testing (see Appendix L) were caused by the compression creep testing. The SiC-containing HfB_2 specimens were inspected at 200 kV, 10 mA, and 2 min. No detectable flaws were observed.

3.2.1 Density

In general, materials with the greater density have increased strength, fracture toughness, and resistance to fatigue crack growth. Furthermore, denser materials have fewer pores and provide fewer pathways and/or the surface area for the oxidizing environment to attack the material. Therefore, increased density enhances oxidation resistance. As previously mentioned, much effort has been invested in improving the densification of processed UHTCs.

The Archimedes method, a 0.1-mL graduated cylinder, and an ACUPEAK 1330 pycnometer were used to determine the densities for the HfB_2 -containing specimens. A pycnometer uses pressure differentials to determine volume. Archimedes' principle states: "A body whole or partially immersed in a fluid will be buoyed up by a force equal to the weight of the fluid that it displaces [132]." In addition, the volume of water displaced equals the volume of the portion of the body immersed in a fluid. A schematic of the Archimedes set is shown in Fig. 6, and a full description of the methodology is in Appendix G.

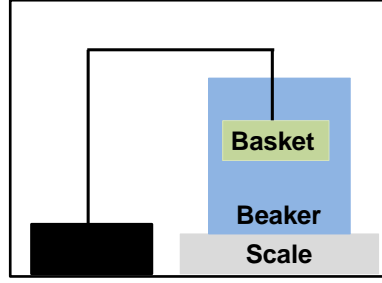


Fig. 6. Schematic of Archimedes density apparatus.

The theoretical densities and average calculated densities for the various HfB_2 -containing compositions used in this study given in Table 1. It is not entirely unexpected that densities can be greater than the theoretical density [109]. Byproducts created during the sintering process can affect the final density. The theoretical densities for the compositions containing 10 and 20 vol% SiC were calculated via the rule of mixtures using 10.5 g/cc for HfB_2 and 3.21 g/cc for SiC. Multiple specimens were used from each UHTC campaign. Evaluating the standard deviation and ANOVA results determined that each campaign puck had a consistent density.

Table 1. Theoretical and average densities for the various HfB_2 -SiC compositions.

	Theoretical Density (g/cc)	Calculated Density (g/cc)
HfB_2 -a	10.5	10.5
HfB_2 -c	10.5	10.6
HfB_2 -10SiC	9.77	10.2
HfB_2 -20SiC-a	9.40	9.33
HfB_2 -20SiC-c	9.40	9.43

3.2.2 Microstructure

Scanning Electron Microscope (SEM: Hitachi TM 3000 Tabletop Microscope, Tokyo, Japan) (see Appendix E) and transmission electron microscopy (TEM: FEI/Philips CM200, USA) (see Appendix E) were used to obtain images of the grain

structure of the specimens. The micrographs in Fig. 7 are the as-processed microstructures of the compression creep pucks: (Fig. 7a) HfB_2 -a, (Fig. 7b) HfB_2 -c, (Fig. 7c) HfB_2 -20SiC-a, and (Fig. 7d) HfB_2 -20SiC-c. TEM analysis did not reveal any intergranular films within the grain boundaries of the HfB_2 -a or HfB_2 -c specimens. The image in Fig. 7c revealed that the HfB_2 -20 vol% SiC puck (HfB_2 -20SiC-a) contained numerous SiC conglomerates and areas of larger HfB_2 grains.

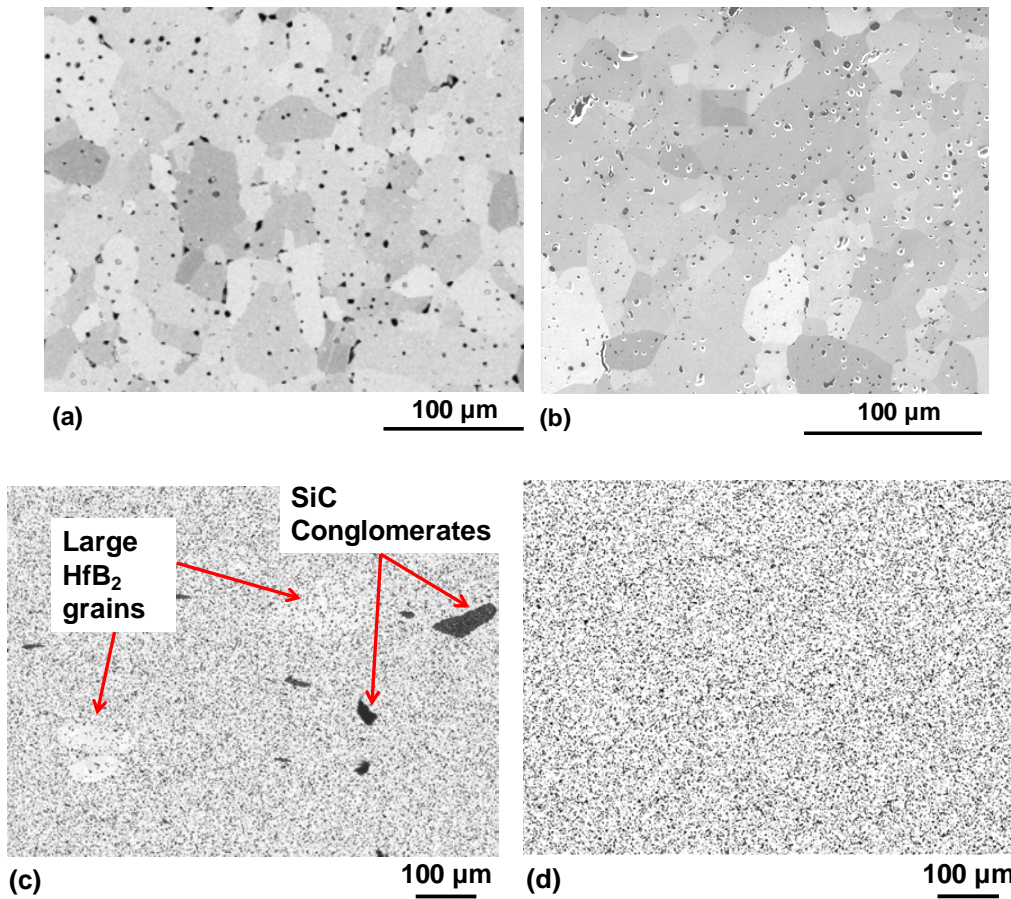


Fig. 7. SEM micrographs showing microstructure of (a) HfB_2 -a, (b) HfB_2 -c, (c) HfB_2 -20SiC-a, and (d) HfB_2 -20SiC-c.

3.2.3 Grain Size

Grain size of the material can have a strong effect on properties and performance. Electron backscatter diffraction (EBSD: FEI/Philips XL30 SEM) (see Appendix E) was used to determine the grain sizes of HfB₂ and SiC (Fig. 8). Specimens were polished to 0.5 μm to ensure clear grain boundary distinction. It was determined the grains were randomly orientated. Table 2 lists grain sizes of the various HfB₂-SiC compositions. The HfB₂-10 vol% SiC grain sizes were unable to be determined due to software malfunction. As expected, the HfB₂ grain sizes decreased as the SiC percentage increased.

Table 2. Average grain sizes for the various HfB₂-SiC compositions.

	Grain Size (μm) HfB ₂	Grain Size (μm) SiC
HfB ₂ -a	18.7	-
HfB ₂ -c	16.9	-
HfB ₂ -10SiC	3.73	-
HfB ₂ -20SiC-a	1.28	0.418
HfB ₂ -20SiC-c	2.44	0.469

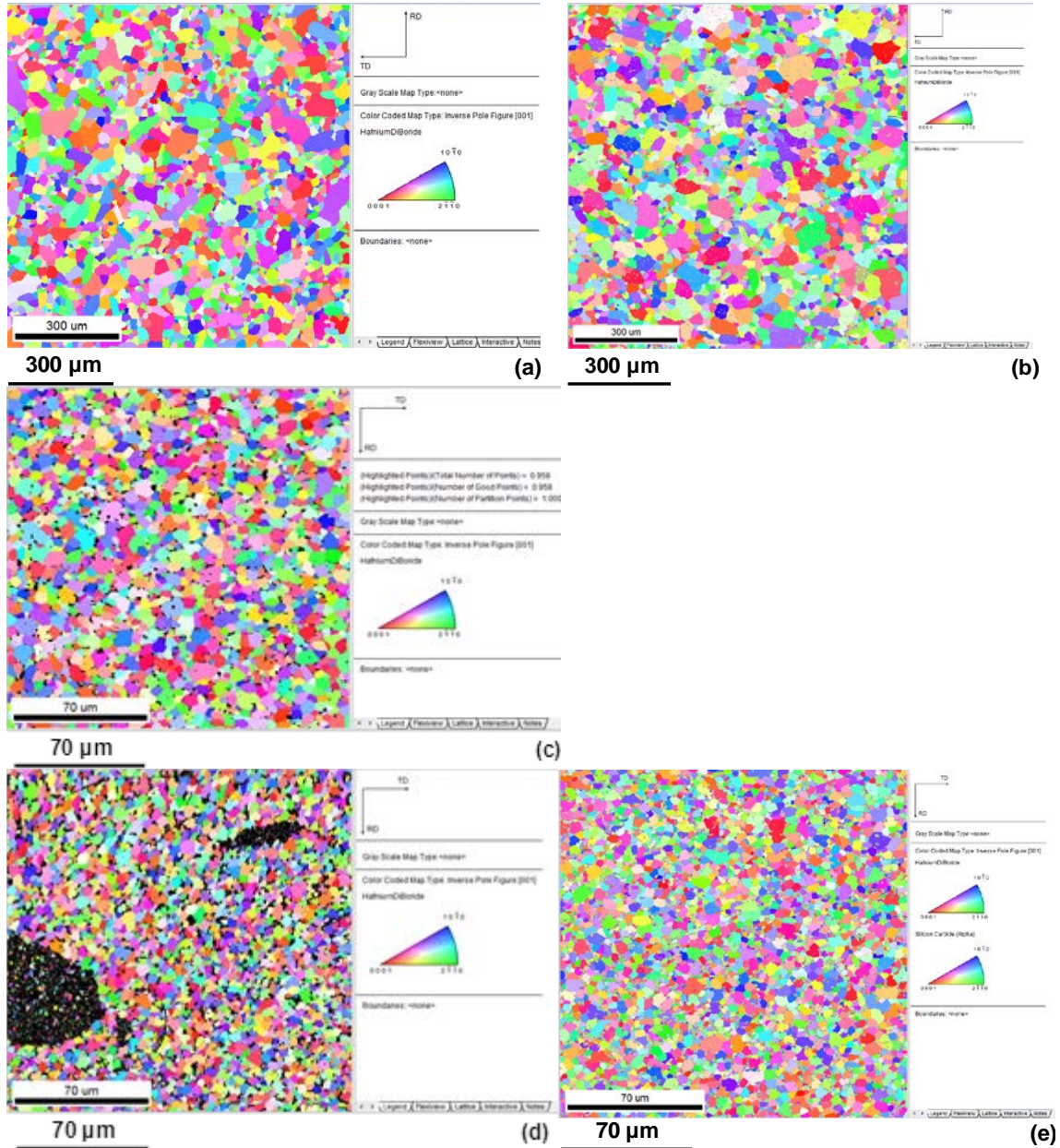


Fig. 8. EBSD micrographs for various HfB₂-containing campaigns. (a) HfB₂-a, (b) HfB₂-c, (c) HfB₂-10SiC, (d) HfB₂-20SiC-a, and (e) HfB₂-20SiC-c.

3.2.4 Physical Dimensions

Images of the pre- and post-test specimens were obtained (Appendix C) using both an optical camera and Zeiss optical microscope (Appendix E). There were slight variations in physical dimensions due to the differing amounts of polishing needed to

remove EDM oxidation and post-machining surface flaws. Surface flaws could provide a source for crack initiation during creep testing. A minimum of 5 measurements of width and depth dimensions of the cross-section were taken within the gauge section of each specimen. A micrometer was used to calculate the measurements taken in order to determine the proper load necessary to reach the desired stress. Recession of the HfB_2 was determined from the pre- and post-measurements using the optical microscope.

3.3 Experimental Facility

It has been recognized that the available UHTC specimens, which have a form of a parallelepiped with the largest dimension of 19 mm, do not lend themselves to testing in tension. In order to ensure accurate load control and strain measurement, the design and construction of an experimental facility and support structures for the purpose of testing HfB_2 -containing specimens under monotonic and sustained compression at elevated temperatures in the 1300-1600°C range in air was required. Due to the elevated temperatures, commercial-off-the-shelf (COTS) equipment was inadequate. Modifications were required to maintain accurate measurements during long duration mechanical testing at 1300-1600°C.

The base experimental facility included the following COTS items:

- servo-controlled MTS 810 mechanical testing machine with a test load capacity up to 5,500 lbs (25 kN),
- hydraulic water-cooled MTS 647.02B wedge grips,
- single zone resistance heated-furnace capable of operating at temperatures up to 1800°C (see Fig. 9) (Mellen, model TD18-1.5x1.25-1Z-RV),

- Eurotherm 3504 temperature controller,
- MTS Flex Test 40 digital controller was used for input signal generation and data acquisition.

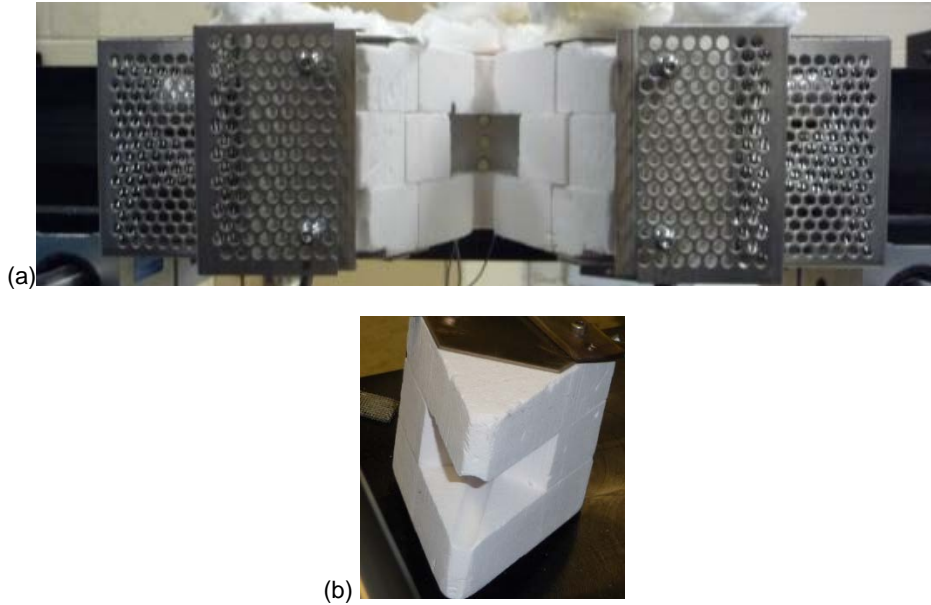


Fig. 9. (a) Single zone resistance heated furnace and (b) "pie slice" door for furnace.

Strain measurements were accomplished using a MTS 632.53E-14 high temperature, low contact force extensometer with a 12.77 mm gauge length. Strain is measured by the change in length within this gauge section as determined by the vertical displacement of the extensometer rods. The ends of the extensometer rods were machined with a 60° chisel tip and positioned in direct contact with the test specimen (Fig. 10a). Low flow air cooling and a heat shield were used to protect the extensometer from the high temperatures (Fig. 10b).

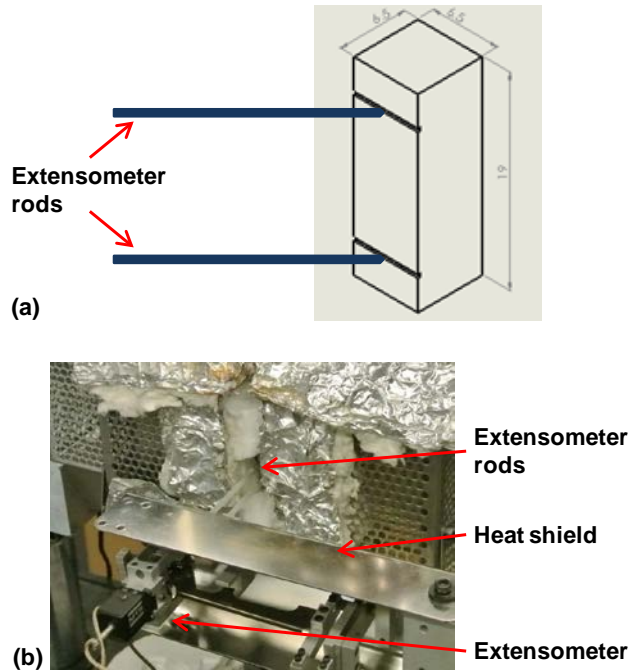


Fig. 10. (a) Schematic of extensometer rod placement on test specimen, and (b) photograph of extensometer and rods in place during high temperature testing.

The Mellon design for the pie slice originally had two openings to allow for the insertion of instrumentation. As a result of the invalidation of measurements due to the extensometer rods coming into contact with the Experimental Facility, the material between the openings had to be removed, creating a single larger opening. This modification prevented contact from occurring during subsequent compression creep testing.

In anticipation of test temperatures exceeding 1300°C, parts used to construct the environmental facility had to be carefully selected to assure safe and reliable operation at ultra-high test temperatures. MGT 450C UL rated cables were used to avoid degradation due to prolonged exposure to high temperatures. Nickel plated copper lugs were employed, as well as nuts, bolts, and washers made of alloyed high temperature materials

of silicon bronze and nickel-copper throughout the facility. High temperature nickel anti seize lubricant and thread sealant was applied to facility parts as a preventative measure against bonding at high temperatures.

During original runs of the furnace, it was revealed that the furnace could not reach and maintain the desired temperatures necessary to enable ultra-high temperature mechanical testing of UHTC's. This led to several modifications of the furnace system.

The furnace employed two MoSi_2 heating elements (see Fig. 11a) positioned on opposite sides of the internal chamber (see Fig. 11b). The MoSi_2 elements exhibited significant creep at elevated temperatures leading to deformation and catastrophic failure. Through the course of the large creep deformation, the center portion of a MoSi_2 heating element collapsed, causing the two end rods to come in contact with one another. As a result, additional alumina support blocks were designed and fabricated specifically to keep the two end rods of the MoSi_2 heating elements in their original position; requiring the redesign of the heating elements to allow for clearance from the alumina blocks. These alumina support blocks were placed on the exterior of the furnace as shown in Fig. 12. Due to the MoSi_2 heating elements becoming brittle upon cooling, the alumina support blocks played a dual role by also restricting the embrittled elements from fracturing when opening or closing the furnace. In order to minimize the embrittlement and to prolong the service life of the MoSi_2 heating elements, two fans were installed to provide additional cooling to the end rods of the MoSi_2 elements outside the furnace as shown in Fig. 13.

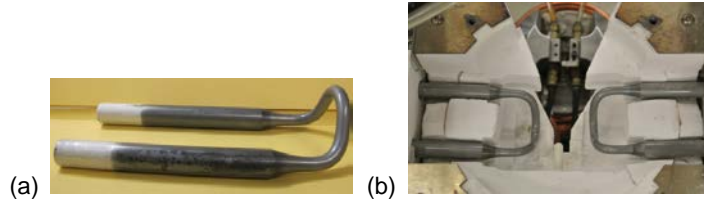


Fig. 11. (a) A MoSi₂ heating element, and (b) in place MoSi₂ heating elements.



Fig. 12. Alumina blocks supporting the MoSi₂ elements on the exterior of the furnace.

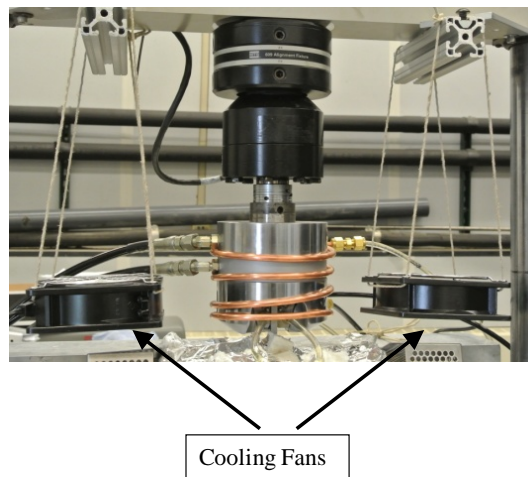


Fig. 13. Fans provide additional cooling to the end rods of the MoSi₂ elements outside the furnace.

To prevent heat loss and dramatic temperature fluctuations as a result of furnace inconsistencies during ultra-high temperature testing, high temperature foil-backed alumina blankets were placed on the top, bottom, and front of the furnace. This also aided in reducing the load on the heating elements as shown in Fig. 14. (Foil backed Rescor 370FT alumina blanket (Cotronics Corp) is rated to over 1600°C).

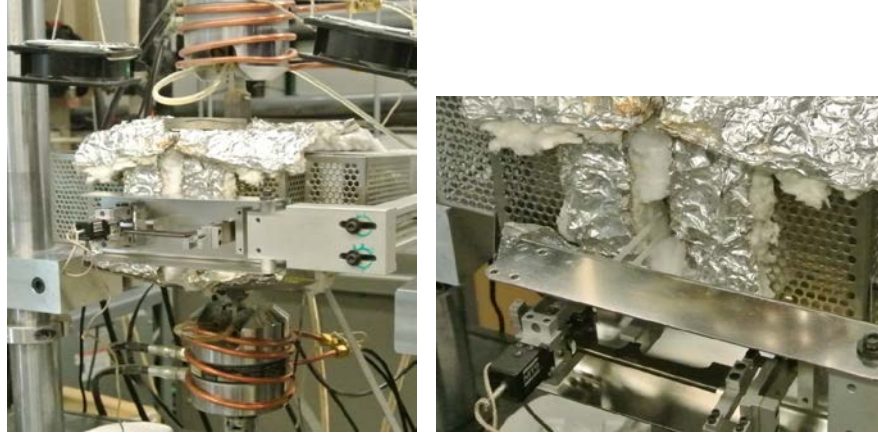


Fig. 14. Foil-backed alumina wrapped around Experimental Facility for testing of UHTC specimens at 1300-1600°C.

The furnace controller uses a non-contacting platinum-rhodium (Pt-Rh) U-type thermocouple exposed to the ambient environment near the test specimen. The Pt-Rh thermocouple may oxidize at test temperatures. In order to prevent the oxidation byproducts from contaminating the test specimen and/or the MoSi_2 heating elements, the Pt-Rh thermocouple was encased in a yttria-fully-stabilized-zirconia tube with an enclosed end.

The environmental test facility is integrated with an MTS servo-controlled mechanical testing machine in order to perform tests at 1300-1600°C in a laboratory air. The testing facility employs water-cooled MTS 647.02B hydraulic wedge grips. However, because the test temperatures are to exceed 1300°C, additional cooling was necessary to prevent heat damage to the load cell and to the grips. Cooling coils made of copper tubing were wrapped around the hydraulic wedge grips (see Fig. 15). Chilled water circulates through the copper tubing providing cooling to the load cell located directly above the top grip and stationary cell located directly below the bottom grip, consequently providing additional cooling to both sets of grips.

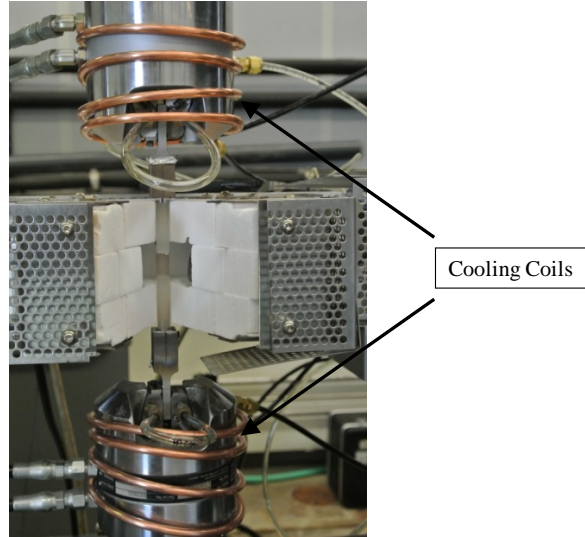


Fig. 15. Cooling coils wrapped around the MTS hydraulic wedge grips.

For testing of mechanical properties at 1300 °C, 203-mm long alumina extensometer rods were employed. Since the goal of this study was to reach 1600 °C, the extensometer rod length was extended to 254-mm to provide addition heat protection for the extensometer. During initial validation, strain measurements using alumina extensometer rods proved to be unreliable. The real-time scope of the strain showed erratic results. The test was continued since the cause was undetermined. At the end of test, it was discovered the alumina extensometer rods had undergone superplastic deformation (Fig. 16). The slight force the rods exert on the specimen was enough to cause the deformation. The alumina extensometer rods were successfully replaced with extensometer rods machined from SX sapphire rods supplied by Swiss Jewel Co.



Fig. 16. Alumina extensometer rods that were deformed after 14.9 hrs at 1500°C under a 25 MPa load for 14.1 hrs.

Once completed, the furnace height was approximately 100 mm and the width of the furnace assembly was ≤ 375 mm (i.e., the furnace was designed to fit between the columns of the testing machine). The height of the test chamber was ~ 31 mm (see Fig. 9a). The furnace had a pie-slice-shaped section that could be removed for access to the internal chamber (see Fig. 9b).

A furnace support structure (Fig. 17) was also designed and built specifically to allow the furnace to be positioned such that the test specimen could be located in the hot zone without disrupting the alignment of the specimen in the testing machine. This was made possible by allowing the furnace to smoothly move to the front or back of the testing machine via rails. Once the specimen is installed and aligned in the testing machine, the furnace can be brought forward along the rails of the support bracket and positioned to enclose the specimen for testing.

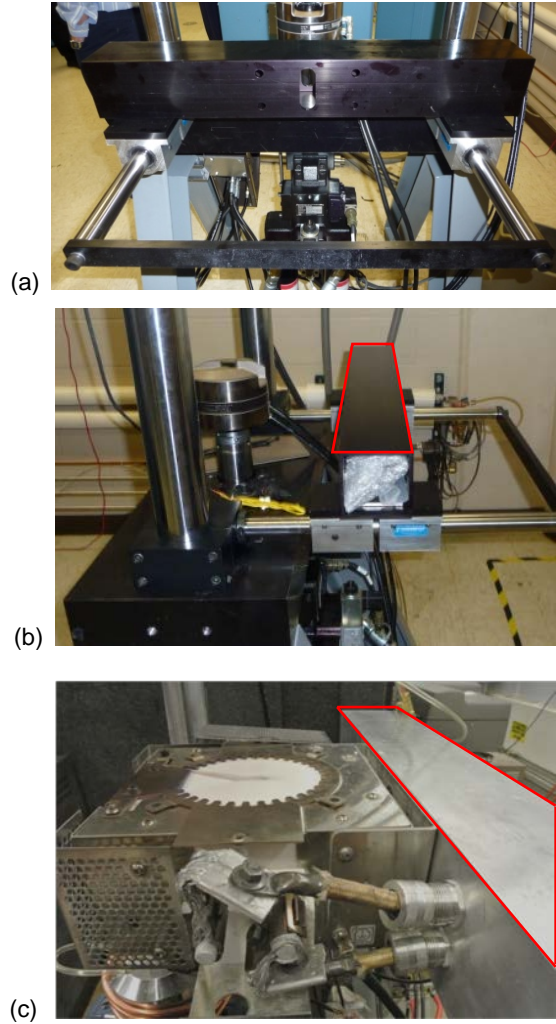


Fig. 17. Furnace support structure and rail system. (a) Back view of furnace support, (b) side view of furnace support, and (c) side view of furnace support with furnace in place. The top of the rail is highlighted in red for orientation.

3.4 Test Methodology

The test method developed for testing the small HfB_2 -containing specimens in compression was built upon experiences with compression creep testing of small cube-shaped specimens of high-purity polycrystalline YAG at 1300°C [65]. For this study, specially designed pushrod holders were secured onto a 305-mm long bar and then placed into the MTS hydraulic wedge grips. The bar assisted in ensuring that the holders were in line with one another. Compression tests of small HfB_2 -SiC specimens employed

pushrods made of single crystal YAG. The pushrods were mounted in the specially designed holders. Thin copper foil disks were placed in the holders to provide a cushion between the steel holder and SX YAG pushrods. Once the pushrods were secured into the holder, they were carefully brought together to visually verify that they were aligned. In some cases, the rods had to be rotated in the holder or the holder screws had to be adjusted. The MTS crossheads were adjusted such that the $\text{HfB}_2\text{-SiC}$ specimen was centered with a portion of the top and bottom pushrods located inside the hot zone of the furnace. The HfB_2 -containing specimen was placed between the pushrods (see Fig. 18). To prevent bonding and interaction between the pushrods and the $\text{HfB}_2\text{-SiC}$ specimen, alumina spacers were placed between the top and bottom surfaces of the $\text{HfB}_2\text{-SiC}$ specimen and the single crystal YAG pushrods. Careful alignments were accomplished visually to confirm that the test specimen and alumina spacers were visually aligned in the load train¹. A 75 MPa preload was applied to hold the test specimen in place. During the temperature ramp portion of creep testing, the screws securing the SX YAG pushrods were loosened to accommodate thermal expansion of the SX YAG.

¹ The author looked through the extensometer holder to provide a reference for alignment.

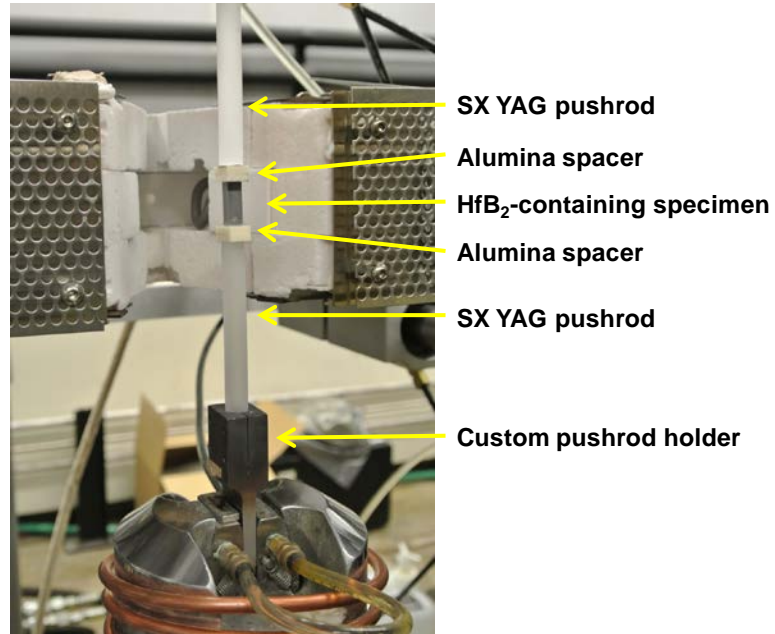


Fig. 18. Experimental set-up for compression testing of HfB₂-SiC specimens.

Once the load train was properly aligned, the furnace was moved into position via the rail system. The pie slice was then inserted, and the furnace was considered closed. After the furnace was closed, the furnace, with the exception of the extensometer rod opening, was covered with the alumina blanket. Last of all, the extensometer holder was rotated into place and the extensometer rods were positioned in contact with the grooves on the HfB₂-SiC specimen. This method provided an accurate measurement of compressive strain of the HfB₂-containing specimens.

3.4.1 Testing Facility Temperature Calibration

The MoSi₂ resistance heating elements supply heat via a current that runs through the elements. The amount of voltage applied determines the amount of heat generated by the heating elements. The voltage controller and control thermocouple were calibrated to ensure the specimen reached the desired target temperature. To calibrate the temperature

control, use of the same material as the test experiment is recommended. Unfortunately, with HfB_2 available on a limited basis, a SX YAG specimen of approximately the same volume as the HfB_2 specimen was used to thermally calibrate the experiment setup.

Two thermocouples were utilized to calibrate the furnace as well as verify that the temperature remained consistent through the length of the specimen. The thermocouples were inserted into the opening meant for the extensometer rod (Fig. 19). The furnace controller (using the aforementioned non-contacting thermocouple exposed to the ambient environment near the test specimen) was adjusted to determine the temperature set-point needed to achieve the desired temperature of the test specimen. Handcrafted alumina plugs were put in the openings to hold the thermocouples in place against the specimen.



Fig. 19. Temperature calibration of experimental facility for testing of UHTC specimens at 1300-1600°C.

Originally, temperature calibrations were to be run at 1300, 1400, 1500, 1600, and 1700°C. It was determined that the furnace could not reach 1700°C. The temperature calibration setup consisted of 3 thermocouples: one control and two feedbacks. The

initial temperature point of the control thermocouple was the desired temperature setting. The specimen was then thermally soaked until the real-time scope indicated that thermal expansion was complete. (These tests are the basis of the 1 hour thermal soak for the creep experiments.)

3.4.2 Obtaining High Temperature Strain Measurements

Previous mechanical testing of UHTCs utilized either three- or four-point bending tests. These tests rely on measuring the displacement of the test fixtures to determine mechanical characteristics. Strain measurements are derived from the application of beam axis theory which may induce errors. During initial validation tests utilizing a SX YAG test specimen, it was determined that a direct correlation between strain and crosshead displacement was not possible. Direct measurement of high temperature strain is crucial for accurate determination of change in dimension. This requires non-slip contact with the test specimen.

HfB₂ is too brittle for extensometer rod indentations; indenting the specimens could induce cracks. Previous creep results for polycrystalline YAG were obtained by cutting grooves near the top and bottom of the test specimens [65]. In an attempt to avoid applying this solution to the HfB₂ specimens; it was decided to cut the ends of the extensometer rods to chisel tips. The contact faces of the test specimen and SX YAG pushrod were chamfered such that the chisel tips would be in grooves created by their interface (Fig. 20a). This did not prove to be consistently successful. The first creep test yielded a coefficient of thermal expansion (CTE) of $4.7 \cdot 10^{-6}/\text{C}$. This result was satisfactory in comparison to the average CTE of $7.9 \cdot 10^{-6}/\text{C}$ as reported by VLOC

[131], the supplier of the SX YAG rods. During the second YAG creep test, the chisel tips slid off the circular chamfer of the SX YAG pushrod; the CTE was drastically higher than the VLOC average. It was decided that grooves cut into the HfB_2 test specimens would be the best option to obtain reliable, repeatable strain measurements (Fig. 20b). This conclusion proved to be correct.

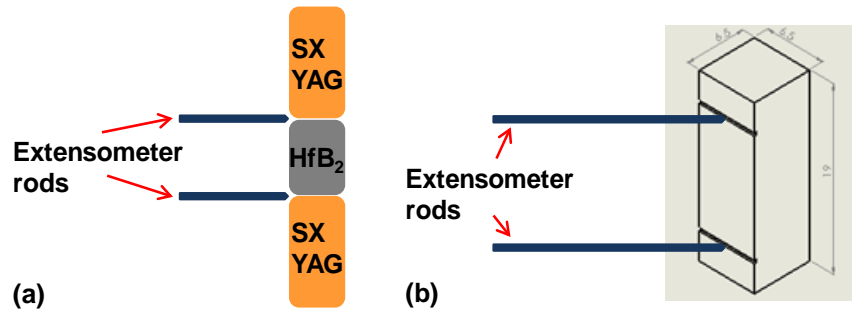


Fig. 20. Schematics of (a) originally-planned extensometer location and (b) final Test Method extensometer location.

3.5 Interactions within the Test Environment between Test Fixtures and HfB_2

An initial test was performed to validate the developed experimental facility and the developed test method. The initial validation compression creep test was of HfB_2 specimen (HfB_2 -1a) under a compressive stress of 25 MPa for ~15 hrs at 1500°C in laboratory air (Fig. 21a). Single crystal yttrium aluminum garnet (YAG, $\text{Y}_3\text{Al}_5\text{O}_{12}$) pushrods of 10-mm diameter were used to apply compressive stress to the HfB_2 test specimen. The single crystal YAG pushrods were physically separated from the HfB_2 test specimen by 99.99% pure platinum (Pt) foil (Alfa Aesar Premion©). At the end of the test, a white crustaceous deposit was seen on the surface of the specimen (Fig. 21b). This crustaceous deposit was most abundant at the HfB_2 specimen closest to the SX YAG pushrods. Scanning electron microscopy (SEM) and energy dispersive spectroscopy

(EDS: Hitachi Bruker Quantax 70, Tokyo, Japan) evaluation of the cross-section revealed Al- and Y-containing deposits were limited to the exterior portion of the scale (Fig. 22 c and d). It was concluded that an interaction between SX YAG and HfB_2 had occurred.

The deposits on the Pt foil (Fig. 23 a and b) led the author to believe that some sort of product was flowing over the Pt foil to react with the HfB_2 . A subsequent creep test was conducted. For this experiment run the Pt foil was greatly expanded and shaped to form a bowl encompassing the ends of the SX YAG pushrods. SX sapphire extensometer rods were also introduced to this experiment run.

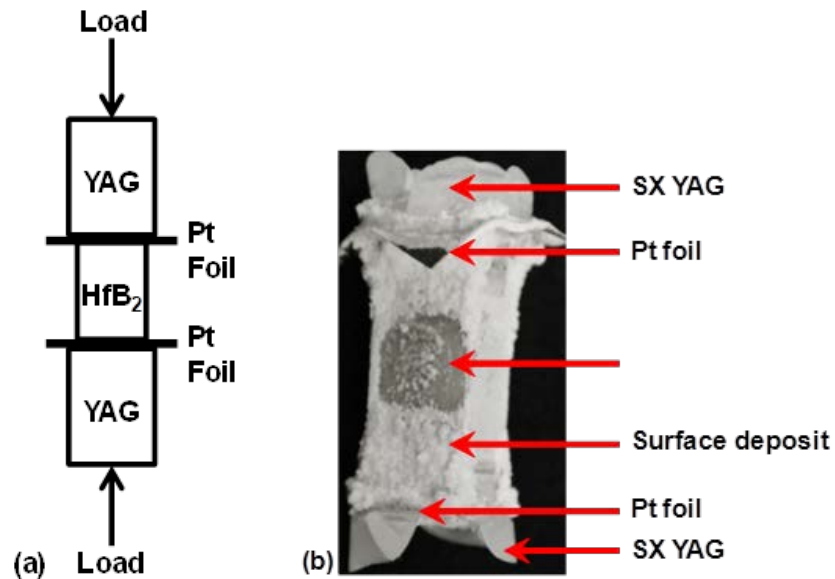


Fig. 21. (a) Schematic of initial validation test of HfB_2 . and (b) Photograph of HfB_2 -1a specimen after ~15 hrs at 1500°C in laboratory air under a 25 MPa compressive stress

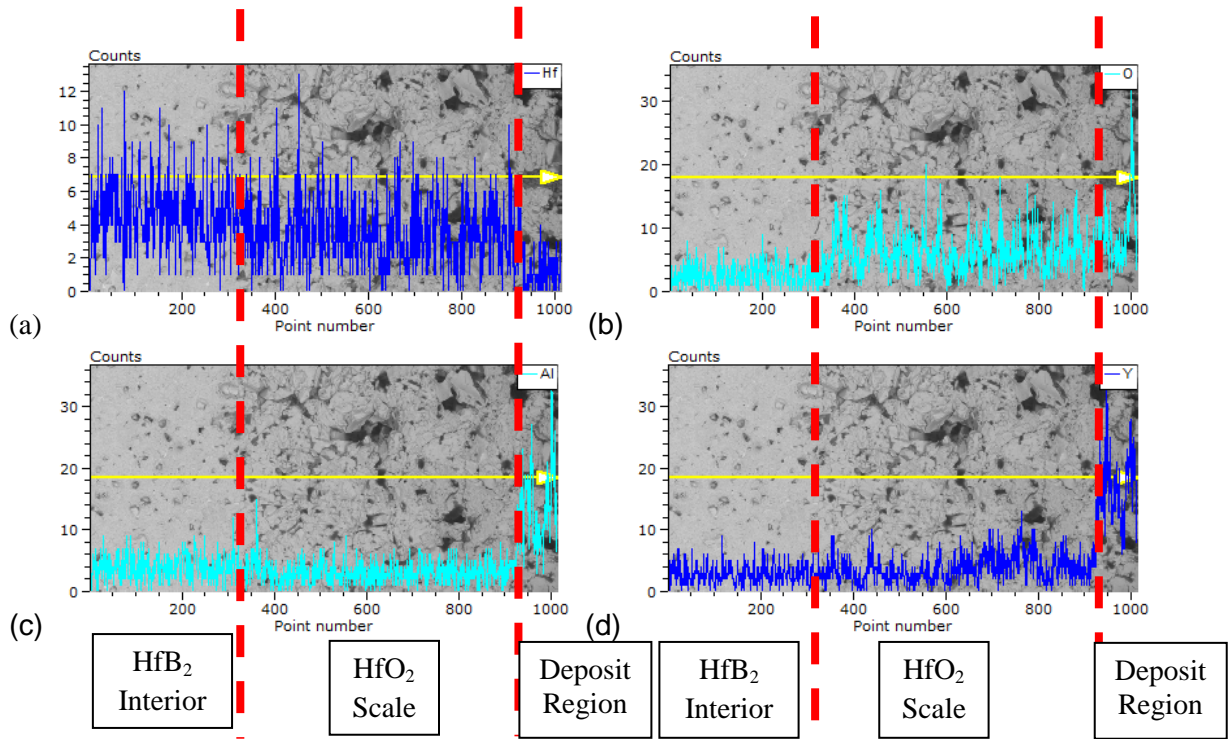


Fig. 22. EDS line analysis of (a) Hf, (b) O, (c) Al, and (d) Y returns of HfB₂-1a specimen after 14.9 hrs at 1500 °C under a compressive load of 25 MPa for 14.1 hrs in the presence of SX YAG and Pt foil. Al- and Y-containing deposits are limited to the deposit region.

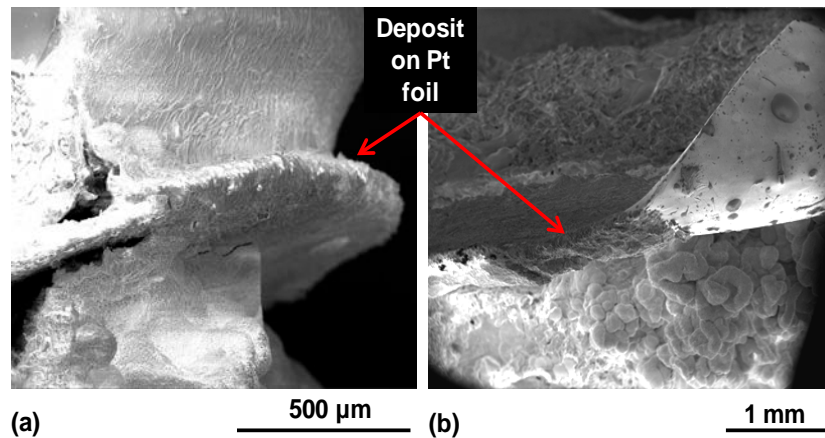


Fig. 23. SEM micrographs showing deposits seen on surface of Pt foil.

An *in situ* examination was made of the specimen during the temperature ramp portion of the creep test. It was observed that a coating was already starting to develop around 900°C. Due to facility issues, the temperature could not maintain 1500°C. For 1

hr the temperature fluxuated between 900 and 1500°C before the test was aborted. An appreciable amount of deposit was already on the specimen (Fig. 24a). Upon completion of the experiment, a white encrustation was observed on the surface of the specimen with the greatest concentration at both ends (Fig. 24b). Once again, Al and Y peaks are present in the crustaceous deposit that formed on the exterior of the HfB₂-3a specimen (Fig. 25). SEM/EDS analysis also revealed a lack of discernible Pt foil at the original HfB₂/SX YAG interface, but it was found in the grain boundary triple points throughout the specimen, which is explained in greater detail in Section 4.1.2. Thus, the Pt foil ceased to act as a physical barrier, placing HfB₂ in direct contact with YAG. Subsequently, it was conjectured that direct physical contact between HfB₂ and SX YAG resulted in the formation of the encrustation on the surface of the HfB₂ specimen.



Fig. 24. (a) Photograph of HfB₂-3a after aborted test run to 1500°C for 1 hr, followed by 1 hr temperature fluxuation from 900 - 1500 °C



Fig. 24. (b) Photograph of HfB₂-3a after test run at 1500°C for 7.3 hrs at 1500°C under a compressive load (25, 50 MPa) for 6.2 hrs

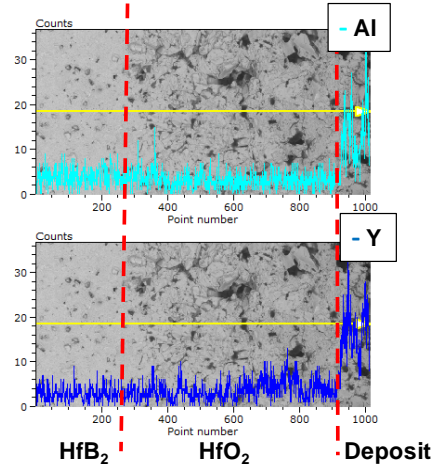


Fig. 25. Micrograph of x-ray count returns of cross-section, indicating Al- and Y-containing deposit is limited to the surface of the oxide layer.

To characterize and understand the interaction with Pt and formation of the crustaceous deposit, a series of HfB_2 test specimens were subjected to heat treatment (under zero load) at 1500°C in various test configurations (Fig. 27 and Fig. 46) described in detail in Chapter IV. Following the heat treatment experiments, the test specimens were sectioned and polished to a $1\text{-}\mu\text{m}$ finish using a diamond slurry. The post-test microstructure was characterized using SEM, EDS, and transmission electron microscopy (TEM) for chemical analysis.

IV. High Temperature Compatibility of HfB₂ with Pt Foil, SX YAG, and Alumina

The main objective of the Air Force Institute of Technology research into UHTCs is to characterize their high temperature mechanical properties in air and steam environments. To achieve this objective, materials that can perform under these conditions are needed to conduct testing. This material selection is not a trivial matter.

As detailed in Section 3.5, the preliminary tests performed to validate the developed Experimental Facility and Test Methods revealed an interaction between HfB₂ and the test fixture materials. Before the Test Method can be considered valid, it is important to demonstrate that materials used for the test fixtures do not cause degradation of the test specimen in a given test environment. Hence the interaction of HfB₂, Pt foil, and SX YAG must be carefully analyzed to answer the following questions:

- 1) What is the nature of the interaction between HfB₂, SX YAG, and Pt?
- 2) Does the aforementioned interaction cause degradation of HfB₂? If so, what is the form of degradation?
- 3) How do we modify the test method to avoid or minimize the aforementioned interaction?

A series of heat treatment tests were conducted to investigate, characterize, and determine mitigation of the interactions between HfB₂, SX YAG, and Pt.

4.1 Thermal Compatibility of HfB₂ and Pt Foil at 1500°C and 1600°C in Air

Unexpectedly, it was observed that Pt from the Pt foil diffused into the grain boundaries of the HfB₂ specimens of the first two compressive creep tests (HfB₂-1a and

HfB₂-3a) as described above. An as-processed sample was polished to 1 μm to evaluate the pre-test microstructure via SEM and EDS. Empty grain boundary triple points and channels were observed (Fig. 26), confirming that Pt was not a contaminant in the as-processed HfB₂.

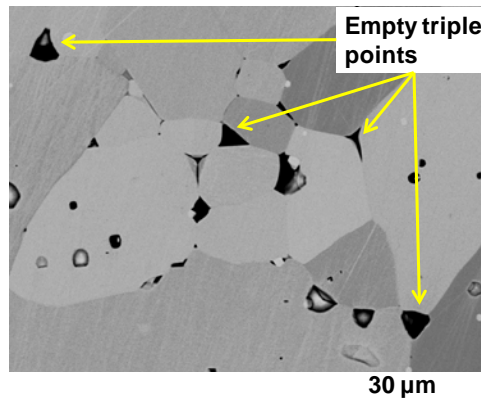


Fig. 26. SEM micrograph showing as-processed HfB₂ sample annotating several of the empty grain boundaries.

4.1.1 Thermal Compatibility of HfB₂ and Pt at 1500°C and 1600°C in Air -

Experimental Setup

Following the initial validation experiments, Pt was found in the triple point grain boundaries, indicating an interaction between HfB₂ and Pt. The objective of the heat treatment tests performed with high purity Pt foil is to determine if an interaction between HfB₂ and SX YAG was facilitated by the applied load or if SX YAG was a factor. To meet this objective, HfB₂ test specimens were subjected to heat treatment (under zero load) at 1500°C in an ambient air tube furnace under three different conditions: (Test 2) 24 hrs in laboratory air with the specimen physically separated from SX YAG by Pt foil (Fig. 26a), (Test 3) 24 hrs in laboratory air with the specimen in contact with Pt foil (Fig.

26b), and (Test 4) Pt-wrapped HfB₂ heat treated in tube furnace for 24 hrs at 1600°C in air (Fig. 26c). The results of the HfB₂-3a specimen were used for the analysis discussion of Test 1 (Section 4.1.2).

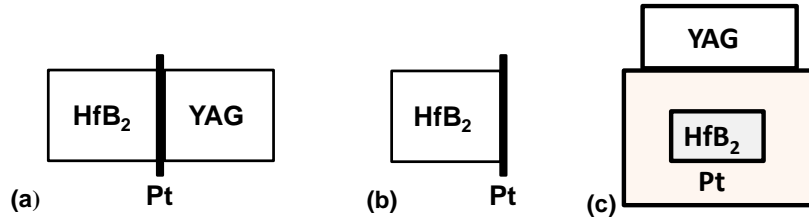


Fig. 27. Schematic drawing of the heat treatment experimental setup for HfB₂ and Pt interaction evaluation. (a) (b) HfB₂ and SX YAG separated by Pt foil under no load, (b) HfB₂ in contact with Pt foil only, and (c) Pt-wrapped HfB₂.

The creep test utilizing Pt foil spacers (Fig. 21a) (Test 1) resulted in the SX YAG rod adhering to the HfB₂ sample. Conversely, the SX YAG rod was easily separated from the HfB₂ following a no load heat treatment (Fig. 27b). Remarkably, no visible Pt foil could be found on either the HfB₂ specimens or the SX YAG when the HfB₂ specimens were separated from the SX YAG in the first three cases. All four test specimens were sectioned and polished to 1 µm using diamond slurry. The post-test microstructure was characterized using SEM along with EDS for compositional analysis.

As expected, all HfB₂ specimens tested exhibited oxidation behavior consistent with that described in literature [46,104]. Oxidation at 1500°C in air resulted in a dense adherent oxide scale consisting of two phases, HfO₂ and B₂O₃. A porous HfO₂ scale had a columnar structure with a glassy B₂O₃ partially filling the channels between the columnar grains. The post-test microstructures of all HfB₂ specimens (i.e. the specimens heat

treated under 25 MPa and the specimens heat-treated under zero stress) were characterized using SEM together with the EDS for elemental analysis. The specimens oxidized in the presence of SX YAG also developed a crustaceous deposit.

The HfB₂ specimens were sectioned in a manner that permitted examination and characterization of the surface in direct contact with Pt foil. As previously mentioned, upon conclusion of these heat treatment experiments, the Pt foil was not visible on either the HfB₂ or YAG surfaces that were in direct contact with Pt. This observation was further confirmed via the EDS analysis of the HfB₂ surface originally in contact with Pt. Conversely, the SEM/EDS analysis of the unoxidized HfB₂ region revealed that Pt had diffused into the triple points (where 3 grains meet) throughout the entire unoxidized core of the HfB₂ specimens.

4.1.2 Thermal Compatibility of HfB₂ and Pt Foil during Compression Creep –

Test 1 Analysis

The Test 1 HfB₂ specimen was sectioned along both the plane perpendicular and the plane parallel to the loading direction and then polished to 1 μ m. Worthy of note is the presence of an oxide layer on the surface of the HfB₂ specimen that was in contact with the Pt foil/SX YAG pushrod (i.e., not exposed to the gaseous oxidizing furnace environment) (Fig. 28a). The load applied via the SX YAG pushrods in combination with the flexible Pt foil between the SX YAG pushrods and the HfB₂ specimen was expected to prevent the oxidizing furnace environment from reaching the top and bottom surfaces of the HfB₂ specimen. It is possible that an oxygen-containing species from the SX YAG oxidized the HfB₂. Notably, there was no discernible Pt foil at the HfB₂/SX

YAG interface (Fig. 28a). Only slight increases in the Pt returns on the exterior of the scale that formed at the HfB_2 /SX YAG interface were able to be discerned via EDS analysis (Fig. 28b). A SEM examination of the unoxidized interior of the specimen revealed Pt diffused into the grain boundaries throughout the entire specimen. An example is shown in Fig. 29a with the accompanying EDS spectra in Fig. 29b. The only location that the Pt foil remained intact was where the Pt foil had extended past the SX YAG so there had been no contact with either HfB_2 or SX YAG during testing (Fig. 30).

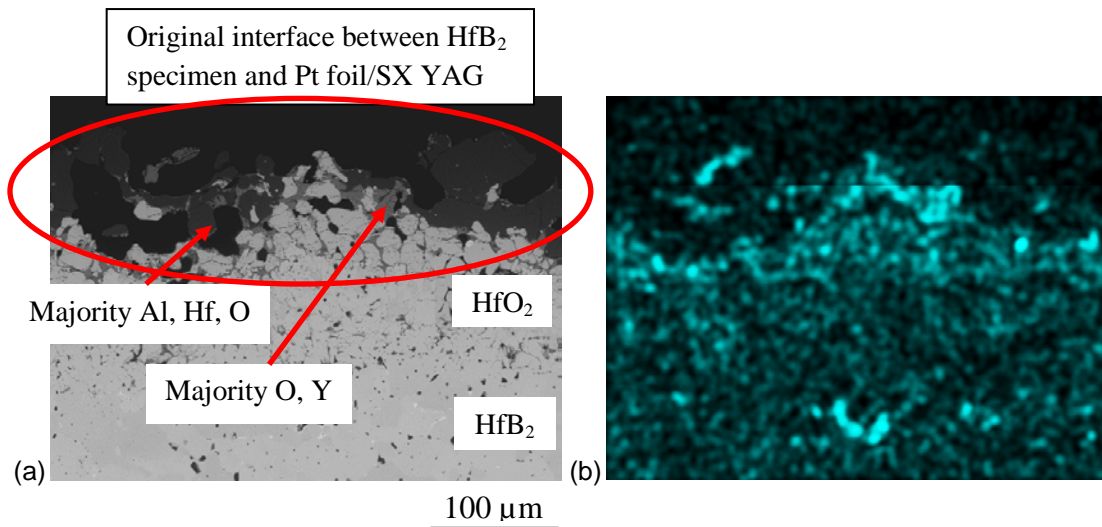


Fig. 28. (a) SEM micrograph and (b) EDS Pt map analysis of area of contact between HfB_2 specimen and Pt foil/SX YAG pushrod after 7.3 hrs at 1500°C under a compressive load (25, 50 MPa) for 6.2 hrs. There is not any discernible Pt present at this interface. Note that the HfB_2 oxidized, forming a HfO_2 layer. There was also a layer containing Al, Hf, O, and Y.

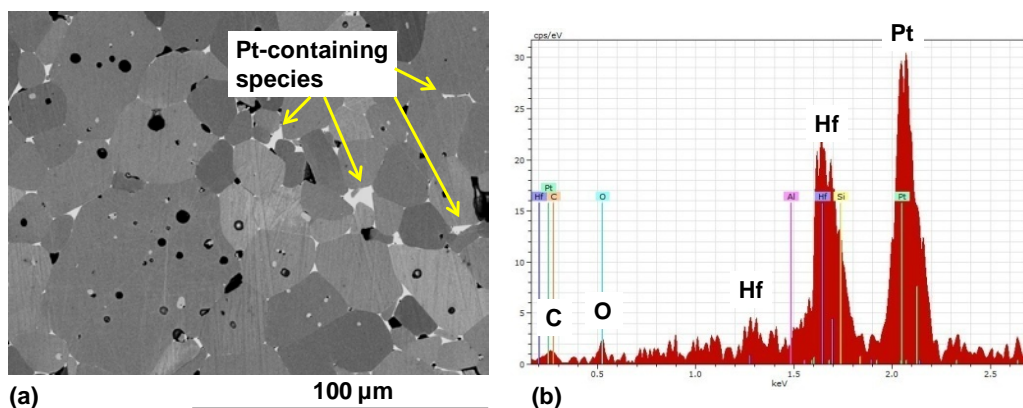


Fig. 29. (a) SEM micrograph of unoxidized bulk of HfB₂ specimen after 7.3 hrs at 1500°C under a compressive load (25, 50 MPa) for 6.2 hrs in the presence of SX YAG and Pt foil. Several areas of Pt-containing species in the HfB₂ grain boundaries have been annotated. (b) EDS spectra of Pt-containing area.

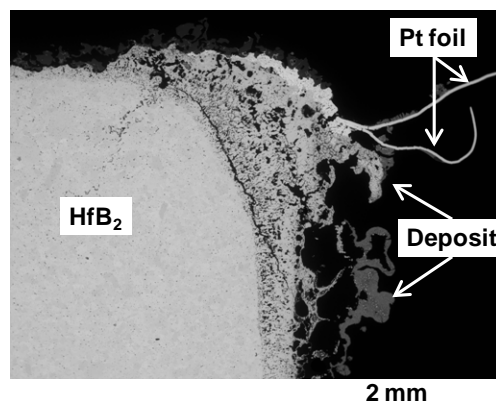


Fig. 30. SEM micrograph showing deposits on Pt foil of HfB₂ specimen after 7.3 hrs at 1500°C, 6.2 hrs under a compressive load (25, 50 MPa) in the presence of SX YAG. Post-test, intact Pt foil has been annotated.

Transmission electron microscopy (TEM) revealed that the majority of the Pt was contained in the triple points. The grain boundaries from the triple point in Fig. 31 did not contain Pt. The majority of grain boundaries did not contain Pt. The few grain boundary channels that did contain Pt (example shown in Fig. 32) were found in the cross-section area closest to the end of the specimen that was originally in contact with the Pt foil and SX YAG. The Pt in the triple points and narrower (32 nm wide) did not

have a significant amount of Hf, only approximately 5 at%. An exception was a "chunk" of Pt found in a grain boundary channel that was on average 85 nm wide (Fig. 33). This "chunk" was found to be comprised of almost equal amounts of Hf and Pt.

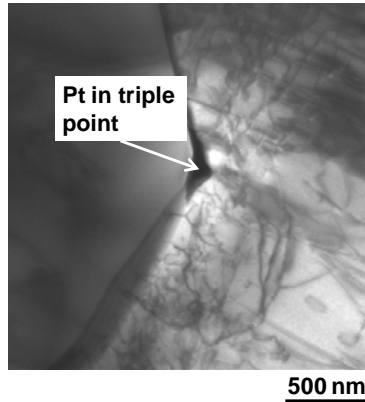


Fig. 31. TEM micrograph of Pt in triple point in unoxidized bulk of HfB_2 specimen after 7.3 hrs at 1500°C , 6.2 hrs under a compressive load (25, 50 MPa) in the presence of SX YAG.

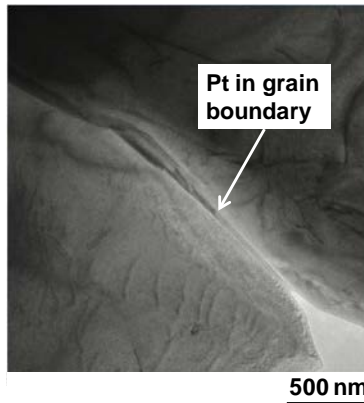


Fig. 32. TEM micrograph of Pt in grain boundary in unoxidized bulk of HfB_2 specimen after 7.3 hrs at 1500°C , 6.2 hrs under a compressive load (25, 50 MPa) in the presence of SX YAG..

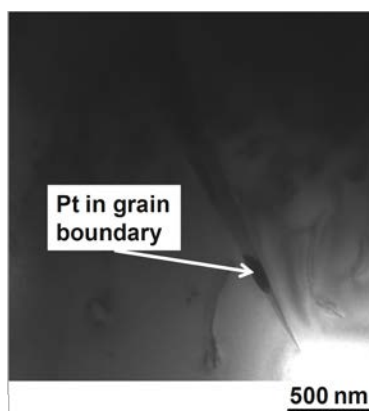


Fig. 33. TEM micrograph of chunk of Pt in grain boundary in unoxidized bulk of HfB_2 specimen after 7.3 hrs at 1500°C , 6.2 hrs under a compressive load (25, 50 MPa) in the presence of SX YAG.

4.1.3 Thermal Compatibility of HfB_2 and Pt Foil in the Presence of SX YAG under Zero Load – Test 2 Analysis

In order to determine whether compressive stress contributed to the formation of the crustaceous surface deposit in the initial validation tests, a HfB_2 specimen was heat treated in a tube furnace for 24 hrs under zero stress at 1500°C in air with the specimen physically separated from SX YAG by Pt foil (Fig. 27a). The heat treatment under zero stress resulted in the formation of the crustaceous surface deposit similar to that in Fig. 24. No effect of compressive load was found. The crustaceous deposit covered the entire surface of the HfB_2 specimen, including the area of contact with Pt foil. Remarkably, no visible Pt foil could be found when the HfB_2 specimen was separated from the SX YAG. The post-test microstructures of the HfB_2 -1a heat treated under a 25 MPa load and that heat treated under zero stress were characterized using SEM together with the EDS for elemental analysis. Similar results were obtained, further supporting the conclusion that the low compressive stress of 25 MPa had little effect on the formation of the surface deposit or its morphology and composition.

The HfB_2 , Pt foil, and SX YAG of Test 2 were configured in the same manner as Test 1, but were not subjected to a compressive load (Fig. 27a). A deposit scale formed on the entire surface of the HfB_2 sample (Fig. 34). Platinum foil was not observed on the SX YAG puck or the HfB_2 specimen when the two were separated. (Fig. 34b) (Note the presence of the crustaceous white deposit in that same region.) The EDS wide-area spectrum analysis of the annotated region in Fig. 34b revealed no significant Pt peaks, confirming the absence of Pt foil on the surface of the specimen in this original area of contact between HfB_2 , Pt foil, and SX YAG. (Fig. 35) A closer examination of different morphologies in the aforementioned area revealed a lack of significant amounts of Pt in any of the constituents.

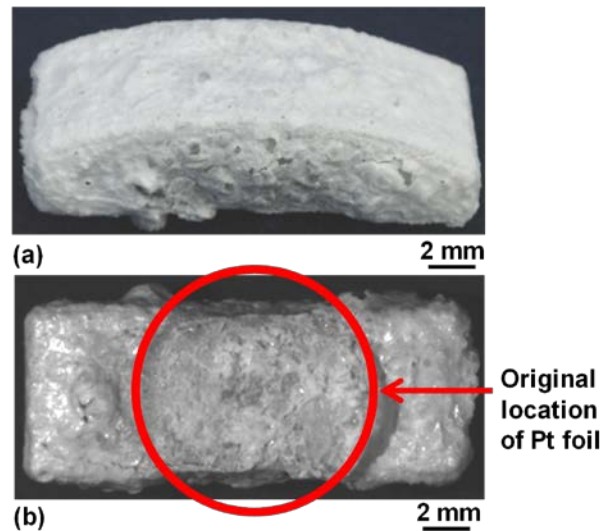


Fig. 34. Photographs of HfB_2 specimen after 24 hrs at 1500°C under zero load in the presence of SX YAG and Pt foil. A crustaceous white deposit has formed over the entire surface of the HfB_2 specimen. (a) Top and side view. (b) Annotated image of original vicinity of Pt foil on the bottom of the HfB_2 specimen.

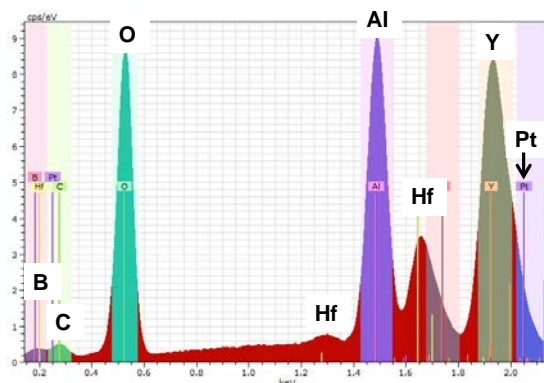


Fig. 35. EDS wide-area analysis of original area of Pt foil on deposit on HfB₂ specimen after 24 hrs at 1500°C under no load in the presence of SX YAG. It is covered in the white deposit comprised of Al, C, Hf, O, and Y. Note the lack of a distinct Pt peak.

The HfB₂ specimen was sectioned for SEM/EDS analysis. The cross-section included (i) the edge of the HfB₂ specimen in contact with the Pt foil, (ii) the interior of the HfB₂ specimen, and (iii) the edges of the HfB₂ specimen exposed to the environment inside the tube furnace (Fig. 36). Figure 37a shows that the surface exposed to the tube furnace environment has 3 layers (with some deposit intrusions into the HfO₂ layer. The HfO₂ layer and crustaceous deposit are more intermixed on the interface surface (Fig. 37b). Aluminum and yttrium was found throughout the oxide scale/deposit on the surface that had been in contact with Pt and SX YAG (Fig. 38). It is worth noting that the deposit on the area of contact between the Pt foil and HfB₂ was thinner than that on the surfaces of the HfB₂ specimen exposed to the furnace environment (0.16 and 0.26 mm, respectively). It is evident in Fig. 38 that a distinct line indicating Pt foil was not present at the original interface between the HfB₂ and SX YAG. In contrast, the triple point grain boundaries of the unoxidized HfB₂ interior contained significant amounts of Pt (Fig. 39).

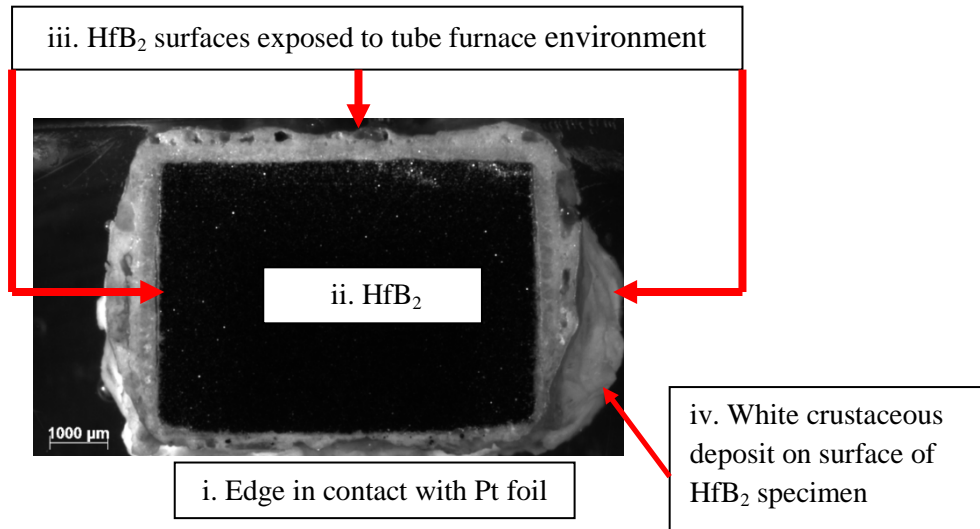


Fig. 36. Reflected light optical micrograph of cross-section of HfB_2 specimen after 24 hrs at 1500°C under no load in the presence of SX YAG and Pt foil. Note that no Pt foil is evident in the original area of contact of the Pt foil with the HfB_2 specimen and that the deposit in this area is thinner than the surfaces of the HfB_2 specimen exposed to the tube furnace environment.

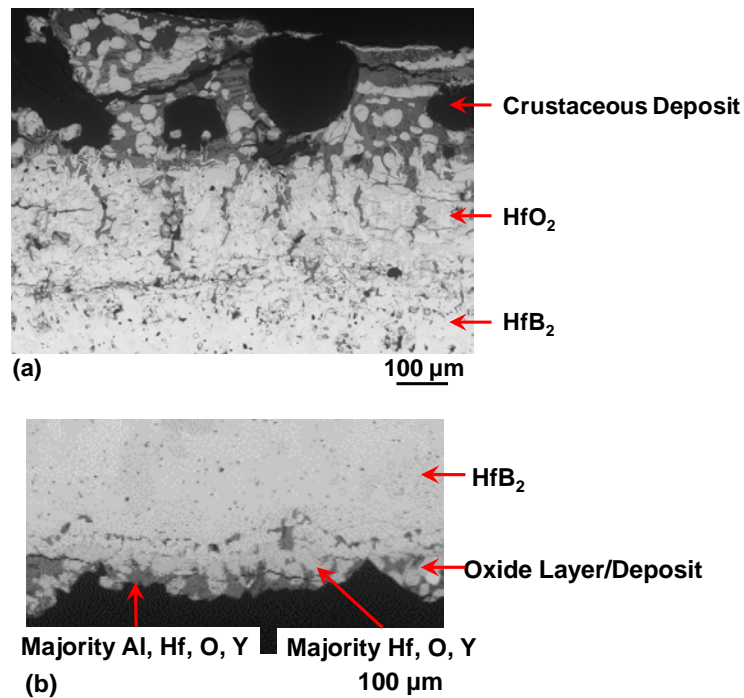


Fig. 37. SEM micrograph showing cross-sections of the (a) surface exposed to the tube furnace environment and (b) HfB_2 and Pt foil/SX YAG contact area of HfB_2 specimen exposed to tube furnace environment after 24 hrs at 1500°C under no load in the presence of Pt foil and SX YAG.

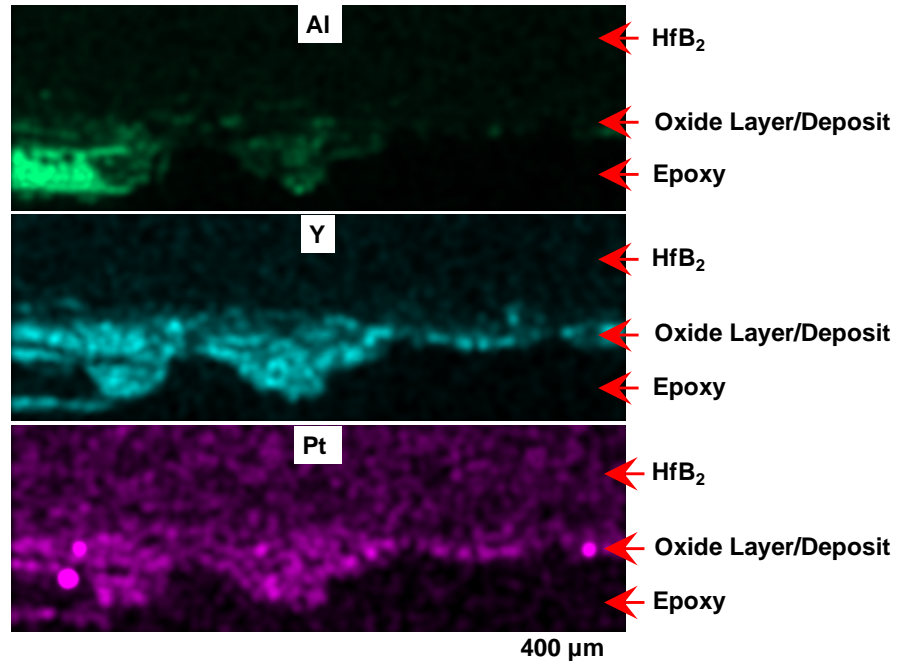


Fig. 38. EDS map analysis of Al and Y locations in the cross-section of the HfB₂ and Pt foil/SX YAG contact area of HfB₂ specimen exposed to tube furnace environment after 24 hrs at 1500°C under zero load in the presence of Pt foil and SX YAG .

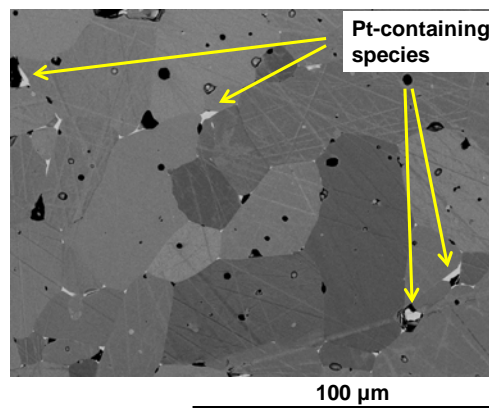


Fig. 39. SEM micrograph showing unoxidized bulk of HfB₂ specimen after 24 hrs at 1500°C under zero load in the presence of Pt foil and SX YAG. Pt-containing species are found in many of the HfB₂ grain boundaries.

4.1.4 Thermal Compatibility of HfB₂ and Pt Foil under Zero Load – Test 3

Analysis

As mentioned above, upon conclusion of Tests 1 and 2, the Pt foil was not visible on either the HfB₂ or SX YAG surfaces that were in direct contact with Pt foil. This

observation was further confirmed via EDS analysis of the HfB_2 surface, originally in contact with Pt foil. This observation was further confirmed via the EDS analysis of the HfB_2 surface originally in contact with Pt foil. Conversely, the SEM/EDS, as well as TEM, analysis of the unoxidized HfB_2 region revealed that Pt had diffused into the grain boundaries throughout the entire unoxidized core of the HfB_2 specimen. To confirm these findings, a HfB_2 specimen was placed in direct contact with Pt foil and heat treated for 24 hrs at 1500°C in air (Fig. 27b). After heat treatment, a slight discoloration of the entire specimen was observed (Fig. 40). Notably, the white crustaceous deposit was not seen. The HfB_2 specimen was sectioned and polished and extensive SEM/EDS analysis was performed. Test 3 illustrated that Pt diffusion through HfB_2 grain boundaries under zero load and resulted in the absence of the white crustaceous deposit when SX YAG was not present in the test chamber.

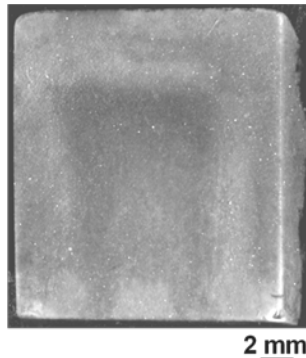


Fig. 40. Optical micrograph of HfB_2 specimen after 24 hrs at 1500°C under zero load and without the presence of SX YAG.

Sectioning, polishing, and SEM analysis of the Test 3 HfB₂ specimen surface not in direct contact with the Pt foil revealed that the discoloration was a thin scale on the surface of the HfB₂ specimen (Fig. 41). Evaluation of the unoxidized HfB₂ bulk revealed that Pt had diffused into the triple points throughout the entire specimen (Fig. 42).

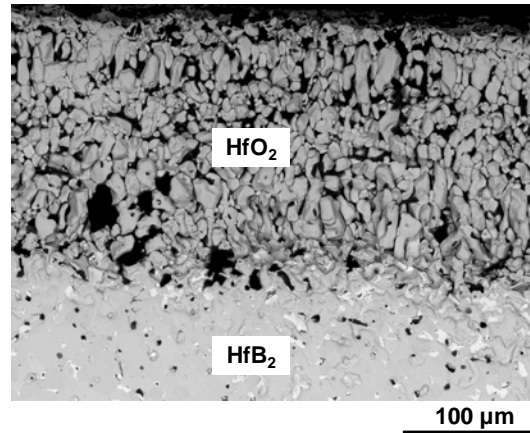


Fig. 41. Cross-sectional SEM micrograph of the surface of the HfB₂ specimen exposed to the tube furnace environment after heat treatment with Pt for 24 hrs at 1500°C in air.

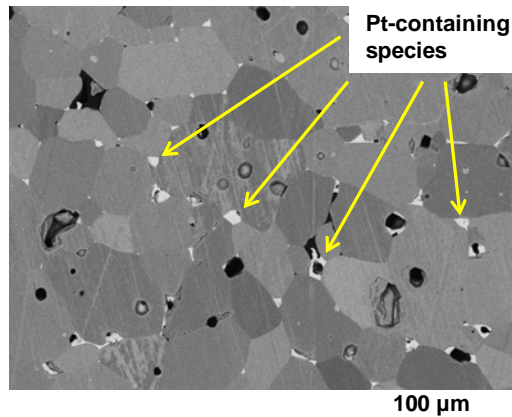


Fig. 42. Annotated SEM micrograph showing HfB₂ oxidized while in contact with Pt under no load at 1500°C for 24 hrs without the presence of SX YAG. Platinum containing species (arrows) are seen in the grain boundaries throughout the unoxidized HfB₂.

4.1.5 Thermal Compatibility of HfB₂, Pt Foil, and SX YAG at 1600°C in Air under Zero Load – Test 4 Analysis

Test 4 involved heat treating HfB₂ wrapped in Pt foil with SX YAG (Fig. 27c) at 1600°C for 24 hrs. This test yielded more dramatic results. Following the test, the sample could not be separated from the crucible base, and the Pt foil could not be removed from the sample. The sample was bisected for analysis. The micrograph in Fig. 43 reveals the degradation of the HfB₂ sample. The bright areas in Fig. 43 are comprised mostly of ~51 at% Al and 17 at% Pt. The average Hf at% was only 0.24 in the bright area. The bright areas are surrounded by a composition that had an average of 71.43 at% Al, 1.72 at% Pt, and 0.14 at% Hf. There are no areas that are comprised mostly of Hf and/or O. Figure 44a reveals the low levels of, and lack of concentration of Hf in the post-test specimen; the HfB₂ appears to be completely diffused throughout the cross-section. Quantitative EDS analysis shown in Table 3 supports this finding. Analysis of the various constituents shows that the maximum Hf at% of any constituent was only 0.31 at%. It is readily evident in Fig. 44b that there are no delineations indicating the location of the original Pt foil surrounding a rectangular sample of HfB₂.

EDS quantitative analysis revealed Pt in varying amounts throughout most of the components of the post-test bulk. Figure 44 a and b demonstrates that Pt moved throughout the original HfB₂ specimen. The bright areas of Fig. 44a are areas of Hf, and Fig. 44b reveals the areas of highest Pt returns. These bright areas correspond to one another. The logical conclusion is that the Pt diffused throughout the HfB₂.

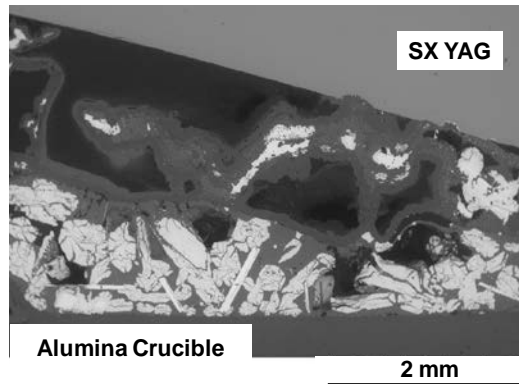


Fig. 43. SEM micrograph showing cross-section of Pt-wrapped HfB_2 topped with SX YAG after 24 hrs at 1600°C in tube furnace in air.

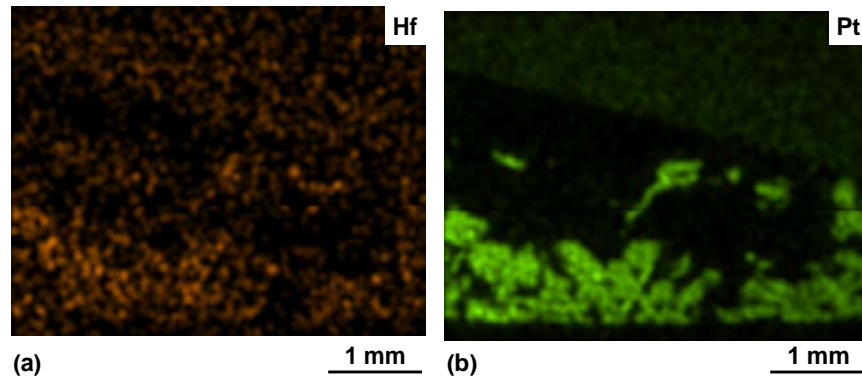


Fig. 44. EDS map of (a) Hf and (b) Pt in Test 4.

Table 3. Maximum atomic% of select elements in various constituents of HfB_2 specimen subjected to Test 4.

Element	Hf	Al	O	Pt	Y
Max wt%	0.31	79	52	22	52

At temperatures above 1500°C , HfB_2 has been proven to dissolve into molten Ni and its alloys [133]. Test 4 suggests that HfB_2 would completely dissolve into Pt-containing species at 1600°C . There is no reported literature on the phase diagrams of the Hf-B-Pt or Hf-O-Pt systems, but Hf and Pt are known to form multiple alloys (Hf_xPt_y) [134,135]

4.1.6 Thermal Compatibility of HfB₂ and Pt at 1500°C and 1600°C in Air –

Discussion

Intergranular penetration of HfB₂ by molten Pt, while unexpected, is not a unique phenomenon. But the complete diffusion of Pt_xB_y throughout a nearly dense specimen is a distinctive characteristic. Most wetting studies of Group IV transition metals revealed only limited intergranular penetration of the substrate [133,136].

The penetration wetting of HfB₂ by molten Ni alloys was reviewed by Passerone *et al.* [133]. Wetting of HfB₂ by molten Ni is driven mainly via the highly dissolutive reactivity in the Ni-HfB₂ system. At high temperatures HfB₂ easily dissolves into the molten Ni forming a binary liquid. At the interface, the HfB₂ will subsequently precipitate out upon cooling, creating an irregular surface. On the other hand, Ni_xB_y alloys have shown reduced interfacial interactions; therefore, improved wetting properties. Pure Ni grain boundary penetration was aided by the significant dissolution of HfB₂ into the Ni. Grain boundary penetration without significant HfB₂ grain dissolution was achieved by alloying Ni with B. Complete infiltration of 80% dense HfB₂ was achieved by utilizing Au.

Transmission electron microscopy analysis (TEM) was unable to definitively determine the composition of the Pt alloy that infiltrated the HfB₂ grain boundaries in this test. Chunks of a Pt alloy containing Hf were found within a grain boundary channel that was wider than the channels that did not contain any Pt pieces. A conclusion could be drawn that some portion of HfB₂ grains dissolved into the Pt. On the other hand, the Pt found in the triple points and in narrow channels did not contain Hf. The work by Passerone *et al.* [133] supports an assumption that Pt formed an alloy with B.

This study was conducted at 1500°C; melting of the Pt foil was not expected since Pt usually melts at 1768°C. Loehman *et al.* [127] discovered an interaction between their HfB₂-20 vol% SiC samples and Pt thermocouples that caused the thermocouples to melt above 1000°C. The degradation of the Pt thermocouples was attributed to the formation of PtSi within the thermocouple from the oxidation products of SiC (possibly SiO). Various compositions of Pt_xSi_y have been shown to melt between 986 and 1229 °C [137]. This phenomenon was also observed experimentally between HfB₂ and Ni. Sobczak *et al.* [138] observed that a Ni sample in contact with HfB₂ started melting at ~1300°C, ~150 °C lower than the melting point of Ni. Their observations were in a good agreement with the thermodynamic calculations of Passerone *et al.* [139] that determined Ni in the Ni/HfB₂ system starts to form a liquid at ~1100°C.

Platinum is known to form a boride alloy [134,137,140-142]. This study proposes that Pt reacts with boron in HfB₂ or B₂O₃ to form various Pt_xB_y, compositions of which have been known to melt at 825 °C [141]. This phenomenon was observed in a wetting study between Ni and ZrB₂ in which a Ni₂B compound was created [133]. At the test temperatures of this study, the Pt foil would transition into molten Pt_xB_y and be drawn into grain boundaries to pool in the triple points. There are several mechanisms that could have caused the Pt_xB_y to diffuse into the grain boundaries. The Pt_xB_y could have been drawn into the grain boundaries via capillary action. Pt is known to have weak van der Waals forces that make it an excellent catalyst material [143,144]. Once the Pt_xB_y started to flow, these forces would attract the molten Pt to the grain boundary walls. For a fluid to form an intergranular film, these adhesion forces between the molten Pt_xB_y and grain boundary walls must meet the following condition:

$$2\gamma_{SL} < \gamma_{SS} \quad (6)$$

where γ_{SL} and γ_{SS} are the energies of solid-liquid and solid-solid interfaces, respectively [145,146].

Ceramic grain boundaries are known to have localized space charges and lower partial pressures in comparison to the bulk material [147-150]. Once again, the Pt van der Waals forces are influential. The molten Pt would be drawn to the grain boundary space charges, pulling the Pt_xB_y into the grain boundaries. It is also possible that the lower partial pressures within the grain boundaries caused the Pt_xB_y to be drawn into the grain boundaries due to natural fluid dynamics.

The lack of Pt in most of the post-test grain boundary channels is most likely due to dewetting. Grain boundaries can dewet during the course of testing via two different mechanisms as shown schematically in Fig. 45. If the dislocation spacing decreases or the number of dislocations increases so that the misorientation angle between grains transitions from θ^* to θ^{**} , the grain boundary will dewet at θ^{**} . Also, if the grain boundaries are at misorientation θ^* , the grain boundary would dewet as the temperature decreased from T_2 to T_1 . As the grain boundary channels dewet, the triple points are a natural pooling location. Triple points can also act as a capillary upon cooling, drawing in the molten Pt [148].

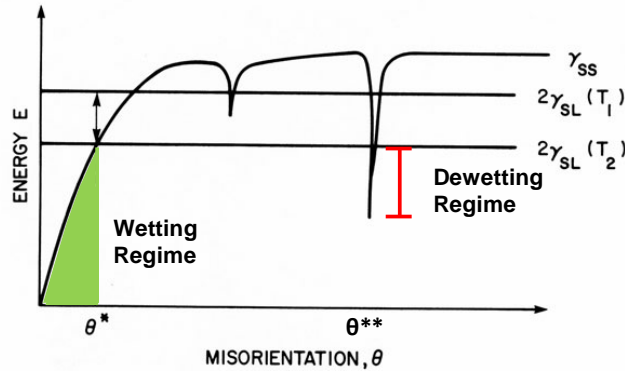


Fig. 45. Schematic diagram of solid-solid and solid-liquid interface energies. (After Clark [145], Used with permission)

4.2 Thermo-chemical Compatibility of HfB₂ with SX YAG at 1500°C in Air

4.2.1 Thermo-chemical Compatibility of HfB₂ with SX YAG at 1500°C in Air -

Experimental Setup

Initially, 99.99% pure Pt foil was introduced into the Test Method developed in this work in order to prevent physical contact between the HfB₂ and SX YAG. Tests 1, 2, and 4 of this study included Pt foil as a physical barrier between the HfB₂ and the SX YAG pushrods. The results revealed that Pt diffused into the grain boundaries of the HfB₂ specimens. This effectively removed the physical barrier between the HfB₂ and the SX YAG, placing the HfB₂ specimen and SX YAG into direct contact. It was postulated that this direct contact resulted in the formation of the white crustaceous deposit observed on the surface of the HfB₂ specimens in Tests 1 and 2. The mechanisms behind formation of the Al- and Y-containing crustaceous layer on the surface of the HfB₂ specimens were explored in heat treatment experiments, where HfB₂ specimens were exposed to 1500°C in air for 18 hrs in different contact combinations with SX YAG and alumina.

Hafnium diboride test specimens were exposed to 1500°C in laboratory air for 12-18 hrs in different contact combinations with SX YAG and alumina. The schematic drawing of the heat treatment experimental setup is shown in Fig. 46. The contact combinations were: (Case A) HfB₂ specimen in contact with SX YAG, (Case B) HfB₂ specimen separated from SX YAG by a 1-mm-thick 99.8% pure alumina spacer, (Case C) HfB₂ specimen separated from SX YAG by a very large 3-mm-thick 99.8% pure alumina spacer, (Case D) HfB₂ specimen in close proximity (~3 mm) but not in contact with SX YAG, and (Case E) one piece of HfB₂ was placed in direct contact with SX YAG and another approximately 3 mm apart from SX YAG. All heat treatment experiments were performed in a horizontal MoSi₂ resistance-heated tube furnace. The specimens were placed in a 900-mm long alumina tube of 50-mm diameter closed on both ends with alumina plugs.

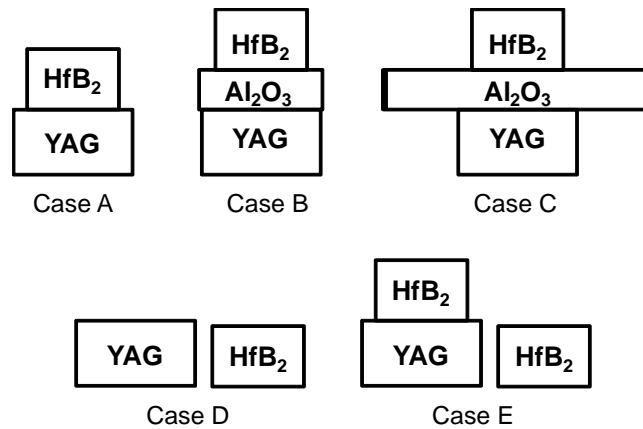


Fig. 46. Schematic drawing of the heat treatment experimental setup: (Case A) HfB₂ in contact with SX YAG, (Case B) HfB₂ and SX YAG separated by alumina spacer, (Case C) HfB₂ specimen separated from SX YAG by a very large 3-mm-thick 99.8% pure alumina spacer, (Case D) HfB₂ specimen in close proximity (~3 mm) but not in contact with SX YAG, and (Case E) one piece of HfB₂ was placed in direct contact with SX YAG and another approximately 3 mm apart from SX YAG.

The surfaces of the heat-treated specimens were examined using X-ray diffraction (XRD: Rigaku Ultima IV X-Ray Diffractometer, Tokyo, Japan (Appendix E). The Rietveld refinement program MAUD [151] was used to determine phase fractions from the X-ray diffraction patterns. The heat-treated specimens were then sectioned and polished to a 1- μm finish using diamond slurry for examination and chemical analysis. The microstructures were characterized using SEM together with EDS for elemental analysis. Both pieces of equipment are shown in Appendix E.

4.2.2 Thermo-chemical Compatibility of HfB_2 with SX YAG at 1500°C in Air – HfB_2 in Contact with SX YAG (Case A)

Two experiments utilizing the setup of Case A were conducted (Fig. 46). The first heat treatment experiment ran for 12 hrs, and the second test ran for 18 hrs. Upon completion of both heat treatment experiments, a white crustaceous deposit was observed on the surfaces of the HfB_2 specimen exposed to the tube furnace environment, indicating an interaction between SX YAG and HfB_2 (Fig. 47a and Fig. 48a). The deposit appeared to be less compact on the HfB_2 surfaces exposed to the furnace environment (Fig. 47a and Fig. 48a) than on the HfB_2 surface in direct contact with SX YAG (Fig. 47b and Fig. 48b).

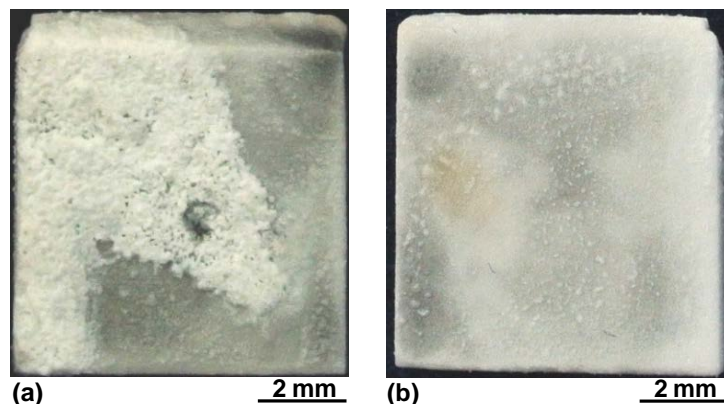


Fig. 47. Photographs of HfB₂ after heat treatment in contact with SX YAG for 12 hrs at 1500°C in air. (a) HfB₂ surface exposed to furnace environment and (b) HfB₂ surface that was in contact with SX YAG.

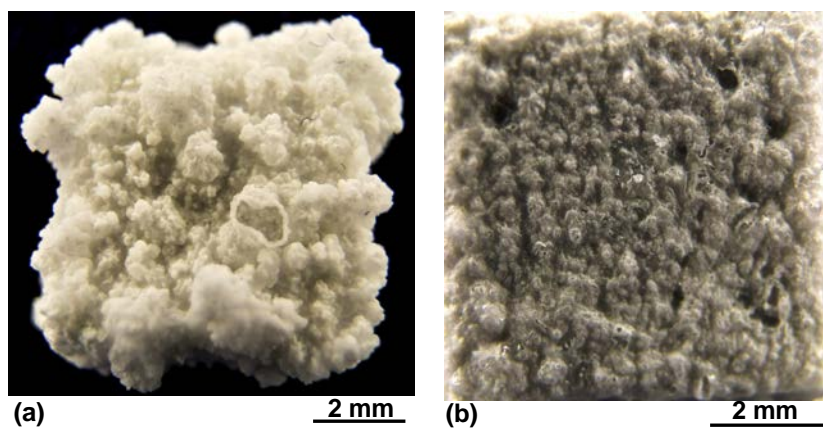


Fig. 48. Photographs of HfB₂ after heat treatment in contact with SX YAG for 18 hrs at 1500°C in air. (a) HfB₂ surface exposed to furnace environment and (b) HfB₂ surface that was in contact with SX YAG.

The surfaces of the HfB₂ specimens were examined using SEM, EDS, and XRD to determine the composition of the surface scales. The specimen heat treated for 12 hrs was examined using SEM and EDS. The crustaceous deposit on the surface contained Al and Y. Due to the dramatic texture of the surfaces, parallel beam methodology was employed to evaluate the surface of the 18 hr test specimen. Crystallographic Information Files (CIFs) from Crystallography Open Database were used to characterize the X-ray returns. The XRD patterns of the HfB₂ surfaces revealed the presence of two

phases: cubic yttria-stabilized hafnia (c-YSH) and polycrystalline (PX) YAG. The crustaceous deposit on the 18-hr-tested HfB_2 surface exposed to the furnace environment was composed of approximately 5% c-YSH and 95% PX YAG (see XRD pattern in Fig. 49.).

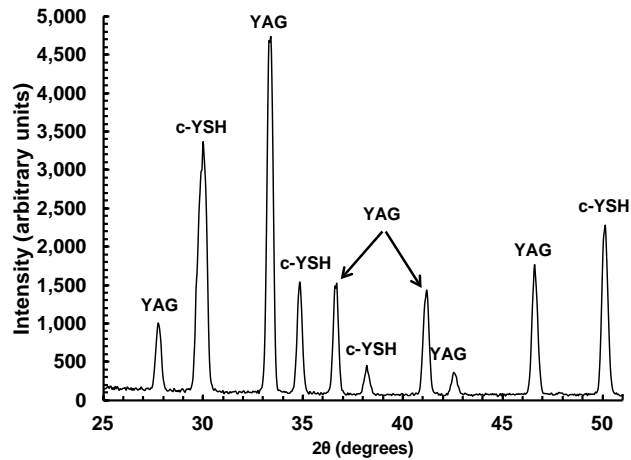


Fig. 49. XRD of HfB_2 surface exposed to the furnace environment. HfB_2 heat treated in contact with SX YAG for 18 hrs at 1500°C in air. c-YSH and PX YAG phases are readily identified.

In contrast, the deposit on the HfB_2 surface that was in contact with SX YAG was composed of approximately ~45% c-YSH and ~55% PX YAG. The different morphologies of the exposed-to-the-tube furnace surface deposits (Fig. 47a) in comparison to the in-contact-with-alumina surfaces (Fig. 47b) may be caused by the compositional difference. However, the more pronounced growth of deposit on the surface exposed to the furnace environment (Fig. 47a) may be also due to lack of physical constraint. The XRD analysis of the SX YAG surface that was in direct contact with HfB_2 revealed the presence of the following phases: PX YAG, $\text{Y}_4\text{Al}_2\text{O}_9$ (yttrium aluminum monoclinic, YAM), and YBO_3 .

Another indication of an interaction with SX YAG is revealed by the rod itself. The SX YAG had an apparent deposit (Fig. 50). Of interesting note is that the SX YAG area of direct contact with the HfB_2 had been consumed; it was at a lower level than the original surface. Due to the YAG's single-crystal composition, when the x-ray beam encounters a single crystal area, the x-rays are directly reflected back into the detector resulting in spikes in the return of the graph. Due to the intensity of the spikes, the other returns were close to the background noise. As such, phase quantity could not be determined. The phases on the contact surface of SX YAG are $\text{YAM (Y}_4\text{Al}_{12}\text{O}_9)^2$, and PX YAG, and YBO_3 .

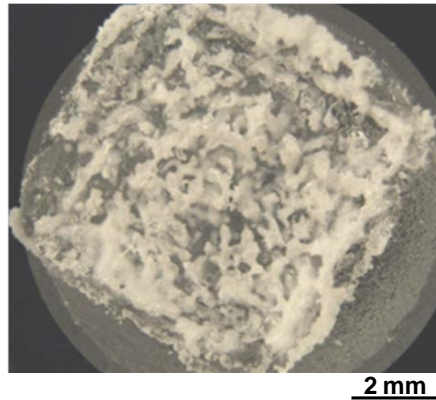


Fig. 50. Photograph of surface of SX YAG in direct contact with HfB_2 for 18 hrs at 1500°C in the tube furnace when HfB_2 and SX YAG were in contact.

The HfB_2 specimens were sectioned and examined with SEM and EDS to further characterize the deposits formed on the HfB_2 surfaces exposed to the furnace environment (Fig. 51a and Fig. 52a). The SEM micrographs in Fig. 51b and Fig. 52b reveal a presence of three distinct layers: unoxidized HfB_2 , HfO_2 scale, and the

² SX YAG has been shown to decompose into $\text{YAM (Y}_4\text{Al}_{12}\text{O}_9)$ in the presence of HfB_2 at 1600°C [130,152].

crustaceous surface deposit. The EDS analysis in Fig. 53 and Fig. 54 shows the presence of the Y- and Al- containing species in the crustaceous surface deposit, but not in the HfO_2 scale of either specimen.

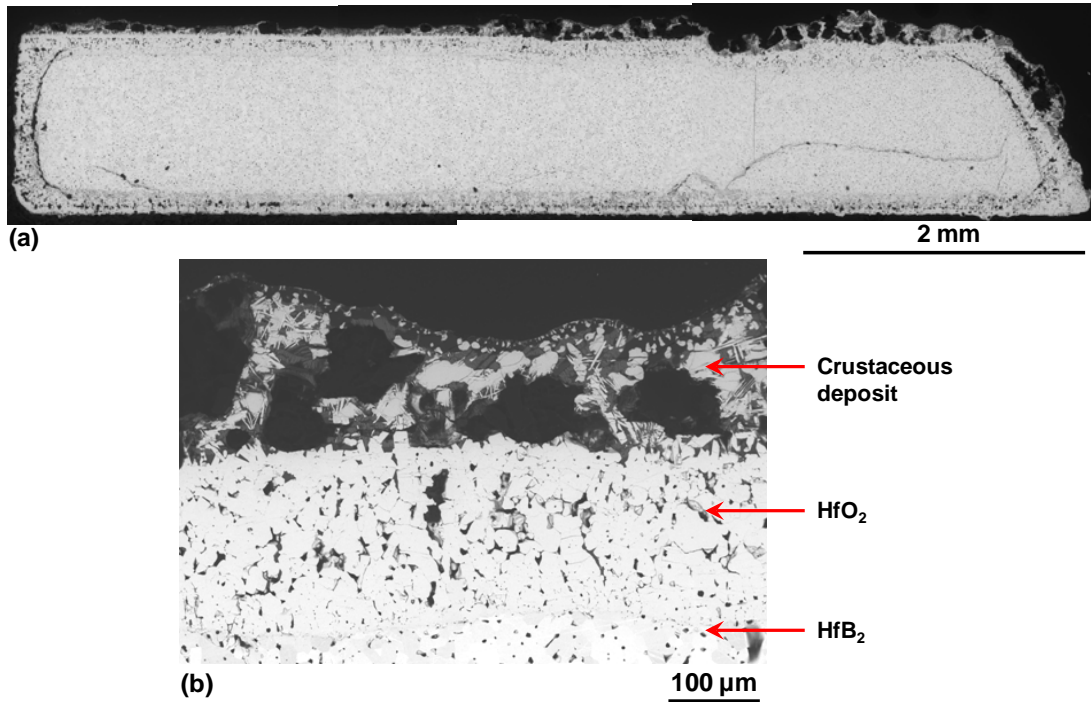


Fig. 51. SEM micrographs showing HfB_2 cross-section after heat treatment in contact with SX YAG for 12 hrs at 1500°C in air. (a) Cross-sectional view. (b) HfB_2 surface exposed to furnace environment. Note the three regions: unoxidized HfB_2 , HfO_2 scale, and a crustaceous deposit.

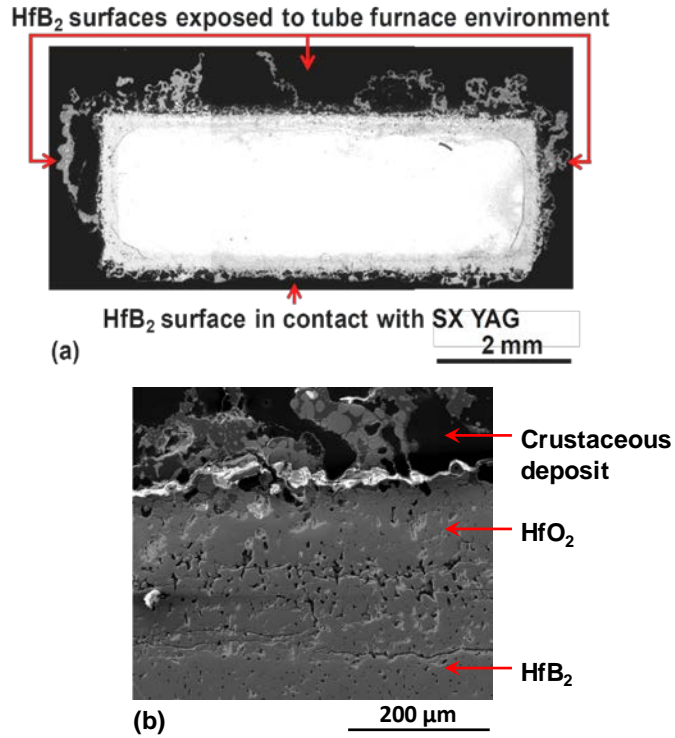


Fig. 52. SEM micrographs showing HfB₂ cross-section after heat treatment in contact with SX YAG for 18 hrs at 1500°C in air. (a) Cross-sectional view. (b) HfB₂ surface exposed to furnace environment. Note the three regions: unoxidized HfB₂, HfO₂ scale, and a crustaceous deposit.

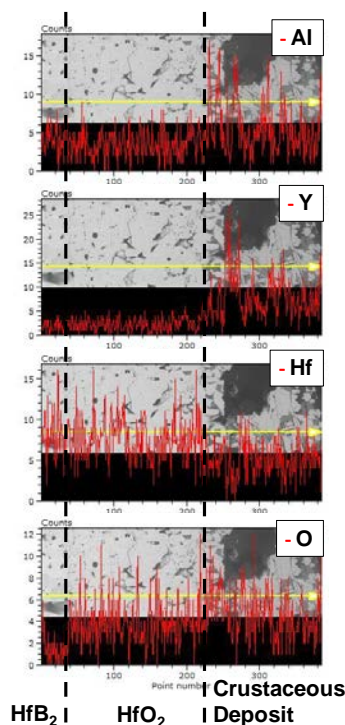


Fig. 53. EDS line analysis of specimen after heat treatment in contact with SX YAG for 12 hrs at 1500°C in air. The EDS line analysis showing level of presence of Al, Y, and Hf in the unoxidized HfB_2 , in the HfO_2 scale and in the crustaceous layer. Note that the Al- and Y-containing deposit resides on the surface of the oxide scale.

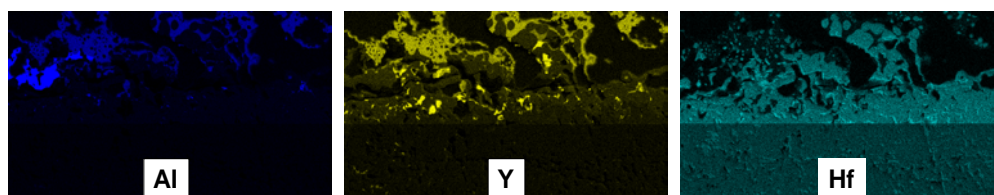


Fig. 54. HfB_2 after heat treatment in contact with SX YAG for 18 hrs at 1500°C in air. The EDS map analysis showing areas of Al, Y, and Hf. Note that the Al- and Y-containing deposit resides on the surface of the oxide scale.

4.2.3 Thermo-chemical Compatibility of HfB_2 with SX YAG at 1500°C in Air – HfB_2 Separated from SX YAG by Alumina (Case B and Case C)

Case A was conducted to determine if physically separating the HfB_2 and SX YAG would prevent the formation of the crustaceous deposit. High purity alumina was chosen because of its known high temperature stability. Upon conclusion of the test, a

white crustaceous deposit was not observed, but other deposits were found on the surface. Case 3 was conducted to determine if a greater physical separation could prevent any deposits from forming on the surface of the test specimens.

Profoundly different results were obtained from the heat treatment when the HfB_2 specimen was separated from SX YAG by 1-mm-thick alumina in Case B (Fig. 46) and a 35.5 x 153 x 6.6 mm in Case C (Fig. 46) spacer. The optical micrographs of the HfB_2 surfaces are shown in Fig. 55 and Fig. 56. Note that there is no visible growth of the crustaceous deposit (Fig. 55 and Fig. 56) seen when HfB_2 was heat treated in contact with SX YAG (Fig. 47 and Fig. 48). The surfaces of the HfB_2 specimen in Case B that were exposed to the furnace environment (Fig. 55a) are nearly flat, but have a speckled appearance. The original grey color of the HfB_2 specimen is still visible. On the other hand, the post-test surface of the HfB_2 specimen tested in Case C had a nearly flat, peach-colored appearance (Fig. 56a). The original grey color of the HfB_2 specimen is nearly fully covered with deposit but still visible in the center. The HfB_2 surface that was in contact with alumina (Fig. 55b and Fig. 56b) has a nearly flat, sandy appearance. When the large alumina spacer was used, oxidation or the formation of deposit occurred to a greater degree at the edges.

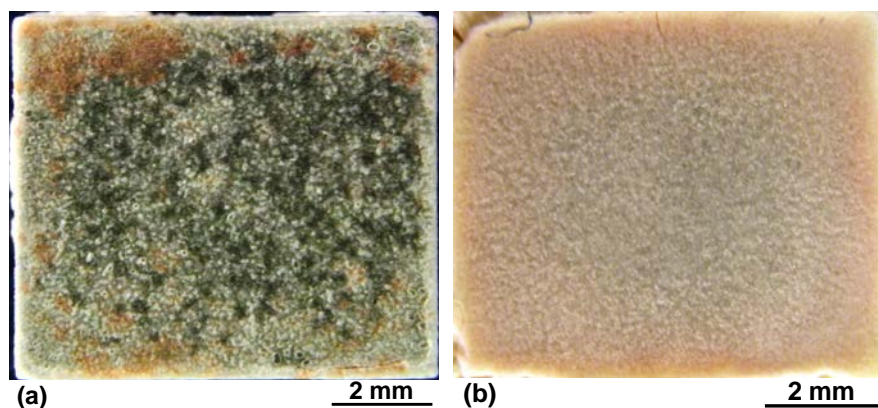


Fig. 55. Photographs of HfB₂ heat treated for 18 hrs at 1500°C in air with Al₂O₃ separating the HfB₂ from SX YAG. (a) HfB₂ surface exposed to furnace environment, (b) HfB₂ surface that was in contact with Al₂O₃. (Case B)

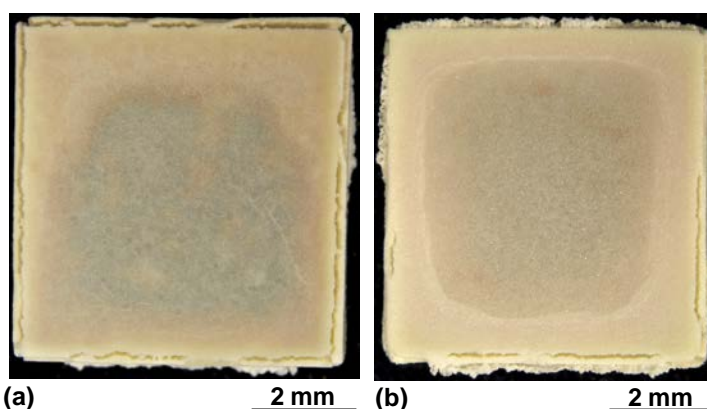


Fig. 56. Photographs of HfB₂ heat treated for 18 hrs at 1500°C in air with large alumina spacer separating the HfB₂ from SX YAG. (a) HfB₂ surface exposed to furnace environment, (b) HfB₂ surface that was in contact with Al₂O₃. (Case C)

The XRD analysis of the specimens of Case B and Case C revealed the presence of monoclinic hafnia (m-HfO₂), YBO₃, and Al₂O₃. The XRD pattern of Case B (Fig. 57) indicates that the deposit on the HfB₂ surface exposed to the furnace environment is comprised of ~62% m-HfO₂ and ~38% YBO₃ with trace amounts of Al₂O₃. The HfB₂ surface that was in direct contact with the alumina spacer was found to be nearly 100% m-HfO₂ with a slight orientation preference or mostly m-HfO₂ with trace amounts of YBO₃.

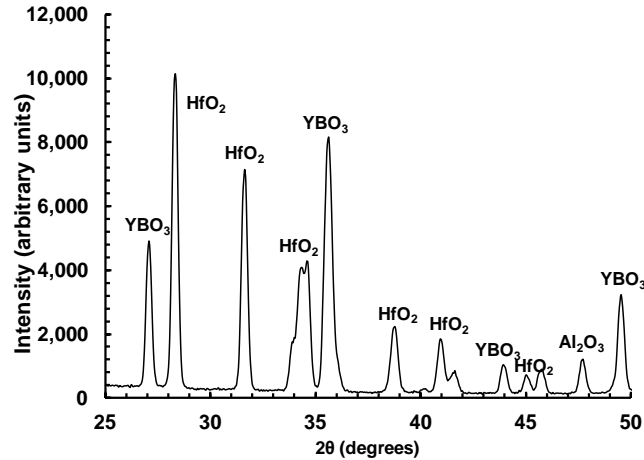


Fig. 57. HfB_2 heat treated for 18 hrs at 1500°C in air with alumina separating the HfB_2 from SX YAG. XRD return of the HfB_2 surface exposed to the furnace environment shows m- HfO_2 , YBO_3 and Al_2O_3 phases.

The HfB_2 specimens were cross-sectioned to determine the layer morphology.

The SEM examination revealed a porous m- HfO_2 scale with a columnar grain structure on all surfaces of the HfB_2 specimens (Fig. 58 and Fig. 59). The oxide scale was much thicker on the HfB_2 surface of Case B in direct contact with alumina (average scale thickness ≈ 0.19 mm) than on the HfB_2 surfaces exposed to the furnace environment (average scale thickness ≈ 0.07 mm). The oxide scale on the HfB_2 surface of Case C that was in direct contact with alumina (average scale thickness ≈ 0.20 mm) was greater than on the HfB_2 surfaces exposed to the furnace environment (average scale thickness ≈ 0.17 mm).

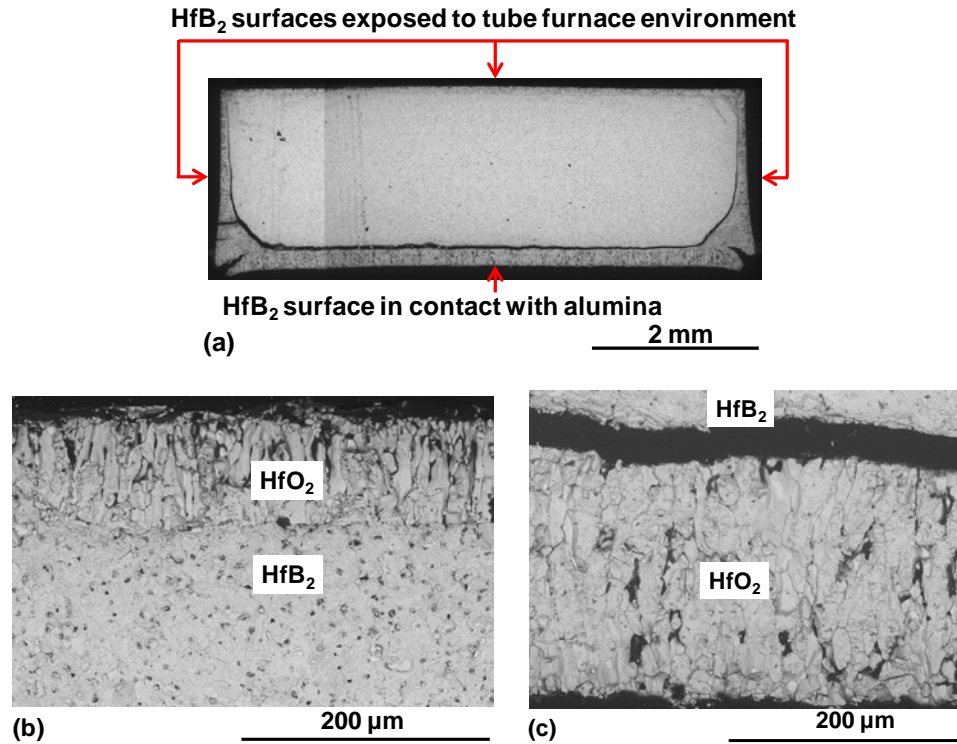


Fig. 58. SEM micrographs of HfB₂ heat treated for 18 hrs at 1500°C in air with alumina separating the HfB₂ from SX YAG. (a) Cross-sectional view. (b) HfB₂ surface exposed to furnace environment. (c) HfB₂ surface that was in contact with alumina.

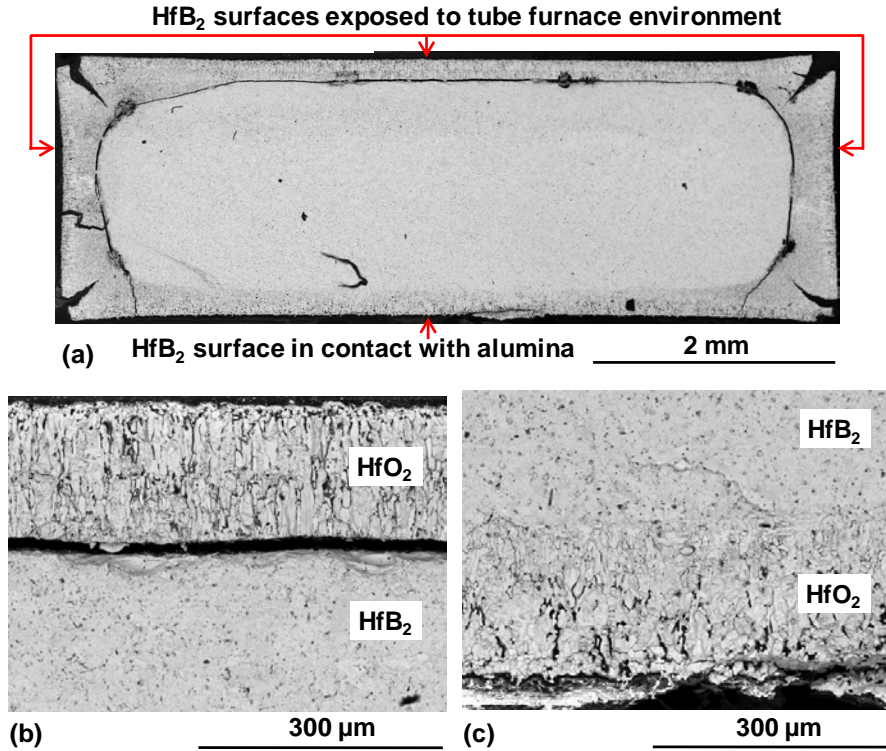


Fig. 59. SEM micrographs of HfB₂ heat treated for 18 hrs at 1500°C in air with very large alumina spacer separating the HfB₂ from SX YAG. (a) Cross-sectional view. (b) HfB₂ surface exposed to furnace environment. (c) HfB₂ surface that was in contact with alumina.

4.2.4 Thermo-chemical Compatibility of HfB₂ with SX YAG at 1500°C in Air –

HfB₂ in Close Proximity but Not in Contact with SX YAG (Case D)

Upon completion of the heat treatment experiment of Case D, a white crustaceous deposit was not observed. The surfaces of the HfB₂ specimen were nearly flat, cream-colored with some areas of dark red (Fig. 60). The SEM micrographs in Fig. 61 reveal a difference in morphology of the cream-colored and red-hued areas of the HfB₂ surface deposit. The EDS analysis showed that the cream-colored areas contained mainly Hf and O, while the red-hued areas also had an appreciable Al content. The XRD analysis of the HfB₂ surface determined the presence of m-HfO₂, Al₂O₃, YBO₃ and a trace amount of c-YSH. The HfB₂ specimen was sectioned and examined with SEM.

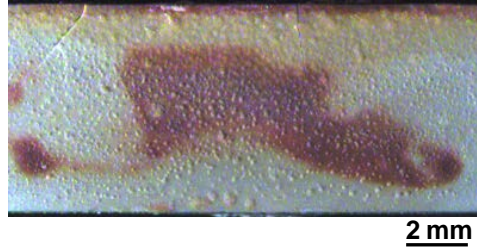


Fig. 60. Photograph of HfB_2 heat treated for 18 hrs at 1500°C in air in close proximity (~ 3 mm) but not in contact with SX YAG.

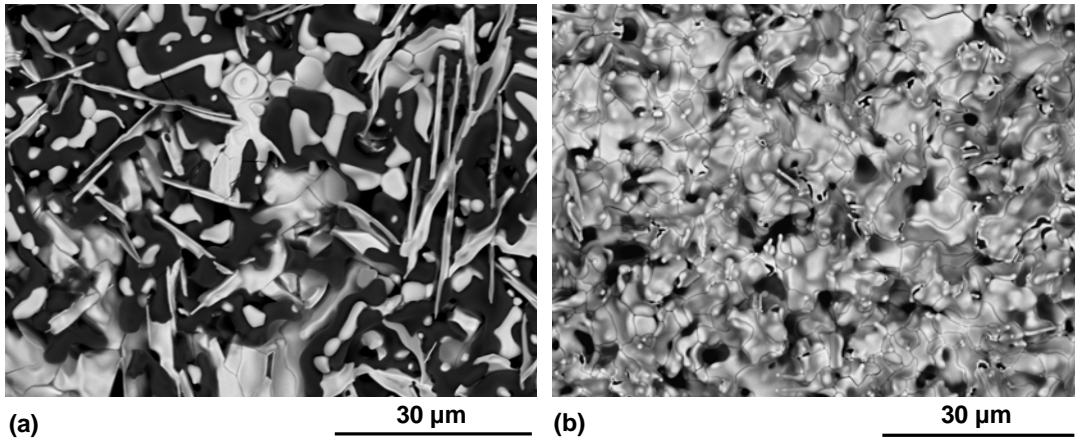


Fig. 61. SEM micrographs of HfB_2 specimen heat treated for 18 hrs at 1500°C in air in close proximity (~ 3 mm) but not in contact with SX YAG. SEM micrographs of the HfB_2 surface, (a) red-hued and (b) cream-colored areas of Fig. 60.

The micrographs of the cross-section in Fig. 62 show that a porous m- HfO_2 scale with a columnar grain structure has formed on all surfaces of the HfB_2 specimen. Remarkably, the m- HfO_2 scale on the HfB_2 surface facing SX YAG is considerably thicker (0.2 mm on average) than that formed on the HfB_2 surface facing away from SX YAG. It is possible that the presence of SX YAG accelerates the oxidation of HfB_2 .

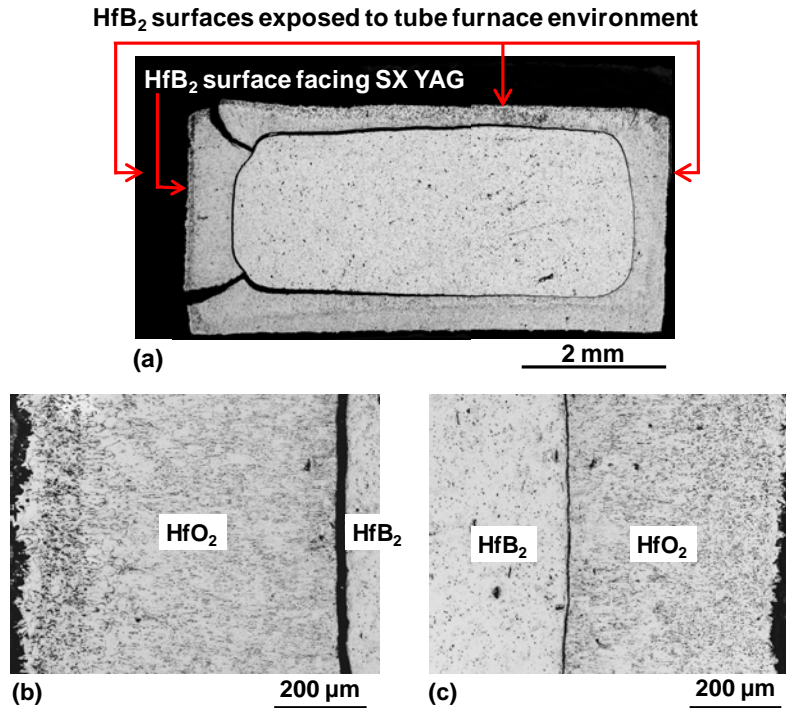


Fig. 62. SEM micrographs of HfB₂ heat treated for 18 hrs at 1500°C in air in close proximity (~3 mm) but not in contact with SX YAG. (a) Cross-sectional view. (b) HfB₂ surface facing SX YAG. (c) HfB₂ surface facing away from SX YAG.

4.2.5 Thermo-chemical Compatibility of HfB₂ with SX YAG at 1500°C in Air –

HfB₂ in Contact with SX YAG and another HfB₂ specimen Approximately 3 mm apart from SX YAG (Case E)

It was hypothesized that it was the direct contact between HfB₂ and SX YAG that produced the significant volume of gases necessary to facilitate the creation of the crustaceous deposit. To test this hypothesis, an experiment was conducted in which HfB₂ was tested in contact with and in proximity to SX YAG simultaneously. One HfB₂ specimen was placed in direct contact with SX YAG, and a second HfB₂ specimen was placed ~3mm away from the SX YAG within the same tube furnace thus ensuring exposure to equal amounts of gases (Case E).

Upon completion of Case E, a crustaceous deposit was observed only on the surface of the HfB_2 specimen in direct contact with SX YAG (Fig. 63a). Surprisingly, the appearance and composition of this crustaceous deposit were different from those of the deposit produced on the surface of the HfB_2 heat treated for 18 hrs in contact with SX YAG in Case A. The crustaceous deposit produced in Case E (Fig. 63a) appeared to be smoother and more compact than that in Fig. 48a (Case A). Surface areas exposed to the tube furnace environment displayed distinct pink- and yellow-hued areas, while the surface area that was in contact with the alumina support only displayed a yellow-hued appearance (Fig. 63c and Fig. 63d).

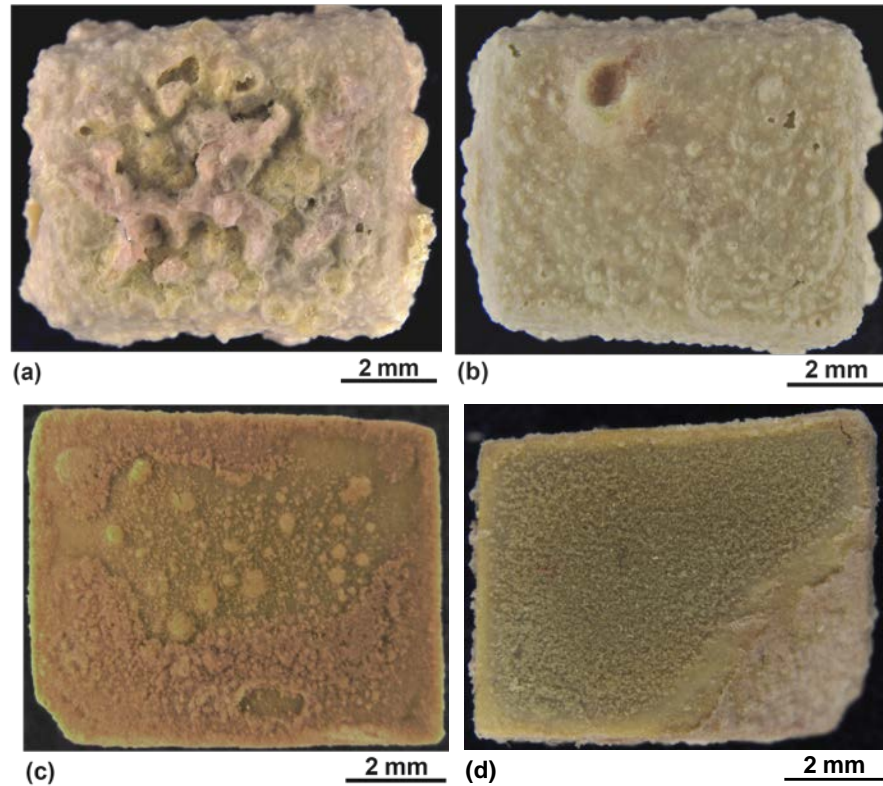
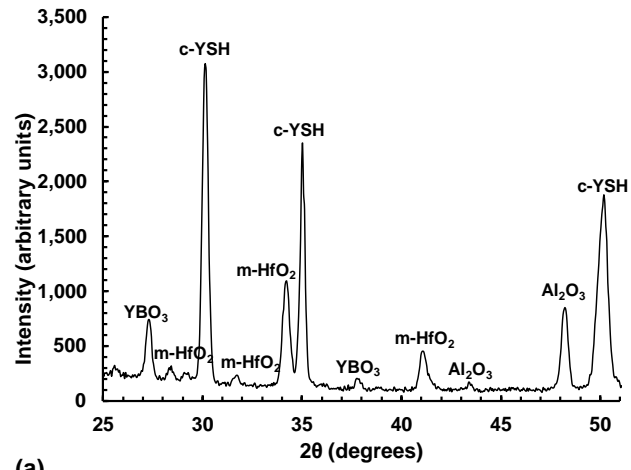
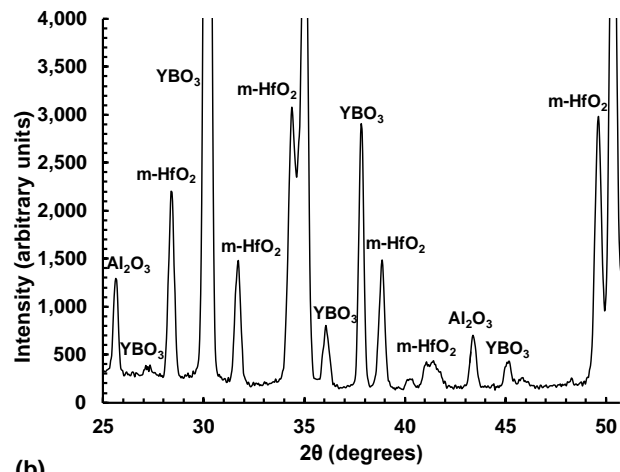


Fig. 63. Photographs of one piece of HfB_2 in contact with SX YAG and another, approximately 3 mm apart from SX YAG after heat treatment for 18 hrs at 1500°C in air. (a) In-contact HfB_2 surface exposed to furnace environment, (b) In-contact HfB_2 surface that was in contact with SX YAG, (c) In-proximity HfB_2 surface exposed to furnace environment, and (d) In-proximity HfB_2 surface that was in proximity.

The surfaces of Case E were evaluated using XRD and EDS. The XRD pattern of the crustaceous surface deposit obtained in Case E showed the presence of the following phases: c-YSH, m-HfO₂, YBO₃, and Al₂O₃ (Fig. 64a). Recall that the surface deposit produced in Case A consisted of c-YSH and PX YAG. Notably, PX YAG was not detected on the surface of the HfB₂ heat treated in contact with SX YAG in Case E. In addition, a crustaceous deposit was not observed on the surface of the HfB₂ specimen heat treated ~3 mm apart from the SX YAG (Fig. 63c). The XRD analysis of the HfB₂ surface exposed to the tube furnace environment determined the presence of m-HfO₂, Al₂O₃, YBO₃ and a trace amount of c-YSH (Fig. 64b). Energy-dispersive X-ray spectroscopy (EDS) of the surfaces revealed that the pink- and yellow-hued areas of Fig. 63 c and d had significantly different morphologies. The yellow-hued area (Fig. 65a) had a smoother surface than that of the pink-hued area (Fig. 65b). The EDS analysis of these areas revealed that the pink-hued areas had increased amounts of Al₂O₃ (Fig. 65c). A cross-section of the specimen confirmed that the crustaceous deposit of the HfB₂ specimen in contact with SX YAG was more compact (Fig. 66) than that of Case A (Fig. 52a).



(a)



(b)

Fig. 64. XRD return of surfaces exposed to the tube furnace environment of a) HfB₂ in contact with SX YAG in the presence of another HfB₂ and (b) HfB₂ in the presence of HfB₂ in contact with SX YAG.

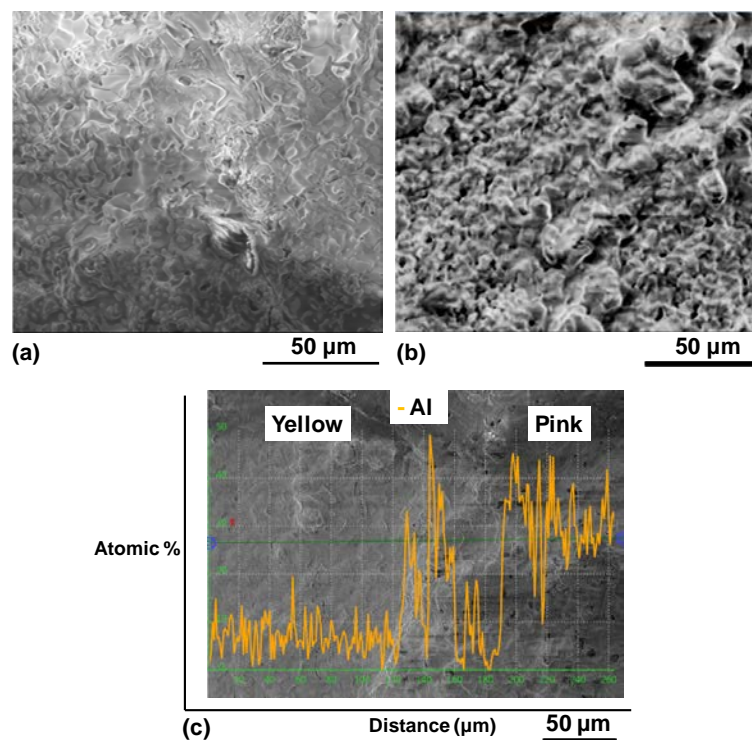
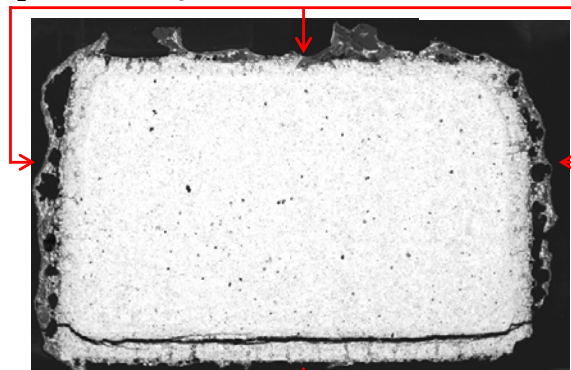


Fig. 65. SEM micrographs of (a) pink-hued and (b) yellow-hued area and (c) XRD returns of atomic percentage of Al of surface of HfB_2 separated from HfB_2 in contact with SX YAG by air and exposed to tube furnace air environment for 18 hrs at 1500°C .

HfB_2 surfaces exposed to tube furnace environment



**HfB_2 surfaces in contact with SX YAG
2 mm**

Fig. 66. SEM micrograph of cross-section of one piece of HfB_2 in contact with SX YAG with another (not pictured), approximately 3 mm apart from SX YAG after heat treatment for 18 hrs at 1500°C in air.

4.2.6 Thermo-chemical Compatibility of HfB_2 with SX YAG at 1500°C in Air -

Discussion

To summarize the results, heat treatment of HfB_2 at 1500°C in air in the presence of SX YAG caused formation of Y- and Al- containing deposits on the surface of HfB_2 . Heat treatment of HfB_2 in contact with YAG resulted in a surface deposit consisting of c-YSH and PX YAG. Conversely, heat treatment of HfB_2 separated from SX YAG by Al_2O_3 gave rise to a surface layer consisting of m- HfO_2 , YBO_3 and Al_2O_3 . Finally, heat treatment of HfB_2 in close proximity (~ 3 mm) but not in contact with SX YAG produced a surface deposit consisting of m- HfO_2 , YBO_3 , Al_2O_3 and a trace amount of c-YSH. A summary of the deposits produced on the surface of HfB_2 samples is given in Fig. 67.

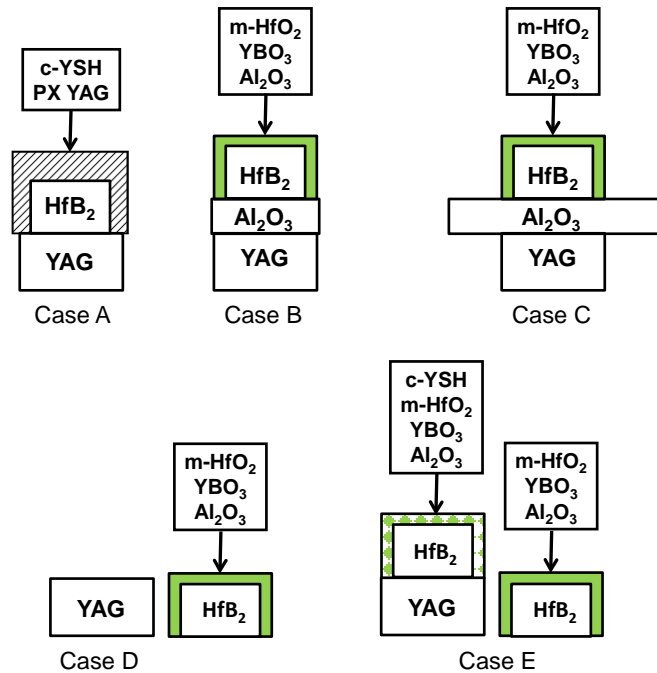


Fig. 67. Schematic showing surface deposits produced during heat treatment for 18 hrs at 1500°C in air: (a) HfB_2 in contact with SX YAG, (b) HfB_2 and SX YAG separated by alumina spacer, (c) HfB_2 in close proximity (~ 3 mm) but not in contact with SX YAG.

It is believed that the formation and transport of gaseous species is required for the aforementioned surface deposits to occur. The Pt foil of the HfB₂-3a specimen (Case 0) that was in contact with neither HfB₂ nor SX YAG was examined using EDS. There were two pieces of Pt foil that were placed between the HfB₂ and SX YAG. Deposits containing Al, Hf, O, and Y were seen on both of those pieces of Pt foil (Fig. 68). The only mechanism for deposits to have formed on the Pt foil is through gaseous transportation.

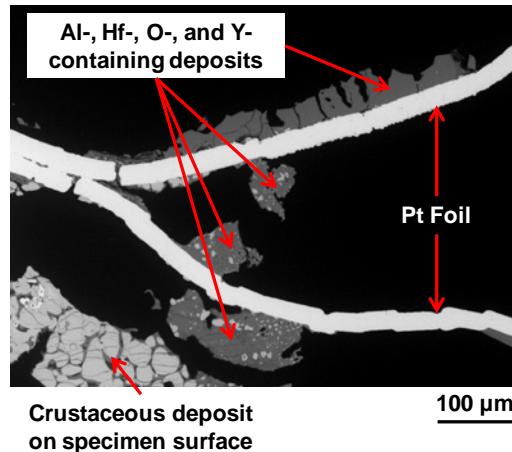
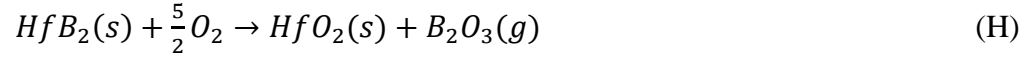


Fig. 68. SEM micrograph of gaseous products that condensed on surfaces of Pt foil

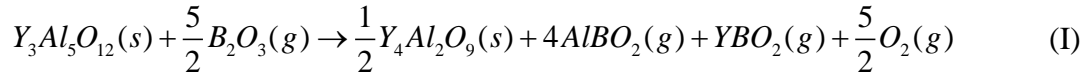
Mah *et al.* [152] reported the carbothermal reduction of SX YAG into YAlO₃ (yttrium aluminum perovskite, YAP), YAM, and Y₂O₃ in the presence of CO (g) due to loss of Al-containing gases. Mah and Parthasarathy [130] proposed that a reduction of SX YAG into AlBO₂ (g) and YAP in the presence of B₂O was thermodynamically extremely favorable at 1600°C in air. A Gibbs free energy evaluation (described in Appendix J) revealed that the degradation of SX YAG into YAM in the presence of B₂O₃ (g) was

favorable in comparison to $YAl_3(BO_3)_4$ (yttrium aluminum borate, YAB) and YAP at all temperatures. Recent studies demonstrated that B_2O_3 (g) reacted with Y^{3+} cations in various compositions to produce YBO_2 (g) [153,154].

The intermediate gaseous species is B_2O_3 (g) produced in the course of oxidation of HfB_2 according to [33,34,46,98,109]:

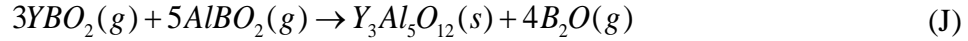


It is postulated that in all heat treatment experiments, the B_2O_3 (g) reacts with SX YAG to produce YAM, $AlBO_2$ (g) and YBO_2 (g) according to:



When HfB_2 was heat treated in contact with SX YAG, c-YSH containing crustaceous deposit was found on the surface of the m- HfO_2 scale. We postulate that the surface m- HfO_2 is transformed to c-YSH due to Y^{3+} cations replacing Hf^{4+} cations in the lattice structure. It has been shown that at 1500°C approximately 4–31 mole % Y^{3+} cations is required to transform m- HfO_2 to c-YSH [155,156]. In this case, possible sources of Y^{3+} cations are: (i) the YBO_2 gas produced in Rxn. I and adsorbed onto the surface of the m- HfO_2 scale and (ii) the diffusion of Y^{3+} cations from SX YAG into the surface of the scale. Diffusion of Y^{3+} cations, which proceeds through the least restrictive structural regions (i. e. a free surface) is further assisted by the presence of the Hf^{4+} cation vacancies. In a recent study, Xia [157] noted that Hf^{4+} cation vacancies within the m- HfO_2 scale tend to migrate towards the surface. Hence, transformation of m- HfO_2 to c-YSH takes place on the surface of the m- HfO_2 scale.

It is also believed that c-YSH acts as a catalyst to promote the reaction between the adsorbed $AlBO_2$ and YBO_2 gases generated in Rxn. J to produce PX YAG and a gaseous boron-containing species (assumed to be B_2O) on all surfaces of the HfB_2 specimen heat treated in contact with SX YAG. A description of how a catalyst works is in Appendix I.



The free energies of reactions (I) and (J) were evaluated using available data [155,158-162][158-162]. The reactions (I) and (J) were thermodynamically highly favorable at 1500°C.

When HfB_2 is separated from SX YAG by Al_2O_3 during heat treatment, the $AlBO_2$ and YBO_2 gases produced in Rxn. I are adsorbed onto the surface of the m- HfO_2 scale. When a molecule is adsorbed onto a surface, it can be physically constrained more than when it is a gaseous species. For this to occur, it must release energy and transition to a lower energy state. As a result, $AlBO_2$ and YBO_2 transition into Al_2O_3 and YBO_3 , respectively. In a comparison of Gibbs free energy, Al_2O_3 has a greater negative value than $AlBO_2$ [160]. The interpretation was that it is not improbable that $AlBO_2$ transitions into Al_2O_3 . When YBO_2 gas is formed, a Y atom adopts a 1+ oxidation state to balance the ionic charge of $(BO_2)^{1-}$. However, because Y has a standard oxidation state of 3+, yttrium borate is likely to be more stable in a solid form as YBO_3 . Therefore, it is likely that when YBO_2 gas is adsorbed onto the surface of m- HfO_2 it transitions to YBO_3 solid

to achieve a lower energy level. It is recognized that m-HfO₂ is nonstoichiometric [163]. Furthermore, m-HfO₂ has been shown to lose O²⁻ anions [163], which are readily incorporated by YBO₂ to achieve a more stable state as YBO₃.

When HfB₂ specimen was heat treated in close proximity but not in contact with SX YAG, Al₂O₃ and YBO₃ were found on the surface of HfB₂. The AlBO₂ and YBO₂ gases produced in Rxn. I interact with the m-HfO₂ scale and transition to Al₂O₃ and YBO₃ as was the case when HfB₂ was separated from SX YAG by Al₂O₃ during heat treatment.

Case E revealed that it was not the volume of gases present in the chamber that created the amount of c-YSH needed to form PX YAG. Otherwise, both HfB₂ specimens would have had PX YAG deposits. It is proposed that HfB₂ must be heat treated in contact with SX YAG to create the c-YSH required to facilitate formation of PX YAG.

Recent studies reported that cubic form of yttria-stabilized zirconia (c-YSZ) exhibits greater catalytic properties and disassociates molecules of various gases more readily than monoclinic zirconia (m-ZrO₂) [164-170]. Because hafnia closely resembles zirconia in chemical properties [171-174], it is likely that the same conclusion holds regarding the catalytic properties of c-YSH vs. those of m-HfO₂. It is believed that the c-YSH acts as a catalyst to lower the activation energy of Rxn. J between AlBO₂ and YBO₂ gases to form PX YAG. In contrast, the surface deposits produced when HfB₂ is separated from SX YAG contain both c-YSH and m-HfO₂ upon which Al₂O₃ and YBO₃ are found. It is possible that the presence of m-HfO₂ lowers catalytic properties of the c-YSH by some means (e.g., absorbing some of its lattice energy). As a result, Rxn. J to produce PX YAG does not take place.

There are several rationales which explain increased catalytic properties of c-YSH in comparison to m-HfO₂. (1) Y³⁺ has an increased reactivity in comparison to Hf⁴⁺. Yttrium has an ionization energy of 6.2173 eV, and hafnium has an ionization energy of 6.82507 eV [175]. (2) As Y³⁺ cations replace Hf⁴⁺ cations in the lattice structure of m-HfO₂, an O²⁻ anion is removed from the lattice. An increase in oxygen vacancies has been shown to increase the catalytic capability, including adsorbability, of a material [168-170,176]. (3) It has been shown that the lattice energy of c-YSZ is greater than that of m-ZrO₂ [157,164]. An increase in lattice energy causes increasing vibration within the lattice. The increased vibration energy is sufficient to stretch and break the bonds in the molecules of the adsorbed gases, allowing the molecular fragments to react [177].

Another explanation lies in the hydroxyl groups (OH⁻) that are on the surface of every oxide layer (Fig. 69) [166,178]. As a material is heated, water not desorbed and removed from the system reacts to form hydroxyl groups on the surface of the oxide [178]. The formation of hydroxyl groups depends on the electron charge density of oxygen atoms in the surface layer. The greater the electron charge density, the increased likelihood of hydroxyl groups attaching to the surface. This charge density is influenced by the electronegativity of the metal cation that is bonded to the oxygen. The greater the electronegativity difference between oxygen and metal cation, the greater the electron charge density, leading to a greater number of hydroxyl groups [179]. The Pauling electronegativity value for O is 3.5, Hf is 1.3, and Y is 1.2 [177]. Ytria has the greatest electronegativity difference with O; relatively more OH groups form on the c-YSH [180]. The intensity of a portion of the hydroxyl groups is higher in c-YSH due to the replacement of Zr⁴⁺ by Y³⁺ at edges, kinds, steps, and corners [181].

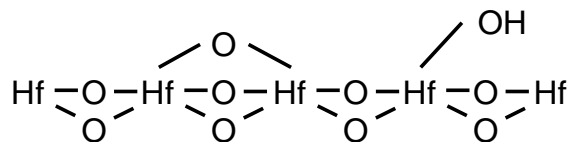


Fig. 69. Schematic of surface layer of HfO_2 with hydroxyl groups.

The number of hydroxyl groups contributes to the amount and reactivity of adsorbate [167,179,180]. Adsorbates insert themselves into the hydroxyl groups and receive extra protons, resulting in the increase in their chemical reactivity [166,178]. As surface hydroxyl groups start to decrease around 100°C [166], the number of hydroxyl groups reduces to nearly zero on a monoclinic transition metal oxide once heat treated up to 900°C [166]. Cubic YSZ has been found to rehydroxylate easier than m- ZrO_2 after initial heat treatment [166,180]. Yttrium in the lattice structure of hafnia has a higher affinity for hydroxyl groups than Hf [166].

The increased catalytic properties of the c-YSH may be due to a cyclic process as a result of the open configuration of the test furnace chamber. It is postulated that as "fresh" laboratory air is heated within the chamber, the water vapor dissociates on the defects caused by the Y^{3+} cations [166,181]. The newly formed hydroxyl groups bind themselves to the Y in the lattice of c-YSH [166]. The extreme temperature of the test chamber also causes the continuous removal of hydroxyl groups. It has been reported that the removal of hydroxyl groups create strained sites that are catalytically active [178].

4.3 High Temperature Compatibility of HfB_2 with Pt Foil, SX YAG, and Alumina

The original Test Method included high purity Pt foil to provide a physical barrier between HfB_2 and SX YAG. Initial validation of the Test Method revealed an interaction

between HfB_2 and SX YAG had occurred during testing (Fig. 22b and Fig. 24b). A series of heat treatment tests characterized this interaction. High purity Pt foil was deemed unsuitable to be used as a separating barrier for HfB_2 and SX YAG. Its instability in the presence of HfB_2 resulted in contact between the HfB_2 and SX YAG.

The crustaceous deposit that formed on the surfaces was due to the adsorption and reaction of SX YAG degradation byproducts. However, it was the B_2O_3 (g) released during the oxidation of HfB_2 that caused the degradation of SX YAG. An attempt was made to isolate the SX YAG via Pt sputtercoating. This attempt to prevent gaseous boron attacks on the SX YAG was unsuccessful. A complete description of the experiment is in Appendix H.

High purity alumina was chosen as a replacement interlayer to separate HfB_2 and SX YAG. A crustaceous deposit did not form on the surface of the HfB_2 specimens when the alumina separated the HfB_2 and SX YAG. Henceforth, the Test Method was updated to use alumina spacers to separate HfB_2 and SX YAG during mechanical testing (Fig. 70).

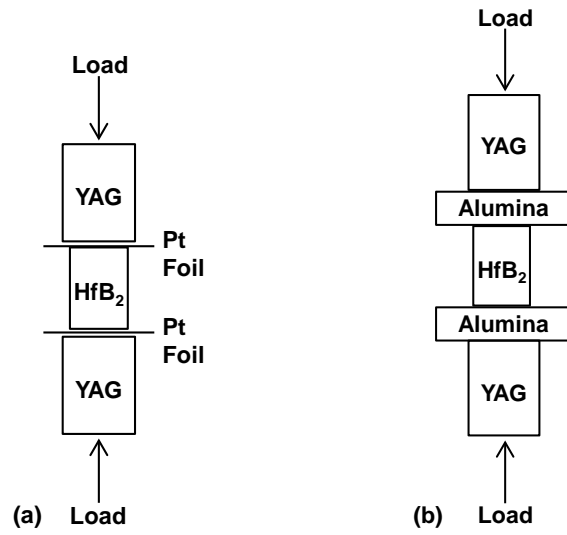


Fig. 70 Schematic drawings of (a) original test method load train utilizing Pt foil and (b). revised test method load train utilizing alumina.

V. Validation of Experimental Test Facility and Test Method

This research aimed

1. To develop, build and validate of an experimental facility for mechanical testing of UHTC samples in air at temperatures up to and including 1500°C.
2. To develop and validate a method to perform compression creep tests of small HfB₂ samples in air at temperatures up to and including 1500°C.

The Experimental Facility was designed and built. A detailed description of the experimental facility is given in Section 3.3. The Test Method developed in this work is presented in Section 3.4.

The thermo-chemical compatibility of HfB₂ with (1) SX YAG, (2) Pt, and (3) alumina was examined in multiple contact combinations during furnace heat treatment exposures at 1500°C and 1600°C in air. It was found that in all experiments, while SX YAG was unstable with HfB₂. The thermo-chemical interaction between HfB₂ and SX YAG that created a crustaceous deposit was mitigated when high purity alumina was utilized as an interlayer. The reaction products were characterized using optical, SEM, EDS, and XRD. The mechanisms of formation were identified. Based on these findings the Test Method developed in this work had to be modified. The revised Test Method does not include Pt foil in the test setup and employs alumina spacers to prevent direct contact between the HfB₂ specimen and SX YAG push-rods. The revised test setup is shown in Fig. 70.

Chapter 3 and Chapter 4 addressed the experimental facility and methods and an evaluation of the thermal compatibility of HfB_2 with SX YAG, Pt foil, and alumina in detail. In order to accomplish this experimental endeavor, extensive work was performed in establishing the experimental facilities and procedures. It is desired to obtain high temperature mechanical measurements of HfB_2 -containing UHTCs directly. Most studies concerning creep characteristics utilize flexure tests. Due to the difference in creep between tension and compression, assuming the neutral axis to be fixed to determine simple beam theory parameters with which to calculate strain can introduce an error in strain measurements [182]. The experimental facility and the test method developed in this work were experimentally validated by performing a series of pilot tests on HfB_2 -based UHTC samples at 1500°C in air. In these tests, specimens of HfB_2 , containing 0, 10, and 20 vol% SiC were subjected to compression creep at stresses ranging from 25-100 MPa. Accurate strain measurement was accomplished with the MTS uniaxial high-temperature extensometer equipped with 23-cm long SX sapphire extension rods.

Results of the pilot compression creep tests are presented in this section. In addition to validating the test facility and test method, these results provide interesting information regarding potential interaction between creep and oxidation.

The use of alumina to separate the SX YAG from HfB_2 was sufficient to minimize interaction between SX YAG and HfB_2 . The crustaceous deposit was not observed on the surfaces of any of the HfB_2 -containing specimens. To confirm this observation, their surfaces were submitted to XRD analysis. Neither c-YSH nor PX YAG was found. For the most part, the oxidation layers were consistent with literature.

5.1 Creep Specimen Interaction with Alumina

However, there were indications of an interaction between the alumina spacers and the compression creep specimens. A crust comprised of $m\text{-HfO}_2$, Al_2O_3 , and YBO_3 formed at the HfB_2 /alumina interface of the creep specimens. For the monolithic HfB_2 specimens, the crust was evident to varying degrees. The $\text{HfB}_2\text{-c}$ specimens had a deposit (Fig. 71b) that was more abundant than the $\text{HfB}_2\text{-a}$ specimens (Fig. 71a). The crust on the $\text{HfB}_2\text{-10 vol\% SiC}$ (Fig. 71c) and $\text{HfB}_2\text{-20 vol\% SiC}$ (Fig. 71d) specimens was much less evident. If present, it was limited to a thin line at the interface between the creep specimens and alumina spacers.

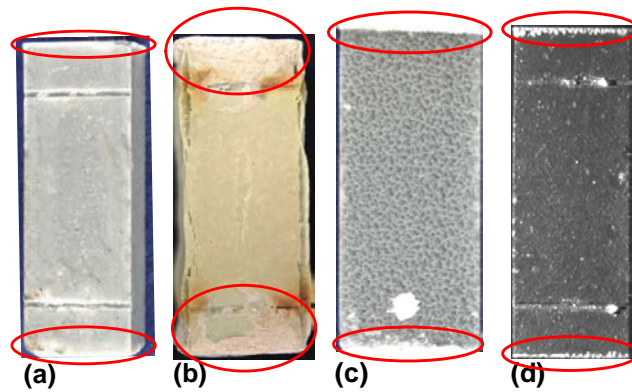


Fig. 71. Photographs and optical micrographs of representative examples of crust found on compression samples. (a) $\text{HfB}_2\text{-a}$, (b) $\text{HfB}_2\text{-c}$, (c) $\text{HfB}_2\text{-10 vol\% SiC}$, and (d) $\text{HfB}_2\text{-20 vol\% SiC}$.

The degradation of alumina is supported by the evidence of color changes in the alumina (Fig. 72). Figure 72 (left) is a sample of the as-provided alumina. Figure 72 (center) was heat treated in air while it was in direct contact with HfB_2 and SX YAG in the configuration as shown in Fig. 46a. The entire spacer was lighter in color than the as-provided alumina. The center of the alumina that was in contact with the HfB_2 appeared lightest in color than the rest of the spacer. This lightening of color was seen in the

alumina spacers used in the tube furnace heat treatments and the compression creep tests. It is presumed that this lightening is due to the loss of an oxygen-containing species. The alumina spacers were subjected to EDS and x-ray photoelectron spectroscopy (XPS). Unfortunately, neither EDS nor XPS was able to resolve the exact composition differences of the different hued alumina spacers. As such the exact cause of the color change cannot be determined.



Fig. 72. Photographs of (Left) As-provided alumina spacer, (center) alumina spacer in contact with HfB_2 and exposed to an air environment for 18 hrs at 1500°C , and (right) alumina spacer in an argon environment for 18 hrs at 1500°C .

This lightening of alumina was most complete in an argon environment. An experiment was run with HfB_2 in direct contact with SX YAG in an argon environment for 18 hrs at 1500°C in the configuration shown in Fig. 46a. (For full details, see Appendix N.) It has been postulated that the alumina spacer that was used as the support was the source of oxygen to oxidize the HfB_2 , facilitating the formation of the deposit. In the case of an argon environment, the alumina turned almost a pure white (Fig. 72 (right)). The alumina spacer could have become almost white due to a greater loss of oxygen-containing species due to the negligible partial pressure of oxygen in an argon atmosphere.

One supposition for the thicker oxide scale in contact with alumina or the oxidation of HfB_2 in an argon environment is that the alumina is vaporizing at 1500°C over the 18 hr test duration. Opeka *et al.* [22] calculated that Al_2O_3 could start vaporizing into Al_2O gas as low as 800°C . The gaseous Al_2O might accelerate the initial oxidation of HfB_2 . The Al^{3+} cations could form $\text{Al}(\text{g})$ or react with $\text{B}_2\text{O}_3(\text{g})$ to form AlBO_2 . Aluminum would not show up in the oxide scale since either of the gases would be removed from the oxide scale by the escaping B_2O_3 gas. The calculated volatility diagrams of Al_2O_3 and B_2O_3 (Fig. 73 and Fig. 74, respectively) at 2227°C show that $\text{B}_2\text{O}_3(\text{g})$ has a higher vapor pressure than $\text{Al}_2\text{O}(\text{g})$. It is presumed for this argument that the gases will remain relatively the same at 1500°C .

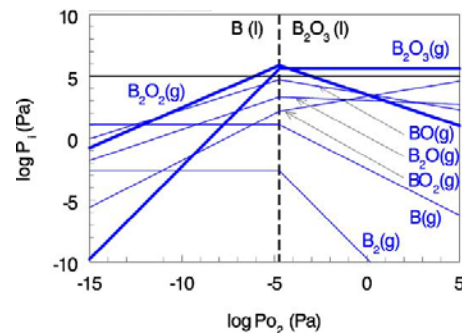


Fig. 73. Volatility diagram for B- B_2O_3 at 227°C as calculated in Opeka *et al.* [22]. (Reprinted with permission.)

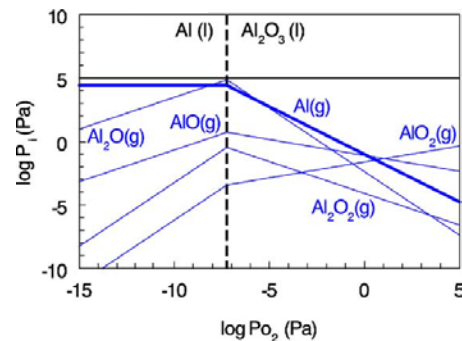


Fig. 74. Volatility diagram for Al- Al_2O_3 at 227°C as calculated in Opeka *et al.* [22]. (Reprinted with permission.)

The crust on the monolithic HfB₂ and HfB₂-20 vol% SiC creep specimens did not extend into the gauge sections of the creep specimens. The HfB₂/alumina interface ends of several post-test specimens were polished to a depth necessary to remove the crust. The cross-section was comprised of unoxidized HfB₂ bulk with an oxide scale. This discovery proves that if one wanted to link the crust development to oxidation of the HfB₂/alumina interface similar to that of the HfB₂/Pt/SX YAG interface in Fig. 28, the oxidation depth would not extend to the gauge section of the test specimen. In addition, the slight amount of crust that developed on the surface did not interfere with the oxidation of the test specimens within their gauge sections. Therefore, the compression creep strain measurements are valid.

5.2 CTE and Thermal Strain Comparisons at 1500°C in Air

Coefficient of thermal expansion (CTE) and thermal strain are a good validation that the temperature calibration methodology utilizing SX YAG is appropriate to determine the temperature setpoint for UHTC testing. Strain measurements were captured during the temperature ramp/soak portion of the UHTC compression creep tests (Fig. 75 and Fig. 76).

5.2.1 HfB₂ - CTE and Thermal Strain

Completion and analysis of the HfB₂ compression creep tests revealed the average CTE was $7.28 \cdot 10^{-6} \text{ K}^{-1}$ (Table 4). This is within a reasonable error range of the reported CTE of $7.49 \cdot 10^{-6} \text{ K}^{-1}$ for monolithic HfB₂ at 1500°C [127]. As a result of the alumina rods warping, the CTE for HfB₂-1a was not included.

The thermal strain data displayed in Fig. 74 was also used to validate the Experimental Facility and Test Methods. The creep data for HfB₂-3a was not included in the creep rate analysis due to the presence of Pt within the grain boundaries. (Discussed in Section 4.1.1). The thermal strain during the temperature ramp and soak stages of the creep tests indicated that the Pt might affect the thermal strain; the thermal strain for the HfB₂-3a specimen was greater than that of the other HfB₂ specimens. The thermal strain for HfB₂-2c never reached equilibrium during the thermal soak; an additional temperature recalibration was conducted.

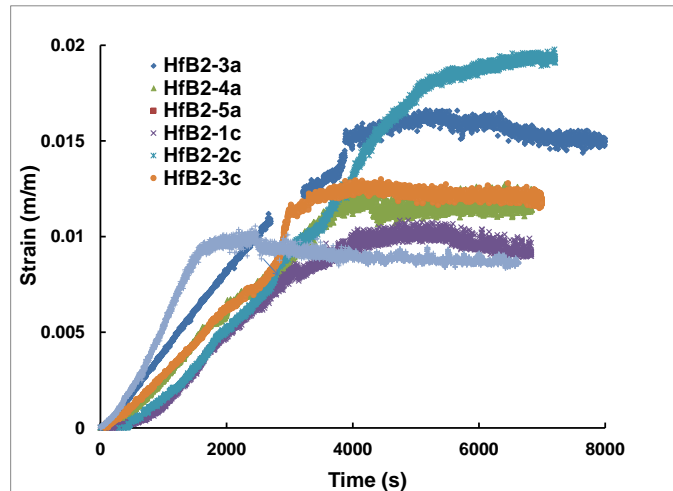


Fig. 75. Thermal strains of HfB₂ from room temperature to 1500°C to include approximately 1 hr of thermal soak.

The thermal strains were considered within reasonable range within one another, providing a validation of the Experimental Facility and Test Method for monolithic HfB₂ at 1300-1500°C in air.

Table 4. Calculated CTE and equilibrium thermal strains for various HfB₂ specimens under various compressive loads at 1500°C in air.

HfB ₂	CTE 10 ⁻⁶ K ⁻¹	Thermal Strain (%)
^{3,4} HfB ₂ -1a	10.6	invalid
^{5,5} HfB ₂ -3a	8.34	invalid
^{6,6,7} HfB ₂ -4a	6.47	1.23
^{6,7,8} HfB ₂ -4a	6.92	1.05
^{6,7,9} HfB ₂ -5a	6.49	1.19
^{6,7,10} HfB ₂ -5a	9.51	1.35
^{6,7} HfB ₂ -1c	7.00	1.06
^{6,7} HfB ₂ -2c	6.99	Not reached
^{6,7} HfB ₂ -3c	6.69	1.25
^{6,7} HfB ₂ -4c	7.13	0.93

5.2.2 HfB₂ - 20 vol% SiC - CTE and Thermal Strain

SiC has a slightly lower CTE than HfB₂. Therefore; increasing amounts of SiC should decrease the CTE of the composite material. Though it is expected that the CTE for increasing SiC content will decrease per the rule of mixtures, Loehman *et al.* [127] reported that pure HfB₂ is the exception to the rule. They believe that this may be due to microcracking in the highly porous structures of monolithic HfB₂. The CTE for increasing SiC content in the current study follows this expectation; i.e., the CTE of the HfB₂ specimens with a SiC additive decreases as SiC content increases (Table 5). The CTE for the HfB₂-10 vol% SiC specimen was calculated to be 7.45 10⁻⁶ K⁻¹, with the average CTE for the HfB₂-20 vol% SiC specimen calculated to be 7.18 10⁻⁶ K⁻¹. The HfB₂-20 vol% SiC-1a specimen did not experience mechanical failure during the test,

³ Alumina extensometer rods. Creep rate measurements are not valid.

⁴ Pt foil spacer only. Creep rate measurements are not valid.

⁵ Sapphire extensometer rods

⁶ 99.8% pure alumina spacer

⁷ 1st run of HfB₂-4a

⁸ 2nd run of HfB₂-4a

⁹ 1st run of HfB₂-5a

¹⁰ 2nd run of HfB₂-5a

enabling strain to be measured during both the heat up and cooldown portions of the test. The CTE for the temperature ramp up and cooldown portions of the test have almost the same absolute values: $9.55 \times 10^{-6} \text{ K}^{-1}$ and $-10.3 \times 10^{-6} \text{ K}^{-1}$, respectively. This similarity in values validates the strain measurements taken during the 50 MPa and 75 MPa compressive load portions of the test (the extensometer rods were adjusted at the end of the 25 MPa compressive load portion of the test).

All of the creep data for the HfB_2 -20 vol% SiC specimens was utilized for their creep mechanism determination, as the HfB_2 -20 vol% SiC thermal strains were considered to be within a reasonable range (Fig. 76). Once again CTE and thermal strain provided a validation of the Experimental Facility and Test methods for HfB_2 with additions of SiC at 1300-1500°C in air.

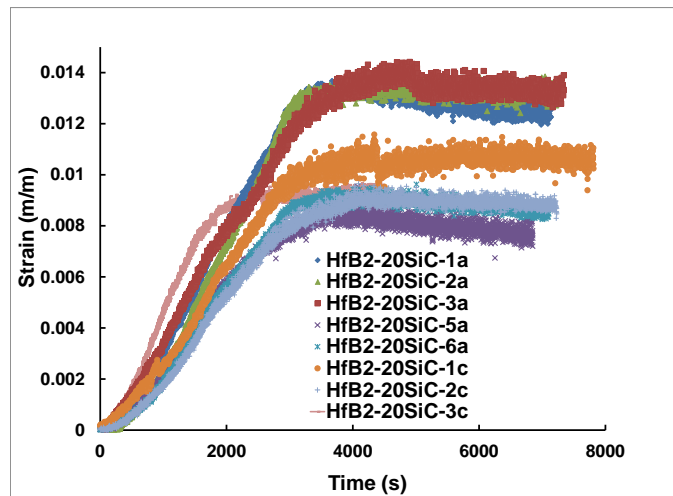


Fig. 76. Thermal strains of HfB_2 -20 vol% SiC from room temperature to 1500°C to include approximately 1 hr of thermal soak.

Table 5. Calculated CTE and thermal strains for various HfB₂-20 vol% SiC specimens under various compressive loads.

HfB ₂	CTE 10 ⁻⁶ K ⁻¹	Thermal Strain (%)
^{6,7} HfB ₂ -20SiC-1a	9.55	1.36
^{6,7} HfB ₂ -20SiC-2a	9.75	1.38
^{6,7} HfB ₂ -20SiC-3a	8.52	1.37
^{6,7} HfB ₂ -20SiC-5a	5.84	0.89
^{6,7} HfB ₂ -20SiC-6a	6.43	0.94
^{6,7} HfB ₂ -20SiC-1c	7.45	1.09
^{6,7} HfB ₂ -20SiC-2c	3.32	0.93
^{6,7,11} HfB ₂ -20SiC-3c	6.77	0.94
^{6,7,12} HfB ₂ -20SiC-3c	6.99	1.15

5.3 Pilot Compression Creep Tests at 1500°C in Air

To validate the Experimental Facility and Test Methods described in Sections 3.3 and 3.4, a series of pilot compression creep experiments of HfB₂-containing specimens were performed at 1500°C in laboratory air. The tests were conducted to provide an initial estimate of the stresses that HfB₂-containing UHTCs would experience measureable strain. At 1500 °C in laboratory air, HfB₂ specimens with 0, 10, and 20 vol% SiC had measureable creep at compressive loads as low as 25 MPa.

An evaluation of the creep strains at various compressive stresses can elucidate the dominate creep mechanisms of a material at a certain temperature. The basic governing equation for steady-state creep dynamics is given by

$$\dot{\epsilon} = \left(\frac{ADGb}{kT} \right) \left(\frac{b}{d_g} \right)^m \left(\frac{\sigma}{G} \right)^n \quad (1)$$

Experimentally, the stress-based exponent, n, can be determined by plotting the natural log of the strain rate ($\dot{\epsilon}$) vs natural log of the applied stress (σ) plot of all of the specimens [17,183]. Based on Eqn. 1, a power law curve is fitted to the data. This will

¹¹ 1st run of HfB₂-20SiC-3c

¹² 2nd run of HfB₂-20SiC-3c

result in a linear line whose slope (n) is defined by the exponent (n) of the power law curve (Fig. 77). The value of the slope is the value of the creep equation stress exponent, n. As described in Appendix B and seen in Fig. 77, the dominant creep mechanism can be determined.

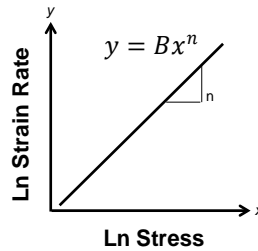


Fig. 77. Example plot to determine creep equation stress exponent.

5.3.1 Pilot Compression Creep Tests – HfB₂

Single load compression creep tests of HfB₂ were conducted at loads from 25 through 100 MPa. The creep stress, time (min), strain (%), and minimum rate (s⁻¹) are summarized in Table 6.

Table 6. Summary of creep results for HfB₂ specimens at 1500°C in air.

Specimen	Creep Stress (MPa)	Creep Time (min)	Creep Strain (%)	Minimum Creep Rate (s ⁻¹)
HfB ₂ -1c	25	960	0.38	1.54 x 10 ⁻⁸
HfB ₂ -4a	50	210	0.32	2.48 x 10 ⁻⁷
HfB ₂ -2c	50	530	0.92	3.36 x 10 ⁻⁷
HfB ₂ -3c	75	380	0.16	6.12 x 10 ⁻⁸
HfB ₂ -4c	75	170	0.17	1.82 x 10 ⁻⁷
HfB ₂ -5a	100	180	0.57	3.24 x 10 ⁻⁷

Creep rate as a function of applied stress is presented in Fig. 78. Fitting the creep results obtained for HfB₂ specimens at 1500°C in laboratory air with the power-law equation (Eqn. 1) resulted in a stress exponent (n) of 1.7. This coincides with the stress exponents found in literature. Melendez-Martinez *et al.* [57] reported secondary creep

rates were $\sim 6 \times 10^{-8} \text{ s}^{-1}$ at 1400°C and 298 MPa, $\sim 10^{-7} \text{ s}^{-1}$ at 1500°C and 298-408 MPa, $2 \times 10^{-7} \text{ s}^{-1}$ at 1600°C and 220 MPa. At 1500°C the stress exponent was 1.7. At 1600°C and stresses below 220 MPa, the stress exponent was 0.6. A creep mechanism was not identified. Talmy *et al.* [17] reported a stress exponent of ~ 1 for pure ZrB_2 , which coincides with diffusion as the dominant creep mechanism.

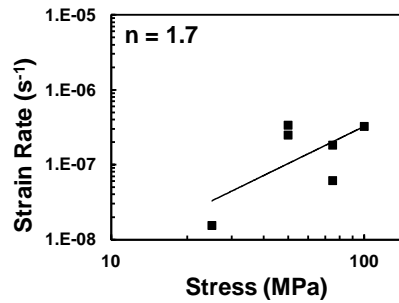


Fig. 78. Minimum creep rate as a function of applied stress for HfB_2 specimens at 1500°C in air.

The creep strain for the 75 MPa compressive creep tests had surprising low creep strain that did not follow the trend of increasing load increased the creep strain. The 75 MPa compressive creep curves were lower than that of 25 MPa. There is no current explanation on why the 75 MPa compressive creep curves are an aberration. However, they were consistent with one another over several tests encompassing both HfB_2 campaigns. The creep rates were replotted with the 75 MPa compressive tests removed due to their anomalous creep strains (Fig. 79). This resulted in a stress exponent of 2.2.

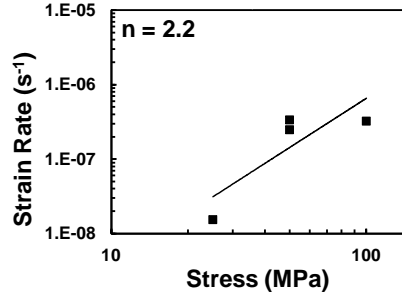


Fig. 79. Minimum creep rate as a function of applied stress (sans 75 MPa compressive tests) for HfB₂ specimens at 1500°C in air.

During the course of the compressive tests, the HfB₂ specimens were machined from two different HfB₂ pucks (HfB₂-a and HfB₂-c). Although the same composition, different campaigns inevitably will have variations in HfB₂ grain sizes. In this study, the grain sizes of the two monolithic HfB₂ pucks were 18- and 17-μm. Equation 2 was developed by Armani [65] to normalize the data to 1-μm in order to take into account the different grain sizes and consider the sensitivity of the strain rates to grain size. The strain rate is multiplied by the ratio of the actual grain size to 1-μm raised to the grain size exponent, m. The grain size exponent is chosen based on determining the creep mechanism.

$$\dot{\epsilon} = \dot{\epsilon}_{actual} \left(\frac{d_{act}}{1\mu m} \right)^m \quad (2)$$

A stress exponent (n) of 2 corresponds to either a diffusional or grain boundary creep mechanism. Diffusional creep is the most reported and accepted mechanism for polycrystalline ceramics such as diborides [17,114,183-185]. At a constant temperature, low stresses and small grain sizes (as in this study) favor diffusion creep. It is expected that UHTCs experience more diffusion creep since their application is dominated by high temperatures and low tension. As a result, the grain size exponent m = 1 was chosen to normalize the compressive creep strain rates. The results are summarized in Table 7.

Table 7. Summary of normalized creep results for HfB₂ specimens at 1500°C in air.

Specimen	Creep Stress (MPa)	Minimum Creep Rate (s ⁻¹)	Normalized Minimum Creep Rate (s ⁻¹)
HfB ₂ -1c	25	1.54×10^{-8}	4.39×10^{-6}
HfB ₂ -4a	50	2.48×10^{-7}	8.63×10^{-5}
HfB ₂ -2c	50	3.36×10^{-7}	9.59×10^{-5}
HfB ₂ -3c	75	6.12×10^{-8}	1.75×10^{-5}
HfB ₂ -4c	75	1.82×10^{-7}	5.19×10^{-5}
HfB ₂ -5a	100	3.24×10^{-7}	1.13×10^{-4}

The normalized creep rates were plotted versus creep stress with and without the 75 MPa compressive stresses in Fig. 80 and Fig. 81. The normalized creep rates were changed such that there was less spread in the data. However, the strain rate stress exponents remained the same.

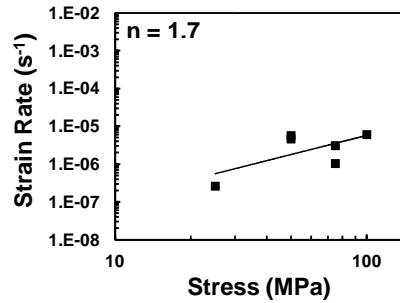


Fig. 80. Normalized minimum creep rates as a function of applied stress for HfB₂ specimens at 1500°C in air.

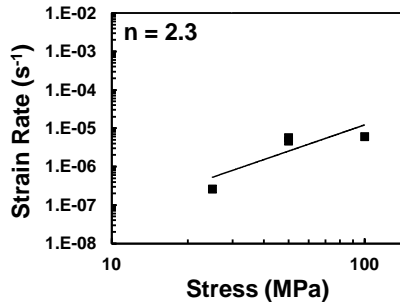


Fig. 81. Normalized steady-state creep rate as a function of applied stress (sans 75 MPa compressive tests) for HfB₂ specimens at 1500°C in air.

5.3.2 Pilot Compression Creep Tests – HfB₂ – 10, 20 vol% SiC

While SiC alone is extremely creep resistant, as an additive it enhances creep of the dominant material. This is demonstrated when SiC is added to HfB₂ causing a decrease in the grain size of the HfB₂ which reduces resistance [13,15,17,33,46,109,186]. In addition, during sintering, portions of the SiC may form a glassy intergranular film [148,149]. This glass film cannot support stress; thus allowing greater deformation. At high temperatures, the viscosity of the glassy film decreases; thus aiding vacancy diffusion or grain boundary sliding, once again decreasing creep resistance. If the intergranular film did not form during sintering, it can form when subjecting SiC-doped material to high temperatures. The grain boundaries of the dominant material are high energy sites in comparison to grain interiors [187-190]. This additional energy causes the SiC to form a glassy intergranular film at lower temperatures than stand-alone SiC. Putting all these factors together, it is presumed that increasing the amount of SiC doping of HfB₂ would increase the creep strain and rate.

Single load compression creep tests of HfB₂ with 10 and 20 vol% SiC were conducted at loads from 25 through 100 MPa. The experimental data of this study followed the above predictions; the creep strain for the HfB₂ with 10 and 20 vol% SiC specimens were greater than those of the HfB₂ specimens. The creep stress (MPa), time (min), strain (%), and minimum rate (s⁻¹) are summarized in Table 8.

Table 8. Summary of creep results for HfB₂-20 vol% SiC specimens at 1500°C in air.

Specimen	Creep Stress (MPa)	Creep Time (min)	Creep Strain (%)	Minimum Creep Rate (s ⁻¹)
HfB ₂ -10% vol SiC	25	97	1.1	1.68 x 10 ⁻⁶
HfB ₂ -20% vol SiC-1a	25	300	1.3	5.20 x 10 ⁻⁷
HfB ₂ -20% vol SiC-2a	25	900	1.2	2.65 x 10 ⁻⁸
HfB ₂ -20% vol SiC-3a	25	900	1.3	1.69 x 10 ⁻⁸
HfB ₂ -20% vol SiC-1c	25	900	0.42	3.58 x 10 ⁻⁸
HfB ₂ -20% vol SiC-6a	50	690	1.5	1.34 x 10 ⁻⁷
HfB ₂ -20% vol SiC-2c	50	510	0.39	4.52 x 10 ⁻⁸
HfB ₂ -20% vol SiC-5a	100	190	2.8	1.16 x 10 ⁻⁶
HfB ₂ -20% vol SiC-3c	100	29	0.082	7.74 x 10 ⁻⁷

The SiC conglomerates of the HfB₂-20SiC-a campaign do not have an effect on strain rates. The strain rate exponent for each of the separate campaigns was the same as strain rate exponent of combined campaigns. The HfB₂-20 vol% SiC creep rate as a function of applied stress is presented in Fig. 82. Fitting the creep results obtained for HfB₂-20 vol% SiC specimens at 1500°C in laboratory air with the power-law equation described earlier in Section 2.6 resulted in a stress exponent of 1.9. Bird *et al.* [114] reported the ZrB₂-20 vol% SiC stress exponent increased with increasing temperature, from $n = 1$ at 1400 °C to $n = 2.2$ at 1800°C. Specifically, at 1500°C $n = 1$, and at 1550°C $n = 1.7$. They concluded that the creep behavior is dominated by grain boundary sliding accommodated by diffusion. Talmy *et al.* [17] reported a stress exponent of ~ 1 for ZrB₂ 0-25 vol% SiC.

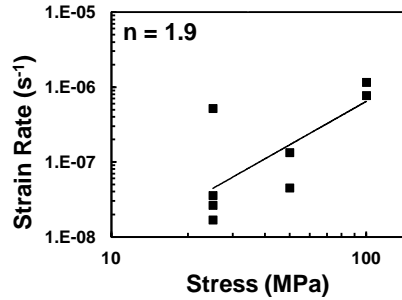


Fig. 82. Minimum creep rate as a function of applied stress for HfB₂-20 vol% SiC specimens at 1500°C in air.

The HfB₂-20 vol% SiC specimens were machined from two different HfB₂-20 vol% SiC campaigns (HfB₂-20SiC-a and HfB₂-20SiC-c). The pucks had different HfB₂ grain sizes (1.3-and 2.4-μm, respectively). Equation 5 was used to normalize the data to 1 μm in order to take into account the different grain sizes. As explained in Section 5.3.1, grain size exponent $m = 1$ was used to normalize the creep strain rates of the HfB₂-20 vol% SiC specimens. The results are summarized in Table 9. The normalized creep rates were plotted versus creep stress in Fig. 83. The normalized creep rates were changed such that there was less spread in the data. The strain rate stress exponent increased to 2.1.

Table 9. Summary of normalized creep results for HfB₂-20vol% SiC specimens at 1500°C in air.

Specimen	Creep Stress (MPa)	Steady-State Creep Rate (s ⁻¹)	Normalized Minimum Creep Rate (s ⁻¹)
HfB ₂ -20%vol SiC-1a	25	5.20 × 10 ⁻⁷	8.45 × 10 ⁻⁷
HfB ₂ -20%vol SiC-2a	25	2.65 × 10 ⁻⁸	4.31 × 10 ⁻⁸
HfB ₂ -20%vol SiC-3a	25	1.69 × 10 ⁻⁸	2.75 × 10 ⁻⁸
HfB ₂ -20%vol SiC-1c	25	3.58 × 10 ⁻⁸	1.89 × 10 ⁻⁶
HfB ₂ -20%vol SiC-6a	50	1.34 × 10 ⁻⁷	2.18 × 10 ⁻⁷
HfB ₂ -20%vol SiC-2c	50	4.52 × 10 ⁻⁸	2.13 × 10 ⁻⁷
HfB ₂ -20%vol SiC-5a	100	1.16 × 10 ⁻⁶	2.69 × 10 ⁻⁷
HfB ₂ -20%vol SiC-3c	100	7.74 × 10 ⁻⁷	4.61 × 10 ⁻⁶

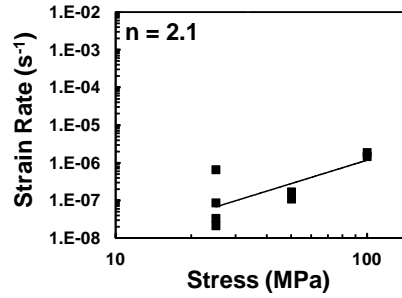


Fig. 83. Normalized minimum creep rate as a function of applied stress for HfB₂-20 vol% SiC specimens at 1500°C in air.

It is the author's opinion that the compression creep tests validate the experiment test facility and methods. The stress exponents of the monolithic and HfB₂-20 vol% SiC strain rates fall within those values reported by literature. The oxidation and recession of the compression creep tests were evaluated in the following chapter to confirm that the updated test method was also applicable to HfB₂ specimens containing 20 vol% SiC.

VI. Oxidation and Recession of HfB₂-containing UHTCs at 1500°C in Air

In this work all HfB₂-containing specimens were exposed to air environment at 1500°C. While oxidation of HfB₂ specimens occurred in all tests, different morphologies of the oxide scale were obtained during no-load exposures and during compression creep tests.

Figure 84 a - c shows the microstructure of the HfB₂ specimens heat treated under zero load at 1500°C (a) alone, (b) in contact with Pt, (c) and separated from SX YAG by alumina. The oxide scales produced in these tests are consistent with those reported in literature [46,50,97,104,109,110]. The inner bulk of their oxide layers as shown in Fig. 84 a - c have a columnar structure, while the outer surface has a nodular appearance. The same observation is true for the monolithic HfB₂ specimens separated from SX YAG by alumina and subjected to compression creep tested at 25 MPa (Fig. 84d). In many instances, the oxide layer has separated from the specimen bulk. This is a common occurrence attributed to CTE differences between the oxide and the diboride [97] and to oxide layer volume changes that accompany phase transitions during heating and cooling [171,191].

The scale morphology appeared less columnar when HfB₂ was heat treated in direct contact with SX YAG or when HfB₂ was separated from SX YAG by alumina and subjected to compression creep at higher loads. In these cases, the HfO₂ grains appear less elongated and randomly oriented (Fig. 85).

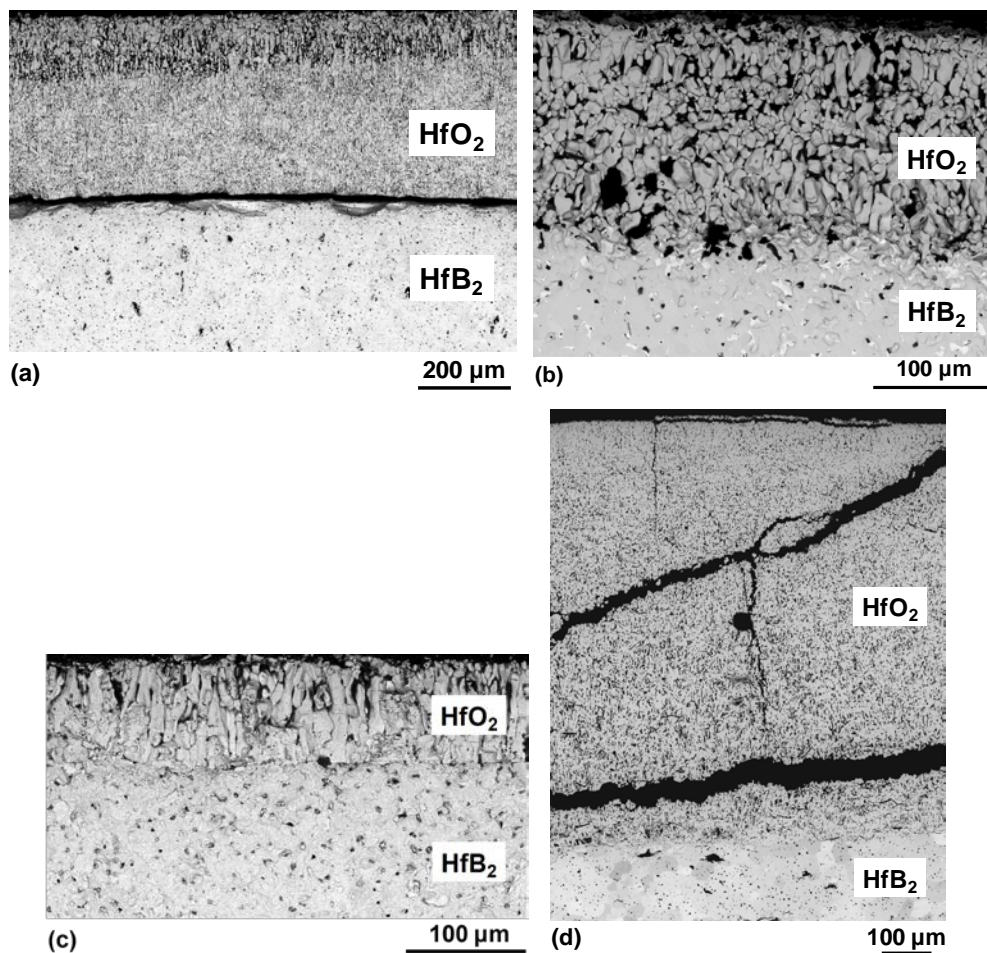


Fig. 84. SEM micrographs of columnar oxide scale on HfB_2 heat treated at 1500°C (a) alone under zero load, (b) in contact with Pt under zero load, (c) separated from SX YAG by alumina under zero load, and (d) separated from SX YAG by alumina under 25 MPa compression

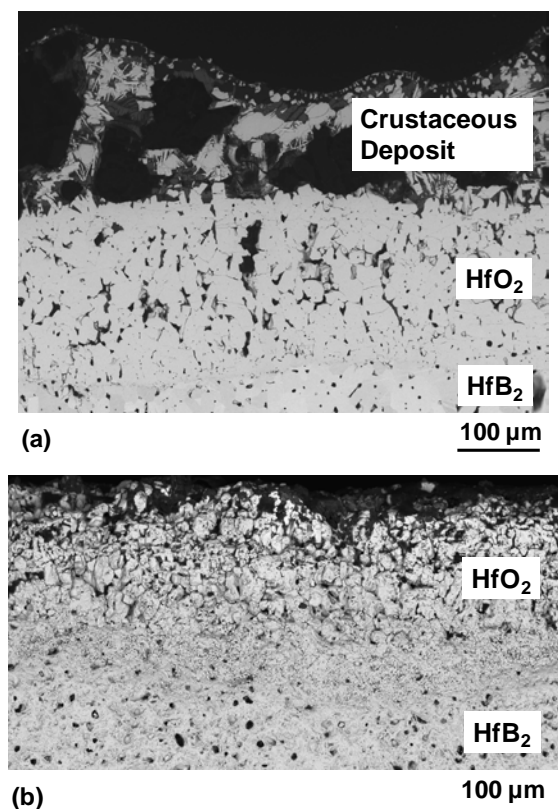


Fig. 85. SEM micrographs of equiaxed oxide scale on HfB_2 heat treated (a) in direct contact with SX YAG and (b) separated from SX YAG by alumina under higher compressive loads.

The HfB_2 -SiC specimens had an oxide layer that was only on occasion columnar. In many instances, the borosilicate scale contained discontinuous layers of HfO_2 or HfSiO_4 . This finding was consistent with literature as discussed in Section 5.5.

A concrete determination of the effect of load cannot be made from the creep test data of this experiment. Due to various failures (as described in Appendix M), the creep tests were of varying durations. In an attempt to make a comparison, experimental values of oxidation layer thicknesses and recession thicknesses were compared with predictions of Parthasarathy *et al.* [104,110] oxidation models at 1500°C . Direct comparison to literature is difficult, since most oxidation studies have been conducted on ZrB_2 -

containing UHTCs. Due to short exposure times (1 hr or less), data from oxidation studies conducted on HfB₂-containing UHTCs [33,46,109,120] cannot be used for direct comparison with the results of this study.

6.1 Oxidation of HfB₂ under Compressive Load at 1500°C in Air

The oxidation model by Parthasarathy *et al.* [104] was used to predict the values of HfB₂ oxidation scale thickness for various heat treatment times used in this study. The model uses a parabolic equation based on properties of the oxide scale itself to determine its thickness (Eqn.3). The degree of recession of HfB₂ is determined by Eqn. 4. The model predictions were compared to the experimental results (Fig. 86).

$$L^2 = 2 \left[\frac{2}{5} \left(\frac{V_{MeO_2}}{\rho_{MeO_2}} \right) \left(\frac{f}{1-f} \right) D_{O_2} \frac{C_{O_2}^a - C_{O_2}^i}{(1-q)} \right] t \quad (3)$$

$$R = L(1-f) \frac{M_{HfB_2}/\rho_{ZrB_2}}{M_{HfO_2}/\rho_{ZrO_2}} \quad (4)$$

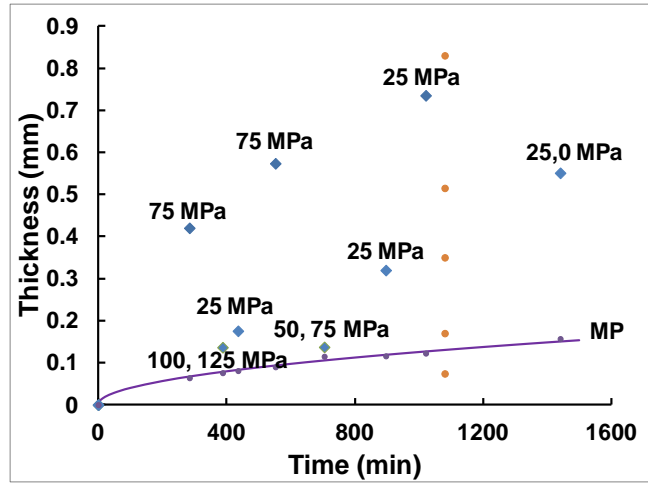


Fig. 86. Oxidation thicknesses of HfB₂ specimens under various compressive loads at 1500°C in air. MP represents the model prediction curve.

For all of the compression creep tests, the HfO₂ layer was thicker than the model predictions. This would imply that the load affects the oxidation of HfB₂. The fact that a load was applied appears to have more of an impact on oxidation than the amount of load itself. However, a concrete determination of the effect of compressive load on oxidation cannot be made due to the wide range of oxidation scale thicknesses of the HfB₂-a specimens that did not experience a compressive load. The values of the zero load oxidation tests are the unlabeled points in Fig. 86.

It was also observed that there appeared to be several trends in the data. A closer look at the data showed that the trends coincided with different HfB₂ microstructures. Different prediction curves based on the Parthasarathy *et al.* HfB₂ oxidation model [104] were drawn to coincide with each microstructure (Fig. 87). Since the variables within the brackets of Eqn. 3 are not dependent on HfB₂ properties, they were reduced to a single value, *A* (Eqn. 5). The value of *A* was adjusted for each set of HfB₂ samples oxidation values.

$$L^2 = 2[A]t \quad (5)$$

The recession curves in Fig. 88 coincide with the oxidation curves of Fig. 87. Increased oxidation in comparison to the Parthasarathy *et al.* [104] model would also create greater recession values in comparison to the model.

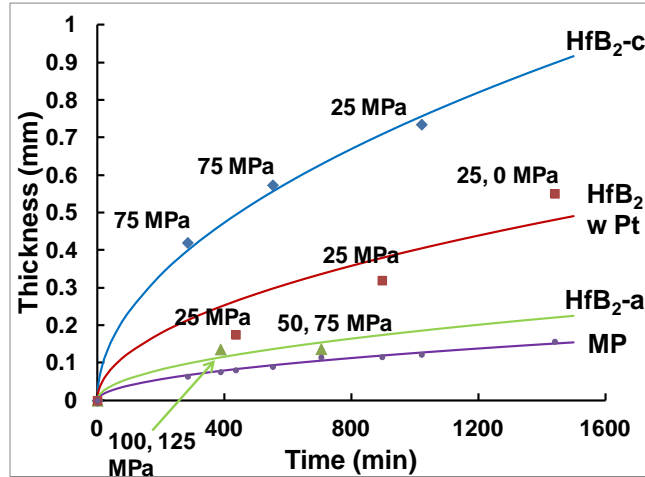


Fig. 87. Oxidation curves of various HfB_2 microstructures under various compressive loads at 1500°C in air. Points without labels are the tube furnace heat treatment results. MP represents the model prediction curve.

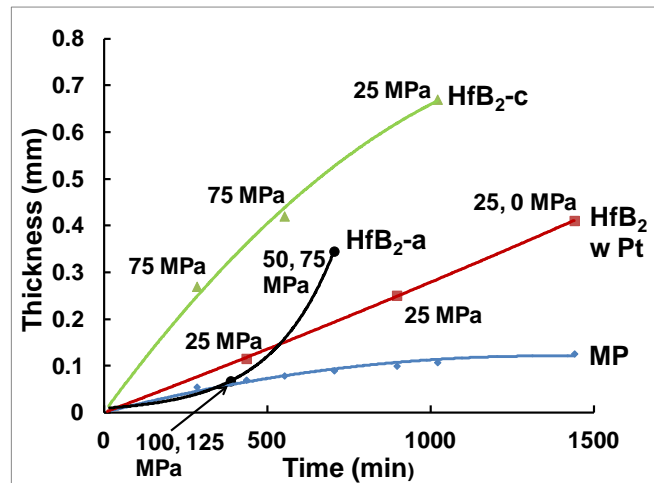


Fig. 88. Recession curves of various HfB_2 microstructures under various compressive loads at 1500°C in air. MP represents the model prediction curve.

According to Eqn. 3, oxidation scale thickness is dependent on the diffusion of oxygen through the oxidation scale. This implies that the microstructure of the HfB_2 does not play a role in the thickness of the oxide scale. However, it is believed that the microstructure of HfB_2 has a larger effect than previously thought. The three experimental curves in Fig. 87 were produced using specimens with different

microstructures. The HfB₂-a and HfB₂-Pt specimens had an average HfB₂ grain size of 19- μ m. HfB₂-Pt contained Pt within its triple point grain boundaries. The HfB₂-c specimen had 17- μ m grains, on average. Further SEM and EDS analysis was conducted on as-processed HfB₂ specimens and on the Pt-infused HfB₂.

The HfB₂-a campaign had HfO₂ subgrains within the HfB₂ (Fig. 89a). Grains of HfO₂ were also found within some of the grain boundaries. Moreover, SiC was also observed within some of the grain boundaries and open triple points (Fig. 89b). The HfB₂-Pt oxidation values are from the HfB₂-1a and HfB₂-3a specimens that were subjected to compression creep testing at 1500 °C. Recall that Pt had diffused throughout the previously open triple points and larger grain boundaries of the specimens (Fig. 90). The HfB₂-c campaign did not have any SiC or HfO₂ within its grain boundaries (Fig. 91). It also appeared to have more porosity than that of the HfB₂-a campaign. The degree of porosity was not determined. Recent work has shown that porosity in HfB₂ specimens could be induced by polishing [66,192]. As such, the degree of porosity via visual evaluation of polished specimen micrographs could be inaccurate

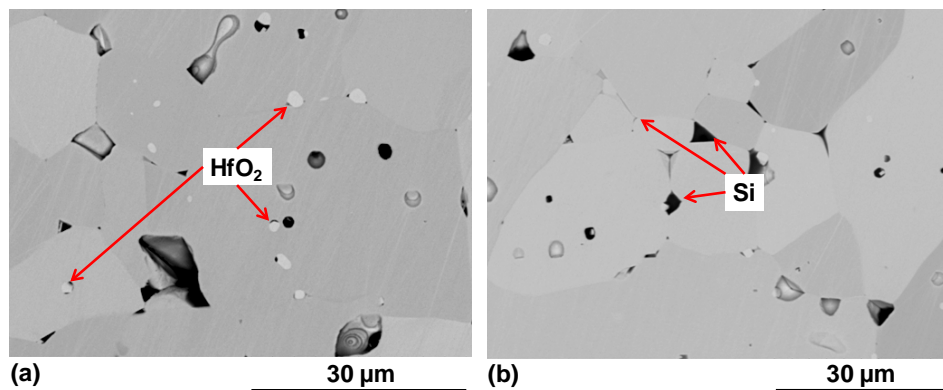


Fig. 89. SEM micrograph of as-provided HfB₂-a campaign with several (a) HfO₂ subgrains and within grain boundaries and (b) Si within open triple points and grain boundaries annotated.

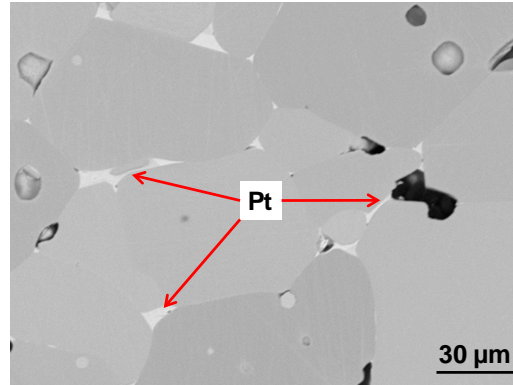


Fig. 90. SEM micrograph image showing unoxidized bulk of HfB₂-3a specimen after 7.3 hrs at 1500 °C under a compressive load (25, 50 MPa) for 6.2 hrs.

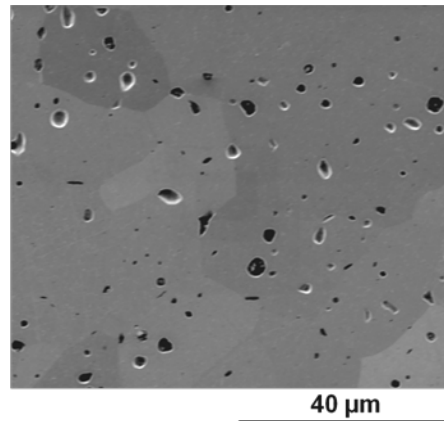


Fig. 91. SEM micrograph showing as-processed HfB₂-c campaign microstructure.

The differences in the microstructure of the test specimens could be the source of differing oxidation curves. Porosity and the presence of HfO₂ grains could create a thicker oxidation scale in comparison to perfectly dense HfB₂. For a certain depth of HfB₂, increasing either of the latter reduces the amount of HfB₂ to be oxidized. The same amount of oxygen could affect a greater thickness of HfB₂. The smaller grain size of the HfB₂-c specimens created the thickest oxidation scale. Smaller grains create more pathways for oxygen ingress. Smaller grains also create more surface area for oxygen to attack. Or the HfB₂-c oxidation curve is greater than the other two since Pt and SiC in the grain boundaries and triple points can slow the ingress of oxygen into the HfB₂.

However, $\text{HfB}_2\text{-Pt}$ and $\text{HfB}_2\text{-a}$ are from the same as-provided campaign. The oxidation curves for $\text{HfB}_2\text{-Pt}$ and $\text{HfB}_2\text{-a}$ are different due to the presence of Pt and SiC in the grain boundaries. Platinum has been shown to dissociate oxygen and enhance oxidation of Zr alloys [193]. On the other hand, Aoki *et al.* [194] and Badwal *et al.* [195] reported that Si-containing impurities in grain boundaries have been shown to hamper diffusion of oxygen across grain boundaries. One reason is that SiC reacts with oxygen more readily than HfB_2 with oxygen; therefore, less oxygen would be available to oxidize HfB_2 . Figure 92 uses $\text{ZrB}_2\text{-SiC}$ to illustrate that SiC oxidizes sooner than ZrB_2 ¹³. Once again, due to the similarity between Hf and Zr, the same can be said for the oxidation of $\text{HfB}_2\text{-SiC}$.

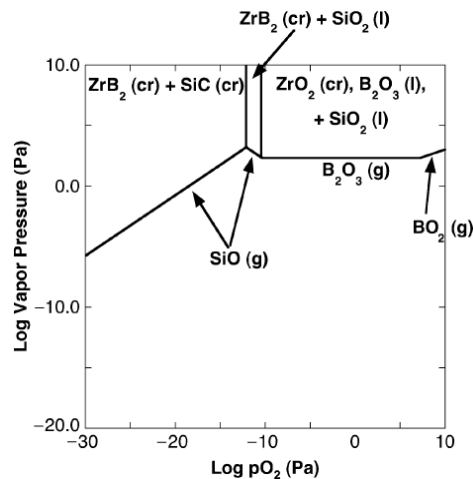


Fig. 92. Volatility diagram of $\text{ZrB}_2\text{-SiC}$ at 1500°C . (Fahrenholtz [196], Reprinted with permission.)

¹³ This is the reason that the oxidation of $\text{HfB}_2\text{-SiC}$ creates a SiC-depleted layer. See Appendix A.

It is believed that oxygen diffusion into the grain boundaries of HfB_2 has a minimal impact on the development of the oxide scale. The equation for oxide scale thickness (Eqn. 3) does not include oxidation properties of HfB_2 . The equation for recession (Eqn. 4) does take into account the density bulk property of HfB_2 . However, it is possible that the compressive load increases the impact that HfB_2 microstructure has on its oxidation.

This is likely due to the HfB_2 grain boundaries at the surface of the specimens. When a specimen experiences compressive strain, the gauge section length is decreased. There are two mechanisms that allow this to occur: densification and cross-section expansion. (It was not possible to differentiate the change in cross section from recession to that of compression expansion.) As a result of expansion, the exterior grain boundaries are weakened due to slight grain separation which allowed greater oxygen ingress into the bulk. The grain boundary weakening is not caused by a grain separation great enough to cause a density change significant enough to affect Eqn. 4. .

The thermo-chemical compatibility study presented in Section 3.5.2 demonstrated that proximity to or contact with SX YAG and/or alumina could affect the oxidation behavior of HfB_2 . A HfB_2 specimen was heat treated for 18 h at 1500°C in contact with an alumina spacer in a tube furnace in order to establish baseline oxidation behavior of HfB_2 (Case 0). Post-test SEM imaging of the HfB_2 specimen revealed the oxide scale with the columnar structure consistent with that reported in literature [46,85,109]. The SEM image in Fig. 93 also revealed that oxide scales of different thickness were produced on the different surfaces of the HfB_2 specimen. The scale formed on the HfB_2 surface in contact with the alumina spacer was thinner than that on the surfaces exposed

to the tube furnace environment. The average scale thickness on the HfB_2 surface exposed to the tube furnace environment is 0.830 mm. The average scale thickness on the HfB_2 surface in contact with the alumina spacer is 0.429 mm.

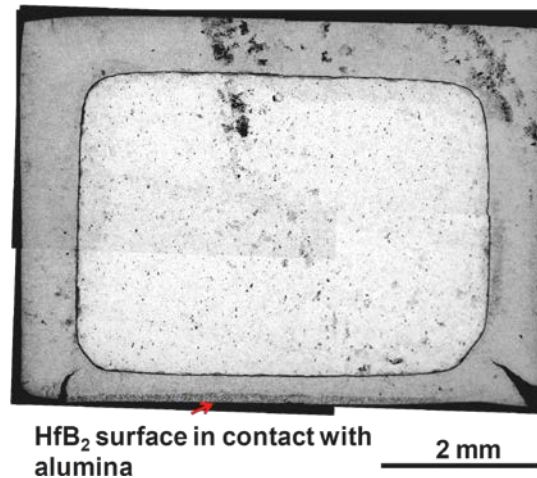


Fig. 93. SEM micrograph of cross sectional view of the HfB_2 specimen heat treated for 18 hrs at 1500°C in air in contact with alumina.

The oxide scales of several of the tube furnace interaction tests were evaluated for their thicknesses to determine any effect of the presence of alumina (Fig. 94).

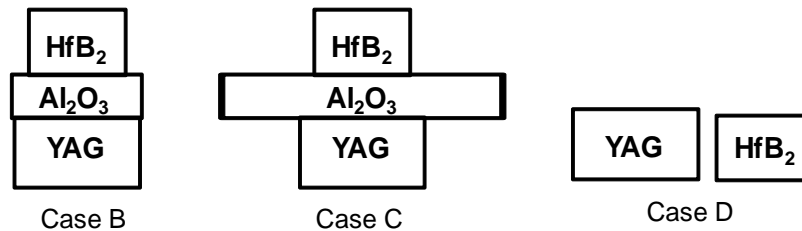


Fig. 94. Schematic of heat treatment tests evaluated for the possible effect of alumina on oxidation scale thickness

When HfB_2 was heat treated separated from SX YAG using an alumina spacer (Case B), the SEM examination revealed a porous m- HfO_2 scale with a columnar grain structure on all surfaces of the HfB_2 specimen. Notably, the oxide scale was much thicker on the HfB_2 surface that was in direct contact with alumina (average scale

thickness ≈ 0.19 mm) than on the HfB_2 surfaces exposed to the furnace environment (average scale thickness ≈ 0.07 mm). The scale thickness on the sides of the HfB_2 specimen was thicker near the bottom and thinned as it approached the top surface. When a very large alumina spacer was used (Case C), the oxidation scales were much closer in average value. The oxide scale exposed to the furnace environment had an average scale thickness of ≈ 0.17 mm, and the scale on the HfB_2 surface that was in direct contact with alumina had an average scale thickness of ≈ 0.20 mm.

Case D was conducted with a HfB_2 specimen placed ~ 3 mm away from SX YAG. Once again the oxide scale was much thicker on the HfB_2 surface in direct contact with alumina (average scale thickness $\approx .49$ mm) than on the top HfB_2 surface exposed to the furnace environment (average scale thickness ≈ 0.35 mm).

A cross-section of Case D was obtained such that every surface of the specimen was not in contact with the alumina as a result of the specimen's curved bottom as shown in Fig. 95. The oxide scale on the top of the specimen (average scale thickness ≈ 0.53 mm) was similar to the oxide scale on the bottom of the specimen (average scale thickness ≈ 0.50 mm).

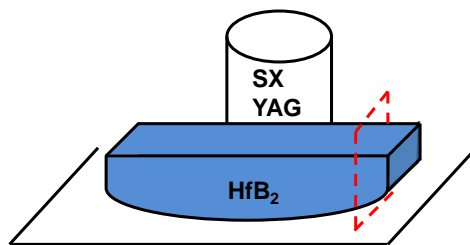


Fig. 95. Schematic of "alumina-free" cutting plane.

A summary of the oxide scales is shown below in Table 10. It is not possible to make a definitive statement about the effect of alumina. This analysis revealed two different interesting oxidation aspects. When SX YAG is not present in the test chamber (Case 0), the oxide scale is greater on the surfaces exposed to the tube furnace environment than that in contact with alumina. When SX YAG is present and a surface is in contact with alumina, the oxide scale in contact with alumina is thicker than that exposed to the tube furnace environment. The oxidation scale on the surface exposed to the tube furnace environment is generally thinner than in Case 0. This could be due to the presence of gaseous AlBO_2 and YBO_2 in the tube furnace environment. These gases could be decreasing the partial pressure of O_2 in the tube furnace environment, which would decrease the amount of oxygen available for the oxidation of HfB_2 . The Al_2O_3 or YBO_3 deposits that form on the surface of HfB_2 could also provide a degree of oxidation protection, slowing the ingress of oxygen through the oxide scale pores.

Table 10. Average oxide scale thicknesses (mm) of oxide scales of different cases of HfB_2 heat treated in contact with alumina for 18 hrs at 1500°C in air.

Oxide Scale	(Case 0) Contact w/ Alumina	(Case B) Separated from SX YAG w/ Alumina	(Case C) Separated from SX YAG w/ Large Alumina	(Case D) Contact w/ Alumina in Presence of SX YAG	(Case D) No Contact w/ Alumina
Exposed	0.83	0.07	0.17	0.35	0.53
Contact	0.43	0.19	0.20	0.49	0.50

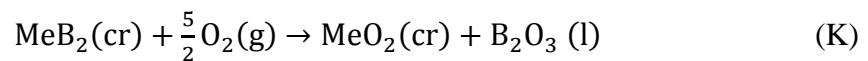
The two cross sections of Case D evaluated indicate that the proximity of SX YAG can increase the oxidation of HfB_2 (see Table 11). In Case D, the oxide scale was thicker on the HfB_2 surface facing SX YAG (average scale thickness ≈ 0.68 mm) than on

the HfB₂ surface on the HfB₂ surface facing away from SX YAG (average scale thickness ≈ 0.46 mm). As mentioned, the specimen had a curved bottom such that a cross-section was obtained such that no surface was in contact with the alumina. The oxide scale of this second section was thicker on the HfB₂ surface facing SX YAG (average scale thickness ≈ 0.63 mm) than on the HfB₂ surface facing away from SX YAG (average scale thickness ≈ 0.40 mm). In both cases, the oxide scales top surface exposed to the tube furnace environment and that in contact with alumina are thicker on the side of the HfB₂ specimen in proximity to SX YAG.

Table 11. Oxide scale thicknesses (mm) of various areas of 3 different cross-sections of HfB₂ after heat treatment for 18 hrs at 1500°C in air.

Oxide Scale	(Case 0) Contact w/ Alumina	(Case 4) Contact w/ Alumina in Presence of SX YAG	(Case 4) No Contact w/ Alumina
Top Scale (Left Side)	0.83	0.32	0.36
Top Scale (Prox to SX YAG)	0.83	0.38	0.70
Left Scale	0.76	0.46	0.40
Right Side	0.76	0.68	0.63
Bottom Scale (Left Side)	0.43	0.46	0.41
Bottom Scale (Prox to SX YAG)	0.43	0.68	0.59

The question arises as to how does the proximity of SX YAG accelerate the oxidation of HfB₂? In general, the oxidation of monolithic refractory diborides exposed to air at elevated temperatures can be considered stoichiometric [13,32,104]. The oxidation reaction is given by



where Me = Zr or Hf. Oxidation of the metal diboride results in an evaporation-resistant refractory metal oxide that forms a porous skeleton on the surface of the specimen and a liquid boria (B_2O_3) that fills the pores between the oxide grains. At temperatures below $\sim 1200^\circ\text{C}$, the liquid B_2O_3 in the pores provides oxidation protection [23,97,101,104,128]. At lower temperatures the rate-limiting step of oxidation is the diffusion of oxygen through the liquid boria. Oxygen is assumed to dissolve in boria and continue to diffuse to the substrate-scale interface where the oxidation reaction occurs. At temperatures above 1400°C , oxidation dynamics change such that the oxide scale consists of two layers. Layer 1 is the glassy liquid B_2O_3 that fills the base of the refractory metal oxide skeleton. At the same time, the liquid B_2O_3 at the surface evaporates, leaving a refractory metal oxide porous layer (layer 2) that does not offer any protection from further oxidation. The oxidation rate is now limited by Knudsen diffusion of molecular oxygen through the capillaries between nearly columnar blocks of the metal oxide. (Fig. 96) It has been shown that the decrease in oxidation resistance protection for refractory diborides at the higher temperatures corresponds with the evaporation of B_2O_3 from the oxide scale [101-103,128,197]. This is supported by various thermodynamic and kinetic models [22,104,106].

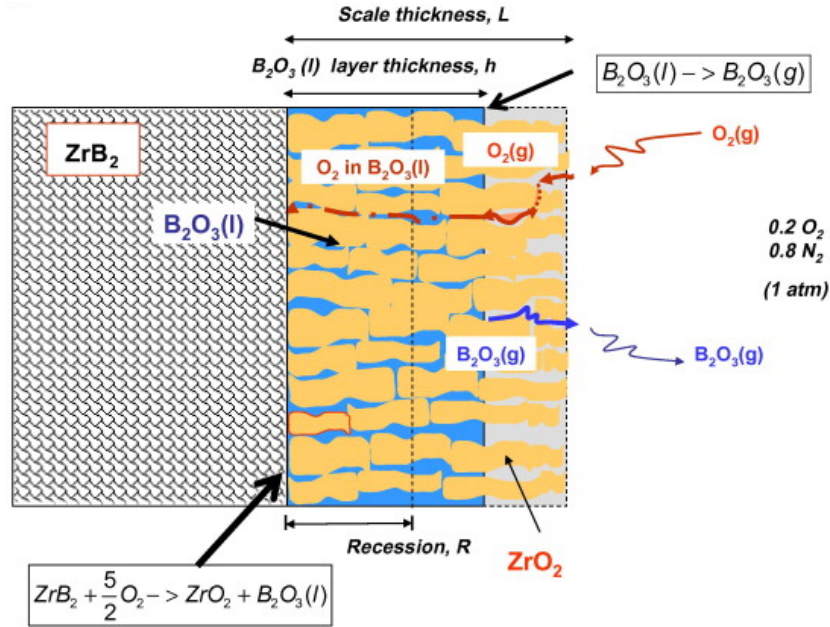
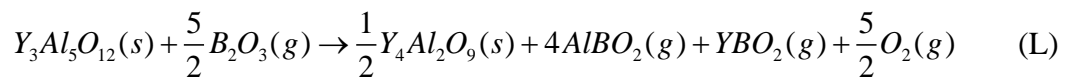


Fig. 96. Schematic of mechanisms involved in oxidation of ZrB_2 in air at temperatures in the 1400-1800°C range. The distance L represents the diffusion distance in a pore over which gaseous oxygen must diffuse to reach the boria. (Parthasarathy *et al.* [104], Reprinted with permission.)

The relative rates of filling the pores with B_2O_3 by oxidation at the substrate-scale interface and of the evaporation of B_2O_3 determine the extent to which the pores are filled with the protective B_2O_3 . It is proposed that the interaction of gaseous B_2O_3 with SX YAG accelerates the evaporation of B_2O_3 and the oxidation of HfB_2 .



As shown in Rxn. L, this interaction not only consumes B_2O_3 but also produces oxygen. As the amount of oxygen increases, more is available to diffuse through the oxide scale to oxidize HfB_2 . This could be of no consequence if oxygen diffusion through the oxide scale capillaries is already at a maximum. The partial pressure of oxygen could be of more consequence. Fahrenholtz and Hilmas [128] calculated the vapor pressures of gaseous B_2O_3 produced by the vaporization of liquid B_2O_3 in the ZrB_2

oxide scale (Fig. 97). As the partial pressure of oxygen increases, so does the vaporization of B_2O_3 . The increased rate of liquid B_2O_3 loss could also be contributed to the partial pressure of B_2O_3 . As the amount of B_2O_3 in the local atmosphere decreases due to interaction with SX YAG, B_2O_3 evaporation accelerates to reach the gaseous B_2O_3 saturation level [177]. There is a stagnant boundary layer on the surface of an oxidizing UHTC. Consider that the SX YAG emphasizes a distinct boundary for this layer of air above the surface of the oxide scale. The amount of air above the oxide scale is contained enough such that gaseous B_2O_3 remains in close proximity to the oxide scale. At first, B_2O_3 (g) molecules will simply evaporate and enter the air. But once a few B_2O_3 (g) molecules are present in the air, some of the B_2O_3 (g) molecules will reenter the liquid B_2O_3 . Once the B_2O_3 (g) in the air reaches a certain concentration, the rate of B_2O_3 evaporation will equal the rate of B_2O_3 (g) liquefaction. The solution of B_2O_3 (g) in air has become saturated.

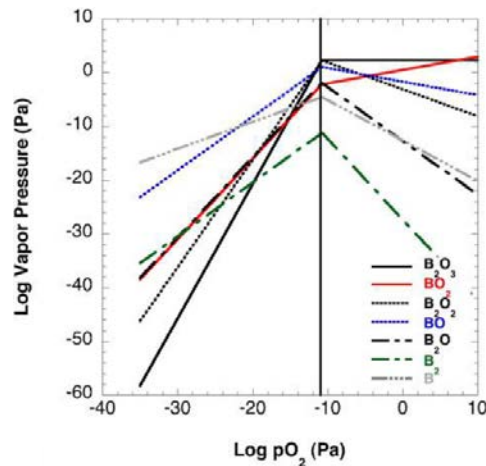


Fig. 97. Vapor pressure diagram of various B-O species as a function of oxygen partial pressure at 1500°C as calculated in Fahrenholtz and Hilmas [128]. (Reprinted with permission)

When the HfB_2 was placed on one side of SX YAG, the SX YAG also showed signs of increased degradation. Several tube furnace experiments in which SX YAG was in proximity to HfB_2 (Fig. 98a) show signs of increased interaction on the side facing the HfB_2 (Fig. 98d). The opposite face of the SX YAG remained relatively smooth (Fig. 98b). Figure 98c is the transition between those faces.

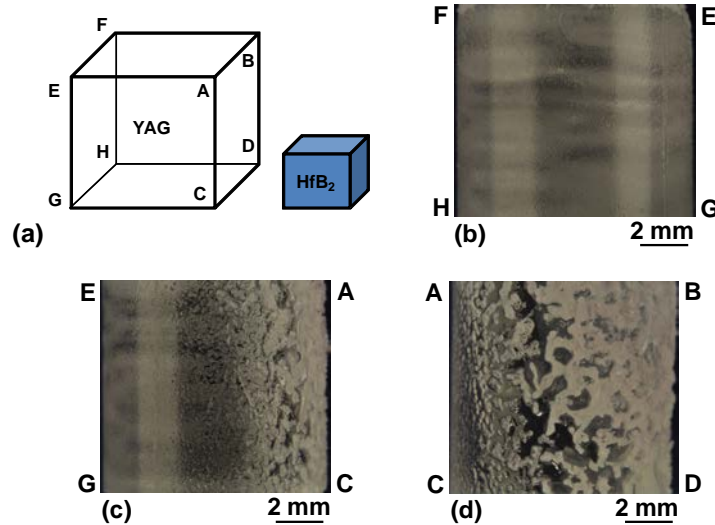


Fig. 98. (a) Schematic of HfB_2 in proximity to SX YAG. Photographs of the (b) Back side of SX YAG (FEGH), (c) side of SX YAG (EACG), and (d) front side of SX YAG that was exposed to HfB_2 (ABDC) for 18 hrs at 1500°C in an air.

As it should be expected, the presence of alumina inhibits the oxidation of HfB_2 . On the other hand, the presence of SX YAG can be both an inhibitor and enhancer of the oxidation of HfB_2 . The gaseous byproducts of the decomposition of SX YAG reduce the amount of oxygen in the local atmosphere, causing the overall oxide scale to be thinner. When the SX YAG is evenly distributed beneath the HfB_2 , the gaseous byproducts of the decomposition of SX YAG adsorb onto the surface of HfB_2 as Al_2O_3 and YBO_3 . It is possible that these byproducts retard the ingress of oxygen through the oxide scale pores, causing the oxide scale exposed to the tube furnace to be thinner than the oxide scale in

contact with alumina. The SX YAG placed in close proximity to HfB_2 possibly created a boundary layer which increased the evaporation of B_2O_3 . This increased the oxidation of the HfB_2 surface in the closest proximity to SX YAG.

6.2 Oxidation of HfB_2 -20 vol% SiC under Compressive Load at 1500°C in Air

As mentioned previously, the different microstructures of HfB_2 -20SiC-a and HfB_2 -20SiC-c did not affect the strain rate. However, oxidation of the two campaigns of HfB_2 -20 vol% SiC resulted in physical differences of the specimen surfaces after compression creep testing at 1500 °C in air. X-ray diffraction analysis revealed the surface of the HfB_2 -20SiC-a specimens was comprised of m- HfO_2 and HfSiO_4 with a "blistered" appearance as seen in Fig. 99. (Borosilicate glass is amorphous and would not be present in XRD returns.) The HfB_2 -20SiC-c specimens have a shinier appearance as seen in Fig. 100. As a result of SEM analysis, it was determined that the white areas were richer in boron, while the darker areas contained more silicon.

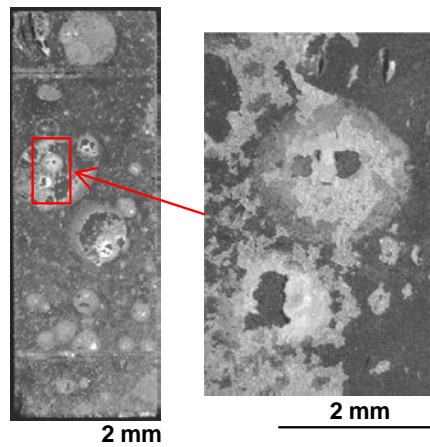


Fig. 99. Photo micrographs of representative HfB_2 -20SiC-a specimen after compression creep testing at 1500°C.

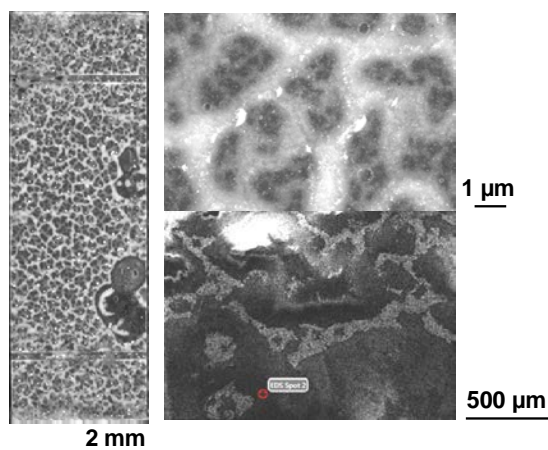


Fig. 100. Photograph and SEM micrographs of representative HfB₂-20SiC-c specimen after compression creep testing at 1500°C.

The surface patterns in Fig. 99 and Fig. 100 are a form of the deposits as seen on the surfaces of ZrB₂-15 vol% SiC oxidized at 1550 °C as reported by Karlsdottir *et al.* [198,199] and Shugart *et al.* [200]. The oxidation of ZrB₂-SiC produces ZrO₂, liquid boria (B₂O₃), and very viscous silica (SiO₂). Once dissolved, the B₂O₃ and SiO₂ liquids combine to form a borosilicate. ZrO₂ can dissolve into the borosilicate, creating two different borosilicate-based liquids of large viscosity contrast. Karlsdottir *et al.* [199] proposed that the ZrO₂-borosilicate creates convection cells (i.e., "viscosity fingers") that rise up through the borosilicate to deposit ZrO₂ on the surface.

The oxidation morphology of the oxidation layers of HfB₂-20 vol% SiC of the current study was evaluated using the FEI/Philips Quanta 1 SEM and EDS (Appendix E). SEM micrographs of the cross-section revealed areas of HfO₂ or HfSiO₄ on, and within, the borosilicate glass (Fig. 101)¹⁴ along the same vein as the "viscous fingers" described above by Karlsdottir *et al.* This was more prevalent in the HfB₂-20SiC-a specimens than the HfB₂-20SiC-c specimens. HfO₂ is known to dissolve into borosilicate, but usually at

¹⁴ This was also observed on specimens heat treated with zero load.

temperatures above 1600°C [201]. It is presumed that the HfO_2 dissolved into the borosilicate at the lower temperature of the current work as a result of the long duration of the creep tests. The patterns on the surface of the specimens are likely the B_2O_3 evaporating on the surface, leaving behind HfO_2 or HfSiO_4 . The layers within the borosilicate glass could occur during cooling, with the HfO_2 or HfSiO_4 precipitating out of the borosilicate. Boria can dissolve more ZrO_2 at higher temperatures [198,200]; this must also hold true for HfO_2 .

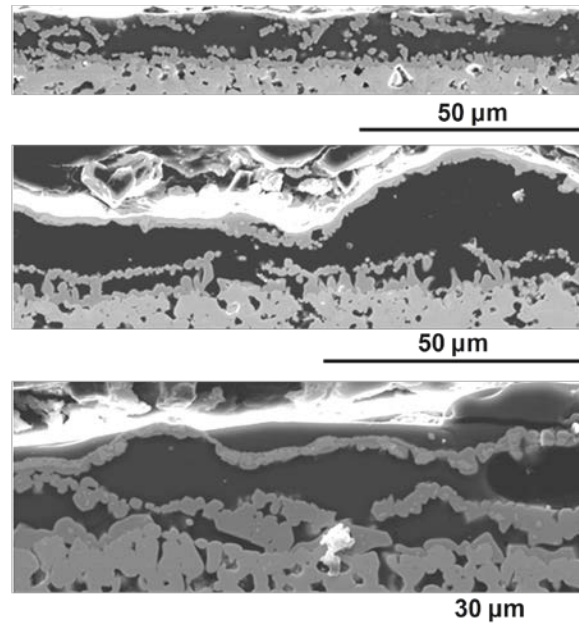


Fig. 101. SEM micrographs of representative areas of HfO_2 or HfSiO_4 from different HfB_2 -20 vol% SiC on and within borosilicate glass.

Another observation was the uneven nature of the oxidation. There was an almost undulating pattern as seen in Fig. 102. The areas of thicker borosilicate glass generally coincides with areas of thinner HfO_2 scale. Also, there are areas where borosilicate glass was minimal or nonexistent even with little to no oxide scale (Fig. 103). These variations are not entirely unexpected. Carney *et al.* [46,66], Monteverde *et al.* [69,101], and

Shugart *et al.* [200,202] reported on the variability and lack of repeatability of borosilicate glass and oxide layer thicknesses. Initial oxidation of $\text{ZrB}_2\text{-SiC}$ creates pools of borosilicate glass; after 1 minute a continuous layer covers the surface. This initial uneven distribution creates areas of increased oxidation as well as a localized increased bubble formation of gaseous CO and B_2O_3 in the borosilicate. When these bubbles burst, protective borosilicate coverage is decreased. Some of these bubbles can remain intact (and provide oxidation protection) until the end of testing (Fig. 104).

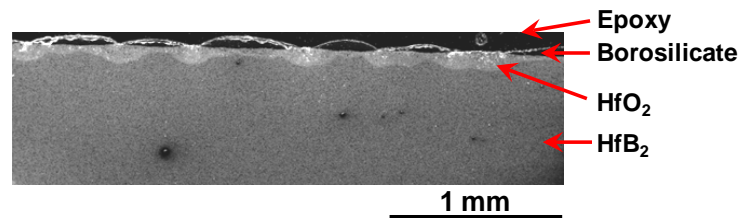


Fig. 102. SEM micrograph of undulating variations in glass and oxide layer thicknesses of $\text{HfB}_2\text{-20 vol% SiC}$ specimens after compression creep testing at 1500°C in air.

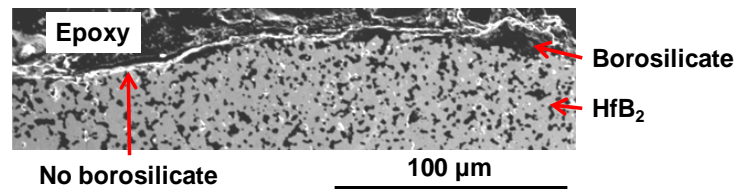


Fig. 103. SEM micrograph of little to no borosilicate glass protection and oxide layer of $\text{HfB}_2\text{-20 vol% SiC}$ specimens after compression creep testing at 1500°C in air.

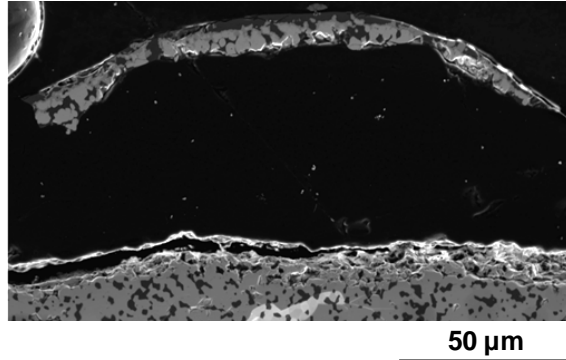


Fig. 104. SEM micrograph of bubble on surface of HfB_2 -20 vol% SiC after compression creep testing at 1500 C in air.

In some areas a large gap between the CaldoFix mounting media and the specimen developed (Fig. 105). (This was also reported by Parthasarathy *et al.* [110].) While it can be assumed that the glass or scale was removed during polishing, this assumption was not made. CaldoFix is the softer material so it can be assumed that it polished away quicker. Also, the CaldoFix can crack as seen in Fig. 106. This material can also break away entirely, leaving the gap. The glass and scale were measured using the Bruker SEM image measurement tool based on the observed glass and scale. The precipitates in the borosilicate scale were included in the oxide scale measurement but not the borosilicate glass.

Recession values could not be directly determined as the oxide scale lacked the necessary thickness to be distinguished using an optical microscope. To achieve adequate resolution, the Quanta 1 SEM and EDS system was used. To determine recession, the pre- and post-test outer dimensions of the test specimens were measured using an optical microscope. The average borosilicate and oxide scales were determined utilizing at least 40 measurements that encompassed all four sides of the specimen. This value was multiplied by 2 and subtracted from the final outer dimensions.

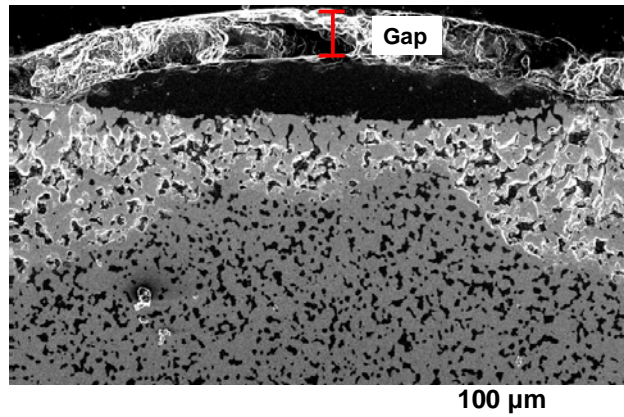


Fig. 105. SEM micrograph with annotated gap between specimen and CaldoFix.

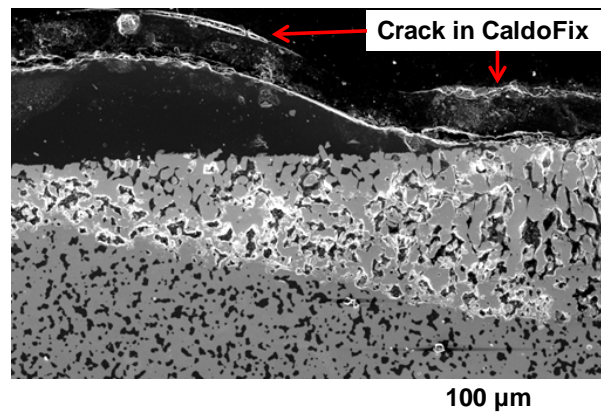


Fig. 106. SEM micrograph with crack in CaldoFix annotated.

Oxidation of the HfB_2 -20 vol% SiC creep specimens was compared to the Parthasarathy model [110] (Fig. 107). The curve drawn for the borosilicate glass fell below the model predictions, as it was less steep than the model would have predicted. The true viscosity for Hf-containing borosilicate is not known. It is usually estimated from the viscosity of SiO_2 , B_2O_3 , and one intermediate composition [198]. It is surmised that the viscosity is less than estimated, particularly for the long durations at 1500°C of the current study. The downward flow of borosilicate glass has been observed and reported [66]. As such, gravity would "pull down" the scale to a greater degree. Another possibility is that there is a limited glass thickness that can maintain enough surface

tension and adhesion to remain on the surface of the test specimen, regardless of how much borosilicate is generated. Similar to the monolithic HfB_2 results, the HfO_2 scale was thicker than the model prediction (Fig. 108). This correlates with the fact that the borosilicate glass is lower than predicted. A thinner borosilicate glass layer would provide less oxidation protection, resulting in a thicker oxide scale. As the borosilicate glass experimental curve was shallower than the model prediction, the oxide scale experimental curve also a steeper curve than the model prediction (Fig. 108).

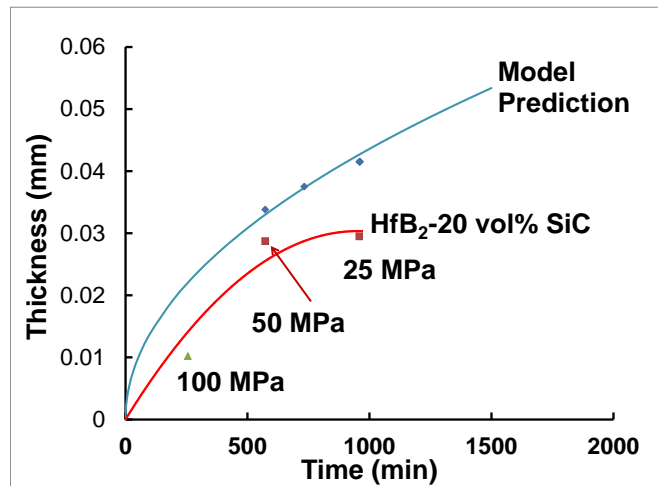


Fig. 107. Comparison of model predictions to experimental results of borosilicate glass layer of HfB_2 -20 vol% SiC after compression creep testing at 1500°C in air.

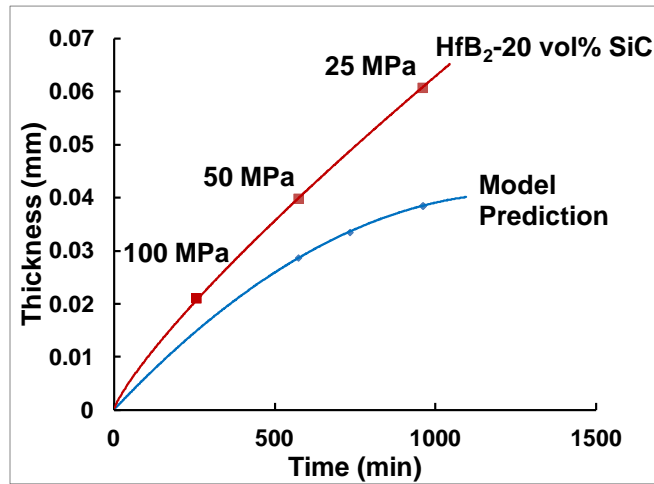


Fig. 108. Comparison of model predictions to experimental results of oxide scale of HfB₂-20 vol% SiC after compression creep testing at 1500°C in air.

VII. Concluding Remarks

One of the main objectives of the Air Force Institute of Technology research into ultra-high temperature ceramics (UHTCs) is to characterize their mechanical properties in extreme environments. The characterization of mechanical properties and performance at relevant service temperatures and environments is necessary to advance the use of UHTCs as a structural material in aerospace applications. During the course of developing the Experimental Facility and Test Method, an unanticipated facet of the importance of material selection came to light. Since test fixture materials were chosen for their high temperature structural integrity, it was assumed the high temperature stability extended to thermal compatibility with hafnium diboride (HfB_2). However, this proved to be incorrect--the thermal compatibility of test fixture material with the test material is a vital issue that must be addressed.

This research investigated, characterized, and mitigated previously unknown interactions between HfB_2 and other high temperature materials. As a result of this research, it is now known that 99.99% pure Pt foil is unstable in the presence of HfB_2 at 1500°C . Platinum foil was rendered unsuitable as an interlayer between HfB_2 and single crystal yttrium aluminum garnet (SX YAG), as it became molten and diffused into the grain boundaries of the HfB_2 . This has future implications for the joining of HfB_2 with other materials. Boria gas that is produced during the oxidation of HfB_2 degrades the surface of SX YAG, releasing AlBO_2 and YBO_2 gases. This has future implications for the use of HfB_2 -containing UHTCs as a structural or thermal protection material. High

temperature compatibility studies need to include boria gas as a variable. While either HfB_2 or HfO_2 might be stable with other materials, boria gas has been shown to be very active.

Penetration of HfB_2 by an external molten metal was studied during investigations into the wettability of HfB_2 for brazing purposes. For this work conducted at 1500 °C, Pt was found to completely infiltrate HfB_2 grain boundaries. The lack of Hf-B-Pt or Hf-O-Pt phase diagrams rendered it impossible to definitively report on the mechanisms behind the diffusion of Pt into HfB_2 . High purity Pt foil was proven insufficient to provide the layer of protection necessary to prevent a thermo-chemical interaction between HfB_2 and SX YAG. The original Test Method was altered to utilize high purity alumina as an interlayer.

A study of thermo-chemical compatibility of HfB_2 with SX YAG was carried out at 1500 °C in air. Yttrium- and Al- containing deposits were found on the surfaces of HfB_2 specimens heat treated while in contact with or in the vicinity of SX YAG. This indicated that SX YAG was not stable in the presence of HfB_2 at 1500°C in air. It is proposed that SX YAG reacts with B_2O_3 gas produced during oxidation of HfB_2 and is reduced into YAM, AlBO_2 (g) and YBO_2 (g). The gases were adsorbed onto the HfO_2 scale; thus, forming various Y- and Al- containing deposits. Surface properties of the HfO_2 scale determined the nature and composition of the surface deposits. The results of the current study demonstrate that SX YAG undergoes degradation in the presence of HfB_2 at elevated temperatures in an oxidizing environment. The degradation is initiated

by contact with the gaseous boria, which is released by oxidizing HfB_2 . Environmental stabilities of other high temperature materials with HfB_2 under oxidizing conditions must be investigated further.

These findings enabled the development and construction of a mechanical testing facility capable of reaching 1700°C in air. The Experimental Facility and Test Method permitted direct, accurate strain measurement, while minimizing thermo-chemical interaction with the test fixtures within the furnace environment. This pilot study on the creep characteristics of HfB_2 -based UHTCs revealed four interesting points. (1) The high temperature thermo-chemical stability of the test material with other high-temperature materials must be investigated. (2) Slight differences in microstructure can produce significant differences in oxidation. (3) Load has an effect on the oxidation performance, but it is unclear to what degree. (4) The creep mechanism for both monolithic HfB_2 and HfB_2 -20 vol% SiC was found to be grain boundary sliding accommodated by diffusion.

A follow-on effort to further investigate the interaction between HfB_2 and SX YAG should be conducted to better characterize the interaction mechanism. An attempt should be made to utilize the Air Force Institute of Technology's high temperature gas phase spectrography via hyperspectral imaging to conclusively determine what gases are released at higher temperatures. Follow-on efforts should include systematic compression creep tests of HfB_2 -containing specimens conducted in air and argon. Higher temperatures mechanical testing in an argon environment will determine the true mechanical properties of the test material. Higher temperatures and loads will provide a more complete picture of high temperature mechanical behavior under compression. The

results of mechanical testing in an oxidizing environment include the properties of the oxide scale. As the oxide scale grows, HfB_2 recesses; a progressively smaller cross-section remains to support the compressive load.

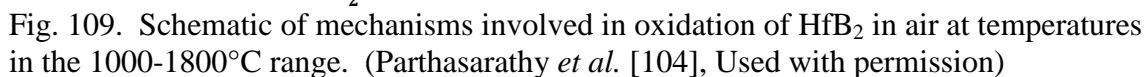
Sustained hypersonic flight is limited by materials due to high operating temperatures, high heat fluxes experienced by small areas/volumes of material, high thermal gradients, oxidation, and corrosion [8]. Advances in structural design for hypersonic missiles and flight vehicles have raised the demand for structural materials that have superior long-term mechanical and retained properties under high temperature, high pressure, and varying environmental factors [203]. UHTCs have the potential to allow hypersonic structural and propulsion components to move beyond single use applications.

Many of the limitations on performance, life and economic viability of current and future Air Force systems are determined by the temperature limitations of materials. High temperature mechanical testing in an operational (i.e., oxidizing) environment is necessary to advance the use of UHTCs as a structural material. This research represented a significant contribution towards understanding the materials and methods required to accomplish high temperature mechanical testing in an oxidizing environment. It is a great step forward in the understanding of the thermo-chemical compatibility of HfB_2 -based UHTCs with other high temperature materials. This understanding goes beyond that of the development of mechanical testing materials and methods. Future engineering designs incorporating HfB_2 -based UHTCs can be influenced with the

knowledge of what materials will be compatible at high temperatures. A thorough understanding of the material degradation and their implications for component life is vital to successful implementation of UHTCs in aerospace applications.

Appendix A
Oxidation Model Framework and Formulation
(Reprinted with permission)

The Parthasarathy *et al.* [104] mechanistic model for the oxidation of Zr, Hf, and Ti (all referred to as Me) assumes that dense MeO_2 is assumed acts as a barrier to oxygen permeation. The porosity between MeO_2 columns is assumed to be continuous. The ambient air is taken to consist of N_2 and O_2 only. A fraction, f , of the oxide scale is considered to be porous and provide a continuous pathway for gas diffusion and for the evaporation of liquid boria at the surface. The surface is assumed to be a perfect sink for boria (B_2O_3). At a given time, t , the oxide scale has a thickness L . The inner portion of the metal oxide scale is filled with liquid boria, forming layer 1 of thickness h . The distance $L-h$ represents the diffusion distance in a pore over which gaseous oxygen must diffuse to reach the boria. Figure 109 shows a schematic of mechanisms involved in oxidation of HfB_2 in air at temperatures in the 1000-1800°C range.



~ 156 ~

At the substrate-scale interface, Eqn. 6 takes place. At steady state the diffusional flux of oxygen must be balanced by the formation rates of MeO_2 and B_2O_3 . So,

$$|J_{O_2}| = \frac{5}{2} \dot{n}_{\text{MeO}_2} = \frac{5}{2} \dot{n}_{\text{B}_2\text{O}_3} \quad (6)$$

The flux of gaseous oxygen in the porous channel that is $L-h$ long is given by

$$|J_{O_2}| = f D_{O_2} \frac{C_{O_2}^a - C_{O_2}^i}{L - h} \quad (7)$$

where D is the diffusion coefficient, C the concentration, the superscript i refers to the interface between liquid and gaseous boria at a distance, h , from the substrate-scale interface, and the superscript a refers to the scale-ambient interface. The diffusion coefficient of gaseous oxygen through a porous region filled with gaseous O_2 , N_2 , and B_2O_3 is given by

$$D_{1,(2,\dots,i)} = \frac{1}{\sum_{i \neq 1}^{i \neq 1} (x_i / D_{1-i})}; \quad x_i = \frac{n_i}{\sum_{j \neq 1}^{j \neq 1} n_j} \quad (8)$$

where n is the mole fraction, subscript $1,(2, \dots, i)$ refers to the diffusivity of species 1 in a medium of species $(2, \dots, i)$, and subscript $(1-i)$ refers to the diffusivity of species 1 in a binary mixture of species 1 and i . The gas diffusion of species 1 in a binary gas mixture of species 1 and 2 is given by

$$D_{1-2} = \frac{0.0018583 T^{3/2} \sqrt{(1/M_1) + \left(\frac{1}{M_2}\right)}}{r_{12}^2 \Omega_D P} \text{ cm}^2/\text{s}; \quad (9)$$

$$\Omega_D = \frac{1.06036}{T^{*0.15610}} + \frac{0.193000}{\exp(0.47635T^*)} + \frac{1.03587}{\exp(1.52996T^*)} + \frac{1.76474}{\exp(3.89411T^*)} \quad (10)$$

where T is absolute temperature, M is the molecular weight (g/mol), P is pressure (atm), $T^* = (kT/\sqrt{(\epsilon_1 \epsilon_2)})$ (k is Boltzman's constant and ϵ is the maximum energy of attraction

between colliding molecules (ergs)) , and $r_{l2} = 0.5(r_1 + r_2)$ is a radius of the porous pathway in Å. But when the size of the pore is small, the mean free path is longer than the characteristic dimension of the system and the pore is unfilled (i.e., layer 2), the diffusion of gases is governed by Knudsen diffusion:

$$D_k = \frac{4}{3} \left(\frac{8RT}{\pi M} \right)^{1/2} \frac{r}{2} \quad (11)$$

where R is the universal gas constant, M is the molecular mass of the diffusing species and r is the radius of the porous pathway. So, the effective oxygen diffusivity is

$$D_{eff} = (D_{1-2}^{-1} + D_k^{-1}). \quad (12)$$

The flux of boria (v) from the surface of liquid boria to the ambient atmosphere is given by

$$J_{B_2O_3} = f D_{B_2O_3} \frac{C_{B_2O_3}^i - C_{B_2O_3}^a}{L - h} \quad (13)$$

Taking $J_{B_2O_3}$ to equal $n_{B_2O_3}$ (quasi-steady state), and combining Eqns. 6-13, the concentration of molecular oxygen at the boria liquid-vapor interface is

$$C_{O_2}^i = C_{O_2}^a - \frac{5}{2} \frac{D_{B_2O_3}}{D_{O_2}} (C_{B_2O_3}^i - C_{B_2O_3}^a). \quad (14)$$

The concentration of boria at the ambient surface is taken to be zero. The concentration of boria (v) at the liquid-vapor interface is provided by vapor pressure data

$$C_{B_2O_3}^i = \frac{P_{B_2O_3}}{RT}; P_{B_2O_3}(\text{atm}) = 3 \times 10^8 \exp\left(-\frac{45,686}{T}\right). \quad (15)$$

The permeability of oxygen through the liquid boria depends on the oxygen activity gradient across the liquid layer of thickness t . From the ideal gas law, the oxygen partial pressure at the boria liquid-vapor interface is given by

$$P_{O_2}^i = RT C_{O_2}^i. \quad (16)$$

Using thermodynamic data from literature and equating the activities of solid phases to unity, the oxygen activity at the MeB₂- B₂O₃ interface(s) is given by

$$P_{O_2}^s (\text{atm}) = 6 \times 10^9 \exp \left(-\frac{100,070}{T} \right). \quad (17)$$

The oxygen flux across the liquid boria is related to the partial pressure gradient through the oxygen permeability coefficient, Π , as follows:

$$|J_{O_2}(\text{B}_2\text{O}_3)| = \frac{\Pi_{O_2-B_2O_3}}{h} f [P_{O_2}^i - P_{O_2}^s]; \quad (18)$$

The oxygen permeability coefficient, $\Pi_{O_2-B_2O_3}$, is obtained from literature [204]:

$$\Pi_{O_2-B_2O_3} (\text{mol/m s atm}) = 0.15 \exp \left(-\frac{16,000}{T} \right). \quad (18a)$$

At steady state the diffusional flux of oxygen must be balanced by the formation rates of MeO₂ and B₂O₃. Substitute Eqn. 18a into Eqn. 18 and set the right-hand side of the resulting expression equal to the right-hand side of Eqn. 13, which describes the flux of oxygen through the gaseous layer. As a result an equation relating boria layer thickness, h , to the scale thickness, L is obtained:

$$h = qL; \quad (19)$$

$$q = \frac{\Pi_{O_2-B_2O_3} (P_{O_2}^i - P_{O_2}^s)}{D_{O_2} (C_{O_2}^a - C_{O_2}^i) + \Pi_{O_2-B_2O_3} (P_{O_2}^i - P_{O_2}^s)}. \quad (19a)$$

The equations for the rate of change of scale thickness L and mass of the scale W are given by accounting for the requisite balance for the diffusional flux of oxygen using Eqn. 6.

$$\frac{dL}{dt} = \frac{2}{5} \left(\frac{V_{MeO_2}}{\rho_{MeO_2}} \right) \left(\frac{f}{1-f} \right) D_{O_2} \frac{C_{O_2}^a - C_{O_2}^i}{L(1-q)} \quad \text{and} \quad (20)$$

$$\left(\frac{1}{\rho_{MeO_2}}\right) \frac{dW_{MeO_2}}{dt} = \frac{2}{5} J_{O_2} \frac{V_{MeO_2}}{\rho_{MeO_2}} \quad \Rightarrow \quad \frac{dW_{MeO_2}}{dt} = \frac{2}{5} J_{O_2} V_{MeO_2}. \quad (21)$$

where V is molar volume and ρ is density.

Integrating Eqn. 20 yields the parabolic equation for the growth of the oxide scale

$$L^2 = 2 \left[\frac{2}{5} \left(\frac{V_{MeO_2}}{\rho_{MeO_2}} \right) \left(\frac{f}{1-f} \right) D_{O_2} \frac{c_{O_2}^a - c_{O_2}^i}{(1-q)} \right] t \quad (22)$$

where t is time. The total weight change per unit area is given by

$$\frac{\Delta W}{A} = L \rho_{MeO_2} (1-f) + hf \rho_{BO_3} - R \rho_{MeB_2}. \quad (23)$$

where R is recession, defined as the loss of the original unreacted material. The magnitude of this recession is given by

$$R = L(1-f) \frac{V_{MeB_2} / \rho_{MeB_2}}{V_{MeO_2} / \rho_{MeO_2}} \quad (24)$$

The model was validated by comparing predictions with experimental results for oxidation of ZrB_2 from literature. Model predictions were generally in good agreement with experimental results. However, it was determined that the model is sensitive to the pore size (when the pore radius is less than 1 μm) and to the pore fraction. It is recognized that these quantities could vary depending on material processing conditions.

Parthasarathy *et al.* [110] expanded the previous model to account for oxidation kinetics of SiC-containing refractory diborides. As in the initial model, the refractory oxide in the oxide scale is assumed to be impermeable to oxygen. The presence of SiC results in formation of borosilicate glass (B_2O_3 - SiO_3) rather than boria glass. Hence, there is the added consideration of the formation and transport of gaseous CO and SiO

and of the evaporation of SiO and SiO₂ at the surface. Based on experimental results from published literature the model assumes the three-layer morphology of the oxidation scale: (1) a glassy borosilicate top layer, (2) a refractory metal-oxide skeleton filled with liquid borosilicate, and (3) a SiC-depleted layer [11,36,46,75,100,110]. Figure 110a is an SEM image of the microstructure of oxidation scale formed in a ZrB₂-SiC sample. A schematic of the oxidation products and morphology (for temperatures in the 1200-1727°C range) assumed in the model is shown in Fig. 110b.

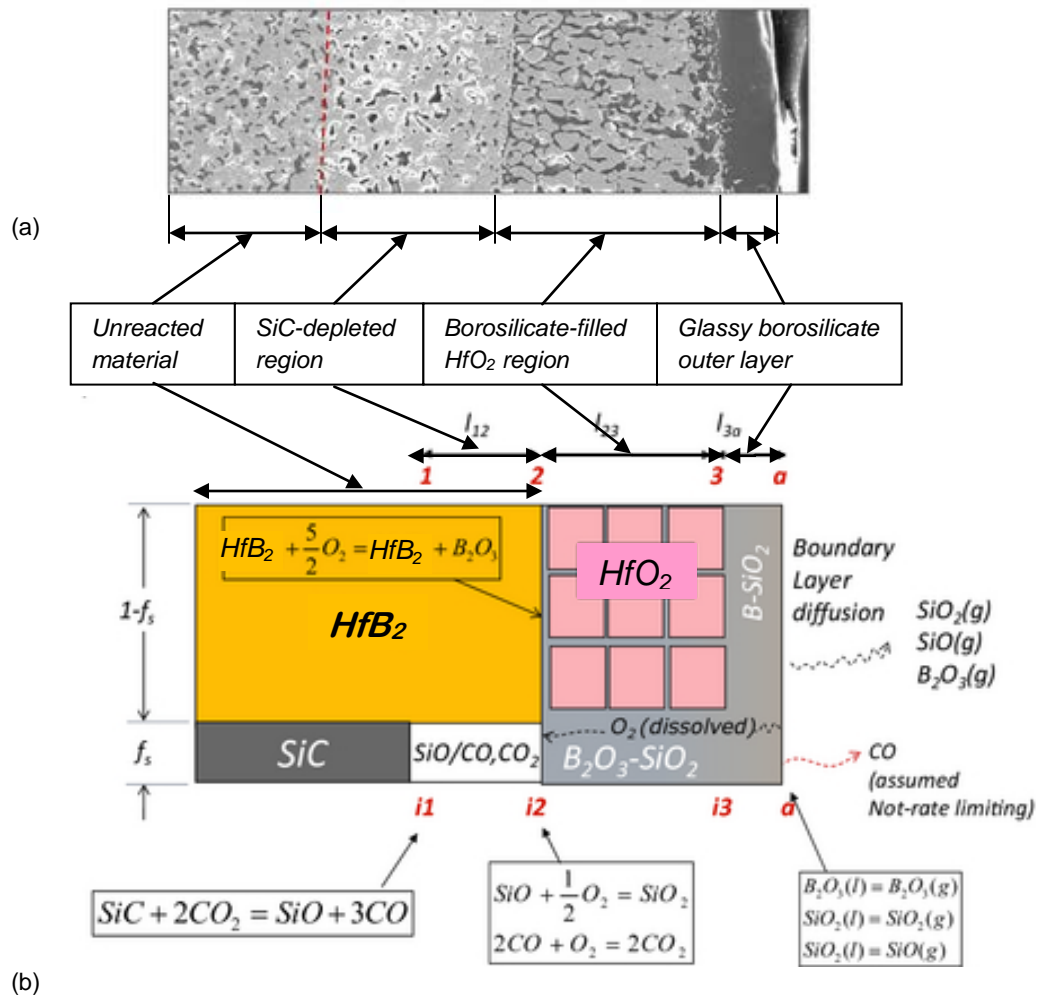


Fig. 110. (a) SEM image of the microstructure of oxidation scale formed in a HfB₂-SiC sample and (b) a schematic of the oxidation products and morphology assumed in the model . (Parthasarathy *et al.* [110], Reprinted with permission.)

The augmented encompasses counter-current gas diffusion in the internal SiC-depleted zone, oxygen permeation through borosilicate glass channels in the oxide scale, and boundary layer evaporation on the surface. Oxidation is dependent on boria and SiO₂ activity and the flow of oxygen through the various layers.

In the original model the morphology of the refractory metal oxide layer was represented by continuous channels. In contrast, the augmented model represents the morphology of the oxide layer as disconnected refractory metal oxide grains surrounded by liquid borosilicate. Molecular oxygen from the atmosphere dissolves into the borosilicate as molecular O₂, diffuses across the external glassy phase, and permeates through the liquid borosilicate to react with the diboride. A portion of this oxygen, assumed to be proportional to the fraction of SiC, f_s , is transported to the SiC-depleted region through a medium of a CO and CO₂ gas mixture within the SiC-depleted region to oxidize SiC. The gaseous CO reaction product is assumed to diffuse through the glassy scale and is assumed not to be rate limiting.

Boria activity, $a_{B_2O_3-i2}$, is taken to be directly proportional to molar ratio and is modeled at the MeB₂-MeO₂ interface ($i2$) as

$$a_{B_2O_3-i2} = \frac{\frac{(1-f_s)}{V_{MeB_2}} \left(\frac{dR_{MeB_2}}{dt} \right)}{\frac{(1-f_s)}{V_{MeB_2}} \left(\frac{dR_{MeB_2}}{dt} \right) + \frac{f_s}{V_{SiC}} \left(\frac{dR_{SiC}}{dt} \right)}; \quad (25)$$

The SiO₂ activity, a_{SiO_2-i2} , is modeled as

$$a_{SiO_2-i2} = 1 - a_{B_2O_3-i2} \quad (26)$$

Here f_s is the volume fraction of SiC and dR/dt is the recession rate. Relating this boria activity and the oxygen partial pressure at the $i2$ interface, the equilibrium constant for the oxidation of the metal diboride is

$$K_{Me} = \frac{a_{MeO_2} a_{B_2O_3-i2}}{a_{MeB_2} (P_{O_2-i2})^{5/2}} \quad (27)$$

The thickness of the SiC-depleted layer, l_{i2} , corresponds to the level of material damage caused by oxidation [11,76,110]. This is the amount of recession. The oxidation of the SiC-depleted region proceeds by the diffusion of CO, CO₂, and SiO gases and the transport of Si, as described by the chemical reactions shown in Fig. 109b. The applicable equilibrium constants are as follows

$$\begin{aligned} K_{CO_2} &= \frac{(P_{CO_2-i2})^2}{(P_{CO-i2})^2 P_{O_2-i2}} \\ K_{SiO} &= \frac{a_{SiO_2-i2}}{P_{SiO-i2} (P_{O_2-i2})^{1/2}}; \\ K_{CO_2} &= \frac{P_{SiO-i1} (P_{CO-i1})^3}{P_{SiC} (P_{CO_2-i1})^2}. \end{aligned} \quad (28)$$

The fluxes of the various gaseous species within the SiC-depleted zone must be consistent with the equilibrium constants of Eqns. 28. Furthermore, the oxidation rate is limited by incoming oxygen flux at $i2$, J_{O_2-i2} , times the area fraction, f_s , of SiC at the $i2$ interface. The following equations represent the fluxes of the various gaseous species within the SiC-depleted zone in moles per unit area per unit time:

$$|J_{CO_2-i2}| = f_s \frac{D_{CO_2-i2}}{RT} 10^5 \frac{P_{CO_2-i2} - P_{CO_2-i1}}{l_{i2}};$$

$$|J_{CO-12}| = f_s \frac{D_{CO-12}}{RT} 10^5 \frac{P_{CO_2-i1} - P_{CO_2-i2}}{l_{12}} = \frac{3}{2} |J_{CO_2-21}|; \quad (29)$$

$$|J_{SiO-12}| = \frac{2}{3} f_s |J_{O_2-32}| = \frac{1}{2} |J_{CO_2-21}|.$$

The partial pressures of CO, CO₂, and SiO at the *i1* and *i2* interfaces, with *l₁₂* being the distance between these two interfaces, can be obtained by solving Eqns. 28 and 29 as:

$$P_{O_2-i2} = \left(\frac{a_{MeO_2} a_{B_2O_3-i2}}{a_{MeB_2} K_{Me}} \right)^{2/5};$$

$$P_{SiO-i2} = \frac{a_{SiO_2-i2}}{K_{SiO} \sqrt{P_{O_2-i2}}};$$

$$P_{SiO-i1} = \frac{2RT |J_{O_2-32}| l_{12}}{3 \times 10^5 D_{SiO-i2}} + P_{SiO-i2};$$

$$\begin{aligned} P_{CO-i1} \left(D_{CO-12} D_{CO_2-12} \sqrt{K_{CO_2} P_{O_2-i2}} \right) - (P_{CO-i1})^{3/2} D_{CO-12} D_{CO_2-12} \sqrt{\frac{K_{CO_2} P_{SiO-i1}}{K_{SiC}}} \\ - 2 D_{CO-12} D_{SiO-12} P_{SiO-i1} - 3 D_{CO_2-12} D_{SiO-12} \sqrt{K_{CO_2} P_{O_2-i2} P_{SiO-i1}} \\ + 2 D_{CO-12} D_{SiO-12} P_{SiO-i2} + 3 D_{CO_2-12} D_{SiO-12} \sqrt{K_{CO_2} P_{O_2-i2} P_{SiO-i2}} = 0; \\ \Rightarrow P_{CO_2-i1} = \frac{(P_{CO-i1})^{3/2} \sqrt{P_{SiO-i1}}}{\sqrt{K_{SiC}}}; \end{aligned} \quad (30)$$

$$P_{CO-i2} = \frac{D_{CO-12} P_{CO-i1} - 3 D_{SiO-12} P_{SiO-i1} + 3 D_{SiO-12} P_{SiO-i2}}{D_{CO-12}};$$

$$P_{CO_2-i2} = P_{CO-i2} \sqrt{K_{CO_2} P_{O_2-i2}};$$

The equations that govern the oxygen flux in the metal oxide/borosilicate region (region between interfaces *i2* and *i3* in Fig. 109b) are given below:

$$|J_{O_2-32}| = \Pi_{O_2-B_2O_3-SiO_2} \frac{P_{O_2-i3} - P_{O_2-i2}}{l_{23}} f_g$$

$$|J_{O_2-a3}| = \Pi_{O_2-B_2O_3-SiO_2(3a)} \frac{P_{O_2-a} - P_{O_2-i3}}{l_{3a}}. \quad (31)$$

Here f_g is the fraction of borosilicate glass. Since $|J_{O_2-32}| = |J_{O_2-a3}|$

$$P_{O_2} = \frac{\Pi_{O_2-B_2O_3-SiO_2(3a)} P_{O_2-a} + f_g l_{3a} \Pi_{O_2-B_2O_3-SiO_2} P_{O_2-i2}}{l_{23} \Pi_{O_2-B_2O_3-SiO_2(3a)} + f_g l_{3a} \Pi_{O_2-B_2O_3-SiO_2}}. \quad (32)$$

The depths of the three layers are determined through recursive numerical analysis. They evolve from an initially small number using rate equations. The SiC-depleted layer length, l_{12} , is given by the difference in recession between MeB₂ and SiC. The rate of change l_{23} is given by the number of moles of MeO₂ formed per unit area per unit time multiplied by the molar volume of MeO₂. The rate of formation of MeO₂ is given by the total flux of oxygen in through region 3-2 less than that used for oxidizing SiO (g) to SiO₂ and CO (g) to CO₂. Thus, the rate of growth of the metal oxide/borosilicate glass and the depth of the SiC-depleted layers are

$$\frac{dl_{23}}{dt} = V_{MeO_2} \left(|J_{O_2-32}| - \frac{3}{2} |J_{SiO-12}| \right) \frac{2}{5} \frac{1}{f_{MeO_2}}. \quad (33)$$

$$\frac{dR_{MeB_2}}{dt} = \frac{dl_{23}}{dt} \frac{V_{MeB_2} f_{MeO_2}}{V_{MeO_2} (1 - f_s)} \quad \text{and}$$

$$\frac{dR_{SiC}}{dt} = |J_{SiO-12}| \frac{V_{SiC}}{f_s} \quad (34)$$

$$l_{12} = R_{SiC} - R_{MeB_2} \quad (35)$$

The rate of growth of the external glassy layer is given by the rate of production of boria and silica less the rate of loss of evaporation at the surface and the amount occupied by borosilicate in the metal-oxide layer:

$$\begin{aligned} \frac{dl_{3a}}{dt} = & \left(\frac{dl_{23}}{dt} \frac{f_{MeO_2}}{V_{MeO_2}} - |J_{O_2-32}| \right) V_{B_2O_3} + (|J_{SiO-12}| \\ & - |J_{SiO_2-vap}| - |J_{SiO-vap}|) V_{SiO_2} - \frac{dl_{23}}{dt} f_g \end{aligned} \quad (36)$$

$$|J_{species-vap}| = \frac{D_{species}}{RT} 10^5 \frac{P_{species-vap}}{\delta_{bdry}} \quad (37)$$

$$\delta_{bdry} = \frac{3}{2} \sqrt{\frac{l_{specimen}}{v_{fluid}}} \left[\frac{\eta_{fluid}}{\rho_{fluid}} \right]^{1/6} (D_{species})^{1/3} \quad (38)$$

The subscript *vap* refers to evaporation, $l_{specimen}$ is the width of the specimen, η is the viscosity of the ambient fluid, v is the velocity of the ambient fluid, and δ is thickness of the boundary layer-dependent evaporation of species.

The model presented above can predict the thickness of the oxide scale, L , the recession of unreacted material, R , and the weight gain of the sample, W , as described by Eqns 39, 40, and 41, respectively.

$$L = l_{12} + l_{23} + l_{3a} \quad (39)$$

$$R = l_{12} \quad (40)$$

$$W = l_{23}(f_{MeO_2}\rho_{MeO_2} + f_g\rho_g) + l_{3a}\rho_g - R_{SiC}f_s\rho_{SiC} - R_{MeB_2}(1 - f_s)\rho_{MeB_2} \quad (41)$$

The predictions of the augmented model were compared with laboratory-furnace-based experimental data from literature. The predictions of scale thicknesses, depletion layer thicknesses, and weight gain were in good agreement with experimental data. In the present research, oxidation occurred under applied load. Comparison of the model predictions with the results of current research showed whether the model can adequately predict the process of stressed oxidation of HfB_2 -SiC samples.

Appendix B

Creep in Ceramics

As we consider the very limited experimental results pertaining to creep of the UHTCs, it is instructive to review creep and its mechanisms in ceramic materials. Creep can be defined as the continuing deformation of a material under constant stress [205]. A typical creep strain vs time curve is shown schematically in Fig. 111. The creep curve can be divided into three regions – primary, secondary, and tertiary. Primary creep (often referred to as transient creep) is characterized by decreasing creep strain rate. Primary creep is generally associated with changes in microstructure (such as grain size, dislocation density) or with the redistribution of stresses. During this time the material will undergo initial rapid elastic elongation or compression. Secondary creep (also referred to as steady-state creep) is characterized by a constant creep strain rate that is generally lower than that of primary creep. In this regime, creep is generally due to deformation of an invariant microstructure. Tertiary creep is characterized by an increasing creep rate. This creep regime is associated with failure initiation, namely formation of voids or cracks. Tertiary creep in ceramics is typically very short or can be non-existent [183].

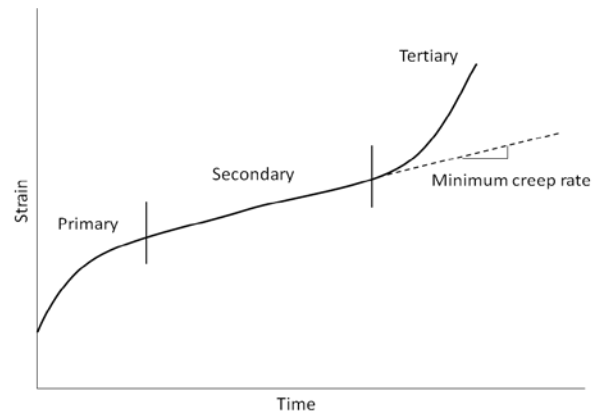


Fig. 111. Typical creep strain vs. time curve

In order to control creep in ceramics, it is necessary to identify the mechanisms behind this process. Because the largest amount of creep strain is typically accumulated during the steady-state creep regime, the emphasis is on the mechanisms behind the steady-state creep. At elevated temperature, steady-state creep in fine polycrystalline solids can involve dislocation mechanisms (dislocation creep) as well as diffusional mechanisms (diffusional creep).

Dislocations are line defects in a crystal. Dislocations can move through a crystal lattice by dislocation glide or by dislocation climb. Dislocation glide represents a movement of a dislocation along a single (slip) plane, during which atoms are displaced from one regular lattice site to an equivalent site. Dislocation climb occurs when the atoms along parts of the dislocation line exchange places with the nearby vacancies. Because dislocation climb requires diffusion of vacancies, it is more likely to occur at elevated temperature. Diffusion-controlled climb allows dislocations to avoid obstacles that impede their glide. Dislocation climb combined with dislocation glide gives rise to dislocation creep. The creep rate may be controlled by either dislocation climb or dislocation glide, although dislocation climb typically dominates.

Diffusion creep is caused by the stress-induced diffusion of vacancies through the microstructure of the material. When material is subjected to a greater degree of compression in one direction relative to another, vacancies migrate in the direction of compression. This results in a transport of matter from the direction of maximum compression to the direction of maximum tension, causing permanent strain in the material. Diffusion creep by transport of matter through the grains, or lattice diffusion, is called Nabarro-Herring creep. Diffusion creep by transport of matter along the grain boundaries is called Coble creep. For both Nabarro-Herring and Coble creep mechanisms, it is assumed that the grain boundaries act as perfect sources or sinks for vacancies. (Note that this was experimentally determined by Talmy *et al.* [17] for ZrB_2 – 0-25 vol% SiC and Hu Ping [186] for ZrB_2 – 30 vol% SiC.) However, these processes may also be controlled by a reaction at the interface, resulting in an interface (boundary) reaction-controlled diffusional creep.

In addition to dislocation mechanisms and diffusion mechanisms, creep in polycrystalline solids can involve grain boundary sliding. Glassy-phase forming additives are frequently used to promote densification of ceramics. Therefore, many ceramic materials contain a glassy phase in the grain boundaries. At elevated temperature, the glassy phase softens and permits creep to proceed by grain boundary sliding. Notably, the creep rate is controlled by the viscosity of the glassy phase and not by the sliding process.

The aforementioned creep mechanisms can be mathematically described by the same equation:

$$\dot{\epsilon} = \frac{AD\mu b}{kT} \left(\frac{b}{d}\right)^m \left(\frac{\sigma}{\mu}\right)^n \quad (42)$$

where $\dot{\epsilon}$ is the steady-state creep rate, A is a dimensionless constant, D is the diffusion coefficient or diffusivity, μ is the shear modulus, b is the Burgers vector, d is the grain size, k is the Boltzmann constant, T is the absolute temperature, σ is the applied stress, m is the grain size exponent and n is the stress exponent. The diffusion coefficient, D, can be expressed as:

$$D = D_0 \exp\left(\frac{-Q}{RT}\right) \quad (43)$$

where D_0 is a frequency factor, Q is the creep activation energy, and R is the universal gas constant.

The predominant creep mechanisms can be identified by analyzing creep data and determining values of the grain size exponent, m, and of the stress exponent, n. For example, the analysis of the dislocation climb-controlled creep yields of n between 4 and 5 [183]. The dislocation glide-controlled creep process is also described with equation (1), but with n = 3. Notably, the value n=1 was established for Nabarro-Herring creep. In this case the dependence between stress and creep rate is linear. The predominant creep mechanisms in fine polycrystalline ceramics and the corresponding values of the grain size exponent, m, and of the stress exponent, n, are summarized in Table 12.

Table 12. Creep Mechanism Exponents [17,183,185].

Creep Mechanism	m	n	Diffusion Path
<i>Dislocation creep mechanisms</i>			
Dislocation glide climb, climb controlled	0	4-5	Lattice
Dislocation glide climb, glide controlled	0	3	Lattice
Dissolution of dislocation loops	0	4	Lattice
Dislocation climb without glide	0	3	Lattice
Dislocation climb by pipe diffusion	0	5	Dislocation core
<i>Diffusional creep mechanisms</i>			
Vacancy flow through grains	2	1	Lattice
Vacancy flow along boundaries	3	1	Grain boundary
Interface reaction control	1	2	Lattice/grain boundary
<i>Grain boundary sliding mechanisms</i>			
Sliding with liquid	3	1	Liquid
Sliding without liquid (diffusion control)	2-3	2	Lattice/grain boundary

[183] D. J. Greene, An Introduction to the Mechanical Properties of Ceramics. Cambridge University Press 1998. Reprinted with permission.

The analysis of Nabarro-Herring creep yields the grain size exponent $m = 2$, while the analysis of Coble creep yields $m = 3$. Because of the inverse cubic dependence of creep rate on grain size, Coble creep will dominate over Nabarro-Herring creep in the case of very small grain sizes [205]. Moreover, the activation energy for grain-boundary diffusion creep is smaller than that required for lattice diffusion. Hence at lower temperatures, Coble creep typically dominates over Nabarro-Herring creep [183].

As mentioned earlier, in the classical treatment of both Coble creep and Nabarro-Herring creep, grain boundaries are assumed to be perfect sources or sinks for vacancies. This approach, which treats a diffusional flow in a polycrystal as a continuum problem, is useful in explaining many experimental observations. However, when the sources and

sinks become small, the diffusional processes may be controlled by a reaction at the interface, leading to an interface reaction-controlled diffusional creep mechanism. In this case the lattice diffusion or the grain boundary diffusion is so rapid that creation and annihilation of point defects at grain boundaries becomes the controlling process [183].

Appendix C

Specimen Appearance after Compression Creep Testing at 1500°C in Air

Images are a mixture of photographs and optical micrographs of the HfB₂-containing compression creep test specimens. The front of the specimen is the face in contact with the extensometer rods. The left and right faces of the specimens are oriented from the perspective of looking at the front of the specimen.

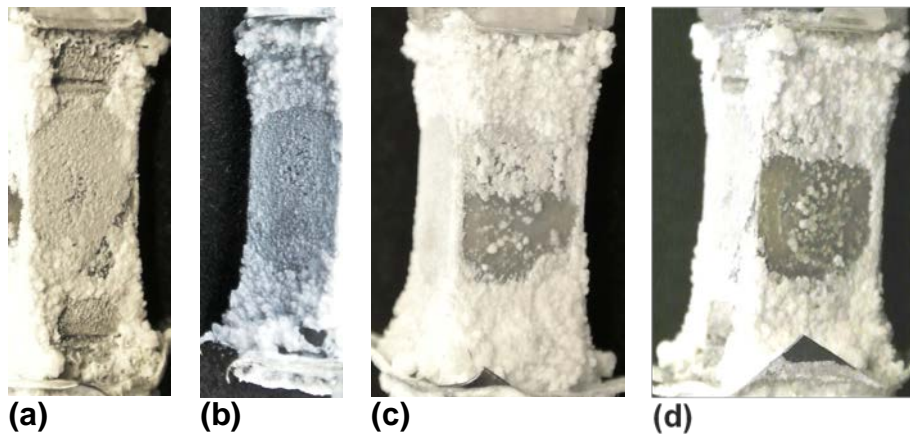


Fig. 112. **HfB₂-1a**: Temp ramp for 0.95 hrs, then at 1500°C for 14.9 hours (0.86 hrs thermal soak, 14.1 hrs under 25 MPa load). (a) Front (b) Back (c) Left (d) Right

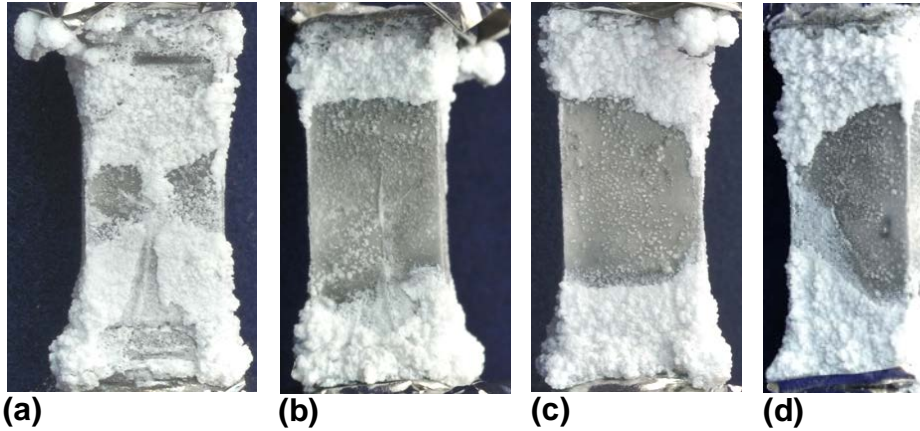


Fig. 113. **HfB₂-3a** Temp ramp for 1.2 hrs, then at 1500°C for 7.3 hours (1.0 hrs thermal soak, 5.1 hrs under 25 MPa load, followed by 1.1 hrs under 50 MPa load). (a) Front (b) Back (c) Left (d) Right

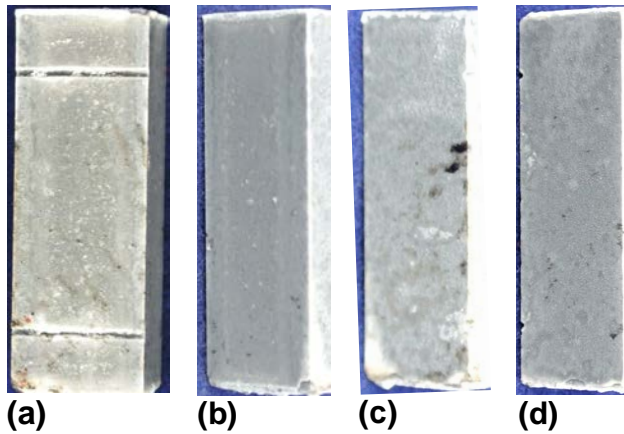


Fig. 114. **HfB₂-4a** First Run: Temp ramp for 0.89 hrs, then at 1500°C for 7.12 hours (0.95 hrs thermal soak, 3.50 hrs under 50 MPa load, followed by 2.31 hrs under 75 MPa load) (a) Front (b) Back (c) Left (d) Right. Second Run: Specimen shattered.

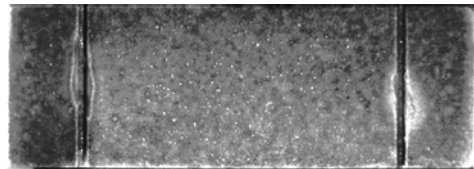


Fig. 115. **HfB₂-5a**. First Run. Temp ramp for 0.98 hrs, then at 1500°C for 4.1 hours (1.0 hrs thermal soak, 3.0 hrs under 100 MPa load. Front

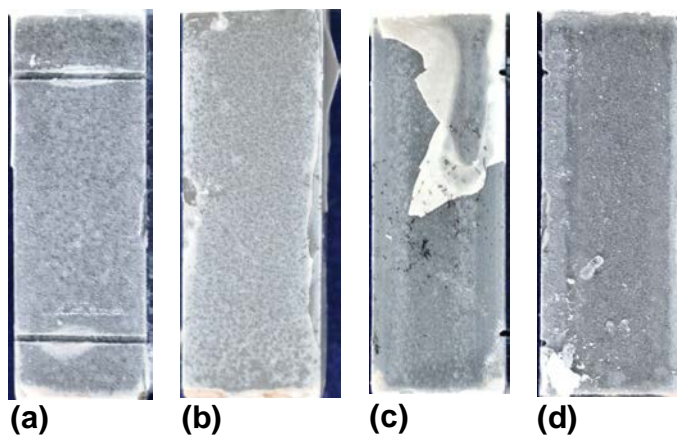


Fig. 116. **HfB₂-5a**: Second Run: Temp ramp for 0.99 hrs, then at 1500°C for 2.41 hours (1.0 hrs thermal soak, 1.3 hrs under 125 MPa load). (a) Front (b) Back (c) Left (d) Right

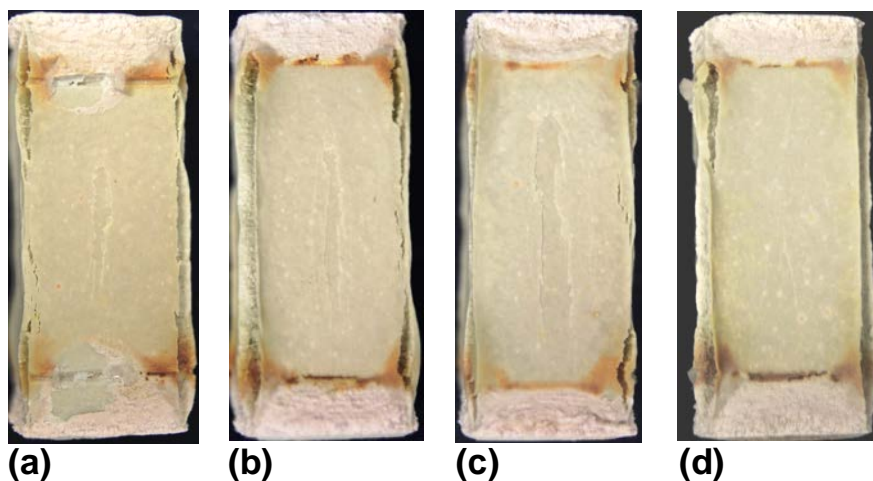


Fig. 117. **HfB₂-1c**: Temp ramp for 1.04 hrs, then at 1500°C for 17.0 hours (0.99 hrs thermal soak, 16 hrs under 25 MPa load). (a) Front (b) Back (c) Left (d) Right

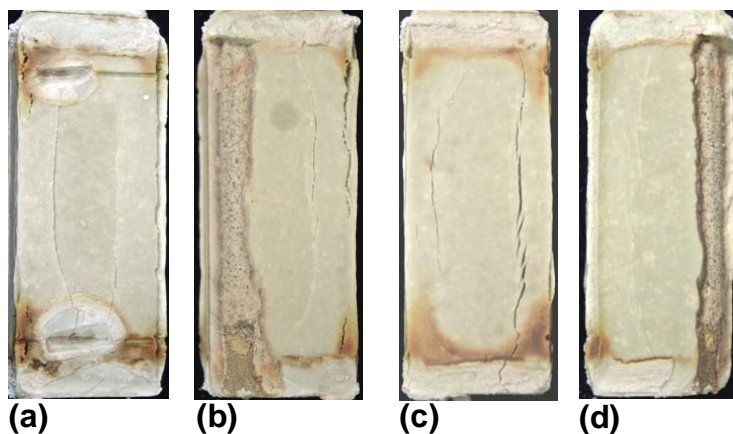


Fig. 118. **HfB₂-2c**: Temp ramp for 1.02 hrs, then at 1500°C for 7.86 hours (0.98 hrs thermal soak, 6.86 hrs under 50 MPa load). (a) Front (b) Back (c) Left (d) Right

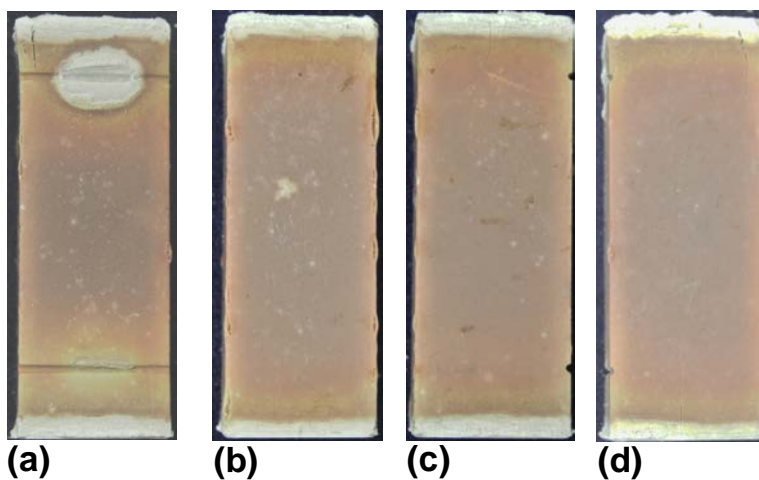


Fig. 119. **HfB₂-3c**: Temp ramp for 0.96 hrs, then at 1500°C for 9.20 hours (0.96 hrs thermal soak, 8.24 hrs under 75 MPa load). (a) Front (b) Back (c) Left (d) Right

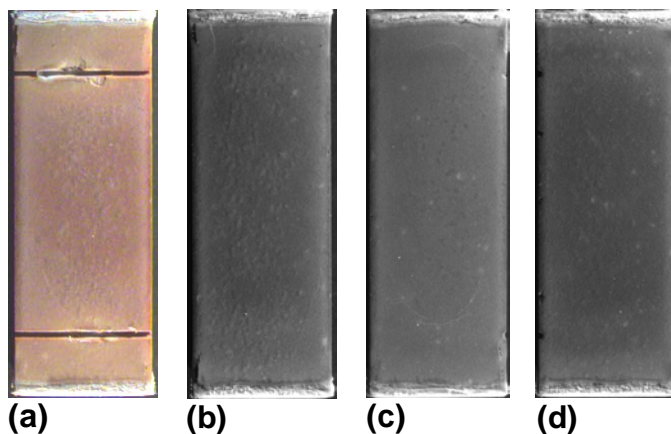


Fig. 120. **HfB₂-4c**: First Run: Temp ramp for .74 hrs, then at 1500°C for 1.31 hours (0.74 hrs thermal soak, 0.57 hrs under 75 MPa load). Second Run: Temp ramp for 1.27 hrs, then at 1500°C for 3.43 hours (0.6 hrs thermal soak, 2.83 hrs under 75 MPa load). (a) Front (b) Back (c) Left (d) Right

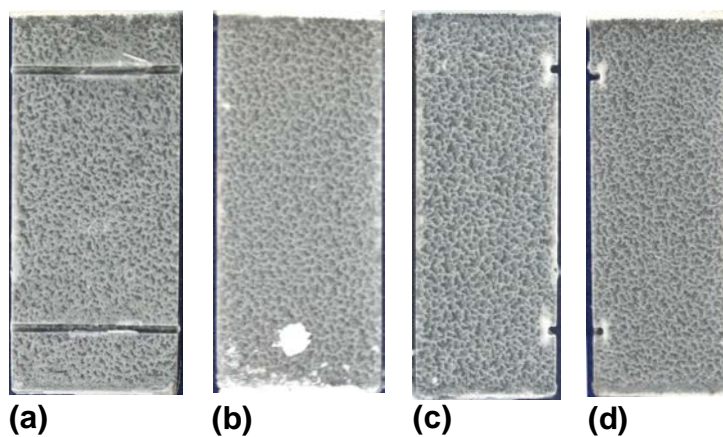


Fig. 121. **HfB₂-10SiC-1**: Temp ramp for 1.18 hrs, then at 1500°C for 7.26 hours (1.04 hrs thermal soak, 5.10 hrs under 25 MPa load, 1.11 hrs under 50 MPa load, followed by 2.11 hrs under 75 MPa load). (a) Front (b) Back (c) Left (d) Right

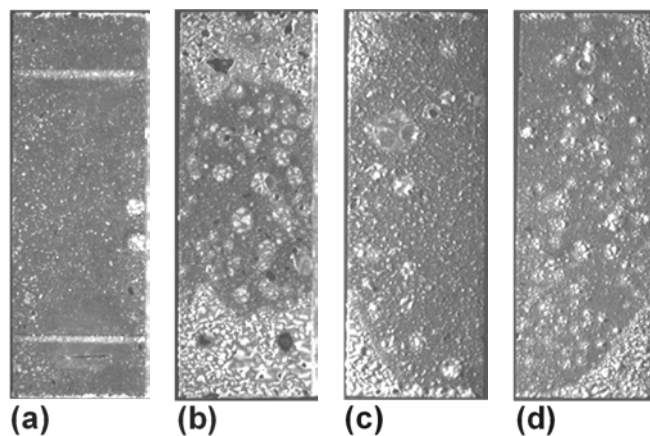


Fig. 122. **HfB₂-20SiC-1a**: Temp ramp for 0.98 hrs, then at 1500°C for 12.2 hours (1.00 hrs thermal soak, 5.05 hrs under 25 MPa load, 4.15 hrs under 50 MPa load, followed by 1.00 hrs under 75 MPa load). (a) Front (b) Back (c) Left (d) Right

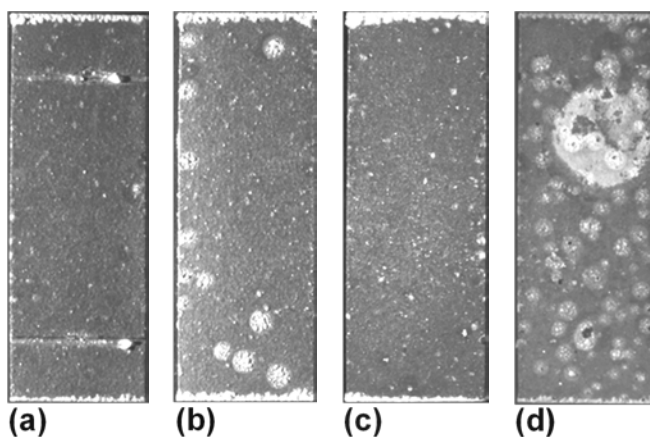


Fig. 123. **HfB₂-20SiC-2a**: Temp ramp for 1.00 hrs, then at 1500°C for 16.0 hours (1.00 hrs thermal soak, 15.0 hrs under 25 MPa load): (a) Front (b) Back (c) Left (d) Right

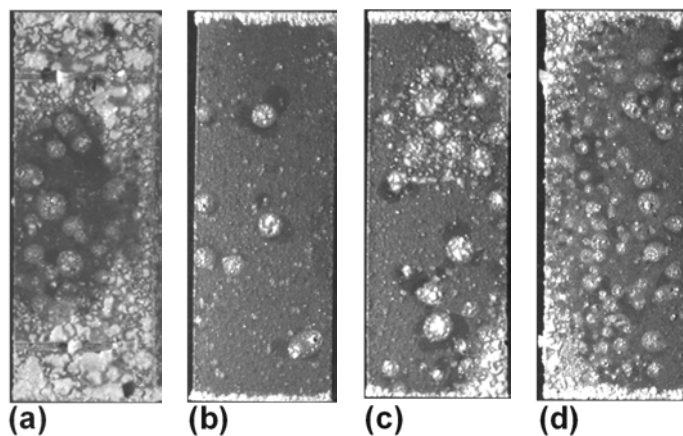


Fig. 124. **HfB₂-20SiC-3a**. Temp ramp for 1.04 hrs, then at 1500°C for 16.0 hours (1.00 hrs thermal soak, 15.0 hrs under 25 MPa load). (a) Front (b) Back (c) Left (d) Right

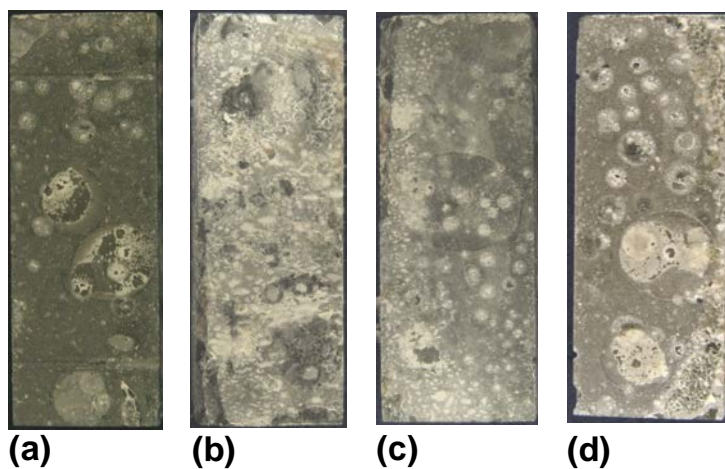


Fig. 125. **HfB₂-20SiC-5a**: Temp ramp for 0.85 hrs, then at 1500°C for 4.26 hours (1.05 hrs thermal soak, 3.16 hrs under 100 MPa load). (a) Front (b) Back (c) Left (d) Right

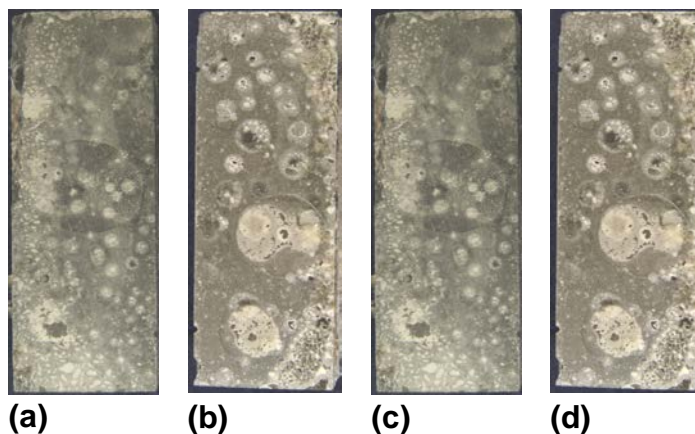


Fig. 126. **HfB₂-20SiC-6a**: Temp ramp for 0.97 hrs, then at 1500°C for 18.2 hours (1.00 hrs thermal soak, 17.2 hrs under 50 MPa load). (a) Front (b) Back (c) Left (d) Right

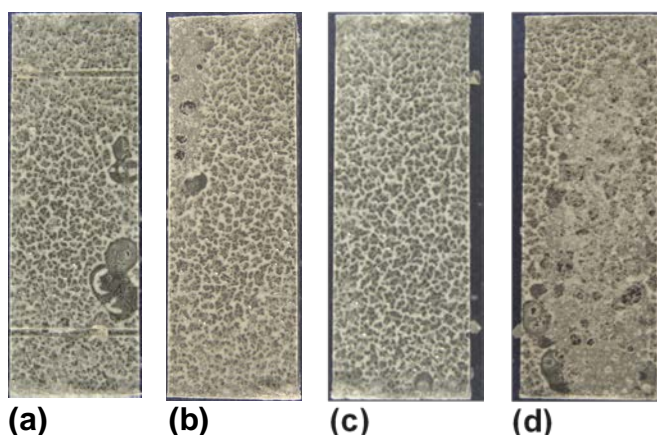


Fig. 127. **HfB₂-20SiC-1c**: Temp ramp for 1.28 hrs, then at 1500°C for 16.0 hours (0.89 hrs thermal soak, 15.1 hrs under 25 MPa load). (a) Front (b) Back (c) Left (d) Right

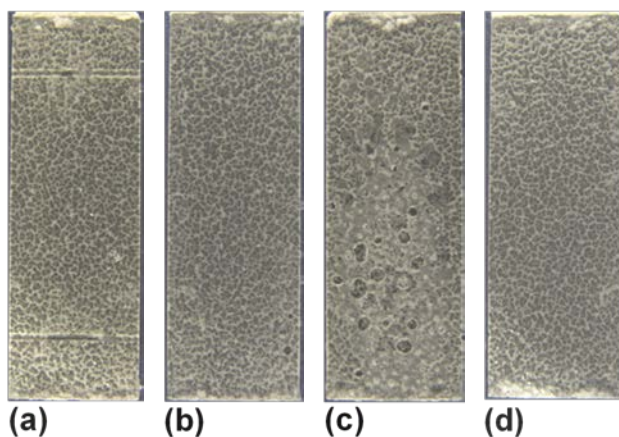


Fig. 128. **HfB₂-20SiC-2c**: Temp ramp for 1.28 hrs, then at 1500°C for 9.55 hours (0.75 hrs thermal soak, 8.80 hrs under 50 MPa load). (a) Front (b) Back (c) Left (d) Right

Appendix D

Compression Creep Tests at 1500°C

To validate the test facility and methods described in Section 3.3 and 3.4, a series of pilot compression creep experiments of HfB₂-containing parallelepiped specimens were performed at 1500°C in laboratory air. Initial testing consisted of step-wise creep tests. These tests were conducted to provide an initial estimate of the loads that HfB₂-containing UHTCs would experience measureable strain. At 1500 °C in laboratory air, these specimens can undergo creep at compressive loads as low as 25 MPa.

Subsequently, single load tests were conducted to remove history as a factor. In an attempt to accurately gauge the effect of history, tests were conducted at similar compressive loads. Unfortunately, there is too much variability in the data to make a definitive assessment. Additional single load tests of the HfB₂-20 vol% SiC were conducted in order to determine if the SiC conglomerates mentioned in Section 3.2.2 had an impact on creep performance.

The step-wise monolithic creep curves are shown in Fig. 129. In general, the curves follow the expected pattern - increased load increases the creep strain. The exceptions were the 125 MPa load test, which was a 2nd step, and the 75 MPa load tests, which encompassed both a first and second run.

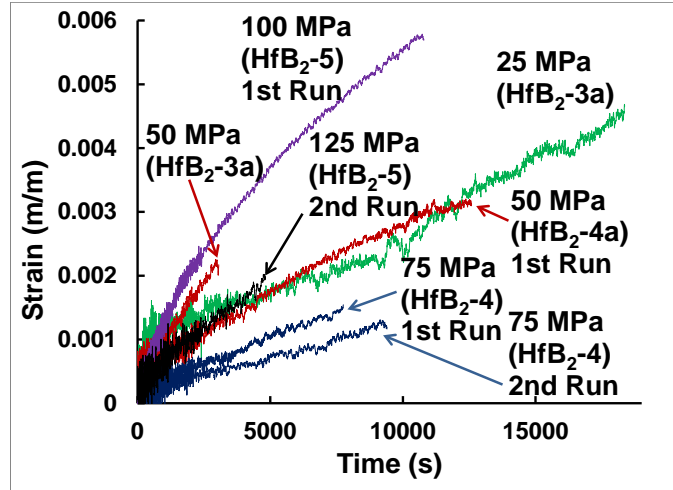


Fig. 129. Strain curves of step-wise creep tests of various HfB₂ specimens.

The single load strain curves from HfB₂-a and HfB₂-b are plotted Fig. 130. As expected, an increase in compressive load increases the amount of creep strain. As seen before, the 75 MPa compressive load tests are anomalous.

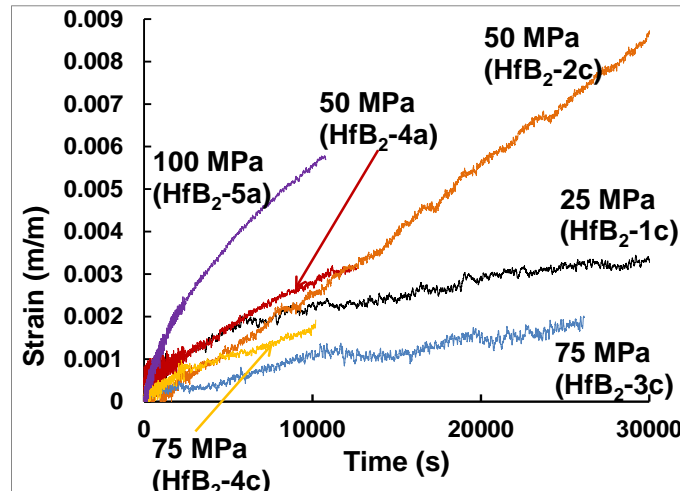


Fig. 130. Strain curves of single load creep tests of various HfB₂ specimens.

The creep strain for the 75 MPa compressive creep tests had surprising low creep strain that did not meet the expectation that an increased load would increase creep strain as seen in Fig. 129. The 75 MPa compressive creep curves were lower than that of 25

MPa. Figure 131 shows the creep curves for 75 MPa compressive tests to include the tests that were run on previously tested specimens. There is no current explanation on why the 75 MPa compressive creep curves are an aberration.

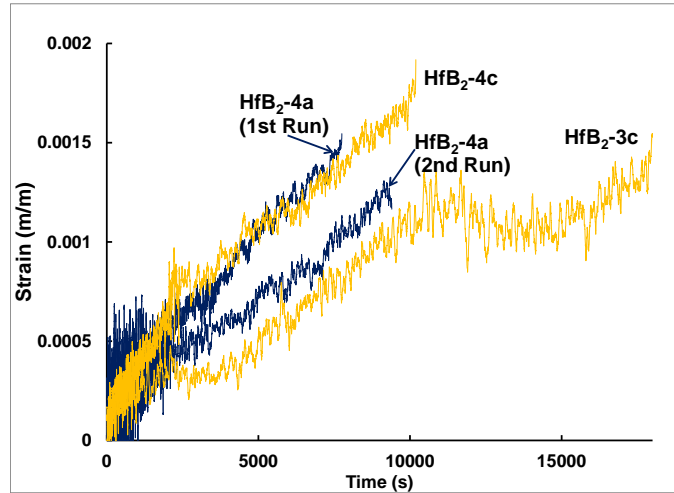


Fig. 131. 75 MPa compressive creep curves of various HfB₂ specimens.

While SiC alone is extremely creep resistant, as an additive it enhances creep of the dominant material. The creep curves in Fig. 132 in general follow that expected trend in that the primary creep strain and rate is greater for the HfB₂ specimens containing SiC as compared to monolithic HfB₂. It is also specifically supported by the 100 MPa load tests on HfB₂ and HfB₂-20SiC-5a, the result of which is that the HfB₂-20vol% SiC specimen had a greater initial strain than monolithic HfB₂.

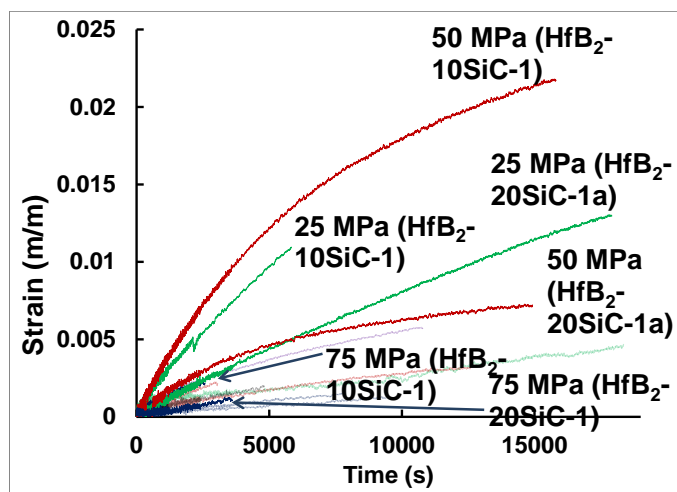


Fig. 132. Strain curves of step-wise creep tests of various HfB₂-SiC specimens.

Similar to the monolithic HfB₂ step-wise creep tests, the 75 MPa creep tests were an anomaly. They had lower creep curves than those tests with lower compressive loads. Also unexpectedly, Fig. 132 reveals that increasing amounts of SiC content does not always increase the primary creep strain and rate -- the HfB₂-20 vol% SiC had lower strain than HfB₂-10 vol% SiC at all step-wise loads. For example, at 45 minutes into the 50 MPa compressive creep test the HfB₂-10 vol% SiC specimen had a creep strain of - .0075 m/m vice -.0035 m/m for HfB₂-20 vol% SiC. There are two possible explanations. The more likely is based on the fact that the HfB₂-20 vol% SiC specimens had large conglomerates of SiC (and areas of larger HfB₂ grains (Fig. 7)) that increased the creep resistance of the HfB₂-20vol% SiC specimens. In addition, previous work showed that large SiC crystallite size increased the creep resistance of SiC fibers [206]. The less likely explanation is based on a previous study of the creep of liquid phase sintered SiC at temperatures above 1575°C in argon under stresses from 90 to 500 MPa [207]. The liquid phase SiC had creep rates that ranged from 3×10^{-8} to 10^{-6} /s. Another study found that SiC in air at 1650°C at 140 MPa had a creep rate of 9.15×10^{-9} /s [208]. A study of

sintered SiC had a creep rate of $9.15 \times 10^{-9}/\text{s}$ at 1943°C and 414 MPa and $2.75 \times 10^{-8}/\text{s}$ at 2293°C and 69 MPa [209]. It is possible that 20 vol% SiC possesses enough SiC to form a liquid phase that is capable of overcoming the effect of smaller HfB₂ grain sizes. But, the increased creep resistance is probably due more to the large size of the conglomerates than the nature of the SiC itself.

To remove history as a factor, single load tests were conducted. In an attempt to accurately gauge the effect of history, tests were conducted at similar compressive loads. Unfortunately, there is too much variability in the data to make a definitive assessment. Additional single load tests of the HfB₂-20 vol% SiC were conducted in order to determine if the SiC conglomerates mentioned in Section 3.1.2.2 had an impact on creep performance.

The creep curves of various single compressive load tests of HfB₂-20 vol% SiC are shown in Fig. 133.

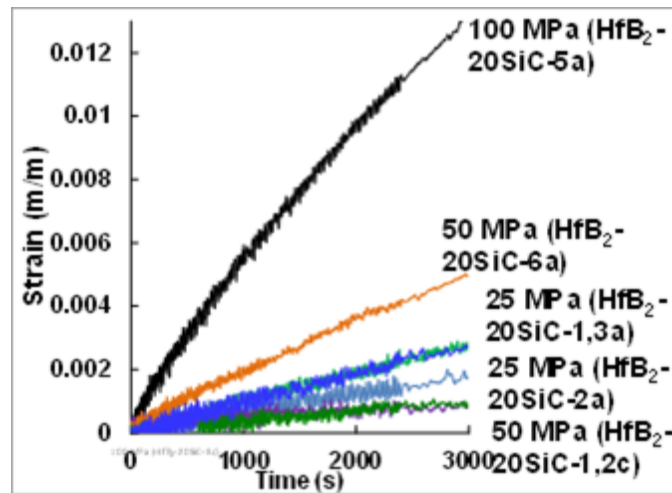


Fig. 133. Creep curve for HfB₂-20 vol% SiC parallelepiped specimens at 1500°C in air at various compressive loads.

Appendix E

Characterization Equipment Used



Fig. 134. ACUPEAK 1330 pycnometer to determine volume via pressure differentials.



Fig. 136. Rigaku Ultima IV X-Ray Diffractometer



Fig. 135. Zeiss optical microscope.

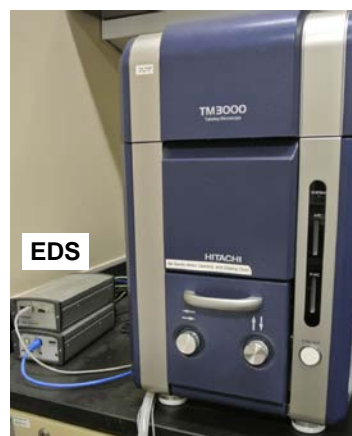


Fig. 137. Hitachi TM 3000 Tabletop Microscope SEM and Hitachi Bruker Quantax EDS



Fig. 138. FEI/Philips XL30 SEM



Fig. 139. FEI/Philips CM-200T TEM

Appendix F

Sample Preparation

The following is just one procedure which can be used to polish specimens before and after testing. Many variations can be applied depending on polisher preference for amount of polishing material, polishing paper, machine methodology, etc.

As-processed material is provided by AFRL in the shape of a puck. It is covered by a carbonized layer. Specimens are cut from pucks using EDM. Polishing is required to remove the carbonized layer and any surface defects in the machined specimens.

Polishing a pre- or post-test specimen to finer than 45 μm takes multiple steps. The decrease in micron size usually follows 45, 30, 15, 9, 6, 3, 1, 0.5 μm . Determining if a step is completed is a combination of opinion and fact. Visually, one can see the surface appearance change as the micron size is stepped down. A microscope exam is used to determine if any surface faces are getting smaller. Also, any scratches should be random in nature. At 0.5 μm the specimen surface should be mirror-like.

For the as-processed microstructure analysis, mount the specimen in order to polish a face to 0.05 μm for EBSD analysis. The Struers Cito-Press 20 (Cleveland, OH) (Fig. 140) was used to hot pressure mount the specimen in an electrically conductive mounting material. The easiest, yet longest duration, polishing method is to automatically polish the specimen (Buehler Vibromet I 400-VPS-274) (Fig. 141). A 0.05 μm powder is placed in solution into the Vibromet, and the mounted specimen placed in a

specialized holder. This method can take several days, but the only time commitment is to periodically check the specimen. Too much polishing can cause too much of the mounting material to wear away.



Fig. 140. Struers Hot Mounting Cito-Press 20.



Fig. 141. Buehler Vibromet I (400-VPS-274).

A shorter duration, but more hands-on commitment, method is to polish by hand. It was found that using card stock, lubricant, and polishing paste as a lapping method to polish the specimen to a 6 μm finish proved to be the most efficient method. A polishing wheel is used as described below to reach a finer finish. A softer buffing cloth on the wheel should be used for 0.5 μm and lower.

Test specimens are machined to approximately 6.7 x 6.7 x 19.5 mm. The faces are polished to approximate final dimensions of 6.5 x 6.5 x 19 mm. Test specimens are polished to a 45 μm using several methods. Care needs to be taken to maintain parallel and perpendicular faces.

The ends are polished using a lapping holder and tool and a 12 inch polishing wheel (Fig. 142). The specimen is placed in the holder less than a mm beyond the end of the holder. Care must be taken not to tighten the screw too much or too close to the end of a specimen as chipping of the specimen can occur. Twelve-inch perforated Buehler Texmet P (or equivalent paper) is utilized due to its' ability to maintain flat (and parallel and perpendicular) surfaces more effectively than other polishing papers. This is a result of Texmet P having less give than other papers. The perforations are meant to capture polished off material, preventing scratching of the specimens. The paper is secured to the polishing wheel using a wheel ring or sticky backed paper. A swirl of 45 μ m slurry combined with a few drops of gentle dishwashing liquid is placed on the polishing paper. A little water is added to the mixture and the holder is used to gently spread the mixture over the paper. The holder is then placed in the large lapping tool and the wheel is then started. A setting of approximately 250 rpm is sufficient. Care must be taken when setting the polishing wheels rpm's. If the rpm's are too high, the specimen will hydroplane rather than get polished. Move the lapping tool around randomly to prevent preferential polishing.

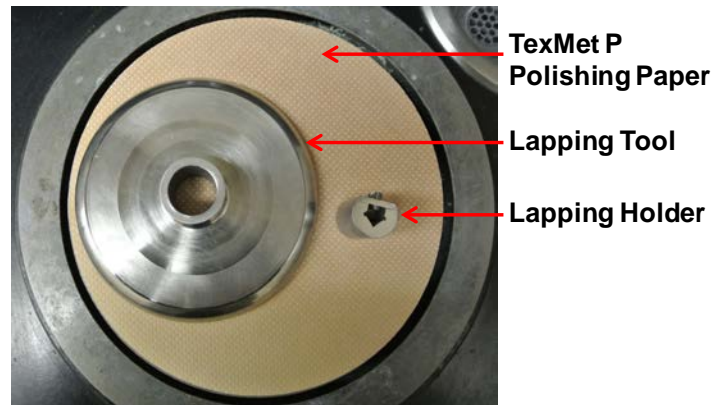


Fig. 142. Twelve-in polishing wheel with TexMet P polishing paper, lapping tool, and lapping holder for the test specimen.

Periodically, evaluate the ends of the specimen using an optical microscope. The goal is to remove any oxidation due to EDM machining, surface cracks, and other imperfections. The amount of time necessary will vary with every specimen. Composition and density between provided pucks will affect the polishing time. Cracks and oxidation induced by machining will be different. If an imperfection is at the edge, it must be weighed on whether to continue removing material from the end of the specimen, or if polishing the face would be more effective.

The sides of the specimen are polished using the Allied High Tech MultiPrep polisher (Rancho Dominguez, CA) (Fig. 143). To use the MultiPrep polisher, specimens must first be mounted on a polishing puck. The puck is machined to provide a completely flat surface within the markings on the puck. If the markings are uneven, the puck could have been ground unevenly. The puck is placed on a hotplate at 200 °C. Crystalbond™ is melted onto the puck. When the Crystalbond™ becomes liquified, the press is used to ensure the specimen is completely flat against the puck. Up to 3 pucks can be polished at one time. A rotation of 75 RPM was used. The amount of weight added and time required can change with every specimen.



Fig. 143. Allied High Tech MultiPrep Polisher

To remove the specimen, place the puck back on the hotplate and reheat until the Crystalbond™ is resoftened. After all four faces have been polished, the specimen is cleaned with acetone to remove remaining traces of Crystalbond™. It can be placed into a small plastic beaker with acetone and placed in a vibrating acetone bath for 5 minutes to remove any Crystalbond™ in the pores.

Most of the post-test microscopy was conducted after specimen polishing. Though polishing of the specimen can be performed without first mounting the specimen to a puck as described above, it is highly recommended as the epoxy aids in protecting the oxide scale and prevents the scale from flaking off entirely. Care must be taken to complete any surface examination prior to mounting. In this study, CaldoFix was the preferred method of mounting. Though it is not a conductive material, the transparency of the mount was deemed to be more important.

1. Use aluminum foil to shape a cup for mounting the specimen. Originally, the rubber curing cups were used, but they degraded and proved very difficult to separate from the specimen (they had to be cut off). It is beneficial to place the cup on another small piece of alumina foil, as small holes in the cup may form as a result of shaping the cup.

2. Mix the CaldoFix per instructions and pour a small amount into the cup. Place the specimen in the cup ensuring the cutting plane is vertical, then add enough CaldoFix to fully cover the specimen.
3. To help the CaldoFix penetrate the scale, place it in a vacuum chamber (Struers CitoVac) (Fig. 144) for 1 min.. If left in too long, the hardener will start to offgas.



Fig. 144. Struers CitoVac vacuum chamber.

4. Place the mounted specimen in the oven (Fisher Scientific OV700F) (Fig. 145) at 55°C for 1-2 hours to remove any small bubbles. Raise the temperature to 73°C and cure for approximately one hour to fully cure the mounted specimen. The specimen is fully cured if you cannot see the aluminum foil deform when the bottom is scratched.



Fig. 145. Fisher Scientific Forced Air Isotemp Oven

5. The specimen is Crystal bonded onto a cutting block and cut using the TEM cutting saw (South Bay Technology Inc Model 600, South Clemente, CA) (Fig. 146). The TEM saw is preferred as it cuts slower and uses a thinner blade than a standard cutting saw. The red lines in Fig. 147 show the locations of cuts made. A standard cutting speed of 7-9 was used for cutting, while a speed of 3-4 was used for cleaning the blade. The blade should be cleaned frequently to remove buildup on the blade. This can be as frequent as every few minutes. The blade position in the cut needs to be shifted periodically. If this is not done, a dead spot can develop in which the blade will spin without cutting. For lubrication, Coolmet is most often used. In some cases, ethylene glycol or 200 proof ethanol is used for cutting lubrication when a non-aqueous cutting is desired. Boron can dissolve into water, making it very difficult to detect accurately via EDS. For the interaction tests, it was desired to preserve, as much as possible, chemical locations.



Fig. 146. South Bay Technology Inc saw Model 600

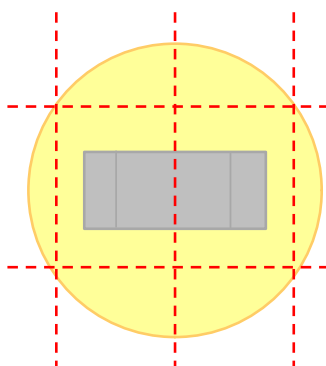


Fig. 147. Schematic drawing of cutting planes of mounted specimen.

Once cutting is complete, it is advisable to remount the specimen half that is to be polished. As previously mentioned, the oxide scale can separate from the unoxidized bulk of the specimen. Re-mounting the specimen using epoxy will fill the gap, providing protection for the scale during the more aggressive initial polishing. Ensure that the surface to be polished is facing up when mounting.

The post-test specimen can be polished by hand or in the Vibromet as described above for optical, SEM, EDS, or EBSD characterization. Transmission electron microscopy requires sample material to be polished down to nanometer scale thicknesses to make them transparent to electrons. One method is to first cut a sliver of the specimen and polish until the sliver is a foil 50 – 100 μm thick. Further polishing is accomplished by firing ions to sputter material from a small area of the surface (i.e., ion milling). This method did not prove to be effective for HfB_2 ; despite an inordinate amount of time invested, most of the material was too thick. A better method was to use a focused ion beam (FIB) to cut a sliver of material from the specimen. Ion milling was then used to further thin the surface. This method provided a larger area to examine; more grain boundaries could be evaluated.

Appendix G Archimedes Method

The Archimedes method was determined to provide the most accurate density for monolithic HfB₂. Archimedes' principle states: "A body whole or partially immersed in a fluid will be buoyed up by a force equal to the weight of the fluid that it displaces [132]" (e.g. Eqn. 44) In addition, the volume of water displaced equals the volume of the portion of the body immersed in a fluid (Eqn. 45).

$$F_{buoyant} = F_{specimen\ in\ water} \quad (44)$$

$$V_{water\ displaced} = V_{specimen\ in\ water} \quad (45)$$

Substituting $F = mg$ into both sides of Eqn. (44) results in

$$m_{water\ displaced} = m_{specimen\ in\ water} \quad (46)$$

In order to find the true density of the test specimens (Eqn. 47a), the Archimedes apparatus utilized determines volume of the displaced water according to Eqns. 47a - 49.

$$\rho_{specimen} = \frac{m_{dry\ specimen}}{V_{specimen}} \quad (47)$$

$$\rho_{specimen} = \frac{m_{dry\ specimen}}{V_{water\ displaced}} \quad (47a)$$

$$V_{water\ displaced} = \frac{m_{water\ displaced}}{\rho_{water\ displaced\ at\ temp}} \quad (48)$$

$$V_{water\ displaced} = \frac{m_{sample\ in\ air} - m_{sample\ in\ water}}{\rho_{water\ displaced\ at\ temp}} \quad (49)$$

Monolithic HfB_2 is a porous material; this porosity of monolithic HfB_2 can absorb more moisture from the air. Therefore; the specimens were dried for 40 minutes at 60°C to remove any moisture. The drying time was determined by taking mass measurements throughout the drying cycle until an instance was reached when the mass measurement remained constant. The monolithic HfB_2 test specimens had the most difference between the dry mass and mass in air. To determine the true density of a material, the effect of porosity must be removed. Each specimen was boiled in water for 30 minutes.

In using the AFRL Archimedes apparatus (Fig. 148), a bridge is placed over the mass scale, and a beaker of water is placed on the bridge. A stand is placed on the mass scale that supports a basket in which the specimen will be submerged. Care must be taken that there are no air bubbles trapped in the open grid of the basket or that it is not touching the beaker. The mass scale is zeroed, the specimen placed in the basket, and the submerged mass measurement quickly taken.

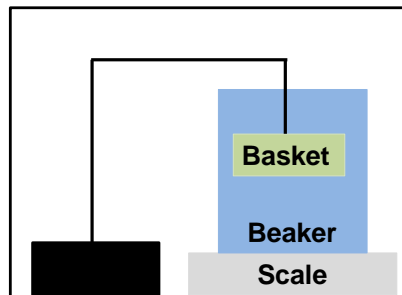


Fig. 148. AFRL Archimedes apparatus setup

Appendix H

Isolating SX YAG

It has been determined that gaseous B_2O_3 interacts with SX YAG. In order to prevent the interaction between the HfB_2 and SX YAG in subsequent tests, several options were considered as a means of isolating the YAG pushrods (e.g., sleeving, evaporative coating, and sputter deposition). Pt sleeving of the YAG pushrods was impractical as Pt foil sheets could not be sealed around the pushrods. Pt tubing was not economically feasible, and evaporative coating was not feasible due to the high melting point of Pt. Although sputterdeposition of Pt had not previously been attempted with the equipment available to this study, and there was no way to know how the Pt would deposit onto the SX YAG, it appeared to be the most practical solution.

The first application of Pt using sputter deposition was for a duration of 10 minutes, resulting in an uneven coating on the SX YAG sample (i.e., the SX YAG could still be seen in some places). A second layer of Pt was sputtered for an additional 15 minutes, resulting in a visually even coating over the entire surface of the SX YAG sample which did not flake off (Fig. 149). Upon closer inspection, the coating appeared to contain numerous cracks (Fig. 150). The cross-sectional examination of the coating as shown in Fig. 151 determined that it was 261 nm thick. Although the Pt was sputtered onto the sample as two different layers, the Pt deposited itself as distinct columns with no apparent distinction between the two separate coatings.



Fig. 149. Photograph of Pt Sputtercoated SX YAG

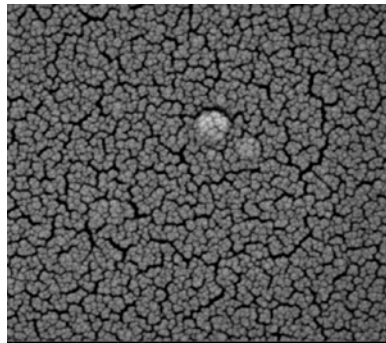


Fig. 150. SEM micrograph of Pt sputter deposition

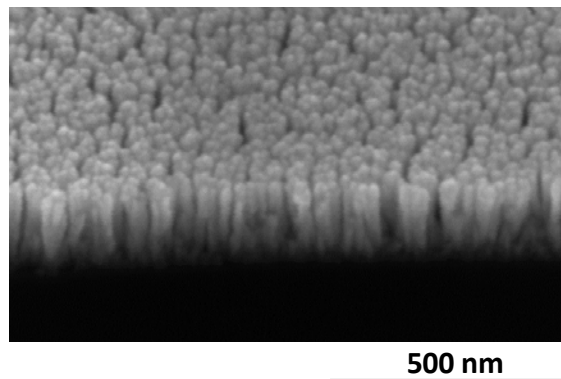


Fig. 151. SEM micrograph of cross-sectional view of Pt sputter deposition

Columnar deposition is a common phenomenon associated with the sputter deposited conductive metals, specifically Ag, Cu, Au, and now Pt. One explanation could be that the charged plasma used in the sputter deposition process imparted slight charges to the Pt particles, affecting the orientation of the Pt deposition.

A tube furnace test was conducted in which the Pt-sputtered SX YAG and the HfB_2 were separated by an alumina spacer (Fig. 152). After 18 hours at 1500 °C, the surface of the SX YAG was completely free of Pt and showed signs of interaction (Fig. 153) similar to that seen in the other tube furnace tests (Fig. 98).

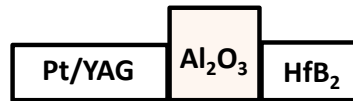


Fig. 152. Schematic of tube furnace test to evaluate Pt deposition.



Fig. 153. Photograph of SX YAG with sputtercoated Pt "blown off" after heat treatment.

The application of a thin coat of Pt by sputter deposition to single-crystal YAG pushrods does not prevent interaction between HfB_2 and single-crystal YAG at high temperatures. Rather than the Pt getting annealed and creating an impervious surface, the space between the Pt columns appears to allow gaseous B_2O_3 to reach the SX YAG. The Pt is then “blown off” the SX YAG by gaseous SX YAG decomposition byproducts

Appendix I Catalysis

This work dealt with the heterogeneous catalytic reactions of gaseous reactants being adsorbed onto a solid catalyst. A catalyst works by reducing the amount of energy necessary to cause a chemical reaction (i.e., activation energy (E_a)) [177]. Figure 154 illustrates the differing amounts of activation energy necessary for reactions to occur when a catalyst is utilized and when it is not. The difference between the two activation energies is the amount of energy that the catalyst provides. Of note is that the catalyst does not change the ΔH of the system; i.e., the energy difference between reactants and products remains the same.

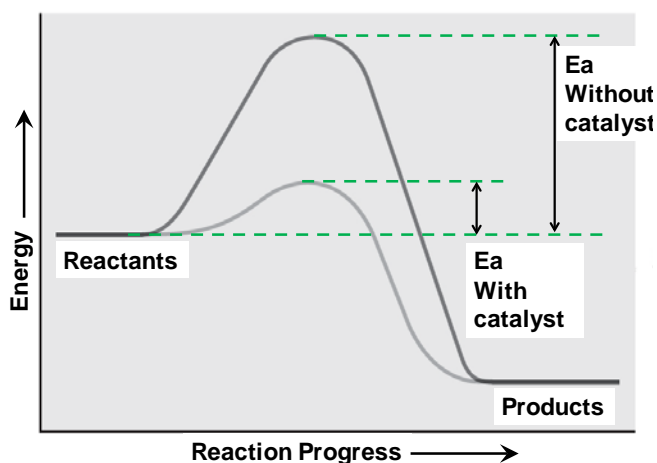


Fig. 154. Activation energy (E_a) needed for reactions with and without a catalyst.

The amount of energy required to take a molecule from its ground energy to its disassociation energy is the activation energy. A chemical system typically tries to stabilize itself in its lowest possible energy state. Atomic collisions and/or vibrations

(possibly from an external source) will increase the energy of a chemical system. When the energy is too great, a molecule will disassociate in order to lower its energy state. It is during this transition state that chemical reactions occur.

The surfaces of the specimens contained Al_2O_3 and YBO_3 rather than Al_2O_3 and Y_2O_3 . Adsorbed AlBO_2 may completely break apart easier than YBO_2 (which just changes its oxidation state) due to the relative stability of gaseous rare earth borates of the form MeBO_2 [210]. Another possible explanation is in the behavior of the elements and chemical structure of the molecules.

Ionization energy is defined as the amount of energy it takes to remove an electron from an atom [177]. Electronegativity of an element is how easy it will accept an electron. Elements with the most reactivity will have either less ionization energy and/or more electronegativity. Al has an ionization energy of 5.9858 eV, and Y has an ionization energy of 6.2173 eV [175]. Al has the greater negativity at 1.50 eV compared to Y's electronegativity of 1.2 eV [177]. Therefore, Al can be viewed as more reactive than Y. In other words, AlBO_2 can be more reactive than YBO_3 .

AlBO_2 is made up of a Al^{+1} cation and a $(\text{BO}_2)^{-1}$ anion [211]. It can be seen in (Fig. 155a) that Al^{+1} forms a single bond with $(\text{BO}_2)^{-1}$; the bond enthalpy of which is 511 kJ/mol [212]. YBO_3 is made up of a Y^{+3} cation and an $(\text{BO}_3)^{-3}$ anion (Fig. 155b) [213]. The Y^{+3} cation forms three single bonds with $(\text{BO}_3)^{-3}$ (Fig. 153b). The bond enthalpy of the Y-O bond is 715 kJ/mol [212]. The interpretation of these figures and the resultant bond energies is that it is easier to break the Al-O bond than the Y-O bond.

Thus, a comparison of the reactivities and bond energies of the cations demonstrates why does AlBO_2 disassociates easier than YBO_3 .

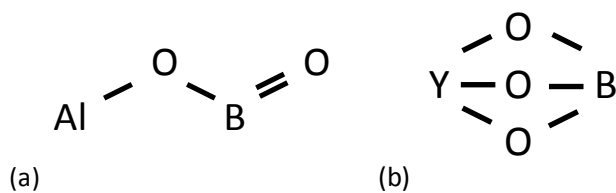


Fig. 155. Molecular structures for (a) AlBO_2 and (b) YBO_3 [214].

Table 13. Summary of comparisons between AlBO_2 and YBO_3 .

	AlBO_2	YBO_3
Ionization Energy	-	+
Electronegativity	+	-
Cation Bond Energy	-	+
Disassociation Energy	-	+

Appendix J

Gibbs Free Energy

Gibbs free energy of a reaction or a system of reactions can be viewed as the balance between the enthalpy (heat (H)) of a reaction and the entropy (disorder (S)) of a system [215]. (Eqn. 50) It can also be described as the driving force behind a chemical reaction. The Gibbs free energies of the various reaction sequences were evaluated to determine which options were most likely to occur when applied to tests performed regarding this research. Exothermic reactions, or negative ΔG values, are a spontaneous reaction in which heat is released. If ΔG is positive, additional energy is required to bring about an endothermic reaction. Endothermic reactions should only occur if the other reactions taking place at the same time are negative enough to make the ΔG of the entire system negative. It is interpreted that the greater the negative value of ΔG , the more likely the reaction is to take place. At the same time, this and the spontaneity comparison is not a concrete determination since reactions with lesser Gibbs free energies, even positive, can take place.

$$G = H - TS \text{ or, in the case of constant temperature, } \Delta G = \Delta H - T\Delta S \quad (50)$$

The following calculation was used to determine the Gibbs free energy for the chemical reactions:

$$\Delta G_{rxn} = \sum G_{products} - \sum G_{reactants} \quad (51)$$

To determine the overall Gibbs free energy of a system of reactions, the individual Gibbs free energy equations are added together.

$$\Delta G_{sys} = \sum G_{products(sys)} - \sum G_{reactants(sys)} \quad (52)$$

YAG has been shown to evolve into YAP (YAlO₃), YAM (Y₄Al₁₂O₉), or YAB (YAl₃(BO₃)₄) [130,152]. Recall that when HfB₂ was oxidized in direct contact with SX YAG (Case A), traces of YAM were found on the contact surface of the SX YAG piece. The Gibbs free energy for the reactions was calculated from 300-2800°C to determine if the different systems of reactions are more likely at different temperatures.

The Gibbs free energy values of the individual molecules came from a variety of sources: NIST-JANAF tables, HSC software, and values and formulas from literature [155,158-162]. As the chemical composition of c-YSH was unable to be definitively determined, an estimate was made based on the c-YSH Gibbs free energy work of Lee and Navrotsky [155]. In their work, the enthalpy of formation of multiple c-YSH campaigns was determined via high-temperature oxide melt solution calorimetry. The average value of x was used to determine the composition based on $Hf_{1-x}Y_xO_{2-\frac{x}{2}}$ -- Hf₃Y₂O₉.

The Gibbs free energy of Al₂O₃ was calculated to be more negative than AlBO₂. This is an indication supporting the theory that AlBO₂ will transition to AlBO₂ upon adsorption. Whether HfB₂ is in direct contact with SX YAG or separated from each other by alumina, the overall system of reactions involving YAM is revealed to be the most likely compared to those involving YAP and YAB. It is shown that the systems of equations involving YAM are the most likely at all temperature ranges (Fig. 156 and Fig. 157).

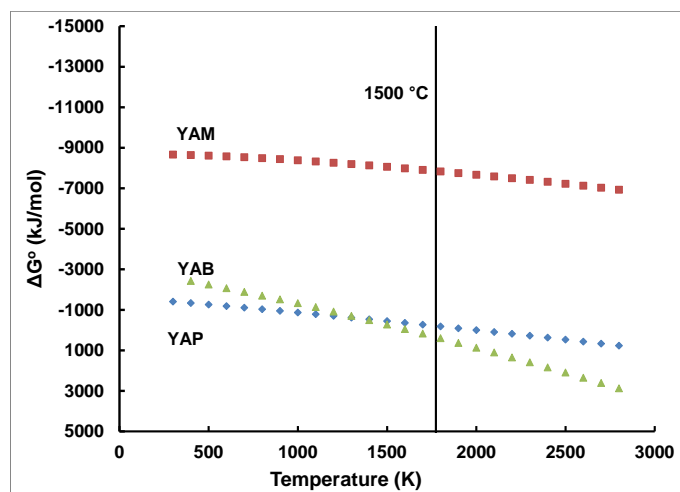


Fig. 156. Gibbs free energies of possible reactions in the system of direct contact between HfB_2 and SX YAG.

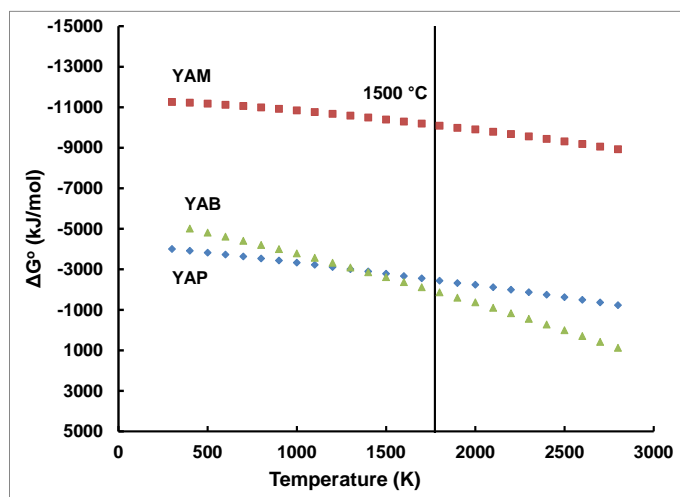


Fig. 157. Gibbs free energies of possible reactions in the system of an alumina spacer between HfB_2 and SX YAG.

Appendix K

Electron Charging

SEM analysis of non-conductive materials can result in images that have significantly brighter areas (Fig. 158). This is due to charging of the specimen. Charging refers to the buildup of electrons on the surface of the specimen [216]. If more electrons arrive at a point on a non-conductive sample than are emitted as a signal (secondary or backscatter electrons) or conducted through the specimen to the holder, a static negative charge builds up. This static charge can also deflect the incoming electron beam, giving the appearance of a moving specimen. This will create blurred images for both SEM imaging and EDS mapping (Fig. 159).

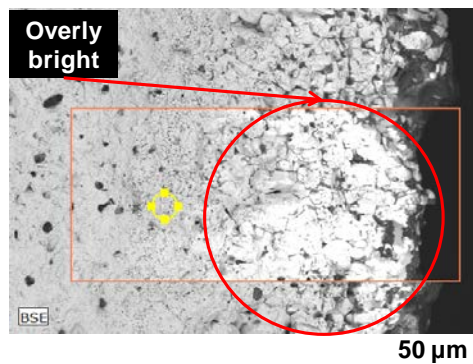


Fig. 158. SEM micrograph of representative image of a charged oxide layer.

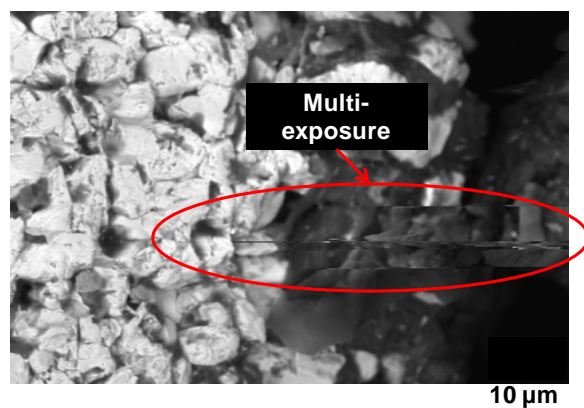


Fig. 159. SEM micrograph of representative image of drifting.

In some cases, the amount of charging was detrimental to the analysis being conducted as a result of micrographs appearing all white due to "flooding" of the detector. Elemental analysis was unreliable since the beam would move; allowing non-target areas to be included in the quantitative analysis.

Charging was overcome with several methods: carbon coating (Edwards Auto 306 Turbo Evaporator (Fig. 160) or Gatan Precision Etching Coating System Model 682 (Fig. 161)), carbon tape, silver paint, copper tape, or a combination thereof. These create a conductive path from the surface of the specimen down to the holder which acts as a ground. In other cases, charging mitigation was not possible when it would interfere with the analysis being conducted. When possible, the electron voltage was decreased, but this increased the uncertainty in heavier metal elemental quantification.



Fig. 160. Edwards Auto 306 Turbo Evaporator



Fig. 161. Gatan Precision Etching Coating System Model 682

Appendix L

Specimen Damage

Despite attempts to ensure defect free pre-test surfaces, two specimens, HfB₂-3a and HfB₂-4a, evidenced post-test cracks that were not induced by polishing. These cracks could have started as surface imperfections. They would have been exacerbated by compressive load and/or oxidation. Oxidation can cause crack growth since HfO₂ has a greater volume than HfB₂. Crack edges are spread further apart, extending the crack tip as the oxidation layer continues to grow.

Cross-sectioning of the HfB₂-3a specimen revealed an unanticipated result – a crack perpendicular to the cut direction (Fig. 162). The SEM image revealed that an oxide scale was throughout the crack (Fig. 163). A magnified SEM image provided further insight into the possible formation of this crack (Fig. 164); it appears that the scale on the sides of the crack and outside of the HfB₂ specimen grew at the same time.

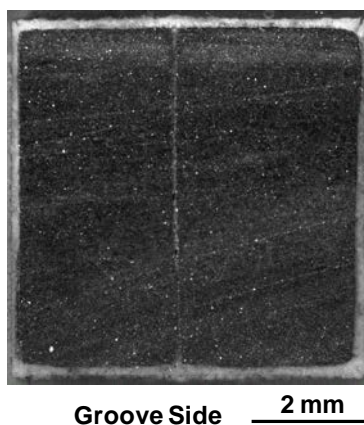


Fig. 162. Optical image of post-test pre-polish cross-section revealing crack in HfB₂-3a after 7.3 hrs at 1500 °C under a compressive load (25, 50 MPa) for 6.2 hours.

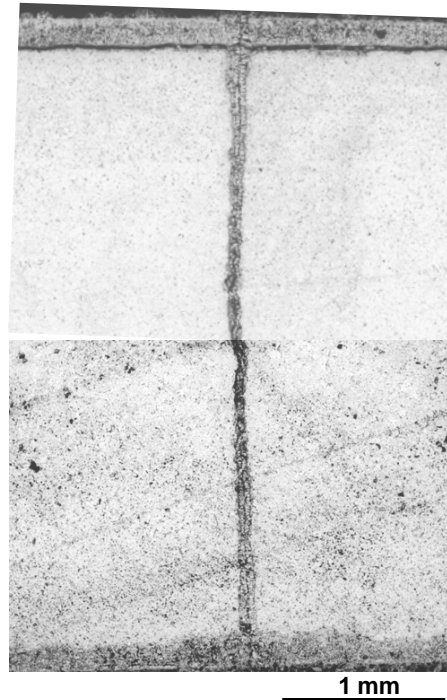


Fig. 163. SEM micrograph of post-test pre-polish crack in HfB₂-3a (Fig. 158) after 7.3 hrs at 1500 °C under a compressive load (25, 50) for 6.2 hours.

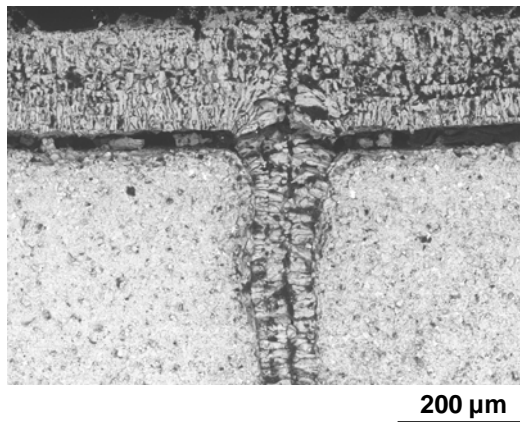


Fig. 164. SEM micrograph of post-test pre-polish outer oxide scale and upper edge of crack intersection of HfB₂-3a after 7.3 hrs at 1500 °C under a compressive load (25, 50 MPa) for 6.2 hours.

For further clarification of the crack surface, a longitudinal cut was made perpendicular to the crack. This cut revealed two cracks as shown in Fig. 165. The larger of the 2 cracks corresponds to the crack seen in the cross-sectional view of HfB₂-3a (Fig. 162).

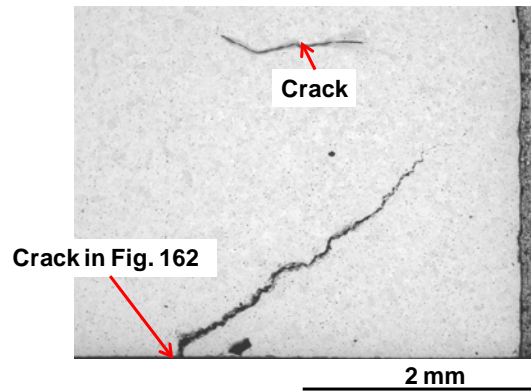


Fig. 165. SEM micrograph of longitudinal view of crack that appeared on cross-section of HfB₂-3a after 7.3 hrs at 1500 °C under a compressive load (25, 50 MPa) for 6.2 hours

Specimen HfB₂-4a was retested for stepwise creep at higher loads. The CTE calculated for HfB₂-4's second test run was consistent with the CTE from the first test run of HfB₂-4. Therefore, it was feasible to reuse the test specimen to evaluate the creep response at higher loads. Unfortunately, the specimen experienced a catastrophic failure. The alumina spacer failed; the displacement correction to maintain the load might have exacerbated the crack propagation that was initiated during the test. The figures below show pre-and post-test optical images of both faces of the HfB₂-4a specimen (Fig. 166 and Fig. 167). Cracks that were not previously seen are evident after the first test run.

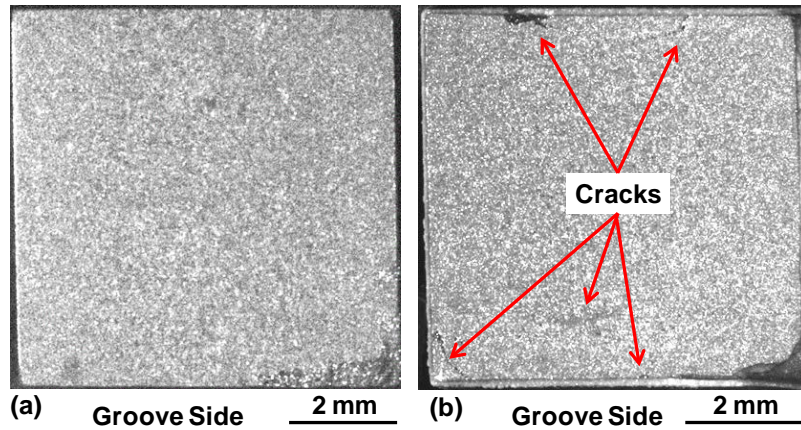


Fig. 166. (a) Optical image of pre-test top face of HfB_2 -4a specimen and (b) Crack-annotated post-test optical image of bottom face of HfB_2 -4a specimen after 7.1 hrs at 1500 °C under a compressive load (50, 75 MPa) for 5.8 hours.

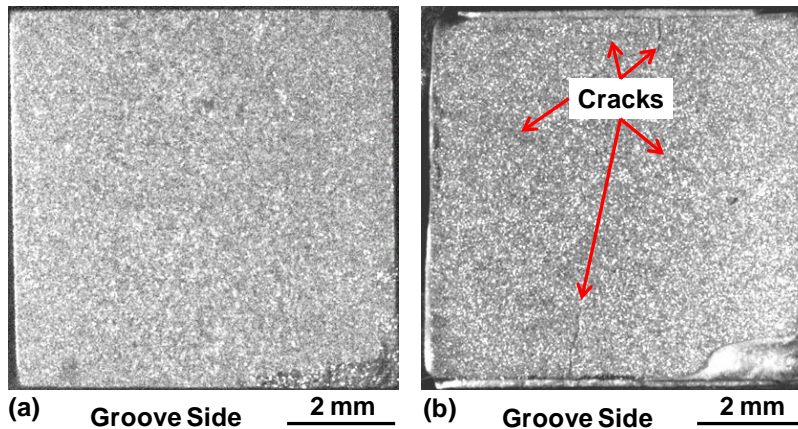


Fig. 167. (a) Optical image of pre-test bottom face of HfB_2 -4a specimen and (b) Crack-annotated post-test optical image of bottom face of HfB_2 -4a specimen after 7.1 hrs at 1500 °C under a compressive load (50, 75 MPa) for 5.8 hours.

Appendix M

Load Train

High purity (99.8%) alumina spacers are considered the best option to separate HfB₂ and SX YAG during high temperature compression testing. However, they are the weak point in the test apparatus. Though various thicknesses and cross-section dimensions were attempted, almost all of the test failures were due to one or both of the alumina spacers cracking. The photographs of Fig. 168 are representative of the alumina spacer failure sequence. Cracking initiates on the side surfaces of the spacers due to the compressive load. As a compressive load is maintained, these cracks continue until they progress through the entire thickness. A sudden increase in strain indicated of imminent catastrophic failure, causing the load train to abruptly shift its displacement in an attempt to maintain the load. On occasion, automatic safeguards failed to arrest the system; the impact would cause the SX YAG pushrods to shatter.

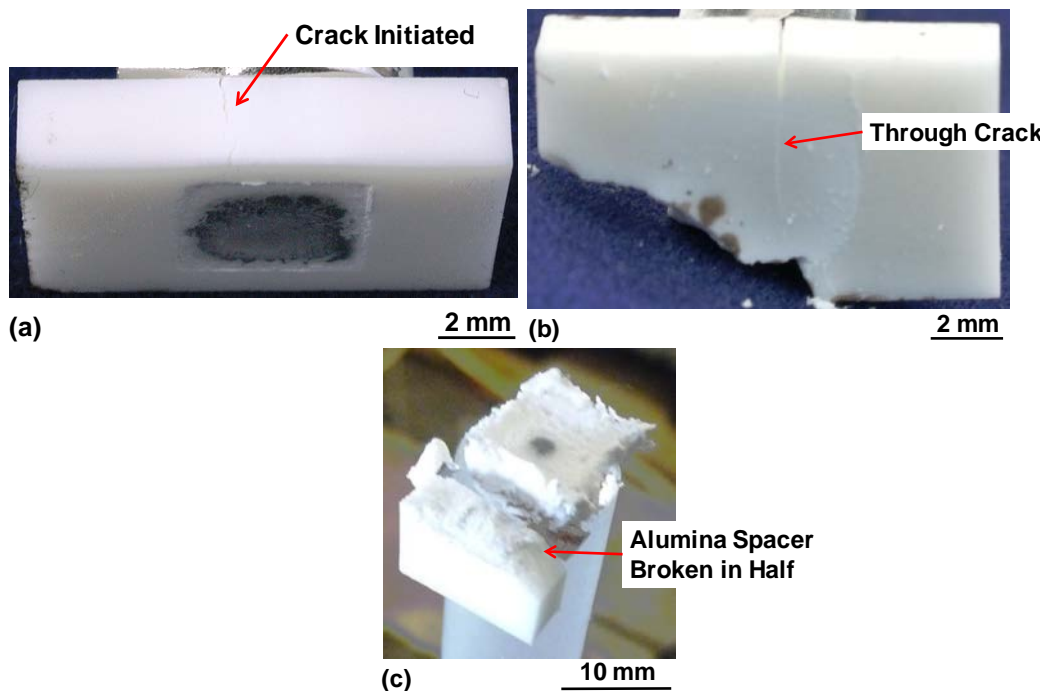


Fig. 168. Representative photographs of alumina spacer failure sequence. (a) Crack initiation on outer edge of spacer. (b) Crack all the way through alumina spacer. (c) Alumina spacer failure.

Upon conclusion of the creep tests of the HfB_2 -containing specimens, no crustaceous deposit was observed. As such, the alumina spacers were used for all of the pilot creep tests.

Appendix N

Heat Treatment at 1500°C in an Argon Environment

To further investigate the interactions between HfB_2 and SX YAG, HfB_2 was heat treated in direct contact with SX YAG in an argon environment under zero load (Case F) under the same conditions as Case A. Contrary to expectation, an encrustation similar in appearance to Case A developed on the sides of the HfB_2 specimen (Fig. 169a). The top of the specimen had significantly less of the encrustation (Fig. 169b). XRD analysis revealed c-YSH and polycrystalline YAG. The HfB_2 surface in direct contact with SX YAG had the same phases.

It has been hypothesized that the crustaceous deposit is initiated by the oxidation of HfB_2 to release boria gas and the presence of a c-YSH layer. Neither should occur in an argon environment; therefore, a crustaceous deposit should have not formed. The tube furnace was flushed 3 times to remove the laboratory air environment within. In some cases, there are still traces of oxygen in the argon. This miniscule amount might have initiated the oxidation. Or gases released from the alumina spacer could have initiated oxidation.

The locations of the crustaceous deposit provides insight into its development. The reduced amount on the top surface of the specimen suggests that the deposit is moving up the side surfaces. This coincides with the theory that Y^{3+} anions diffuses into the HfO_2 layer.

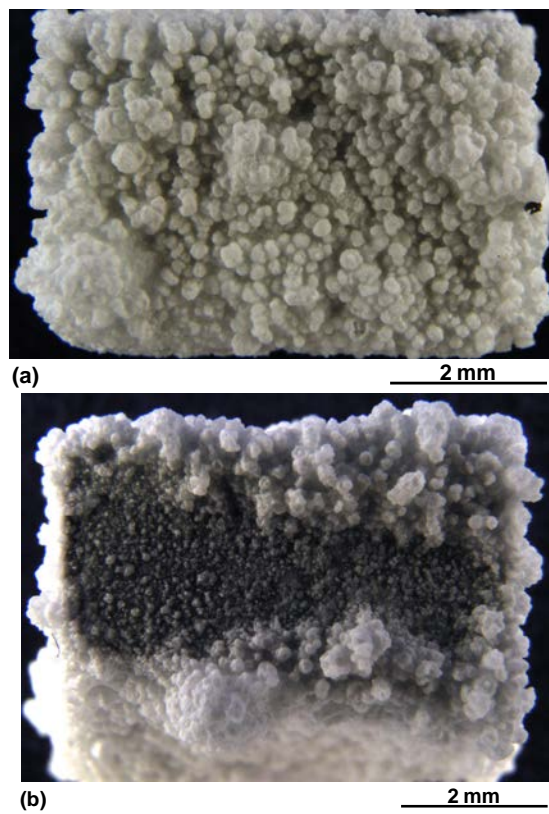


Fig. 169. Photographs of the (a) side surface and (b) top surface of HfB_2 exposed to tube furnace argon environment for 18 hours at 1500°C when HfB_2 and SX YAG were in direct contact.

References

1. 'Milestones of Flight - 1903 Wright Flyer.' (2011, December 1).
<http://www.nasm.si.edu/exhibitions/GAL100/wright1903.html>
2. D. A. Hall, 'Technical Preparation of the Airplane 'Spirit of St. Louis,' National Advisory Committee for Aeronautics. No. 357 (1927).
3. J. E. Rinard, The Smithsonian National Air and Space Museum Book of Flight. Richmond Hill, ON: Firefly Books, 2001.
4. 'Milestones of Flight – North American X-15.' (2011, December 1).
<http://www.nasm.si.edu/exhibitions/GAL100/X-15.html>
5. W. H. Dana, 'X-15 Pilots' Panel,' *Proceedings of the X-15 First Flight Anniversary Celebration*. 143 NASA Conference Publication 3105 (1989).
6. R. G. Hoey, 'X-15 Contributions to the X-30,' *Proceedings of the X-15 First Flight Anniversary Celebration*. 105 NASA Conference Publication 3105 (1989).
7. S. D. Williams, D. M. Curry, D. C. Chao and V. T. Pham, 'Ablation Analysis of the Shuttle Orbiter Oxidation Protected Reinforced Carbon-Carbon,' *J. Thermophys. Heat Transfer*, 9 478-485 (1995).
8. S. M. Johnson, M. J. Gasch, T. H. Squire, J. W. Lawson, M. M. Stackpoole and M. I. Gusman, 'Ultra High Temperature Ceramics: Issues and Prospects,' *High Temperature Ceramic Materials and Composites* 819-831 (2010).
9. S. M. Johnson, 'Ultra High Temperature Ceramics: Applications, Issues, and Prospects,' *Presentation at the 2nd Ceramic Leadership Summit*. (2011).
<http://ceramics.org/wp-content/uploads/2011/08/applications-uhtc-johnson.pdf>.
10. Cantoni, S., Scatteia, L., Alfano, D., 'UHTC Potential Applications in Aerospace,' Centro Italiano Recherche Aerospaziali.
11. M. Pulsonetti, Class handout, 'Scaling Laws for Scramjets. An experimental and Theoretical Investigation to Determine the Scaling Laws for Scramjet Engine Performance at Hypersonic Flight Conditions,' The University of Queensland Australia. 1995.

12. S. V. Ushakov and A. Navrotsky, 'Experimental Approaches to the Thermodynamics of Ceramics Above 1500°C,' *J. Am. Ceram. Soc.*, 95 [5] 1463-1482 (2012).
13. W. G. Fahrenholtz, G. E. Hilmas, I. G. Talmy and J. A. Zaykoski, 'Refractory Diborides of Zirconium and Hafnium,' *J. Am. Ceram. Soc.*, 90 [5] 1347-1364 (2007).
14. W. G. Fahrenholtz and G. E. Hilmas, 'Ultra-High Temperature Ceramics – An Introduction to Ultra-High Temperature Ceramics,' *The A to Z of Materials*, 2012.
15. W. Guo and G. Zhang, 'Oxidation Resistance and Strength Retention of ZrB₂-SiC Ceramics,' *J. Eur. Ceram. Soc.*, 30 [11] 2387-2395 (2010).
16. M. Opeka, J. Zaykoski, I. Talmy and S. Causey, 'Synthesis and Characterization of Zr₂SC ceramics,' *Materials Science & Engineering: A*, 528 [4-5] 1994-2001 (2011).
17. I. G. Talmy, J. A. Zaykoski and C. A. Martin, 'Flexural Creep Deformation of ZrB₂-SiC Ceramics in Oxidizing Atmosphere,' *J. Am. Ceram. Soc.*, 91 [5] 1441-1447 (2008).
18. I. G. Talmy, J. A. Zaykoski and M. M. Opeka, 'High-Temperature Chemistry and Oxidation of ZrB₂ Ceramics Containing SiC, Si₃N₄, Ta₅Si₃, and TaSi₂,' *J. Am. Ceram. Soc.*, 91 [7] 2250-2257 (2008).
19. E. Wuchina, E. Opila, M. Opeka, W. Fahrenholtz and I. Talmy, 'UHTCs: Ultra-High Temperature Ceramic Materials for Extreme Environment Applications,' *Electrochem. Soc. Interface*, Winter 30-36 (2007).
20. A. L. Chamberlain, W. G. Fahrenholtz, G. E. Hilmas and D. T. Ellerby, 'Characterization of Zirconium Diboride-Molybdenum Disilicide Ceramics'; pp. 299-308 in *Advances in Ceramic Matrix Composites IX*. Edited by N. P. Bansal, J. P. Singh, W. M. Kriven and H. Schneider (Eds.). John Wiley & Sons, Inc., Westerville, OH, 2003.
21. F. Monteverde, D. D. Fabbriche and A. Bellosi, 'Zirconium Diboride-Based Composites,' *Euro. Ceramics VIII--Part 2*, 206-213 961-964 (2002).
22. M. M. Opeka, I. G. Talmy and J. A. Zaykoski, 'Oxidation-Based Materials Selection for 2000°C+ Hypersonic Aerosurfaces: Theoretical Considerations and Historical Experience,' *J. Mater. Sci.*, 39 [19] 5887-5904 (2004).
23. M. M. Opeka, I. G. Talmy and E. J. Wuchina, 'Mechanical, Thermal, and Oxidation Properties of Refractory Hafnium and Zirconium Compounds,' *J. Eur. Ceram. Soc.*, 19 2405-2414 (1999).
24. E. Wuchina, M. Opeka, S. Causey, K. Buesking, J. Spain, A. Cull, J. Routbort and F. Guitierrez-Mora, 'Designing for Ultrahigh-Temperature Applications: The Mechanical

and Thermal Properties of HfB_2 , HfC_x , HfN_x and $\alpha\text{Hf(N)}$,' *J. Mater. Sci*, 39 [19] 5939-5949 (2004).

25. S. C. Zhang, G. E. Hilmas and W. G. Fahrenholtz, 'Pressureless Densification of Zirconium Diboride with Boron Carbide Additions,' *J. Am. Ceram. Soc.*, 89 [5] 1544-1550 (2006).

26. S. C. Zhang, G. E. Hilmas and W. G. Fahrenholtz, 'Oxidation of Zirconium Diboride with Tungsten Carbide Additions,' *J. Am. Ceram. Soc.*, 94 [4] 1198-1205 (2011).

27. X. Zhang, G. E. Hilmas and W. G. Fahrenholtz, 'Densification, Mechanical Properties, and Oxidation Resistance of TaC-TaB₂ Ceramics,' *J. Am. Ceram. Soc.*, 91 [12] 4129-4132 (2008).

28. M. Gasch and S. Johnson, 'Physical Characterization and Arcjet Oxidation of Hafnium-based Ultra High Temperature Ceramics Fabricated by Hot Pressing and Field-assisted Sintering,' *J. Eur. Ceram. Soc.*, 30 [11] 2337-2344 (2010).

29. X. Zhang, P. Hu, J. Han and S. Meng, 'Ablation Behavior of ZrB₂-SiC Ultra High Temperature Ceramics Under Simulated Atmospheric Re-entry Conditions,' *Composites Sci. Technol.*, 68 [7-8] 1718-1726 (2008).

30. Gasch, Matthew J., Ellerby, Donald T., Johnson, Sylvia, M., 'Ultra High Temperature Ceramic Composites'; pp. 197-224 in Handbook of Ceramic Composites. Kluwer Academic Publishers 2005.

31. E. V. Clougherty, R. J. Hill, W. H. Rhodes and E. T. Peters, 'Research and Development of Refractory Oxidation-Resistant Diborides, Part II, Volume II. Processing and Characterization,' *AFML-TR-68-190 (DTIC AD 866558)*.

32. E. V. Clougherty, R. L. Pober and L. Kaufman, 'Synthesis of Oxidation Resistant Metal Diboride Composites,' *Trans. TMS-AIME*, 242 [6] 1077-1082 (1968).

33. J. R. Fenter, 'Refractory Diborides as Engineering Materials,' *SAMPE Quarterly*, 2 [3] 1-115 (1971).

34. L. Kaufman, E. V. Clougherty and J. B. Berkowitz-Mattuck, 'Oxidation Characteristics of Hafnium and Zirconium Diboride,' *Trans. Metall. Soc. AIME*, 239 [4] 458-466 (1967).

35. D. E. Wiley, W. R. Manning and O. Hunter, 'Elastic Properties of Polycrystalline TiB₂, ZrB₂, and HfB₂ From Room Temperature to 1300°K,' *J. Less-Common Metals*, 18 149-157 (1969).

36. S. Guo, Y. Kagawa, T. Nishimura and H. Tanaka, 'Thermal and Electric Properties in Hot-Pressed ZrB₂-MoSi₂-SiC Composites,' *J. Am. Ceram. Soc.*, 90 [7] 2255-2258 (2007).
37. J. Han, P. Hu, X. Zhang, S. Meng and W. Han, 'Oxidation-resistant ZrB₂-SiC Composites at 2200°C,' *Composites Sci. Technol.*, 68 [3-4] 799-806 (2008).
38. X. Lu, H. Xiang, L. He, L. Sun and Y. Zhou, 'Effect of Ti Dopant on the Mechanical Properties and Oxidation Behavior of Zr₂[Al(Si)]₄C₅ Ceramics,' *J. Am. Ceram. Soc.*, 94 [6] 1872-1877 (2011).
39. J. Zou, G. Zhang, Y. Kan and P. Wang, 'Hot-Pressed ZrB₂-SiC Ceramics with VC Addition: Chemical Reactions, Microstructures, and Mechanical Properties,' *J. Am. Ceram. Soc.*, 92 [12] 2838-2846 (2009).
40. P. Lespade, N. Richet and P. Goursat, 'Oxidation Resistance of SiC Composites for Protection of Carbon-based Materials,' *Acta Astronaut.*, 60 [10-11] 858-864 (2007).
41. F. Monteverde, 'The Thermal Stability in Air of Hot-pressed Diboride Matrix Composites for Uses at Ultra-high Temperatures,' *Corros. Sci.*, 47 [8] 2020-2033 (2005).
42. T. A. Jackson, D. R. Eklund and A. J. Fink, 'High Speed Propulsion: Performance Advantage of Advanced Materials,' *J. Mater. Sci.*, 39 [19] 5905-5913 (2004).
43. D. M. Van Wie, D. G. Drewry Jr., D. E. King and C. M. Hudson, 'Hypersonic Environment: Required Operating Conditions and Design Challenges,' *J. Mater. Sci.*, 39 [19] 5915-5924 (2004).
44. M. E. White and W. R. Price, 'Affordable Hypersonic Missiles for Long-Range Precision Strike,' *J. Hopkins APL Tech. Digest*, 20 [3] 415-423 (1999).
45. F. Monteverde and L. Scatteia, 'Resistance to Thermal Shock and to Oxidation of Metal Diborides-SiC Ceramics for Aerospace Application,' *J. Am. Ceram. Soc.*, 90 [4] 1130-1138 (2007).
46. C. M. Carney, 'Oxidation Resistance of Hafnium Diboride—Silicon Carbide from 1400 to 2000°C,' *J. Mater. Sci.*, 44 [20] 5673-5681 (2009).
47. Q. N. Nguyen, E. J. Opila and R. Robinson C., 'Oxidation of Ultrahigh Temperature Ceramics in Water Vapor,' *J. Electrochem. Soc.*, 151 [10] B558-B562 (2004).
48. A. Paul, D. D. Jayaseelan, S. Venugopal, E. Zapata-Solvas, J. G. P. Binner, B. Vaidhyanathan, A. Heaton, P. Brown and W. E. Lee, 'UHTC Composites for Hypersonic Applications,' *Am. Ceram. Soc. Bull.* [91] 22-28 (2012).

49. Y. Koh, H. Kim, H. Kim and J. W. Halloran, 'Thermal Shock Resistance of Fibrous Monolithic Si_3N_4 -BN Ceramics,' *J. Eur. Ceram. Soc.*, 24 [8] 2339-2347 (2004).
50. E. J. Opila and M. C. Halbig, 'Oxidation of ZrB_2 -SiC,' *25th Annual Conference on Composites, Advanced Ceramics, Materials, and Structures: A: Ceramic Engineering and Science Proceedings*, 22 [3] 221-228 (2001).
51. A. Rezaie, W. G. Fahrenholtz and G. E. Hilmas, 'Evolution of Structure During the Oxidation of Zirconium Diboride-Silicon Carbide in Air up to 1500°C ,' *J. Eur. Ceram. Soc.*, 27 [6] 2495-2501 (2007).
52. W. C. Tripp, H. H. Davis and H. C. Graham, 'Effect of an SiC Addition on the Oxidation of ZrB_2 ,' *Ceram. Bull.*, 52 [8] 612-616 (1973).
53. F. Monteverde, A. Bellosi and S. Guicciardi, 'Processing and Properties of Zirconium Diboride-based Composites,' *J. Eur. Ceram. Soc.*, 22 [3] 279-288 (2002).
54. F. Monteverde and A. Bellosi, 'Effect of the Addition of Silicon Nitride on Sintering Behaviour and Microstructure of Zirconium Diboride,' *Scr. Mater.*, 46 [3] 223-228 (2002).
55. P. Hu, X. Zhang, J. Han, X. Luo and S. Du, 'Effect of Various Additives on the Oxidation Behavior of ZrB_2 -Based Ultra-High-Temperature Ceramics at 1800°C ,' *J. Am. Ceram. Soc.*, 93 [2] 345-349 (2010).
56. L. Kaufman and E. V. Clougherty, 'Investigation of Boride Compounds for Very High-Temperature Applications,' *RTD-TDR-63-4096*, RTD-TDR-63-4096 Part II (1965).
57. J. J. Melendez-Martinez, A. Dominquez-Rogriquez, F. Monteverde, C. Melandri and G. de Portu, 'Characterization and High Temperature Mechanical Properties of Zirconium Boride-Based Materials,' *J. Eur. Ceram. Soc.*, 22 [14/15] 2543-2549 (2002).
58. F. Monteverde, A. Bellosi and L. Scatteia, 'Processing and Properties of Ultra-high Temperature Ceramics for Space Applications,' *Materials Science & Engineering: A*, 485 [1-2] 415-421 (2008).
59. F. Monteverde and A. Bellosi, 'Efficacy of HfN as Sintering Aid in the Manufacture of Ultrahigh-Temperature Metal Diborides-Matrix Ceramics,' *J. Mater. Res.*, 19 [12] 3576-3585 (2004).
60. D. Sciti, S. Guicciardi, A. Bellosi and G. Pezzotti, 'Properties of a Pressureless-sintered ZrB_2 - MoSi_2 Ceramic Composite,' *J. Am. Ceram. Soc.*, 89 [7] 2320-2322 (2006).

61. D. Sciti, L. Silvestroni and A. Bellosi, 'Fabrication and Properties of HfB_2 - MoSi_2 Composites Produced by Hot Pressing and Spark Plasma Sintering,' *J. Mater. Res.*, 21 [6] 1460-1466 (2006).
62. D. Sciti, F. Monteverde, S. Guicciardi, G. Pezzotti and A. Bellosi, 'Microstructure and Mechanical Properties of ZrB_2 - MoSi_2 Ceramic Composites Produced by Different Sintering Techniques,' *Mater. Sci. & Eng.: A*, 434 [1-2] 303-309 (2006).
63. D. Sciti, L. Silvestroni, G. Celotti, C. Melandri and S. Guicciardi, 'Sintering and Mechanical Properties of ZrB_2 - TaSi_2 and HfB_2 - TaSi_2 Ceramic Composites,' *J. Am. Ceram. Soc.*, 91 [10] 3285-3291 (2008).
64. L. Silvestroni and D. Sciti, 'Effects of MoSi_2 Additions on the Properties of Hf- and Zr- B_2 Composites Produced by Pressureless Sintering,' *Scr. Mater.*, 57 [2] 165-168 (2007).
65. C. J. Armani, *Creep Performance of Oxide Ceramic Fiber Materials at Elevated Temperature in Air and in Steam*; PhD Dissertation, Air Force Institute of Technology, Dayton, OH 2011.
66. C. M. Carney, P. Mogilvesky and T. A. Parthasarathy, 'Oxidation Behavior of Zirconium Diboride Silicon Carbide Produced by the Spark Plasma Sintering Method,' *J. Am. Ceram. Soc.*, 92 [9] 2046-2052 (2009).
67. M. Gasch, D. Ellerby, E. Irby, S. Beckman, M. Gusman and S. Johnson, 'Processing, Properties and Arc Jet Oxidation of Hafnium Diboride-Silicon Carbide Ultra High Temperature Ceramics,' *J. Mater. Sci.*, 39 [19] 5925-5937 (2004).
68. S. R. Levine, E. J. Opila, M. C. Halbig, J. D. Kiser, M. Singh and J. A. Salem, 'Evaluation of Ultra-high Temperature Ceramics for Aeropropulsion Use,' *J. Eur. Ceram. Soc.*, 22 [14-15] 2757-2767 (2002).
69. F. Monteverde, S. Guicciardi and A. Bellosi, 'Advances in Microstructure and Mechanical Properties of Zirconium Diboride-based Ceramics,' *Materials Science & Engineering: A*, 346 [1-2] 310-319 (2003).
70. F. Monteverde and A. Bellosi, 'Development and Characterization of Metal-diboride-based Composites Toughened with Ultra-fine SiC Particulates,' *Solid State Sciences*, 7 [5] 622-630 (2005).
71. T. Lundstrom, 'Transition Metal Borides'; pp. 351-376 in Boron and Refractory Borides. Edited by V. I. Markovich (Ed.). Springer-Verlag, Berlin, 1977.
72. C. Mroz, 'Processing and Properties of Microcomposite TiZrC and TiZrB_2 Materials,' *Ceram. Eng. Sci. Proc*, 14 [9-10] 725-735 (1993).

73. C. Mroz, 'Zirconium Diboride,' *Am. Ceram. Soc. Bull.*, 76 [6] 141-142 (1994).
74. R. Thompson, 'Production, Fabrication, and Use of Borides'; pp. 113-120 in The Physics and Chemistry of Carbides, Nitrides and Borides. Edited by R. Freer (Ed.). Kluwer Academic Publishers, Dordrecht, 1990.
75. L. Y. Chen, Y. L. Gu, L. Shi, Z. H. Yang, J. H. Ma and Y. T. Qian, 'Synthesis and Oxidation of Nanocrystalline HfB_2 ,' *J. Alloys Compounds*, 368 [1-2] 353-356 (2004).
76. L. Chen, Y. Gu, Z. Yang, L. Shi, J. Ma and Y. Qian, 'Preparation and Some Properties of Nanocrystalline ZrB_2 Powders,' *Scr. Mater.*, 50 [7] 959-961 (2004).
77. Y. D. Blum, S. Young and D. Hui, 'Chemical Reactivity: In Search of Better Processing of HfB_2/SiC UHTC Composites'; pp. 103-114 in Ceramic Transactions Vol. 177: Innovative Processing and Synthesis of Ceramics, Glasses, and Composites IX. Edited by J. P. Sing, N. P. Bansal, B. G. Nair, T. Ohji and de Arellano Lopez, Antonio R. (Eds.). American Ceramic Society, Westerville, OH, 2005.
78. H. J. Feng, J. J. Moore and D. G. Wirth, '"Combustion Synthesis of Ceramic-Metal Composite Materials: The Zirconium Diboride-Aluminum System,"' *Int. J. Self-Propagating High Temp. Synth.*, 1 [2] 228-238 (1992).
79. S. K. Mishra (Pathak), S. Das, S. K. Das and P. Ramachandrarao, 'Sintering Studies on Ultrafine ZrB_2 Powder Produced by a Self-propagating High-temperature Synthesis Process,' *J. Mater. Res.*, 15 [11] 2499-2504 (2000).
80. D. D. Radev and D. Klissurski, 'Mechanochemical Synthesis and SHS of Diborides of Titanium and Zirconium,' *J. Mater. Syn. Process.*, 9 [3] 131-136 (2001).
81. A. Bellosi and F. Monteverde, 'Ultra-Refractory Ceramics: The Use of Sintering Aids to Obtain Microstructure Control and Properties Improvement,' *Euro Ceramics VIII--Part 2*, 264-268 787-792 (2004).
82. A. Bellosi, F. Monteverde and D. Sciti, 'Fast Densification of Ultra-High-Temperature Ceramics by Spark Plasma Sintering,' *International Journal of Applied Ceramic Technology*, 3 [1] 32-40 (2006).
83. A. L. Chamberlain, W. G. Fahrenholtz, G. E. Hilmas and D. T. Ellerby, 'High-Strength Zirconium Diboride-Based Ceramics,' *J. Am. Ceram. Soc.*, 87 [6] 1170-1172 (2004).
84. F. Monteverde, 'Beneficial Effects of an Ultra-fine Alpha-SiC Incorporation on the Sinterability and Mechanical Properties of ZrB_2 ,' *Applied Physics A (Materials Science Processing)*, A82 [2] 329-337 (2006).

85. F. Monteverde and A. Bellosi, 'Microstructure and Properties of an HfB_2 -SiC Composite for Ultra High Temperature Applications,' *Adv. Engr. Mat.*, 6 [5] 331-336 (2004).
86. R. Telle, L. S. Sigl and K. Takagi, 'Boride-based Hard Materials'; pp. 802-945 in Handbook of Ceramic Hard Materials. Edited by R. Riedel (Ed.). Wiley-VCH, Weinheim, Germany, 2000.
87. R. L. Coble and H. A. Hobbs, 'Sintering'; pp. 82-100 in Investigation of Boride Compounds for Very High Temperature Applications, NTIS Report AD 428006, Vol. 428006. Edited by L. Kaufman and E. V. Clougherty (Eds.). Federal Scientific and Technical Information, Springfield, VA, 1973.
88. P. S. Kisliy and O. V. Zaverukha, 'Theory and Technology of Sintering, Thermal, and Chemicothermal Treatment Processes,' *Powder Metall. Metal Ceram.*, 9 [7] 549-551 (1970).
89. H. Pastor and R. Meyer, 'An Investigation of the Effect of Additions of Metal Silicides on Titanium and Zirconium Borides From the Point of View of Their Sintering Behavior and Their Resistance to Oxidation at High Temperatures,' *Rev. Int. Htes. Temp. Refract.*, 2 41-54 (1974).
90. A. L. Chamberlain, W. G. Fahrenholtz and G. E. Hilmas, 'Pressureless Sintering of Zirconium Diboride,' *J. Am. Ceram. Soc.*, 89 [2] 450-456 (2005).
91. A. L. Chamberlain, W. G. Fahrenholtz and G. E. Hilmas, 'Reactive Hot Pressing of Zirconium Diboride,' *J. Eur. Ceram. Soc.*, 29 [16] 3401-3408 (2009).
92. A. L. Chamberlain, W. G. Fahrenholtz and G. E. Hilmas, 'Low-Temperature Densification of Zirconium Diboride Ceramics by Reactive Hot Pressing,' *J. Am. Ceram. Soc.*, 89 [12] 3638-3645 (2006).
93. F. Monteverde, 'Progress in the Fabrication of Ultra-high-temperature Ceramics: "In situ" Synthesis, Microstructure, and Properties of a Reactive Hot-pressed HfB_2 -SiC Composite,' *Composites Sci. Technol.*, 65 [11-12] 1869-1879 (2005).
94. F. Monteverde, C. Melandri and S. Guicciardi, 'Microstructure and Mechanical Properties of an HfB_2 -30 vol% SiC Composite Consolidated by Spark Plasma Sintering,' *Mater. Chem. Phys.*, 100 [2-3] 513-519 (2006).
95. V. Medri, F. Monteverde, A. Balbo and A. Bellosi, 'Comparison of ZrB_2 -ZrC-SiC Composites Fabricated by Spark Plasma Sintering and Hot-Pressing,' *Adv. Engr. Mat.*, 7 [3] 159-163 (2005).

96. F. Monteverde, 'Ultra-high Temperature HfB_2 -SiC Ceramics Consolidated by Hot-pressing and Spark Plasma Sintering,' *J. Alloys Compounds*, 428 [1-2] 197-205 (2007).
97. C. B. Barger, R. C. Benson, R. W. Newman, A. N. Jette and T. E. Phillips, 'Oxidation Mechanisms of Hafnium Carbide and Hafnium Diboride in the Temperature Range 1400 to 2100°C,' *J. Hopkins APL Tech. Digest*, 14 [1] 29-36 (1993).
98. J. B. Berkowitz-Mattuck, 'High-Temperature Oxidation III. Zirconium and Hafnium Diborides,' *J. Electrochem. Soc.*, 113 [9] 908-914 (1966).
99. H. C. Graham, H. H. Davis, I. A. Kvernes and W. C. Tripp, 'Microstructural Features of Oxide Scales Formed on Zirconium Diboride Materials'; pp. 35-48 in Ceramics in Severe Environments. Edited by W. W. Kriegel and H. Palmour III (Eds.). Plenum Press, New York, 1971.
100. A. K. Kuriakose and J. L. Margrave, 'The Oxidation Kinetics of Zirconium Diboride and Zirconium Carbide at High Temperatures,' *J. Electrochem. Soc.*, 11 [7] 827-831 (1964).
101. F. Monteverde and A. Bellosi, 'Oxidation of ZrB_2 -Based Ceramics in Dry Air,' *J. Electrochem. Soc.*, 150 [11] B552-B559 (2003).
102. W. C. Tripp and H. C. Graham, 'Thermogravimetric Study of the Oxidation of ZrB_2 in the Temperature Range of 800 to 1500°C,' *J. Electrochem. Soc.*, 118 [7] 1195-1199 (1971).
103. R. J. Irving and I. G. Worsley, 'The oxidation of titanium diboride and zirconium diboride at high temperatures,' *Journal of the Less Common Metals*, 16 [2] 103-112 (1968).
104. T. A. Parthasarathy, R. A. Rapp, M. Opeka and R. J. Kerans, 'A Model for the Oxidation of ZrB_2 , HfB_2 , and TiB_2 ,' *Acta. Mater.*, 55 [17] 5999-6010 (2007).
105. D. Cubicciotti and K. H. Lau, 'Kinetics of Oxidation of Hot-Pressed Silicon Nitride Containing Magnesia,' *J. Am. Ceram. Soc.*, 61 [11-12] 512-517 (1978).
106. W. G. Fahrenholtz, 'The ZrB_2 Volatility Diagram,' *J. Am. Ceram. Soc.*, 88 [12] 3509-3512 (2005).
107. W. Han, P. Hu, X. Zhang, J. Han and S. Meng, 'High-Temperature Oxidation at 1900°C of ZrB_2 -xSiC Ultrahigh-Temperature Ceramic Composites,' *J. Am. Ceram. Soc.*, 91 [10] 3328-3334 (2008).

108. D. Ni, G. Zhang, F. Xu and W. Guo, 'Initial Stage of Oxidation Process and Microstructure Analysis of HfB_2 -20 vol.% SiC Composite at 1500°C,' *Scr. Mater.*, 64 [7] 617-620 (2011).
109. C. M. Carney, T. A. Parthasarathy and M. K. Cinibulk, 'Oxidation Resistance of Hafnium Diboride Ceramics with Additions of Silicon Carbide and Tungsten Boride or Tungsten Carbide,' *J. Am. Ceram. Soc.*, 94 [8] 2600-2607 (2011).
110. T. A. Parthasarathy, R. A. Rapp, M. Opeka and M. K. Cinibulk, 'Modeling Oxidation Kinetics of SiC-Containing Refractory Diborides,' *J. Am. Ceram. Soc.*, 95 [1] 338-349 (2012).
111. E. W. Neuman, G. E. Hilmas and W. G. Fahrenholtz, 'Strength of Zirconium Diboride to 2300°C,' *J. Am. Ceram. Soc.*, 96 [1] 47-50 (2013).
112. I. Spivak, R. A. Andievsky, V. V. Klimenko and V. D. Lazarenko, 'Creep in the Binary Systems TiB_2 -TiC and ZrB_2 -ZrN,' *Soviet Powder Metallurg. Metal Ceram.*, 13 [8] 617-620 (1974).
113. M. Kats, S. S. Ordanyan and V. I. Unrod, 'Compressive Creep of Alloys of the ZrC - ZrB_2 and TiC - TiB_2 Systems,' *Soviet Powder Metallurg. Metal Ceram.*, 20 [12] 886-890 (1981).
114. M. W. Bird, R. P. Aune, F. Yu, P. F. Becher and K. W. White, 'Creep Behavior of a Zirconium Diboride - Silicon Carbide Composite,' *J. Eur. Ceram. Soc.*, 33 2407-2420 (2013).
115. L. Kaufman and E. V. Clougherty, 'Investigation of Boride Compounds for Very High-Temperature Applications,' *RTD-TDR-63-4096*, RTD-TDR-63-4096 Part I (1963).
116. S. Guo, 'Densification of ZrB_2 -based composites and their mechanical and physical properties: A review,' *Journal of the European Ceramic Society*, 29 [6] 995-1011 (2009).
117. L. Kaufman and H. Nesor, 'Stability Characterization of Refractory Materials Under High Velocity Atmospheric Flight Conditions. AD867307,' AFML-TR-69-84 [Part III Vol. III] (1970).
118. L. Kaufman and H. Nesor, 'Stability Characterization of Refractory Materials Under High Velocity Atmospheric Flight Conditions,' AFML-TR-69-84 [Part III Vol. II] (1969).
119. L. Kaufman and H. Nesor, 'Stability Characterization of Refractory Materials Under High Velocity Atmospheric Flight Conditions,' AFML-TR-69-84 [Part II Vol. II] (1969).

120. L. Kaufman and H. Nesor, 'Stability Characterization of Refractory Materials Under High Velocity Atmospheric Flight Conditions,' AFML-TR-69-84 [Part III Vol. 1] (1969).
121. F. Monteverde, 'The Addition of SiC particles into a MoSi₂-doped ZrB₂ Matrix: Effects on Densification, Microstructure, and Thermo-physical Properties,' *Mater. Chem. Phys.*, 113 626-633 (2009).
122. D. Sciti, L. Silvestroni, S. Guicciardi and A. Bellosi, 'Potential and Limits of SiC Chopped Fiber-Reinforced Ultra High Temperature Ceramics,' (2012).
123. L. Silvestroni, D. Sciti, C. Melandri and S. Guicciardi, 'Toughened ZrB₂-Based Ceramics Through SiC Whisker or SiC Chopped Fiber Additions,' *J. Eur. Ceram. Soc.*, 30 [11] 2155-2164 (2010).
124. H. Streckert, D. Hazlebeck, F. Montgomery, K. Norton, I. Schneir, T. Moore, J. Kaae and I. Tzartzas, 'Ceramic Fiber Coatings Development and Demonstration,' AD-A267 286 (1993).
125. E. L. Corral and R. E. Loehman, 'Ultra-High-Temperature Ceramic Coatings for Oxidation Protection of Carbon-Carbon Composites,' *J. Am. Cer. Soc.*, 91 [5] 1495-1502 (2008).
126. J. Martinez-Fernandez, 'Ultra High Temperature Ceramics for Aeropropulsion and Aerospace Use,' *Final Report 15 August 2007 - 28 January 2010*. Contract FA8655-07-1-3087. Departamento de Fisica de la Materia Condensada, University of Seville, SPAIN, July 2008.
127. R. Loehman, E. Corral, H. P. Dumm, P. Kotula and R. Randon, 'Ultra High Temperature Ceramics for Hypersonic Vehicle Applications,' *Sandia Report SAND 2006-2925* (2006).
128. W. G. Fahrenholtz and G. E. Hilmas, 'Oxidation of Ultra-high Temperature Transition Metal Diboride Ceramics,' *International Materials Reviews*, 57 [1] 61-72 (2012).
129. T. Mah and T. A. Parthasarathy, 'Fracture Toughness of Single Crystal YAG,' *Scripta Metallurgica et Materialia*, 28 1383-1385 (1993).
130. T. Mah and T. A. Parthasarathy, 'Effects of Temperature, Environment, and Orientation on the Fracture Toughness of Single-Crystal YAG,' *J. Am. Ceram. Soc.*, 80 [10] 2730-2734 (1997).
131. VLOC, 'Yttrium Aluminum Garnet Laser Materials,' *Product Catalog*. VLOC.

132. D. Halliday, R. Resnick and J. Walker, Fundamentals of Physics. John Wiley & Sons, New York, 1988.
133. A. Passerone, M. L. Muolo, F. Valenza, F. Monteverde and N. Sobczak, 'Wetting and Interfacial Phenomena in Ni-HfB₂ Systems,' *Acta Mater.*, 57 [356] 364 (2009).
134. ASM Handbook: Alloy Phase Diagrams, Vol. 5, ASM International, Materials Park, OH 1997.
135. J. K. Stalick and R. M. Waterstrat, 'The Hafnium-Platinum Phase Diagram,' *J. Phase Equil. and Diff.*, 32 [1] 15-23 (2013).
136. F. Valenza, M. L. Muolo, A. Passerone, G. Cacciamani and C. Artini, 'Control of Interfacial Reactivity Between ZrB₂ and Ni-Based Brazing Alloys,' *J. Mater. Engr. and Perform.*, 21 [5] 660-666 (2012).
137. B. Aronsson and S. Rundqvist, 'Borides, Silicides and Phosphides of the Platinum Metals,' *Platinum Metals Rev.*, 5 [3] 93-95 (1961).
138. N. Sobczak, R. Nowak, A. Passerone, F. Valenza, M. L. Muolo, L. Jaworska, F. Barberis and M. Capurro, 'Wetting and Joining of HfB₂ and Ta with Ni,' *Prace Instytutu Odlewnictwa*, 50 5-14 (2010).
139. A. Passerone, M. L. Muolo, F. Valenza and L. Kaufman, 'Wettability of HfB₂ by Molten Ni(B) Alloys Interpreted by CALPHAD Methods, Part 2: Wetting and Interfacial Reactivity,' *CALPHAD: Computer Coupling of Phase Diagrams and Thermochemistry*, 34 6-14 (2010).
140. Z. Ding, L. Qui, J. Zhang, B. Yao, T. Cui, W. Guan, W. Zheng, W. Wang, X. Zhao and X. Liu, 'Platinum boride nanowires: Synthesis and characterization,' *J. Alloys Compounds*, 521 66-70 (2012).
141. G. V. Samsonov and V. A. Kosenko, 'Conditions of Preparation of Borides of the Platinum-Group Metals,' *Soviet Powder Metallurg. Metal Ceram.*, 10 [8] 614-618 (1971).
142. P. Villars and L. D. Calvert, Pearson's Handbook of Crystallographic Data for Intermetallic Phases. ASM International 1991.
143. G. J. K. Acres, 'The Reaction between Hydrogen and Oxygen on Platinum: Progress in Establishing Kinetics and Mechanisms,' *Platinum Metals Rev.*, 10 [2] 60-64 (1966).
144. A. Guy, 'Platinum-catalysed Oxidation of Ammonia,' *Royal Society of Chemistry Education in Chemistry* March 5, 2015 (2009).

145. D. C. Clarke, 'The Wetting and Dewetting of Grain Boundaries'; pp. 569-576 in Ceramic Microstructures '86, Vol. 21. Edited by J. A. Pask and A. G. Evans (Eds.). Springer US 1987.
146. V. Traskine, P. Protsenko, Z. Skvortsova and P. Volovitch, 'Grain Boundary Wetting in Polycrystals: Wettability of Structure Elements and Liquid Phase Connectivity (Part I),' *Colloids and Surfaces A: Physiochemical and Engineering Aspects*, 166 261-268 (2000).
147. M. W. Barsoum, Fundamentals of Ceramics. Taylor & Francis Group, New York, NY, 2003.
148. C. B. Carter and M. G. Norton, Ceramic Materials, Science and Engineering. Springer Science+Business Media, LLC, New York, NY, 2013.
149. W. D. Kingery, H. K. Bowen and D. R. Uhlmann, Introduction to Ceramics. John Wiley & Sons, New York Chichester Brisbane Toronto Singapore, 1976.
150. R. W. Rice, 'Mechanical Properties of Ceramics and Composites: Grain and Particle Effects'. Marcel Dekker, Inc., New York, NY, 2000.
151. L. Lutterotti, D. Chateigner, S. Ferrari and J. Ricote, 'Texture, Residual Stress, and Structural Analysis of Thin Films Using a Combined X-Ray Analysis,' *Thin Solid Films*, 450 34-41 (2004).
152. T. Mah, K. A. Keller, S. Sambasivan and R. J. Kerans, 'High Temperature Environmental Stability of the Compounds in the Al_2O_3 - Y_2O_3 System,' *J. Am. Ceram. Soc.*, 80 [4] 874-878 (1997).
153. Y. Ashuach, *The Influence of Sintering Additives on the Microstructure and Properties of ALON*; M.S. Thesis, Israel Institute of Technology, Haifa, Israel, 2003.
154. T. M. Hartnett, R. L. Gentilman and E. A. Maguire, 'Aluminum Oxynitride Having Improved Optical Characteristics and Method of Manufacture,' [U.S. Patent 4,481,300] (1984).
155. T. Lee and A. Navrotsky, 'Enthalpy of Formation of Cubic Yttria-Stabilized Hafnia,' *J. Mater. Res.*, 19 [6] 1855-1861 (2004).
156. D. W. Stacy and D. R. Wilder, 'The Yttria-Hafnia System,' *J. Am. Cer. Soc.*, 58 [7-8] 285 (1975).
157. X. Xia, *Computational Modeling Study of Yttria-Stabilized Zirconia*; PhD Dissertation, University College London, London, UK 2010.

158. J. Chase Malcolm W., NIST-JANAF Thermochemical Tables, Vol. Part I, Al-CO. American Chemical Society & American Institute of Physics 1998.
159. Chegg, 'Chemistry,' <http://www.chegg.com/homework-help/questions-and-answers/consider-following-reaction-caco3-s-cao-s-co2-using-thermodynamic-data-tables-calculate-eq-q767336>
160. Chemistry Software Ltd, 'HSC Chemistry,' computer program.
161. V. M. Denisov, L. T. Denisova, I. A. Gudim, V. A. Temerov, G. S. Patrin, N. V. Volkov and L. G. Chumilina, 'Heat Capacity of $\text{YAl}_3(\text{BO}_3)_4$ in the Range of 329-1051 K,' *Doklady Physics*, 58 [12] 533-534 (2013).
162. O. Fabrichnaya, H. J. Seifert, T. Ludwig and Aldinger, Fritz, Navrotsky, Alexandra, 'The Assessment of Thermodynamic Parameters in the Al_2O_3 - Y_2O_3 System and Phase Relations in the Y-Al-O System,' *Scandinavian J. of Metallurgy*, 30 [3] 175-183 (2001).
163. C. T. Lynch, 'Hafnium Oxide'; pp. 193-216 in High Temperature Oxides Part II Oxides of Rare Earths, Titanium, Zirconium, Hafnium, Niobium, Tantalum. Edited by A. M. Alper (Ed.). Academic Press, New York and London, 1970.
164. H. Ding, A. V. Virkar and F. Liu, 'Defect Configuration and Phase Stability of Cubic Versus Tetragonal Yttria-stabilized Zirconia,' *Solid State Ionics*, 215 16-23 (2012).
165. F. Heshmatpour, Z. Khodaiy and R. B. Afhakhanpour, 'Synthesis and Characterization of Pure Tetragonal Nanocrystalline Sulfated 8YSZ Powder by Sol-gel Route,' *Powder Technology*, 224 12-18 (2012).
166. E. Kock, M. Kogler, T. Biele, B. Klotzer and S. Penner, 'In Situ FT-IR Spectroscopic Study of CO_2 and CO Adsorption on Y_2O_3 , ZrO_2 , and Yttria-Stabilized ZrO_2 ,' *J. Phys. Chem C.*, 117 17666-17673 (2013).
167. K. Pokrovski, K. T. Jung and A. T. Bell, 'Investigation of CO and CO_2 Adsorption on Tetragonal and Monoclinic Zirconia,' *Langmuir*, 17 [14] 4297-4303 (2001).
168. K. Tomishige, Y. Ikeda, T. Sakaihorii and K. Fujimoto, 'Catalytic Properties and Structure of Zirconia Catalysts for Direct Synthesis of Dimethyl Carbonate from Methanol and Carbon Dioxide,' *J. Catalysis*, 192 355-362 (2000).
169. X. Xia, R. Oldman and C. R. Catlow, 'Oxygen Adsorption and Dissociation on Yttria Stabilized Zirconia Surfaces,' *J. Mater. Chem.*, 22 [17] 8594-8612 (2012).
170. J. J. Zhu, S. Albertsma, J. G. van Ommen and L. Lefferts, 'Role of Surface Defects in Activation of O_2 and N_2O on ZrO_2 and Yttrium-Stabilized ZrO_2 ,' *J. Phys. Chem. B*, 109 [19] 9550-9555 (2005).

171. R. P. Haggerty, P. Sarin, Z. D. Apostolov, P. E. Driemeyer and W. M. Kriven, 'Thermal Expansion of HfO_2 and ZrO_2 ,' *J. Am. Ceram. Soc.*, 97 [7] 2213-2222 (2014).
172. L. Gao, L. Zhou, J. Feng, L. Bai, C. Li, Z. Liu, J. Soubeyroux and Y. Lu, 'Manganese Doped Hafnia,' *Proceedings of the 38th Ceramics International Conference*, 2305-2311 (2012).
173. R. Ruh and P. W. R. Corfield, 'Crystal Structure of Monoclinic Hafnia and Comparison with Monoclinic Zirconia,' *J. Am. Cer. Soc.*, 53 [3] 126-129 (1970).
174. R. Terki, G. Bertrand, H. Aourag and C. Coddet, 'Cubic-to-Tetragonal Phase Transition of HfO_2 from Computational Study,' *Materials Letters*, 62 1484-1486 (2008).
175. NIST, 'Basic Atomic Spectroscopic Data,'
<http://www.physics.nist.gov/PhysRefData/Handbook/index.cfm>
176. J. A. Rodriguez, J. Hrbek, Z. Chang, J. Dvorak, T. Jirsak and A. Maiti, 'Importance of O Vacancies in the Behavior of Oxide Surfaces: Adsorption of Sulfur on TiO_2 (110),' *Phys. Rev. B*, 65 (2002).
177. S. S. Zumdahl, 'Chemical Principles'. Brooks/Cole, Cengage Learning 2009.
178. J. B. Peri and R. B. Hannan, 'Surface Hydroxyl Groups on γ -Alumina,' *J. Phys. Chem.*, 64 1526-1530 (1960).
179. S. Takeda, M. Fukawa, Y. Hayashi and K. Matsumoto, 'Surface OH Group Governing Adsorption Properties of Metal Oxide Films,' *Thin Solid Films*, 339 220-224 (1999).
180. M. Kogler, E. Kock, T. Biele, K. Pfaller, B. Klotzer, D. Schmidmair, L. Perfler and S. Penner, 'Hydrogen Surface Reactions and Adsorption Studied on Y_2O_3 , YSZ, and ZrO_2 ,' *J. Phys. Chem. C*, 118 8435-8444 (2014).
181. J. Zhu, J. G. van Ommen and L. Lefferts, 'Effects of Surface OH Groups on Catalytic Performance of Yttrium-Stabilized ZrO_2 in Partial Oxidation of CH_4 to Syngas,' *Catalysis Today*, 117 163-167 (2006).
182. S. R. Choi, L. M. Powers, F. A. Holland and J. P. Gyekenyesi, 'Creep of a Silicon Nitride Under Various Specimen/Loading Configurations,' 291-298 (2001; 2007).
183. D. J. Greene, An Introduction to the Mechanical Properties of Ceramics. Cambridge University Press 1998.
184. R. G. Munro, 'Material Properties of Titanium Diboride,' *J. Res Natl. Inst. Stand. Technol.*, 105 709-720 (2000).

185. Z. C. Jou, S. Y. Kuo and A. V. Virkar, 'High Temperature Creep in Polycrystalline AlN-SiC Ceramics,' *J. Mater. Sci.*, 21 3015-3018 (1986).
186. P. Hu and Z. Wang, 'Flexural Strength and Fracture Behavior of ZrB₂-SiC Ultra-high Temperature Ceramic Composites at 1800°C,' *J. Eur. Ceram. Soc.*, 30 [4] 1021-1026 (2010).
187. D. J. Barber and P. G. Meredith, Deformation Processes in Minerals, Ceramics, and Rocks; pp. 138-178. Unwin Hyman, London, England, 1990.
188. C. W. Passchier and R. A. Trouw, Microtectonics. Springer-Verlag, Berlin, 1998.
189. R. H. Vernon, A Practical Guide to Microstructure. Cambridge University Press, Cambridge, 2004.
190. H. R. Wenk, Preferred Orientation in Deformed Metals and Rocks: An Introduction to Modern Texture Analysis; pp. 183-218. Academic Press, Inc, Orlando, 1985.
191. T. A. Parthasarathy, M. K. Cinibulk and M. Opeka, 'Modeling and Evaluating the Environmental Degradation of UHTCs under Hypersonic Flow' in Ultra-High Temperature Ceramics: Materials for Extreme Environment Applications. Edited by W. G. Fahrenholtz, E. J. Wuchina, W. E. Lee and Y. Zhou (Eds.). Wiley 2014.
192. A. DeGregoria, unpublished work, Air Force Institute of Technology, 2015.
193. C. Anghel, *Studies of Transport in Oxides on Zr-based Materials*, Licentiate Thesis, Royal Institute of Technology, KTH, Stockholm, Sweden, 2004.
194. M. Aoki, Y. Chiang, I. Kosacki, L. J. Lee, H. Tuller and Y. Liu, 'Solute Segregation and Grain-Boundary Impedance in High-Purity Stabilized Zirconia,' *J. Am. Ceram. Soc.*, 79 [5] 1169-1180 (1996).
195. S. P. S. Badwal and J. Drennan, 'Yttria-zirconia: Effect of Microstructure on Conductivity,' *J. Mater. Sci.*, 22 3231-3239 (1987).
196. W. G. Fahrenholtz, 'Thermodynamic Analysis of ZrB₂-SiC Oxidation: Formation of a SiC-Depleted Region,' *J. Am. Ceram. Soc.*, 90 [1] 143-148 (2007).
197. T. A. Parthasarathy, R. A. Rapp, M. Opeka and R. J. Kerans, 'Effects of Phase Change and Oxygen Permeability in Oxide Scales on Oxidation Kinetics of ZrB₂ and HfB₂,' *J. Am. Ceram. Soc.*, 92 [5] 1079-1086 (2009).
198. S. N. Karlsdottir, J. W. Halloran and A. N. Grundy, 'Zirconia Transport by Liquid Convection During Oxidation of Zirconium Diboride-Silicon Carbide,' *J. Am. Ceram. Soc.*, 91 [1] 272-277 (2008).

199. S. N. Karlsdottir, J. W. Halloran and C. E. Henderson, 'Convection Patterns in Liquid Oxide Films on ZrB₂-SiC Composites Oxidized at a High Temperature,' *J. Am. Ceram. Soc.*, 90 [9] 2863-2867 (2007).
200. K. Shugart, W. Jennings and E. Opila, 'Initial Stages of ZrB₂-30 vol% SiC Oxidation at 1500°C,' *J. Am. Ceram. Soc.*, 97 [5] 1645-1651 (2014).
201. C. M. Carney, personal communication, Air Force Research Laboratory, 2013.
202. K. Shugart, B. Patterson, D. Lichtman, S. Liu and E. Opila, 'Mechanisms for Variability of ZrB₂-30 vol% SiC Oxidation Kinetics,' *J. Am. Ceram. Soc.*, 97 [7] 2279-2285 (2014).
203. M. Ruggles-Wrenn and J. C. Braun, 'Effects of Steam Environment on Creep Behavior of Nextel™720/alumina Ceramic Composite at Elevated Temperature,' *Materials Science & Engineering: A*, 497 [1] 101-110 (2008).
204. K. L. Luthra, 'Oxidation of Carbon/carbon Composites - A Theoretical Analysis,' *Carbon*, 26 [2] 217-224 (1988).
205. J. B. Wachtman, Mechanical Properties of Ceramics. Wiley 1996.
206. M. Takeda, J. Sakamoto, Y. Imai, H. Ichikawa and T. Ishikawa, 'Properties of Stoichiometric Silicon Carbide Derived From Polycarbosilane,' [4] 133-141 (1994).
207. A. Gallardo-Lopez, A. Munoz, J. Martinez-Fernandez and A. Dominguez-Rodriguez, 'High-temperature Compressive Creep of Liquid Phase Sintered Silicon Carbide,' *Acta. Mater.*, 47 [7] 2185-2195 (1999).
208. G. S. Corman, 'Creep of 6H Alpha-Silicon Carbide Single Crystals,' *J. Am. Ceram. Soc.*, 75 [12] 3421-3424 (1992).
209. J. E. Lane, C. H. Carter Jr. and R. F. Davis, 'Kinetics and Mechanisms of High-Temperature Creep in Silicon Carbide: III, Sintered alpha-Silicon Carbide,' *J. Am. Cer. Soc.*, 71 [4] 281-295 (1988).
210. H. Kishimoto, N. Sakai, K. Yamaji, T. Hotita, Y. Xiong, M. E. Brito and H. Yokokawa, 'Destabilization of Cubic-stabilized Zirconia Electrolyte Induced by Boron Oxide Under Reducing Atmosphere,' *J. Mater. Sci.*, 44 639-646 (2009).
211. Meta-Synthesis, 'Chemical Entity Data Page: Metaborate Ion,' *The Chemical Thesaurus*.
212. M. Winter, 'WebElements: The periodic table on the web,', 2014 [March].

213. A. Vegas, 'New Description of the $\text{Ca}_3(\text{BO}_3)_2$ Structure,' *Acta Crystallographica Section C*, 41 [11] 1689-1690 (1985).
214. National Center for Biotechnology Information, 'PubChem: Open Chemistry Database,'.
215. D. R. Gaskell, 'Introduction to the Thermodynamics of Materials'. Taylor & Francis Group, LLC 2008.
216. J. Porter, 'Charging Presentation,'.

REPORT DOCUMENTATION PAGE				<i>Form Approved OMB No. 0704-0188</i>	
<small>The public reporting burden for this collection of information is estimated to average 1 hour per response, including the time for reviewing instructions, searching existing data sources, gathering and maintaining the data needed, and completing and reviewing the collection of information. Send comments regarding this burden estimate or any other aspect of this collection of information, including suggestions for reducing the burden, to Department of Defense, Washington Headquarters Services, Directorate for Information Operations and Reports (0704-0188), 1215 Jefferson Davis Highway, Suite 1204, Arlington, VA 22202-4302. Respondents should be aware that notwithstanding any other provision of law, no person shall be subject to any penalty for failing to comply with a collection of information if it does not display a currently valid OMB control number.</small>					
PLEASE DO NOT RETURN YOUR FORM TO THE ABOVE ADDRESS.					
1. REPORT DATE (DD-MM-YYYY)		2. REPORT TYPE		3. DATES COVERED (From - To)	
4. TITLE AND SUBTITLE				5a. CONTRACT NUMBER	
				5b. GRANT NUMBER	
				5c. PROGRAM ELEMENT NUMBER	
6. AUTHOR(S)				5d. PROJECT NUMBER	
				5e. TASK NUMBER	
				5f. WORK UNIT NUMBER	
7. PERFORMING ORGANIZATION NAME(S) AND ADDRESS(ES)				8. PERFORMING ORGANIZATION REPORT NUMBER	
9. SPONSORING/MONITORING AGENCY NAME(S) AND ADDRESS(ES)				10. SPONSOR/MONITOR'S ACRONYM(S)	
				11. SPONSOR/MONITOR'S REPORT NUMBER(S)	
12. DISTRIBUTION/AVAILABILITY STATEMENT					
13. SUPPLEMENTARY NOTES					
14. ABSTRACT					
15. SUBJECT TERMS					
16. SECURITY CLASSIFICATION OF:			17. LIMITATION OF ABSTRACT	18. NUMBER OF PAGES	19a. NAME OF RESPONSIBLE PERSON
a. REPORT	b. ABSTRACT	c. THIS PAGE			19b. TELEPHONE NUMBER (Include area code)